

SATELLITE BASED REMOTE SENSING OF HALOGENS IN THE ARCTIC TROPOSPHERE, UNDER THE IMPACT OF ARCTIC AMPLIFICATION

M.Sc.
Ilias Bougoudis



Dissertation zur Erlangung des Grades
Doktor der Naturwissenschaften

 **Universität Bremen**

Institut für Umweltphysik
Fachbereich 1
Universität Bremen
August 2021

Satellite based remote sensing of halogens in the Arctic troposphere, under the impact of Arctic Amplification

Dissertation zur Erlangung des akademischen
Grades des Doktor der Naturwissenschaften

(Dr. rer. nat.)

Volgelegt von **Ilias Bougoudis**

1. Gutachter: Prof. Dr. John P. Burrows

2. Gutachter: Prof. Dr. Thomas Wagner

Betreuer: Dr. Anne-Marlene Blechschmidt

Dissertation eingereicht am: 18.08.2021

Datum des Kolloquiums: 06.10.2021



Universität Bremen
Institut für Umweltphysik
Fachbereich Physik and Elektrotechnik (FB1)
Otto-Hahn-Alle 1, Gebäude NW1
Postfach 330440, D-28334, Bremen

TABLE OF CONTENTS

Abstract	vii
Publications	xi
Acknowledgements	xiii
List of Figures	xv
List of Tables	xxvii
Motivation and Outline	xxix
1 Theoretical Background	1
1.1 The Earth's Atmosphere	1
1.2 Arctic Amplification	4
1.3 Halogens in the Atmosphere	6
1.3.1 Halogens in the Stratosphere	8
1.3.2 Halogens in the Troposphere	9
1.4 Absorption Spectroscopy	12
1.4.1 Solar Spectrum	12
1.4.2 Absorption	13
1.4.3 Scattering	14
1.5 Satellite Remote Sensing	15
1.5.1 DOAS	16
1.5.2 Instruments	17
1.6 Artificial Neural Network	19
2 Methods, Algorithms and Datasets	21
2.1 Satellite Retrieval	21

2.1.1	Approach	21
2.1.2	Sensitivity Tests	27
2.1.3	OMI	32
2.2	Stratospheric Contribution.....	35
2.3	Datasets used in this Study	36
2.3.1	Sea Ice Age.....	37
2.3.2	Meteorological Parameters – Sea Ice Thickness	37
2.3.3	Cyclones	37
2.4	Artificial Neural Network.....	38
3	BrO Column Densities and Trends.....	43
3.1	Arctic	43
3.1.1	Time-series	44
3.1.2	Maps	50
3.2	Hudson Bay	53
3.2.1	Time-series	54
3.2.2	Maps	56
3.3	Trends	58
3.3.1	Arctic.....	59
3.3.2	Hudson Bay	67
3.4	Summary and Discussion	78
4	The Relationship between Tropospheric BrO VCD, Sea Ice and Meteorological Conditions	81
4.1	Relationship of Tropospheric BrO VCD and Sea Ice Age.....	81
4.1.1	Sea Ice Flagging.....	81
4.1.2	Arctic Region (70.0° N to 85.0° N).....	83
4.2	Relationship of Tropospheric BrO VCD and Air Temperature	92

4.2.1 Arctic Region (70.0° N to 85.0° N).....	92
4.2.2 Hudson Bay.....	96
4.3 Relationship of Tropospheric BrO VCD and Mean Sea Level Pressure.....	100
4.3.1 Arctic Region (70.0° N to 85.0° N).....	100
4.3.2 Hudson Bay.....	104
4.4 Relationship of Tropospheric BrO VCD and Wind Speed.....	106
4.4.1 Arctic Region (70.0° N to 85.0° N).....	107
4.4.2 Hudson Bay.....	110
4.5 Relationship of Tropospheric BrO VCD and Boundary Layer Height.....	112
4.5.1 Arctic Region (70.0° N to 85.0° N).....	113
4.5.2 Hudson Bay.....	116
4.6 Relationship of Tropospheric BrO VCD and Other Parameters.....	119
4.6.1 Sea Ice Thickness.....	119
4.6.2 Vertical Wind Velocity.....	120
4.6.3 Cyclonic Activity.....	122
4.7 Summary and Discussion.....	125
5 Artificial Intelligence for Tropospheric BrO VCD Modeling.....	129
5.1 Sensitivity Tests.....	129
5.2 Case Studies.....	135
5.3 Long-term Predictions.....	141
5.4 Summary and Discussion.....	147
6 Conclusions and Outlook.....	149
6.1 BrO Retrieval and Tropospheric BrO Trends.....	149
6.2 Relationship between Tropospheric BrO VCD and Driving Mechanisms.....	150
6.3 Tropospheric BrO VCD Modeling.....	151

Bibliography 153

ABSTRACT

Bromine plays a crucial role in polar atmospheric composition. During springtime, photochemistry converts bromine compounds originating from ice and snow into gaseous reactive bromine radicals (Br), which deplete ozone in the boundary layer, forming bromine oxides (BrO). Due to the autocatalytic nature of the reaction mechanism, it has been called bromine explosion. The strong relationship of bromine photochemistry and release from its sources to ozone depletion events (ODEs) was discovered in the late 1980s. Since then, and because of the importance of tropospheric ozone (the primary source of hydroxyl radical (OH), the major oxidizing agent of the atmosphere), many studies focused on the mechanisms which release bromine into the troposphere and the driving parameters which enhance BrO production and therefore ozone depletion.

Arctic Amplification (AA) is the phenomenon that surface temperature in high latitudes increases more rapidly than at lower latitudes. One of the most profound consequences of AA is the significant changes in sea ice conditions. Sea ice extent, age and thickness are drastically changing. Inevitably, all aspects of the Arctic ecosystem are expected to be affected by Arctic Amplification.

Remote sensing from satellites can be extremely useful for studying the Arctic region. By the end of the 1970s, sea ice concentration was successfully monitored by satellite sensors. Since 1995, we also have the ability to study atmospheric composition worldwide with data retrieved from nadir radiance spectra from a series of European satellite sensors: GOME on ERS-2 (1995 - 2003), SCIAMACHY on ENVISAT (2002 - 2012), GOME-2A on MetOpA (2007 - today) and GOME-2B on MetOpB (2012 - today).

The focus of this thesis is twofold: firstly, to create the first consolidated and consistent long-term (1996 to 2017) tropospheric BrO dataset for the Arctic region and the Hudson Bay (a well-known hotspot for bromine explosion events), retrieved from the four ultraviolet-visible (UV-VIS) sensors mentioned above, in order to assess the changes and the impact that AA has on tropospheric BrO. Since the different satellite instruments have different instrumental attributes and the fact that BrO is a weak absorber in the UV spectral region, many sensitivity retrieval tests have been performed in order to identify the proper fitting settings for each instrument and to derive a high-quality BrO dataset with high consistency between the instruments. Vertical column densities (VCD) of tropospheric BrO are extracted from total (geometric) VCDs, using a climatology of stratospheric BrO VCDs from a chemical transport model. The BrO time-series (geometric and tropospheric VCDs) show remarkable agreement during the overlapping periods between the sensors (the best agreement being between SCIAMACHY and GOME-2A with a

correlation coefficient squared of 0.97). Additionally, the agreement is verified by studying daily and monthly maps of geometric and tropospheric BrO VCD. This agreement allows us to create a merged tropospheric BrO VCD dataset, the basis for deriving geophysical conclusions on the impact of AA on the Arctic BrO atmospheric composition. By studying the trends of tropospheric BrO VCDs, we infer an increase of around 1% per year. The increase is significant during polar spring, reaching 1.5% per year. A similar increase can be observed for the Hudson Bay, where tropospheric BrO VCD have increased around 0.9% per year for the spring period and 2.3% per year for the winter period. However, the increasing trend is not monotonic, and variability on the tropospheric BrO VCD appear (e.g. 2016 and 2017 are lower than 2015 for the Arctic region), as many parameters influence bromine release and subsequent BrO formation.

Secondly, the link of observed tropospheric BrO VCDs to possible bromine sources and favoring weather conditions was investigated. The primary source of inorganic bromine release in the Arctic atmosphere is sea ice, especially first year ice, which is rich in sea salts. Therefore, a long-term sea ice age dataset from NSIDC was compared to the tropospheric BrO VCD dataset. The increase of first year ice extent due to the changes in the Arctic climate is in general agreement with the observed increase in tropospheric BrO, with a moderate daily correlation coefficient of +0.32, but a strong yearly one of +0.62. Also, the increase of the occurrences of first year ice over some regions in the Arctic (i.e. northeast of Greenland) is correlated with the increase of tropospheric BrO VCD in these regions. Apart from the bromine sources, driving mechanisms, like air temperature, wind speed, boundary layer height, and cyclone activity, can contribute to the Amplification, transport, vertical uplifting and recycling of tropospheric BrO plumes. Consequently, similar comparisons have been performed between tropospheric BrO and meteorological data. We infer that the parameter with the most substantial influence on the formation of bromine explosion events is air temperature, with a correlation coefficient of -0.54 (anti-correlation) for the Arctic during spring and -0.78 for Hudson Bay spring. Furthermore, the spatial agreement and correlation between trend maps of tropospheric BrO VCD and air temperature verify the anti-correlation between the two quantities.

However, the bromine release and the formation, transport, and re-cycling of BrO plumes are complex and dynamic phenomena. They depend on many geophysical parameters, and there are also complex relationships between these parameters. Therefore, single individual linear comparisons between tropospheric BrO VCDs and key parameters of BrO formation cannot fully represent the actual relationship between them. This leads us to the effort of employing, for the first time, an artificial intelligence neural network in order to model and predict Arctic tropospheric BrO VCDs using the parameters contributing to tropospheric BrO formation. By training the neural network only with one year of data, it can reproduce accurately (both spatially and in magnitude) many BrO plumes which occurred in other years. This ability of the neural network to efficiently model some bromine explosion events allows us to distinguish them between those occurring at the surface and those at higher altitudes. From studying the effect of each of the individual key parameters on the magnitude of modeled tropospheric BrO VCD, we

conclude that air temperature and mean sea level pressure (which can describe the boundary conditions under which bromine is released) have the highest impact.

PUBLICATIONS

Some parts of this thesis have already been published in peer reviewed articles in scientific journals, conference talks and posters, presentations in seminars. All of them were produced during this thesis. Sections and subsections which contain such parts are indicated with a footnote.

Peer-reviewed publications

1. **Bougoudis, I.**, Blechschmidt, A.-M., Richter, A., Seo, S., Burrows, J. P., Theys, N., and Rinke, A.: Long-term time series of Arctic tropospheric BrO derived from UV–VIS satellite remote sensing and its relation to first-year sea ice, *Atmos. Chem. Phys.*, 20, 11869–11892, <https://doi.org/10.5194/acp-20-11869-2020>, 2020.
2. Seo, S., Richter, A., Blechschmidt, A.-M., **Bougoudis, I.**, and Burrows, J. P.: Spatial distribution of enhanced BrO and its relation to meteorological parameters in Arctic and Antarctic sea ice regions, *Atmos. Chem. Phys. Discuss.*, <https://doi.org/10.5194/acp-2019-996>, 2020.
3. Seo, S., Richter, A., Blechschmidt, A.-M., **Bougoudis, I.**, and Burrows, J. P.: First high-resolution BrO column retrievals from TROPOMI, *Atmos. Meas. Tech.*, 12, 2913–2932, <https://doi.org/10.5194/amt-12-2913-2019>, 2019.

Selected conference contributions

1. Satellite Remote Sensing of Halogens in the Arctic Troposphere (Poster), DPG Spring Meeting, Bremen, 2017, DOI: 10.13140/RG.2.2.21230.61768
2. A Low Cost Forecasting Framework for Air Pollution (Poster), Mathematical Signal Processing and Data Analysis, DOI: 10.13140/RG.2.2.28880.20486
3. Long-term Time-series of Arctic BrO Derived From UV-VIS Satellite Remote Sensing (Poster), 27th International Polar Conference, Rostock, 25 - 29 March 2018, DOI: 10.13140/RG.2.2.33107.48163
4. Long-term Time-series of Arctic BrO Derived From Satellite Remote Sensing (Poster), 2nd (AC)³ Science Conference on Arctic Amplification, 12 – 14 November 2018, Bremerhaven
5. Investigating long-term Evolution of Arctic BrO and Links to Driving Mechanisms and Sources under the Impact of Arctic Amplification (Poster), 2nd (AC)³ Science Conference on Arctic Amplification, 12 – 14 November 2018, Bremerhaven

6. Long-term Time-series of Arctic BrO Derived from Satellite Remote Sensing and its Relation to Driving Mechanisms under the Impact of Arctic Amplification (Poster), EGU General Assembly 2019, 7-12 April 2019, Vienna, Austria
7. Long-term Time-series of Tropospheric BrO over the Arctic Derived From Satellite Remote Sensing and its Relation to Driving Mechanisms under the Impact of Arctic Amplification (Poster), AGU Fall Meeting 2019, 09-13 December 2019, San Francisco, United States
8. Investigating the Relationship between Arctic Tropospheric BrO retrieved using Satellite Remote Sensing and Sea Ice Age and Meteorological Parameters during Arctic Amplification (Poster), EGU General Assembly 2020, 04-08 May 2020, Online

Honors and awards

1. Best poster award in the 2nd (AC)³ Science Conference on Arctic Amplification, Bremerhaven, Germany
2. Poster Award in the 27th International Polar Conference, Rostock, Germany

ACKNOWLEDGEMENTS

As this journey comes to its end, rewinding and remembering all these moments throughout it makes me feel great appreciation for so many people that I met, who contributed, not only in completing the scientific tasks that were assigned to me, but also in helping me become a better person. In addition, the opportunity that was given to me to work and provide one, maybe tiny, but significant contribution, to one of the most challenging problems of our and future generations, climate change, can only make me feel grateful. Therefore, I would firstly like to express my sincere thanks to Professor John P. Burrows and my supervisor Anne-Marlene Blechschmidt for accepting me at the Institute of Environmental Physics at the University of Bremen. I will forever admire the passion and dedication of Professor John P. Burrows on his work, values that helped me and motivated me to continue through my PhD. I should also mention the continuous supervision of Anne-Marlene Blechschmidt, which, although intense at some points, guided me and elevated both my scientific background on the topic and my personality.

I am very thankful to Prof. Thomas Wagner from the Max Planck Institute for Chemistry in Mainz, for accepting to review my PhD thesis and be the second examiner in my defense. I would also like to thank Prof. Mihalis Vrekoussis for both the personal and professional connection we established, and for being the third examiner.

I am extremely grateful to the entire DOAS group (Tim, Lisa, Miriam, Leonardo, Andreas Meier, Anja, Kai, Kezia, Anne, Andreas Richter, Andreas Hilboll, Sora, Bianca, Folkard, Andre, Bram, Enno) for all the nice moments we shared during lunches, meetings and outdoor activities. I would like to individually thank Mr Andreas for showing me the way. Also, many thanks to Stephanie, Anja, Anna and the Heikos for their administrative support and to other colleagues in IUP (Kai-Uwe, Elpida, Evgenia, Nikos, Liza, Soheila, Marco, Luca, Narges) for all the advice and conversations we had. Finally, special thanks to my (AC)³ colleagues from Leipzig and Cologne (Daniel, Ana, Rosa, Carola, Vasilis, Jacob and Elena) for all the nice moments during meetings and conferences.

I am very lucky because all these years, I have been surrounded by wonderful friends, most of them outside academia. Therefore, I owe special thanks to Giannis, Natalia, Maria, Alexis, Sotiria, Marilia, Natasa, Ermioni, Valeriia and Alexandra. Without them, I would not have been able to complete my PhD.

Lastly, I would like to sincerely thank my family for supporting me all these years, and my friends back in Greece with whom we stayed in touch and comforted me during hard times (Stavros, Spyros, Pasxalis, Alexandra, Elena, Panagiotis, Nikolas, Kostas, Evaggelia, Kostas).

LIST OF FIGURES

Figure 1: Surface temperature evolution versus the 1850-1900 average as a pre-industrial reference (Knutson et al., 2017). The contribution of human and natural drivers are based on an empirical approach using multiple linear regression and energy balance models.	xxix
Figure 2: Mean surface temperature anomalies (by location and year, measured in Kelvin), with respect to the 1951-1980 reference time frame. (Figure provided by the NASA Goddard Institute for Space Studies Team through their webpage at https://data.giss.nasa.gov/gistemp/).....	xxx
Figure 3: The bromine explosion (Figure from Jones et al., 2009).....	xxxi
Figure 1.1: The vertical structure of the Earth’s atmosphere, as a function of temperature (https://www.azimuthproject.org/azimuth/show/Blog+-+the+color+of+night).	1
Figure 1.2: Evolution of the composition of the Earth’s atmosphere (http://elte.prompt.hu/sites/default/files/tananyagok/AtmosphericChemistry/ch01.html).....	3
Figure 1.3: Yearly temperature anomalies, based on a long-term temperature average (1951 to 1980), from meteorological stations and ocean areas. Y-axis is latitude, x-axis is the year, color coding shows is the temperature anomaly (NASA GISTEMP, http://data.giss.nasa.gov/gistemp).	5
Figure 1.4: Climatological means of Arctic sea ice extent for the record low years derived from satellite measurements. The grey curve is the long-term average (1981 – 2010) (https://www.meereisportal.de/en/).	6
Figure 1.5: The four main halogens, together with their relative size, melting and boiling point, and state (https://www.slideshare.net/KALYANIPALANICHAMY/aspects-of-halogens).....	7
Figure 1.6: A bromine atom with its energy levels (https://www.shutterstock.com/image-vector/bromine-atom-shell-1259526367).....	7
Figure 1.7: Graphical depiction of the bromine explosion (Simpson et al., 2007).	12
Figure 1.8: The electromagnetic spectrum (https://www.radio2space.com/components-of-electromagnetic-spectrum/).....	13
Figure 1.9: Main absorption bands by atmospheric gases and atmospheric windows. (https://www.chegg.com/).	14

Figure 1.10: Examples of a typical DOAS fit for BrO with the settings used in this thesis. 17

Figure 1.11: A schematic of a typical neural network. 20

Figure 2.1: The absorption cross section of BrO used in this work in vacuum at 223 Kelvin (Fleischmann et al., 2004). 22

Figure 2.2: Evaluation criteria for the retrievals. Top: SCDs of BrO over the Pacific reference area. Bottom: the RMSE of the fit for the same region (50.0° S to 10.0° N latitude and 90.0° W to 125.0° W longitude). 24

Figure 2.3: Evaluation criteria for the retrievals. Top: RMSE of the fit over the Arctic region (70.0° N to 85.0° N latitude, 180° W to 180° E longitude). Bottom: RMSE of the fit for the Hudson Bay (50.0° N to 66.0° N latitude and 264.0° W to 284.0° W longitude). 25

Figure 2.4: Two examples of the application of the pacific correction on GOME-2A retrieval settings. Top: old settings, where the correction has an impact. Bottom: new settings, where the correction can be described as an offset. Both plots are showing BrO SCDs for the Arctic region. 26

Figure 2.5: Evaluation of early retrieval settings. a) SCDs of BrO over the Pacific reference region. b) RMSE of the fit for the Pacific reference region. c) RMSE of the fit for the Arctic region. 28

Figure 2.6: Geometric BrO VCDs for the initial set of settings. 29

Figure 2.7: Sensitivity test with the final cross sections, but not fitting windows. a) SCDs of BrO over the Pacific reference region. b) RMSE of the fit for the Pacific reference region. c) RMSE of the fit for the Arctic region. 30

Figure 2.8: Geometric BrO VCDs for the set of settings with the final cross sections, but not fitting windows. 31

Figure 2.9: Sensitivity test for GOME, with 1nm change of the fitting window (338 – 355 nm (brown) against 337 – 355 nm (blue)). a) SCDs of BrO over the Pacific reference region. b) RMSE of the fit for the Pacific reference region. c) RMSE of the fit for the Arctic region. 32

Figure 2.10: Operational orbit rows of the OMI instrument. Left: An orbit from the year 2005. Right: An orbit from 2017. The missing rows on the right figure are due to the row anomaly. 33

Figure 2.11: Geometric BrO VCDs from OMI for April 2007. 33

Figure 2.12: Counts of OMI instrument for April 2005. Left: Selection of all available rows. Right: Selection only of rows that contribute for all years (2005 – 2017).	34
Figure 2.13: Counts of OMI instrument for April 2011. Left: Selection of all available rows. Right: Selection only of rows that contribute for all years (2005 – 2017).	34
Figure 2.14: Time-series of daily averaged input data over the Arctic used for deriving stratospheric BrO VCDs: Top: stratospheric NO ₂ VCDs [molecules/cm ²] from QA4ECV (GOME, SCIAMACHY and GOME-2A) and TEMIS (GOME-2B. Middle: O ₃ VCDs [DU] from Weber et al. (2013). Bottom: Tropopause height [km] from NCEP reanalysis data. Data for the GOME instrument is colored in red, SCIAMACHY in blue, GOME-2A in green and GOME-2B in brown. All three time-series show daily averages over the Arctic region.	36
Figure 2.15: Schematic representation of the neural network.	39
Figure 2.16: Polar spring averaged correlation coefficients, and root mean square errors between neural network outputs and tropospheric BrO measurements (sensor merged for the overlapping years).	40
Figure 2.17: Top: Polar spring averaged correlation coefficients between tropospheric BrO measurements and neural network outputs for each training year. Bottom: Polar spring averaged time-series of correlation coefficients, and root mean square errors (in percentage) between tropospheric BrO measurements and neural network outputs using the best neural network (i.e. 2007) to reconstruct the entire time-series.	41
Figure 2.18: Polar spring averaged spatial correlation coefficient time-series. Top: Correlation coefficient time-series between each input parameter and measured tropospheric BrO VCDs. Bottom: Correlation coefficient time-series between each input parameter and modeled tropospheric BrO VCDs using the best neural network (i.e. 2007).	42
Figure 3.1: The area defined as "Arctic".	44
Figure 3.2: Time-series of average daily Slant Column Densities of BrO over the Arctic from multiple satellite sensors.	45
Figure 3.3: Long-term time-series of daily average BrO VCDs over the Arctic region. Top: Daily geometric BrO VCDs. Middle: Daily stratospheric BrO VCDs. Bottom: Daily tropospheric BrO VCDs. GOME data is coloured in red, SCIAMACHY in blue, GOME-2A in green and GOME-2B in brown.	46
Figure 3.4: The multiplication factor and its effect on stratospheric and tropospheric BrO VCDs time-series. Top: the actual value of the multiplication factor for every year of the dataset.	

Middle: The stratospheric BrO estimations with the application of the multiplication factor.
 Bottom: The tropospheric BrO measurements with the application of the multiplication factor. .48

Figure 3.5: Climatological seasonal cycles of BrO VCDs in the Arctic derived from different satellite instruments.49

Figure 3.6: Scatter plots of geometric and tropospheric BrO VCDs. The upper row shows geometric BrO VCDs, the lower row tropospheric ones. The first column is GOME – SCIAMACHY, the second column SCIAMACHY – GOME-2A and the third column GOME-2A – GOME-2B. The red line is the best fitting line, while the black dashed line is the 1-1. The r^2 is the correlation coefficient between the two instruments, while the RMSE is the root mean square error between the points and the best fitting line.50

Figure 3.7: Geometric March BrO VCD maps for the Arctic region. Rows indicate different sensors, and columns refer to different years of overlapping periods.51

Figure 3.8: Polar Projection of the tropospheric BrO VCD for bromine explosion events retrieved from the observations of two instruments. Rows indicate the instrument for each case, while columns the date. For each case, four consecutive daily average maps of tropospheric BrO VCDs are shown.52

Figure 3.9: The area defined as Hudson Bay.53

Figure 3.10: Long-term BrO VCD time-series over the Hudson Bay region.54

Figure 3.11: Climatological seasonal cycles of BrO VCDs over the Hudson Bay.55

Figure 3.12: Scatter plots of BrO VCDs over the Hudson Bay.56

Figure 3.13: Geometric BrO VCDs of overlapping periods between the sensors for the Hudson Bay.57

Figure 3.14: Tropospheric BrO VCDs of overlapping periods between the sensors for the Hudson Bay.58

Figure 3.15: From top to bottom: a) time-series of daily averages of tropospheric BrO VCDs over sea ice in the Arctic region, b) The same, but plotted month-wise, c) the extent of the area where tropospheric BrO VCDs exceeded the threshold of 7.0×10^{13} molecules/cm². The best fitting line is plotted for sub-Figures 3.15a and 3.15c.60

Figure 3.16: Linear trends of tropospheric BrO VCDs over different periods. The x-axis shows the starting year, and the y-axis is the ending year of the period.62

Figure 3.17: Linear trends of tropospheric BrO VCDs over different periods based on data for polar spring only. The x-axis shows the starting year, and the y-axis is the ending year of the period.....	63
Figure 3.18: Subsets of the polar spring tropospheric BrO VCD dataset. a) tropospheric BrO VCDs above 7.0×10^{13} molecules/cm ² . b) tropospheric BrO VCDs between 3.0×10^{13} and 7.0×10^{13} molecules/cm ² . c) tropospheric BrO below 3.0×10^{13} molecules/cm ²	64
Figure 3.19: Polar spring anomaly maps of tropospheric BrO VCDs [molecules/cm ²]. For every map, the long-term 22 year average (shown at the bottom right map) has been subtracted from the average of the corresponding year.	66
Figure 3.20: Spatial trend map of tropospheric BrO VCDs.	67
Figure 3.21: From top to bottom: a) time-series of daily averages of tropospheric BrO VCDs based on the sensor merged dataset for the Hudson Bay region, b) the same, but plotted monthly-wise, c) the extent of the area where tropospheric BrO VCDs exceeded the threshold of 7.0×10^{13} molecules/cm ² . The best fitting line is plotted for sub-Figures 3.21a and 3.21c.	68
Figure 3.22: Linear trends of tropospheric BrO VCDs over different periods over the Hudson Bay. The x-axis shows the starting year, and the y-axis is the ending year of the period.	70
Figure 3.23: Linear trends of tropospheric BrO VCDs for the Hudson Bay over different periods based on data for winter only. The x-axis shows the starting year, and the y-axis is the ending year of the period.....	71
Figure 3.24: Linear trends of tropospheric BrO VCDs for the Hudson Bay over different periods based on data for spring only. The x-axis shows the starting year, and the y-axis is the ending year of the period.....	72
Figure 3.25: Subsets of the Hudson Bay winter tropospheric BrO dataset. a) tropospheric BrO VCDs above 7.0×10^{13} molecules/cm ² . b) tropospheric BrO VCDs between 3.0×10^{13} and 7.0×10^{13} molecules/cm ² . c) tropospheric BrO below 3.0×10^{13} molecules/cm ² . From 1998 to 2000 there were no scenes with tropospheric BrO above 7.0×10^{13} molecules/cm ²	73
Figure 3.26: Subsets of the Hudson Bay spring tropospheric BrO dataset. a) tropospheric BrO VCDs above 7.0×10^{13} molecules/cm ² . b) tropospheric BrO VCDs between 3.0×10^{13} and 7.0×10^{13} molecules/cm ² . c) tropospheric BrO below 3.0×10^{13} molecules/cm ² . For 2006 there were no scenes with tropospheric BrO above 7.0×10^{13} molecules/cm ²	75
Figure 3.27: Spatial trend map of tropospheric BrO VCDs during winter months over the Hudson Bay.	77

Figure 3.28: Spatial trend map of tropospheric BrO VCDs during spring months over the Hudson Bay.	77
Figure 3.29: Summary of the trends of tropospheric BrO VCDs presented in the chapter. All trends are calculated on a daily basis. The Arctic polar spring curve is based on Figure 3.15b, while the Hudson Bay Winter and Spring in Figure 3.21b.	79
Figure 4.1: An example of sea ice flagging on tropospheric BrO VCDs maps. From left to right: a) A daily tropospheric BrO VCD map as seen from GOME-2A (01.04.2015), without sea ice flagging, b) the same day, but with the application of sea ice flagging, c) the corresponding sea ice age map for the same day.	82
Figure 4.2: From top to bottom: a) Daily sea ice extent for the Arctic region (in 10^6 km ²), b) same as in Figure 3.3c, but flagged for scenes with sea ice coverage, c) the merged sea ice flagged tropospheric BrO VCDs dataset.	83
Figure 4.3: Relationship of tropospheric BrO to first year ice extent. Top left: polar spring average time-series of tropospheric BrO VCDs over sea ice and first year sea ice extent. Top right: daily polar spring scatter plot between tropospheric BrO VCDs over sea ice and first year sea ice extent. Bottom left: polar spring average time-series of areas where tropospheric BrO VCDs over sea ice exceeded the threshold of 7.0×10^{13} molecules/cm ² and first year sea ice extent. Bottom right: daily polar spring scatter plot between areas where tropospheric BrO VCDs over sea ice exceeded the threshold of 7.0×10^{13} molecules/cm ² and first year sea ice extent.	84
Figure 4.4: Relation of tropospheric BrO to sea ice age. Top left: polar spring average time-series of tropospheric BrO VCDs over sea ice and sea ice age. Top right: daily polar spring scatter plot between tropospheric BrO VCDs over sea ice and sea ice age. Bottom left: polar spring average time-series of areas where tropospheric BrO VCDs over sea ice exceeded the threshold of 7.0×10^{13} molecules/cm ² and sea ice age. Bottom right: daily polar spring scatter plot between areas where tropospheric BrO VCDs over sea ice exceeded the threshold of 7.0×10^{13} molecules/cm ² and sea ice age.	85
Figure 4.5: Same as Figure 4.3, but only for enhanced tropospheric BrO scenes (above 7.0×10^{13} molecules/cm ²).	86
Figure 4.6: Same as Figure 4.3, but only for enhanced tropospheric BrO scenes (above 7.0×10^{13} molecules/cm ²).	87
Figure 4.7: Scatter plots of weekly time-series between tropospheric BrO VCDs and sea ice age. Top left: weekly tropospheric BrO VCDs against weekly first year ice extent. Top right: weekly tropospheric BrO VCDs against weekly averaged sea ice age. Bottom left: enhanced (above 7.0×10^{13} molecules/cm ²) tropospheric BrO VCDs against the corresponding (selected only the	

equivalent scenes) weekly first year ice extent. Bottom right: enhanced (above 7.0×10^{13} molecules/cm²) tropospheric BrO VCDs against the corresponding (selected only the equivalent scenes) averaged sea ice age. The best fitting line is plotted in every scatter plot.....88

Figure 4.8: Polar spring average maps of tropospheric BrO VCDs [10^{13} molec/cm²] and sea ice age [years]. First year ice is denoted with dark blue color.....90

Figure 4.9: Pixel trend maps of tropospheric BrO VCDs (top left), sea ice age (top right) and first year ice frequency (bottom left).91

Figure 4.10: Time-series and scatter plots of tropospheric BrO VCDs and 2m air temperature. Top left: Polar spring averaged time-series of tropospheric BrO VCDs and 2m air temperature from reanalysis data. Top right: The corresponding daily scatter plot of tropospheric BrO (blue curve in the time-series) and ERA-5 2m air temperature (the red one). Bottom left: Polar spring averaged time-series of enhanced tropospheric BrO VCDs (above 7.0×10^{13} molecules/cm²) and 2m air temperature for the corresponding areas from reanalysis data. Bottom right: The corresponding daily scatter plot of enhanced tropospheric BrO (above 7.0×10^{13} molecules/cm², blue curve in the time-series) and ERA-5 2m air temperature (the red one).93

Figure 4.11: Polar spring average maps of tropospheric BrO VCDs [molec/cm²] and ERA-5 2m air temperature [kelvin].....95

Figure 4.12: Spatial trend patterns of tropospheric BrO (left) and ERA-5 2m air temperature (right).....96

Figure 4.13: Time-series and scatter plots between tropospheric BrO VCDs and 2m air temperature for the Hudson Bay region during winters. Top left: Winter averaged time-series of tropospheric BrO VCDs and 2m air temperature from reanalysis data. Top right: The equivalent daily scatter plot between tropospheric BrO and ERA-5 2m air temperature. Bottom left: Winter averaged time-series of enhanced tropospheric BrO VCDs (above 7.0×10^{13} molecules/cm²) and 2m air temperature from this area from reanalysis data. Bottom right: The equivalent daily scatter plot between enhanced tropospheric BrO (above 7.0×10^{13} molecules/cm²) and ERA-5 2m air temperature.97

Figure 4.14: Time-series and scatter plots between tropospheric BrO VCDs and 2m air temperature for the Hudson Bay region during springs. Top left: Spring averaged time-series of tropospheric BrO VCDs and 2m air temperature from reanalysis data. Top right: The corresponding daily scatter plot between tropospheric BrO and ERA-5 2m air temperature. Bottom left: Spring averaged time-series of enhanced tropospheric BrO VCDs (above 7.0×10^{13} molecules/cm²) and 2m air temperature from reanalysis data. Bottom right: The corresponding daily scatter plot between enhanced tropospheric BrO (above 7.0×10^{13} molecules/cm²) and ERA-5 2m air temperature.98

Figure 4.15: Trend maps of tropospheric BrO and air temperature for the Hudson Bay. Top left: trend map of tropospheric BrO during the winter period. Top right: trend map of air temperature during the winter period. Bottom left: trend map of tropospheric BrO during the spring period. Bottom right: trend map of air temperature during the spring period. 99

Figure 4.16: Time-series and scatter plots of the tropospheric BrO VCDs and mean sea level pressure. Top left: Polar spring averaged time-series of tropospheric BrO VCDs and mean sea level pressure from reanalysis data. Top right: The equivalent daily scatter plot between tropospheric BrO VCDs (blue curve in the time-series) and ERA-5 mean sea level pressure (the red one). Bottom left: Polar spring averaged time-series of enhanced tropospheric BrO VCDs (above 7.0×10^{13} molecules/cm²) and mean sea level pressure from reanalysis data. Bottom right: The equivalent daily scatter plot between enhanced tropospheric BrO VCDs (above 7.0×10^{13} molecules/cm², blue curve in the time-series) and ERA-5 mean sea level pressure (the red one). 101

Figure 4.17: Polar spring average maps of tropospheric BrO VCDs [molec/cm²] and ERA-5 mean sea level pressure [hPa]. 103

Figure 4.18: Spatial trend patterns for tropospheric BrO (left) and mean sea level pressure (right) for the Arctic region. 103

Figure 4.19: Time-series and scatter plots between tropospheric BrO VCDs and mean sea level pressure for the Hudson Bay region during winters. Top left: Winter averaged time-series of tropospheric BrO VCDs and mean sea level pressure from reanalysis data. Top right: The equivalent daily scatter plot between tropospheric BrO VCD and ERA-5 mean sea level pressure. Bottom left: Winter averaged time-series of enhanced tropospheric BrO VCDs (above 7.0×10^{13} molecules/cm²) and mean sea level pressure from reanalysis data. Bottom right: The equivalent daily scatter plot between enhanced tropospheric BrO (above 7.0×10^{13} molecules/cm²) and ERA-5 mean sea level pressure. 104

Figure 4.20: Time-series and scatter plots between tropospheric BrO VCDs and mean sea level pressure for the Hudson Bay region during springs. Top left: Winter averaged time-series of tropospheric BrO VCDs and mean sea level pressure from reanalysis data. Top right: The equivalent daily scatter plot between tropospheric BrO and ERA-5 mean sea level pressure. Bottom left: Spring averaged time-series of enhanced tropospheric BrO VCDs (above 7.0×10^{13} molecules/cm²) and mean sea level pressure from reanalysis data. Bottom right: The equivalent daily scatter plot between enhanced tropospheric BrO (above 7.0×10^{13} molecules/cm²) and ERA-5 mean sea level pressure. 105

Figure 4.21: Spatial trend patterns of tropospheric BrO and mean sea level pressure for the Hudson Bay. Top left: trend map of tropospheric BrO during the winter period. Top right: trend

map of mean sea level pressure during the winter period. Bottom left: trend map of tropospheric BrO during the spring period. Bottom right: trend map of mean sea level pressure during spring.	106
Figure 4.22: Time-series and scatter plots between tropospheric BrO VCDs and 10m wind speed. Top left: Polar spring averaged time-series of tropospheric BrO VCDs and 10m wind speed from reanalysis data. Top right: The equivalent daily scatter plot between tropospheric BrO (blue curve in the time-series) and ERA-5 10m wind speed (the red one). Bottom left: Polar spring averaged time-series of enhanced tropospheric BrO VCDs (above 7.0×10^{13} molecules/cm ²) and 10m wind speed from reanalysis data. Bottom right: The equivalent daily scatter plot between enhanced tropospheric BrO (above 7.0×10^{13} molecules/cm ² , blue curve in the time-series) and ERA-5 10m wind speed (the red one).	107
Figure 4.23: Polar spring average maps of tropospheric BrO VCDs [molec/cm ²] and ERA-5 10m wind speed [m/s].	109
Figure 4.24: Spatial trend patterns of tropospheric BrO (left) and 10m wind speed (right) for the Arctic region.....	110
Figure 4.25: Time-series and scatter plots of tropospheric BrO VCDs and 10m wind speed for the Hudson Bay region during winters. Top left: Winter averaged time-series of tropospheric BrO VCDs and 10m wind speed from reanalysis data. Top right: The equivalent daily scatter plot between tropospheric BrO and ERA-5 10m wind speed. Bottom left: Winter averaged time-series of enhanced tropospheric BrO VCDs (above 7.0×10^{13} molecules/cm ²) and 10m wind speed from reanalysis data. Bottom right: The equivalent daily scatter plot between enhanced tropospheric BrO (above 7.0×10^{13} molecules/cm ²) and ERA-5 10m wind speed.	110
Figure 4.26: Time-series and scatter plots of tropospheric BrO VCDs and 10m wind speed for the Hudson Bay region during springs. Top left: Winter averaged time-series of tropospheric BrO VCDs and 10m wind speed from reanalysis data. Top right: The equivalent daily scatter plot between tropospheric BrO and ERA-5 10m wind speed. Bottom left: Spring averaged time-series of enhanced tropospheric BrO VCDs (above 7.0×10^{13} molecules/cm ²) and 10m wind speed from reanalysis data. Bottom right: The equivalent daily scatter plot between enhanced tropospheric BrO (above 7.0×10^{13} molecules/cm ²) and ERA-5 10m wind speed.	111
Figure 4.27: Spatial trend patterns of tropospheric BrO VCD and 10m wind speed for the Hudson Bay. Top left: trend map of tropospheric BrO VCD during the winter period. Top right: trend map of 10m wind speed during the winter period. Bottom left: trend map of tropospheric BrO VCD during the spring period. Bottom right: trend map of 10m wind speed during the spring period.....	112

Figure 4.28: Time-series and scatter plots between tropospheric BrO VCDs and boundary layer height. Top left: Polar spring averaged time-series of tropospheric BrO VCDs and boundary layer height from ERA-5 reanalysis data. Top right: The equivalent daily scatter plot between tropospheric BrO and boundary layer height. Bottom left: Polar spring averaged time-series of enhanced tropospheric BrO VCDs (above 7.0×10^{13} molecules/cm²) and boundary layer height from ERA-5 reanalysis data. Bottom right: The equivalent daily scatter plot between enhanced tropospheric BrO (above 7.0×10^{13} molecules/cm²) and boundary layer height..... 113

Figure 4.29: Polar spring average maps of tropospheric BrO VCDs [molec/cm²] and ERA-5 boundary layer height [m]. 115

Figure 4.30: Spatial trend patterns of tropospheric BrO (left) and boundary layer height (right) for the Arctic region. 115

Figure 4.31: Time-series and scatter plots of tropospheric BrO VCDs and boundary layer height for the Hudson Bay region during winters. Top left: Winter averaged time-series of tropospheric BrO VCDs and boundary layer height from reanalysis data. Top right: The equivalent daily scatter plot between tropospheric BrO and ERA-5 boundary layer height. Bottom left: Winter averaged time-series of enhanced tropospheric BrO VCDs (above 7.0×10^{13} molecules/cm²) and boundary layer height from reanalysis data. Bottom right: The equivalent daily scatter plot between enhanced tropospheric BrO (above 7.0×10^{13} molecules/cm²) and ERA-5 boundary layer height. 116

Figure 4.32: Time-series and scatter plots between tropospheric BrO VCDs and boundary layer height for the Hudson Bay region during springs. Top left: Spring averaged time-series of tropospheric BrO VCDs and boundary layer height from reanalysis data. Top right: The equivalent daily scatter plot between tropospheric BrO and ERA-5 boundary layer height. Bottom left: Spring averaged time-series of enhanced tropospheric BrO VCDs (above 7.0×10^{13} molecules/cm²) and boundary layer height from reanalysis data. Bottom right: The equivalent daily scatter plot between enhanced tropospheric BrO (above 7.0×10^{13} molecules/cm²) and ERA-5 boundary layer height. 117

Figure 4.33: Spatial trend patterns of tropospheric BrO VCD and boundary layer height for the Hudson Bay. Top left: trend map of tropospheric BrO during the winter period. Top right: trend map of boundary layer height during the winter period. Bottom left: trend map of tropospheric BrO VCD during the spring period. Bottom right: trend map of boundary layer height during the spring period. 118

Figure 4.34: Time-series and scatter plots of tropospheric BrO VCDs and sea ice thickness. Top left: Polar spring averaged time-series of tropospheric BrO VCDs and sea ice thickness from ASR-2 reanalysis data. Top right: The equivalent daily scatter plot between tropospheric BrO and

sea ice thickness. Bottom left: Polar spring averaged time-series of enhanced tropospheric BrO VCDs (above 7.0×10^{13} molecules/cm ²) and sea ice thickness from ASR-2 reanalysis data. Bottom right: The equivalent daily scatter plot between enhanced tropospheric BrO (above 7.0×10^{13} molecules/cm ²) and sea ice thickness.....	119
Figure 4.35: Spatial trend patterns of tropospheric BrO VCD (left) and sea ice thickness (right) for the Arctic region.	120
Figure 4.36: Time-series and scatter plots of tropospheric BrO VCDs and vertical wind velocity. Top left: Polar spring averaged time-series of tropospheric BrO VCDs and vertical wind velocity from ERA-5 reanalysis data. Top right: The equivalent daily scatter plot between tropospheric BrO VCD and vertical wind velocity. Bottom left: Polar spring averaged time-series of enhanced tropospheric BrO VCDs (above 7.0×10^{13} molecules/cm ²) and vertical wind velocity from ERA-5 reanalysis data. Bottom right: The equivalent daily scatter plot between enhanced tropospheric BrO VCD (above 7.0×10^{13} molecules/cm ²) and vertical wind velocity.	121
Figure 4.37: Spatial trend patterns of tropospheric BrO VCD (left) and vertical wind velocity (right) for the Arctic region.	122
Figure 4.38: Time-series of tropospheric BrO VCDs and cyclone activity. Top: Polar spring averaged time-series of tropospheric BrO VCDs and unique cyclone frequency. Bottom: Polar spring averaged time-series of tropospheric BrO VCDs maximum cyclone intensity.	123
Figure 4.39: Polar spring average maps of tropospheric BrO VCDs [molec/cm ²] and cyclone intensity.	125
Figure 5.1: Sensitivity tests for the importance of each input parameter, through scatter plots between measured and modeled tropospheric BrO VCD during the training process (2007 polar spring as training dataset).....	130
Figure 5.2: Sensitivity tests for the importance of each input parameter for the reproduction of satellite retrieved tropospheric BrO VCDs based on the neural network. Top: the polar spring averaged spatial correlation coefficient of each year between measured and modeled tropospheric BrO VCDs. Bottom: the polar spring averaged spatial root mean square error of each year between measured and modeled tropospheric BrO VCDs.....	131
Figure 5.3: Effect of each input parameter on the magnitude of modeled tropospheric BrO VCD. On the x-axis of each subplot, the ranging input parameter is shown, while all the other inputs are assigned the constant value of their polar spring average of 2007.....	132

Figure 5.4: Effect of each input parameter on the magnitude of modeled tropospheric BrO VCD. On the x-axis of each subplot, the ranging input parameter is shown, while all the other inputs are assigned the constant value of their polar spring average of each year of the dataset. 134

Figure 5.5: Effect of each input parameter on the magnitude of modeled tropospheric BrO VCD. On the x-axis of each subplot, we see the ranging input parameter, while all the other inputs are assigned a typical constant value of conditions that favour enhanced BrO formation. 135

Figure 5.6: Tropospheric BrO VCD measurements, neural network output, the difference between measurements and model, sea ice age and ERA-5 meteorological conditions on the 01.04.2011..... 136

Figure 5.7: Impact of removing each input parameter on the spatial variability and magnitude of tropospheric BrO VCDs modeled by the neural network for the 01.04.2011..... 137

Figure 5.8: Examples of successful spatial reproduction of enhanced tropospheric BrO plumes by the neural network. 138

Figure 5.9: Tropospheric BrO VCDs, neural network output, error between measurements and model, sea ice age and meteorological conditions on the 07.04.2017. 139

Figure 5.10: Impact of removing individual input parameters on the spatial distribution and magnitude of tropospheric BrO VCDs modeled by the neural network for the 07.04.2017..... 141

Figure 5.11: Comparison of polar spring average maps of tropospheric BrO VCDs from the measurements and the neural network outputs. 142

Figure 5.12: Comparison of polar spring averaged time-series between tropospheric BrO VCDs measurements and neural network outputs. 2007 data was used as the training dataset. 144

Figure 5.13: Past projections of polar spring averaged maps of tropospheric BrO VCDs. 145

Figure 5.14: Future projections of polar spring averaged maps of tropospheric BrO VCDs based on three different projections of greenhouse gas concentrations. 146

LIST OF TABLES

Table 1.1: Fractional concentrations by volume of the major gaseous constituents of the Earth's atmosphere (Wallace and Hobbs, 2006).....	4
Table 1.2: Satellite instruments used in this study and their attributes.	18
Table 2.1: Final parameter selection for all instruments.	27
Table 2.2: Fitting windows used for the different instruments.	27
Table 3.1: Trends of tropospheric BrO VCDs for the Arctic region.....	61
Table 3.2: Trends of the subsets of tropospheric BrO during polar springs.	65
Table 3.3: Trends of tropospheric BrO time-series for the Hudson Bay.	69
Table 3.4: Trends of the subsets of tropospheric BrO during winter months for the Hudson Bay.	74
Table 3.5: Trends of the subsets of tropospheric BrO during spring months for the Hudson Bay.	76
Table 4.1: Summary of the most significant correlations between tropospheric BrO and its driving mechanisms.....	127

MOTIVATION AND OUTLINE

Climate change refers to long-term climate variations that occur over decades or more and eventually re-shape the local or global climate. Such changes happen since the formation of the Earth (for example, the current composition of our atmosphere is a product of many changes, which took place over millions of years). However, since the industrial revolution, around 1760, the climate has been increasingly affected by human activities that are causing global warming and climate change (see Figure 1). The rate of these changes is unprecedented, as, in such a short period, the Earth has transformed to a warmer, less forest-covered, and less biologically diverse place (Steffen et al., 2007). The main contributors to man-made climate change are greenhouse gases, most notably CO₂) emitted from anthropogenic activities, such as fossil fuel combustion, land change and deforestation. The extent to which a potential increase in CO₂ could result in an increased Earth's surface temperature was already investigated more than 100 years ago (Arrhenius, 1896). These unprecedented changes, in combination with the rapid increase of human population (to almost 8 billions), which creates further needs for resources, have motivated the term "Anthropocene" (Crutzen, 2002) for the current era of the Earth system.

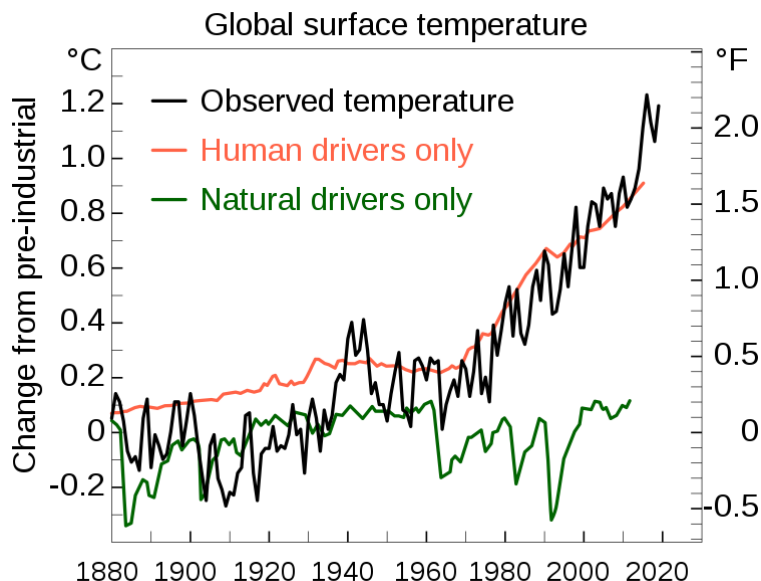


Figure 1: Surface temperature evolution versus the 1850-1900 average as a pre-industrial reference (Knutson et al., 2017). The contribution of human and natural drivers are based on an empirical approach using multiple linear regression and energy balance models.

Although most of the human activities contributing to global warming are taking place locally in cities, the implications on the climate are global. Fifty years ago, an observation-based study predicted a fast Arctic warming (Budyko, 1969). According to it, "Sea ice loss affects Arctic

temperatures through the surface albedo feedback". Since then, numerous studies using both models and measurements have shown that the Arctic is warming at a much faster rate than the rest of the globe (Sellers, 1969; Manabe and Wetherald, 1975). This phenomenon is called Arctic Amplification (Serreze and Francis, 2006; Wendisch, M. et al., 2017; Serreze and Barry, 2011) (see Figure 2).

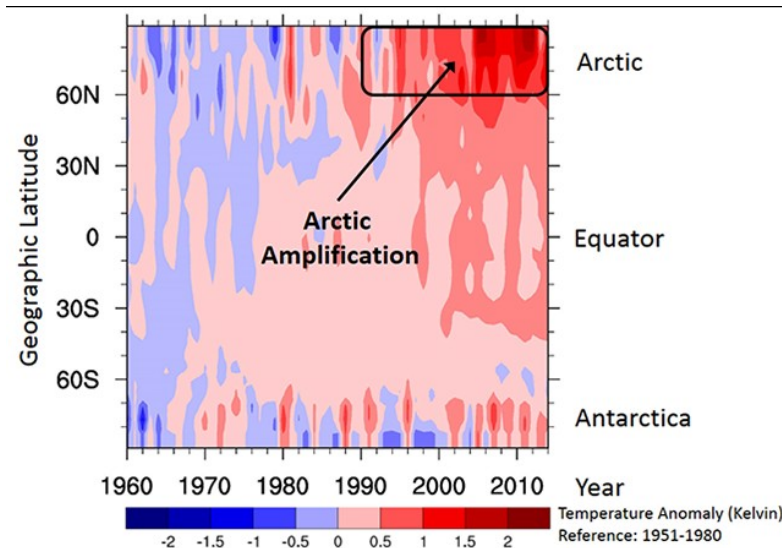


Figure 2: Mean surface temperature anomalies (by location and year, measured in Kelvin), with respect to the 1951-1980 reference time frame. (Figure provided by the NASA Goddard Institute for Space Studies Team through their webpage at <https://data.giss.nasa.gov/gistemp/>).

Even though the leading cause of polar Amplification is widely considered to be the feedback associated with sea ice and snow cover (as the temperature increases, the bright surfaces that were dominant in the Arctic region vanish and are replaced by open water, which, having a lower reflectivity, absorbs more of the incoming solar radiation), model studies are suggesting that the Arctic would still be warmer from the rest of the globe, even without ice or snow (Alexeev et al., 2005). Therefore, it appears that dynamics and heat transport between the tropics and the Arctic also play a role. These rapid and significant changes will impact many other physical, chemical and biological processes in the Arctic region. Additionally, many studies are indicating that the rapidly rising Arctic temperatures are related to extreme weather events in mid-latitudes (Francis and Vavrus, 2012).

Every polar spring, under the presence of sunlight, a unique natural phenomenon takes place in the polar regions: the so-called “bromine explosion” (Barrie and Platt, 1997), a set of auto-catalytic chain reactions, which allow bromine molecules to be released into the Arctic atmospheric boundary layer. The sources of bromine are both inorganic (cold saline surfaces, e.g. sea ice, liquid brine, frost flowers and blowing snow (Sander et al., 2006; Kaleschke et al., 2004; Wagner et al., 2001) and organic (algae, phytoplankton, dissolved organic matter). After the bromine molecules release, photochemistry occurs, where one bromine molecule is split into two

bromine atoms. These atoms, as they miss one electron from their outermost shell, are highly reactive. This is why they react with and strongly deplete ozone, thereby forming bromine oxide (BrO). Since the bromine explosion is an autocatalytic multiphase chain reaction, it has the ability to deplete ozone efficiently and fast, even in the presence of small (ppt) amounts of bromine molecules. A simplified scheme of the inorganic release of bromine molecules and the basic reactions and products involved can be seen in Figure 3:

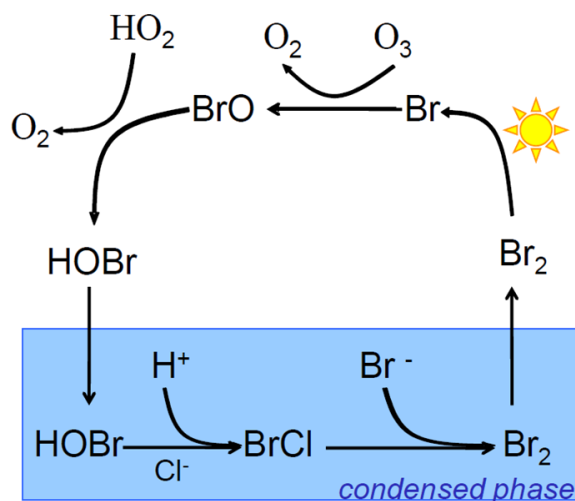


Figure 3: The bromine explosion (Figure from Jones et al., 2009).

After the release of bromine molecules and the formation of BrO, BrO plumes with strongly enhanced BrO concentrations occur under two distinct weather conditions: A stable boundary layer with low wind speeds or an unstable boundary layer with high wind speeds. Also, cold temperatures favour the bromine explosion chemical reaction cycle (Blechschmidt et al., 2016; Jones et al., 2009; Begoin et al., 2010; Zhao et al., 2016). Potential changes in sea ice (which are occurring in the Arctic due to Arctic Amplification) will influence both the organic (more open water, so potentially more organohalogen production) and inorganic (less sea ice coverage, but more salty first year sea ice, which favours the release of bromine) releases of bromine into the Arctic atmosphere. Furthermore, the meteorological conditions that favour the formation and enhancement of BrO plumes (e.g. wind speeds, cyclone activity, mean sea level pressure, and temperature) are affected by the recent changes in the Arctic climate. Since ozone is essential in the Arctic atmosphere, acting both as a greenhouse gas (and therefore modulating the temperature and radiative forcing) and as an oxidizing capacity regulator (as it is the primary source of the hydroxyl radical, OH, the principal oxidizing agent of the atmosphere), potential changes in tropospheric bromine release and formation may impact on the composition and radiative properties of the Arctic troposphere. In addition to the impact of bromine on ozone, BrO is also involved in transforming mercury from the gas to the liquid phase, which can be potentially detrimental, as it can enter the food chain (Ariya et al., 2004).

Satellite remote sensing provides us with a unique opportunity to study the Earth's atmospheric composition on a global scale. Platt and Wagner, 1998 and Richter et al., 1998 were the first to study satellite observations of BrO in the polar regions, using the GOME instrument (Burrows et al., 1999; Chance, 1998). Since then, many other satellite remote sensing studies for BrO followed: Hollwedel et al. (2004) used the instrument to derive a six-year time-series of Arctic BrO (Hollwedel et al., 2004a). Van Roozendael et al. (2004) used measurements from SCIAMACHY and compared them to GOME, showing satisfactory agreement (Van Roozendael et al., 2004), while Theys et al. (2009) used a chemical transport model to isolate the tropospheric BrO component from the satellite column (Theys et al., 2009), and applied this method to the GOME-2A instrument (Theys et al., 2011).

In this study, a consistent long-term consolidated multi-sensor tropospheric Arctic BrO dataset was developed. The dataset spans over 22 years, allowing the investigation of changes that occurred to BrO formation and intensity under the impact of Arctic Amplification. By comparing different datasets (e.g. sea ice age and thickness, temperature), the links between the changes of tropospheric BrO plumes and their sources and driving mechanisms are investigated. Finally, a first effort of modeling tropospheric BrO plumes by employing an artificial neural network was implemented to understand and predict appearances of enhanced BrO and integrate these predictions in models or use them for potential future measurement campaigns.

This thesis is structured as follows:

- In Chapter 1, the theoretical background of the research is introduced: definition and explanation of Arctic Amplification, the chemistry behind the appearance of halogens in the atmosphere, basic principles of absorption spectroscopy, together with the background of satellite remote sensing, the instruments used in the study and an introductory presentation of artificial neural networks are given.
- In Chapter 2, the technical background of the study is described: the methodology followed in order to obtain the BrO VCD from the satellite sensors, the criteria used for the selection of the proper fitting settings, the stratospheric separation applied and finally, the steps followed for obtaining the exemplary neural network architecture for our case are presented.
- In Chapter 3, the retrieved satellite BrO VCD are analysed and presented. The agreement of the overlapping periods between the sensors is highlighted, both from map and time-series comparisons. In addition, the trends and changes observed over time are calculated and discussed for both the magnitude and spatial scale.
- In Chapter 4, the link of the changes of tropospheric BrO VCD to source and driving mechanism datasets is discussed through map comparisons, scatter plots, time-series and trend maps.
- In Chapter 5, the implementation of the artificial neural network for tropospheric BrO VCD modeling is presented. The network's performance is discussed for individual case

studies and for long-term re-construction of maps and time-series, which are compared with satellite measurements.

- Finally, in Chapter 6, a summary of the thesis's main research findings and conclusions are presented, the limitations encountered are described, and an outlook on further improvements in future studies is given.

1. THEORETICAL BACKGROUND

In this first chapter, the theoretical background of the thesis will be presented. Most of the subsections are based on the following books: Seinfeld and Pandis, (1998); Wallace and Hobbs, (2006); Platt and Stutz, (2008); Jacob, (1999); Burrows et al., (2011); Roedel and Wagner, (2017).

1.1 The Earth's Atmosphere

The vertical structure of an atmosphere can be described by the change of pressure, temperature, density and composition, as a function of altitude from the surface. The Earth's atmosphere is divided into five layers using the vertical temperature changes: the troposphere, the stratosphere, the mesosphere, the thermosphere and the exosphere. Figure 1.1 shows the vertical profile of the Earth's temperature at mid-latitudes, together with the layers mentioned above:

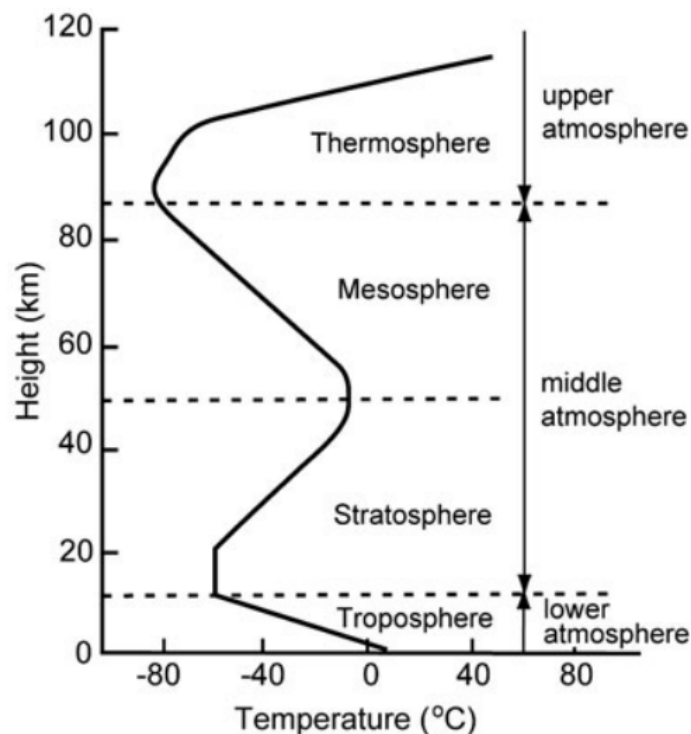


Figure 1.1: The vertical structure of the Earth's atmosphere, as a function of temperature (<https://www.azimuthproject.org/azimuth/show/Blog+-+the+color+of+night>).

The troposphere is the lowest part of the atmosphere, extending from the surface up to approximately 12 km, although this varies based on latitude zones. At the Equator, the tropopause is approximately up to 17 km, while at the poles, it is 9 km or lower. The temperature is generally decreasing with height in the troposphere, the main reason being that solar radiation reaching the ground heats the surface. The stratosphere is the next layer, extending up to approximately 50 km. Here we see a temperature inversion as the temperature is increasing with height. The main reason is the existence of the ozone layer, which absorbs solar ultraviolet radiation. The mesosphere extends from 50 km up to approximately 80 km and is the coldest layer of the atmosphere. This is due to decreasing absorption of solar radiation, as the layer is transparent and without many trace gas molecules. Above the mesosphere, the thermosphere starts and extends up to 100 km. The temperature increases as extreme ultraviolet radiation is absorbed by residual atmospheric gases (O_2 , N_2 , N_2O). The exosphere is the final layer of the atmosphere, where light molecules (e.g. hydrogen and helium) can escape the gravitational field.

The composition of the Earth's atmosphere was not always the same. Rather, the current composition is a result of constant changes. According to current estimations, Earth's first atmosphere was similar to that of the Sun, having large quantities of hydrogen and noble gases. This atmosphere, in combination with high temperatures occurring at that time, vanished to space. The secondary atmosphere mainly consists of H_2O , H_2 , CH_4 , N_2 , CO , but not oxygen. These gases were produced by the internal core of the Earth. Water vapor which escaped the molten rocks of the Earth formed the oceans after the Earth's surface had cooled to a temperature below the boiling point of water, while ultraviolet radiation helped towards the formation of oxygen, which resulted in the creation of life on the planet, through the following overall reaction:



Although nowadays oxygen formation in the atmosphere is through photosynthesis from plants, at that early stage, life did not exist on the planet. From the first little oxygen that was created at that point, ozone (O_3) formed, following the UV photolysis of O_2 . Ozone provided a "shield" for the first living structures on the planet from the hazardous ultraviolet solar radiation. Ozone can be created photochemically under the following set of reactions:



This set of reactions was proposed by Chapman, (1930). The formation of ozone allowed living organisms to survive outside water (where they were initially protected from ultraviolet radiation) and contribute to the formation of oxygen through photosynthesis.

Figure 1.2 shows the evolution of the composition of the Earth's atmosphere.

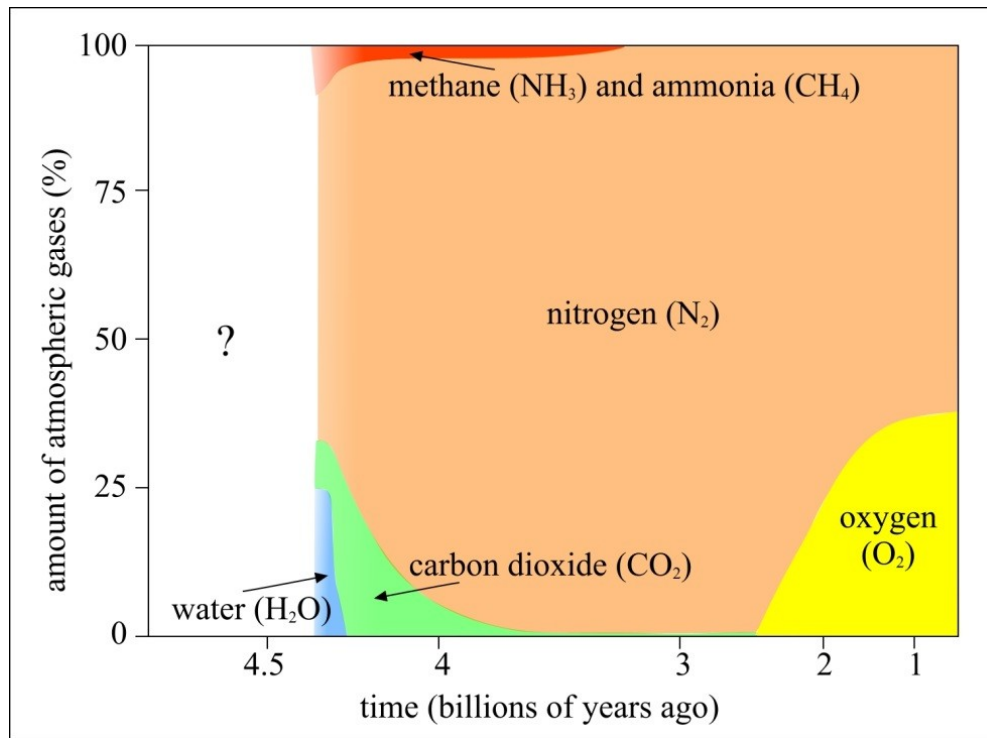


Figure 1.2: Evolution of the composition of the Earth's atmosphere (<http://elte.prompt.hu/sites/default/files/tananyagok/AtmosphericChemistry/ch01.html>).

Nitrogen (N₂), oxygen (O₂) and Argon (Ar) are the most dominant gases in the current composition of the atmosphere, with mixing ratios of 78%, 21% and 0.9%, respectively. Water vapor follows (0.25%). However, its mixing ratio varies, depending on season and latitude. All the remaining gases are present in small mixing ratios and are referred to as trace gases. However, some of them are more reactive and have a significant impact on life upon Earth. For example, greenhouse gases, which can absorb radiation in the infrared spectrum, keep the temperature of the Earth high enough for life to be sustained. Without them, the temperature at the surface of the Earth would have been about -18° Celsius, rather than the present average of $+15^{\circ}$ Celsius.

Table 1.1 summarizes the most important gases of the current atmosphere (adapted from Wallace and Hobbs, (2006).

1. Theoretical Background

Table 1.1: Fractional concentrations by volume of the major gaseous constituents of the Earth's atmosphere (Wallace and Hobbs, 2006).

Constituent	Volume mixing ratio
Nitrogen (N ₂)	78.08 %
Oxygen (O ₂)	20.95 %
Argon (Ar)	0.93 %
Water vapor (H ₂ O)	0 – 5 %
Carbon dioxide (CO ₂)	380 ppm
Neon (Ne)	18 ppm
Helium (He)	5 ppm
Methane (CH ₄)	1.85 ppm
Krypton (Kr)	1 ppm
Hydrogen (H ₂)	0.5 ppm
Nitrous oxide (N ₂ O)	0.3 ppm
Ozone (O ₃)	0 – 0.1 ppm

Since the beginning of the Industrial Revolution (i.e. approximately since 1750), human activities have increased the atmospheric mixing ratio of greenhouse gases, especially of carbon dioxide (i.e. from 280 ppm in 1750 to 413 ppm in 2021). These increases in greenhouse gases concentrations' have brought an increase in the temperature of the surface of the Earth in almost all regions of the planet. However, the most profound increase is occurring in the Arctic region.

1.2 Arctic Amplification

Arctic surface air temperature has risen twice the global mean rate over the past three decades. This phenomenon is called Arctic Amplification (Serreze and Barry, 2011) and our understanding of its causes is inadequate (Pithan and Mauritsen, 2014; Stjern et al., 2019). The most cited explanation for this increase is the ice-albedo positive feedback that is created when the sea ice that existed for many years in the region melts due to an increased temperature. This melting creates more open water, which can absorb more solar radiation (and therefore more heat,

creating a positive feedback, which increases the temperature even more). (Kashiwase et al., 2017). Figure 1.3 shows this rapid increase of air temperature in the Arctic.

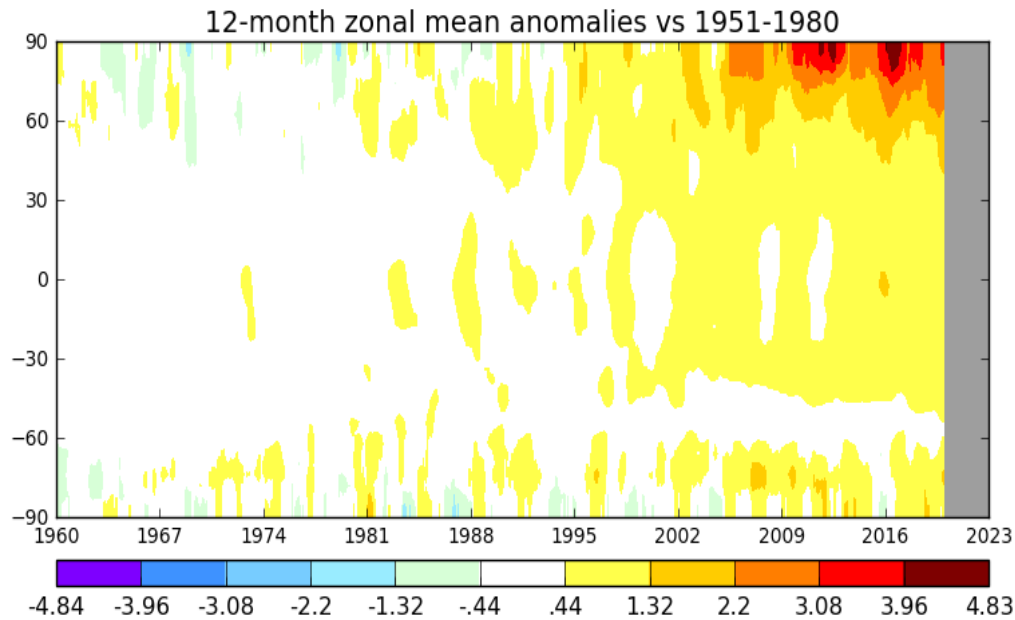


Figure 1.3: Yearly temperature anomalies, based on a long-term temperature average (1951 to 1980), from meteorological stations and ocean areas. Y-axis is latitude, x-axis is the year, color coding shows is the temperature anomaly (NASA GISTEMP, <http://data.giss.nasa.gov/gistemp>).

Significant consequences of the rapidly increasing temperature in the Arctic are the loss of ice, resulting in the reduction of ice extent, thickness and a reduced fraction of multi-year ice (Stroeve et al., 2012) and the increasing rate of loss of the Greenland ice cap (Mouginot et al., 2019). The multi-year ice is being replaced by first year ice, which is more saline. (Galley et al., 2016). The maximum and the minimum yearly sea ice extent started to become noticeably smaller over a decade ago. The minimum sea ice extent, which usually occurs in September, reached its record low in 2012 (Yang and Magnusdottir, 2018). The yearly maximum sea ice extent, which occurs every March, is shrinking significantly (Serreze and Meier, 2019). The thickness of sea ice has declined dramatically in recent years as the portion of thick multi-year ice decreases (Perovich and Richter-Menge, 2009). Sea ice is replaced by open ocean, which, being darker, reduces surface reflectivity in the Arctic. As a result, more of the incoming solar radiation is absorbed by the ocean and its biosphere (e.g. phytoplankton). Consequently, the temperature of the ocean and the air in the boundary layer increases, creating a positive feedback loop. This is one of the most pronounced effects of Arctic Amplification (Hansen et al., 1997; Kirtman et al., 2013). Figure 1.4 shows the rapid decrease in Arctic sea ice extent on a monthly basis compared to a long-term average (1981 to 2010).

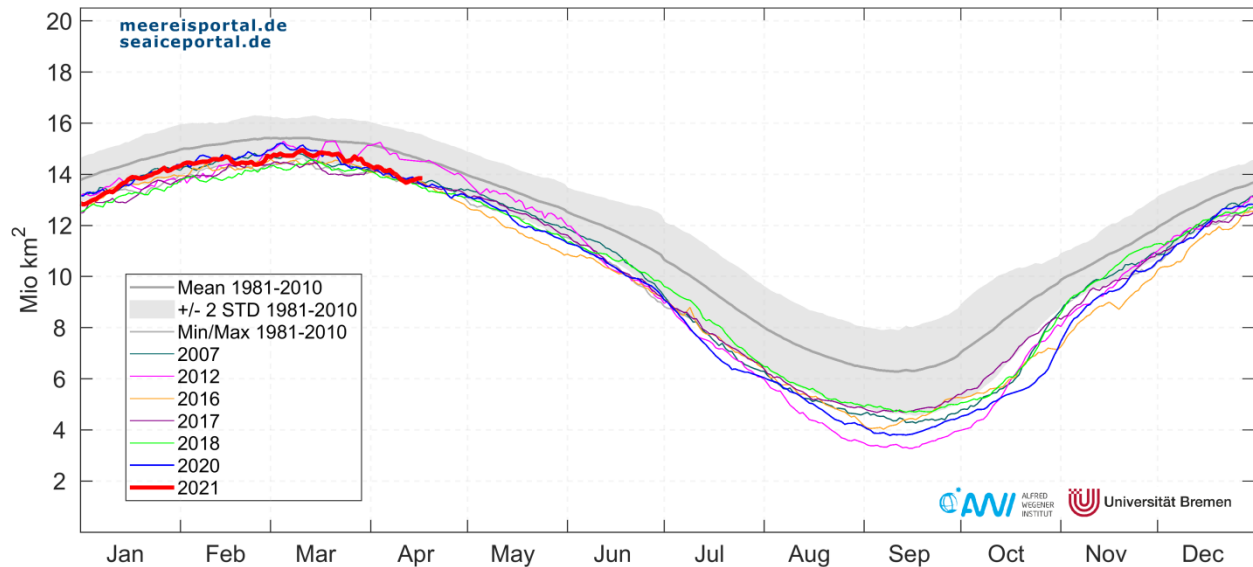


Figure 1.4: Climatological means of Arctic sea ice extent for the record low years derived from satellite measurements. The grey curve is the long-term average (1981 – 2010) (<https://www.meereisportal.de/en/>).

These evolving conditions impact many other physical, chemical and biological processes in the Arctic. However, not only the Arctic is affected by Arctic Amplification. Recent studies suggest that there is an impact on mid-latitudes (Coumou et al., 2018; Cvijanovic et al., 2017), although other studies debate about the impact (Screen, 2017; Fyfe, 2019). In addition, changes in the atmospheric composition over mid-latitudes may potentially accelerate Arctic warming (Krishnan et al., 2020).

1.3 Halogens in the Atmosphere

Halogens are the group 17 in the periodic table. They consist of five elements: fluorine (F), chlorine (Cl), bromine (Br), iodine (I), astatine (At) and the artificially created tennessine (Ts). Their name means “salt-producing”, as they produce a wide range of salts when reacting with metals. Also, most halogens are typically produced from minerals and salts. Halogens are the only periodic table group containing elements in all three primary states of matter at standard temperature and pressure. They are often used as disinfectants and are dangerous, and can be lethally toxic. Also, they are highly reactive, as they have seven valence electrons in their outermost energy level. Therefore, they tend to gain an electron by reacting with other atoms of other elements to satisfy the octet rule. Figure 1.5 shows the basic properties of the four halogen elements.

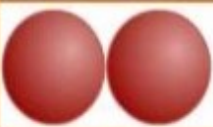
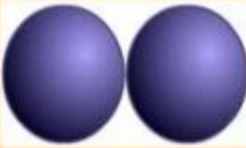
Halogen	Relative size	Melting point (°C)	Boiling point (°C)	State
fluorine		-220	-118	gas
chlorine		-101	-34	gas
bromine		-7	59	liquid
iodine		114	184	solid

Figure 1.5: The four main halogens, together with their relative size, melting and boiling point, and state (<https://www.slideshare.net/KALYANIPALANICHAMY/aspects-of-halogens>).

As we move down in Figure 1.5, there is a decrease in reactivity as the size of the molecule and the atomic mass increase. That means that the power of a halogen to attract an electron to form a negative ion decreases.

Bromine is a chemical element with atomic number 35 and an atomic weight of 79.9. It is liquid at its elemental state and has a red-brown color at room temperature. Its name means “stench” due to its disagreeable smell. Figure 1.6 shows a representation of a bromine atom.

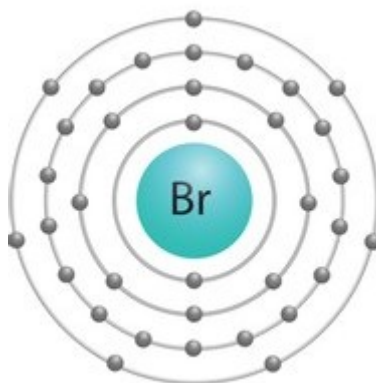


Figure 1.6: A bromine atom with its energy levels (<https://www.shutterstock.com/image-vector/bromine-atom-shell-1259526367>).

Elemental bromine is very reactive and thus does not occur in nature but only in soluble mineral salts. At high temperatures, organobromine compounds dissociate to yield free bromine atoms, a

process that stops free radical chemical chain reactions. Due to this, more than half of the bromine produced worldwide each year is used as fire retardants. Ultraviolet radiation can dissociate bromine molecules in the atmosphere to yield free bromine atoms, which deplete ozone. As a result, many organobromine compounds that were used in the past were linked to stratospheric ozone depletion and are no longer used (Salawitch et al., 2005).

1.3.1 Halogens in the Stratosphere

The dissociation from ultraviolet radiation also applies to chlorine and iodine. The primary source of halogens in the stratosphere is the transport of chlorofluorocarbon compounds (CFCs) or halogenated hydrocarbons (halons) from the troposphere. These compounds were known to be volatile and chemically inert in the troposphere. However, when they reach the stratosphere, through ultraviolet solar radiation, halogen molecules are dissociated. Since the discovery of the Antarctic ozone hole (Farman et al., 1985) and its relationship to halogen species, the Montreal Protocol was agreed upon in 1987. The agreement suggests that the production of CFCs should be reduced by half and eventually end by 1996 in developed countries. The main set of reactions between halogens and ozone are the following (Sinnhuber et al., 2005):



Where X is the halogen atom. This is one way BrO is produced. Halogen species can catalytically destroy ozone until they are converted into stable reservoirs. Another catalytic ozone destruction cycle involving species of different families is the following:



During high chlorine activation (i.e. inside the polar vortex), the following reactions are important (Theys et al., 2009 and references therein):



The reactive halogens are converted into reservoirs in the stratosphere through the following reactions (Cicerone, 1981):





While the following reactions are converting the halogen reservoirs into reactive species (McElroy et al., 1986):



Heterogeneous reactions release halogens (particularly Cl) from the reservoirs and remove nitrogen oxides from the atmosphere. They occur primarily inside polar stratospheric clouds (Molina et al., 1987):



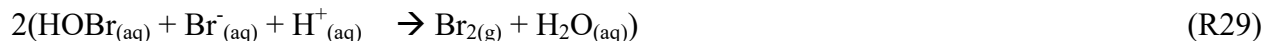
1.3.2 Halogens in the Troposphere

Bromine monoxide (BrO) plays a significant role in the atmospheric chemistry of the Arctic. During polar springtime, episodes of strongly enhanced amounts of BrO have been observed in the boundary layer (Barrie and Platt, 1997). The formation of these intense plumes of BrO results in tropospheric ozone depletion. Tropospheric ozone depletion and the link to halogen chemistry events was first discovered over 30 years ago (Barrie et al., 1988) and has been the subject of many studies and research campaigns over the past three decades (Toohey et al., 1990; Tuckermann et al., 1997; Saiz-Lopez and Glasow, 2012). The release of reactive halogens and the decrease in ozone (O_3) impact the oxidizing capacity of the troposphere. The photolysis of O_3 in the UV-B leads to the formation of the most essential tropospheric oxidising agent, the hydroxyl radical, OH (Lelieveld et al., 2016). Although bromine radicals can contribute to the formation of OH on short timescales, the destruction of ozone caused by reactive bromine

decreases the OH concentrations and is more profound (Stone et al., 2018). While in plumes of tropospheric BrO, the oxidising agents O₃ and OH are reduced, the reactions of BrO also play other vital roles in atmospheric chemistry. For example, BrO efficiently reacts with elemental mercury. This oxidation initiates a process whereby deposition of mercury, Hg, to snow and ice increases. This results in Hg entering the food chain (Lu et al., 2001; Ariya et al., 2004). BrO plumes' rapid and sudden appearance over the polar regions has been called the "bromine explosion"(Barrie and Platt, 1997; Platt and Perner, 1983). It is explained by an autocatalytic multiphase chemical cycle, which occurs on cold saline surfaces (Fan and Jacob, 1992; Sander and Crutzen, 1996). Although there are studies that try to model BrO plumes from their driving mechanisms (Falk and Sinnhuber, 2018; Toyota et al., 2011; Huang et al., 2020), each parameter's exact level of impact on the formation of enhanced tropospheric BrO is uncertain. However, there is the consensus that the potential sources of BrO plumes are (a) rich in sea salts and relatively cold (conditions occurring in potential frost flowers regions; (Kaleschke et al., 2004; Sander et al., 2006), (b) surfaces covered with liquid or frozen brine (Sander et al., 2006), (c) associated with blowing snow (Yang et al., 2020; Blechschmidt et al., 2016; Zhao et al., 2016), (d) surface snow packs (Peterson et al., 2018) and young salty sea ice regions (Wagner et al., 2001; Simpson et al., 2007, 2017). A pH lower than 6.5 is required for efficient bromine activation (Fickert et al., 1999; Halfacre et al., 2019).

Organic sources of BrO, such as oceanic organobromine compounds, have also been discussed in the literature (Salawitch, 2006). Their relatively long lifetimes result in a slow release of Br throughout the Arctic troposphere or beyond and are currently not considered to explain a significant part of the bromine explosion mechanism.

Starting with molecular bromine in the gas phase, the sequence of autocatalytic chain reactions describing the bromine explosion can be written in its simplest form as:

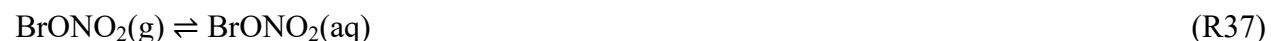


The reason that the set of reactions is called bromine explosion is that each Br atom in the gas phase releases another Br atom from the liquid phase. In short, the autocatalytic multiphase chain reaction releases molecular bromine, Br₂, to be photolysed by solar radiation (hν) (R27). The resulting bromine atoms rapidly remove tropospheric O₃ (R6). The resultant BrO reacts with HO₂ to form HOBr (R15). This enters the aqueous phase or quasi liquid layers on cold brine or snow and ice (R28), where it reacts with halogen ions to release an additional bromine atom as Br₂ to

the atmosphere (R29). The efficiency of such a chain reaction depends on the chain length in the atmosphere. The ratio of the relative rate of chain propagation to chain termination reactions of the chain carriers, i.e. the Br and BrO, determines the chain length. In addition, there are cycles involving chlorine ions, also initiating the release of BrCl, which leads to further catalytic loss of O₃ (Vogt et al., 1996):



The bromine explosion slows down through the depletion of O₃ in the air mass or through reactions of Br or BrO with formaldehyde or NO₂:



The effectiveness of the bromine explosion in ozone depletion can be described by the fact that the process ends when there are no more O₃ molecules (it can nearly completely remove O₃). Figure 1.7 summarizes the bromine release and cycles discussed above.

between two peaks of the electromagnetic wave, while the frequency is the number of wave periods per time. The two quantities are connected with the equation below:

$$c = \lambda \cdot \nu \quad [1.1]$$

where c is the speed of light. The solar spectrum is divided into regions based on these two quantities (Figure 1.8).

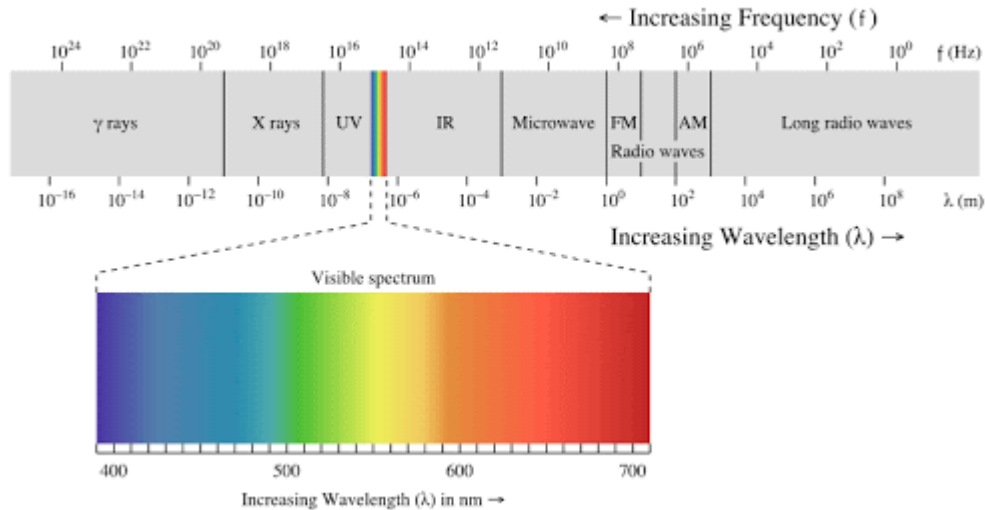


Figure 1.8: The electromagnetic spectrum (<https://www.radio2space.com/components-of-electromagnetic-spectrum/>).

The ultraviolet (UV) part of the spectrum is where BrO absorbs radiation and is suitable for satellite remote sensing. The visible spectrum is the part that humans can understand through vision. It is essential to mention how small the fraction of the visible spectrum is, compared to the whole range of electromagnetic radiation. It covers a range from 400nm to 700nm. This is the only part of the spectrum which we can relate to colors. Sunlight, although it can be seen as a unified color, in reality, consists of a variety of wavelengths. The infrared (IR) part of the spectrum covers the wavelength range from $0.7\mu\text{m}$ to $100\mu\text{m}$, 100 times broader than the visible. Some trace gases (i.e. CO_2) absorb radiation in these regions. Therefore, there are satellite instruments that also provide measurements in this wavelength region.

1.4.2 Absorption

Absorption is a fundamental mechanism that occurs when electromagnetic radiation interacts with the atmosphere. It causes molecules of trace gases to absorb energy in various wavelengths and is described by the Beer-Lambert law:

$$I = I_0 e^{-\int \sum_{j=1}^J \{\sigma_j(\lambda) \rho_j\} ds} \quad [1.2]$$

where I is the measured intensity of the electromagnetic radiation, I_0 is the initial intensity, J is the total number of trace gases absorbing, j denotes a particular trace gas (e.g. BrO), $\sigma(\lambda)$ is the cross section of the absorber at wavelength λ , ρ the concentration of the trace gas. The integral is

taken along the light path s . Ozone, water vapor and CO_2 are three primary gases that can absorb solar radiation at different wavelengths. There are wavelength regions in which light is mainly absorbed, while there are other regions in which light is transmitted. These regions are called atmospheric windows and are useful for satellite remote sensing, as the backscattered radiation can reach the satellite without much attenuation.

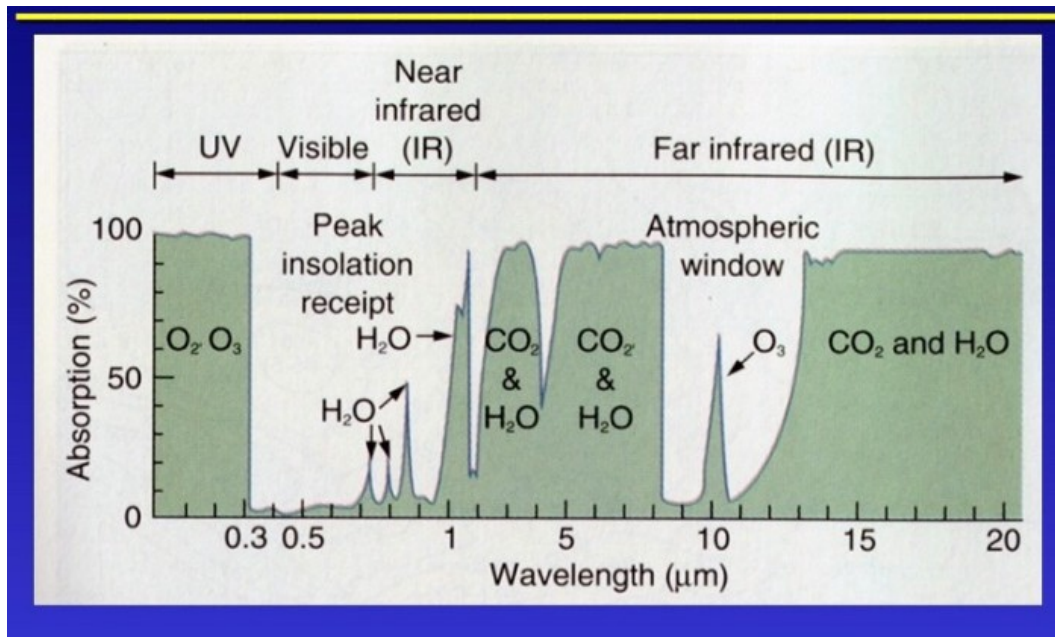


Figure 1.9: Main absorption bands by atmospheric gases and atmospheric windows. (<https://www.chegg.com/>).

1.4.3 Scattering

Scattering is another mechanism of radiative transfer that occurs in the atmosphere. It arises when particles or molecules in the atmosphere interact with radiation and cause its redirection and deviation from a straight trajectory. There are two main categories of scattering: elastic and inelastic scattering. The type and the actual form of scattering depend on many parameters, such as the wavelength, air particles' size, and composition. Rayleigh scattering is the dominant elastic scattering of light. It occurs when the particles are small compared to the wavelength of incoming radiation. It causes shorter wavelengths to be scattered much more than longer wavelengths (the scattering cross section is inversely proportional to the fourth power of the wavelength). This mechanism is mainly the reason why the sky is blue. A simplified equation describing the Rayleigh scattering cross section is given in [1.3] (Nicolet, 1984).

$$\sigma_{\text{Ray}}(\lambda) \approx \frac{4.02 \cdot 10^{-28}}{\lambda^{4.04}} \text{ (m}^2 \text{ mol}^{-1}\text{)} \quad [1.3]$$

Mie scattering occurs when the particles have approximately the same size as the wavelength of the incoming solar radiation. Dust, smoke, and water droplets are common causes of Mie scattering, affecting longer wavelengths than Rayleigh scattering. Mie scattering appears mainly in the lowest parts of the atmosphere, where bigger particles are present in larger numbers, and

there are often clouds. The scattering cross section of Mie scattering can be described as (Platt and Stutz, 2008):

$$\sigma_{\text{Mie}}(\lambda) \propto \frac{1}{\lambda^\alpha} \text{ (m}^2 \text{ mol}^{-1}\text{)} \quad [1.4]$$

where α is the Ångström exponent.

Raman scattering is, in contrast to Rayleigh and Mie scattering, an inelastic form of scattering. This means that the scattering molecule changes its state of excitation during the scattering process, while the frequency of the scattered radiation also changes. In most cases, only the rotational state of the molecule is affected (rotational Raman scattering). However, the vibrational state can also change (vibrational Raman scattering). Although it is rare in the atmosphere (i.e. around 4% of Rayleigh scattering), it is essential, as it can explain changes in the apparent depth of Fraunhofer lines. This effect is referred to as the Ring effect (Grainger and Ring, 1962).

1.5 Satellite Remote Sensing

Solar radiation that is not absorbed or scattered in the atmosphere can reach and interact with the Earth's surface. When radiation reaches its destination, three actions can occur: absorption at the surface, transmission through the surface, or reflection. The total transmitted energy from radiation will interact with the surface in one or more of these three ways, depending on the surface's state. Satellite remote sensing is based on the principle of solar radiation reaching the satellite after interaction with the Earth's surface and atmosphere. The Sun provides a proper power source for remote sensing. Such sensors, which are using an external power source, are called passive remote sensors. On the other hand, active sensors provide the light source themselves. Many satellite sensors are using passive remote sensing. The satellite's orbit is the path that the satellite follows, and it is a critical parameter. Geostationary satellites are placed at a high altitude (i.e. 36.000 km) and observe the same part of Earth's surface at any given time. These satellites rotate with velocities aligned with the Earth's rotation so that they seem to remain stationary. Many satellite sensors are designed to follow a specific orbit (mostly North-South), which, combined with the Earth's rotation (West-East), allows them to observe most of the Earth's surface. These satellites are in polar orbits (altitudes between 200 and 1000 kilometres). Many satellites are also synchronized with the sun (sun-synchronized) to cover every region at a specific local time, which is called the overpass time.

Many satellite remote sensing studies have been dedicated to BrO in the polar regions. Richter et al. (1998), Platt and Wagner. (1998) and Chance (1998) were the first studies on satellite observations of BrO plumes in polar regions, using the GOME instrument (Burrows et al., 1999). Using observations from the same instrument, Hollwedel et al. (2004) derived a six year time-series of Arctic and Antarctic total vertical column densities (VCDs) of BrO. This was the first scientific effort to study the evolution of BrO in the polar regions. The transport of BrO plumes,

which represents a photo-stationary state with production and loss processes and their capability of depleting ozone, far away from the initial release area, was studied with satellite remote sensing (Ridley et al., 2007; Begoin et al., 2010). The relationship between BrO release and young sea ice was also discussed (Wagner et al., 2001), where it was indicated that high BrO concentrations are always found over or near sea ice on the Caspian Sea. Van Roozendaal et al. (2004) used SCIAMACHY observations for Arctic BrO and compared them to GOME data, showing satisfactory agreement between the two different sensors. Theys et al. (2011) compared tropospheric BrO columns derived from GOME-2A to a chemical transport model, showing consistency with possible release mechanisms of bromine. Sihler et al. (2012) compared GOME-2 BrO columns to ground-based measurements in the Arctic, demonstrating good agreement between them. Seo et al. (2019) presented the first BrO retrievals from the TROPOMI instrument, showing high-resolution BrO retrievals with low fitting errors. Other studies have also used satellite remote sensing to link bromine explosion events to their sources and triggering meteorological conditions to understand this complex and significant phenomenon better. For instance, Blechschmidt et al. (2016) investigated a bromine explosion event using GOME-2A and associated its long lifetime with continuous release of bromine molecules from blowing snow along the front of a polar cyclone.

1.5.1 DOAS

The Differential Optical Absorption Spectroscopy (DOAS) method (Platt and Perner, 1983; Burrows et al., 2011) is a method used to estimate concentrations of trace gases in the atmosphere. DOAS evolves from the Beer and Lambert law, which describes the attenuation of electromagnetic radiation in a medium (Equation 1.2). The atmospheric absorption of trace gases of interest can be retrieved by using their characteristic spectral fingerprints. This is achieved by separating the extinction signal into a low frequency and a high frequency part. The low frequency part is treated as a closure term and is fitted by a low order polynomial. The higher frequency term contains the absorption structures of the trace gases. The final output of the retrieval is the slant column density of the trace gas, i.e. the density of the trace gas, integrated along the light path (Platt and Stutz, 2008):

$$\text{SCD}_j = \int \rho_j(s) ds \quad [1.5]$$

The radiance upwelling at the top of the atmosphere is approximated at a given wavelength by

$$I(\lambda) = \alpha(\lambda)I_0(\lambda) e^{-\int \sum_{j=1}^J \{\sigma_j(\lambda)\text{SCD}_j + \sigma_{\text{Ray}}(\lambda)\text{SCD}(\text{Ray}) + \sigma_{\text{Mie}}(\lambda)\text{SCD}(\text{Mie})\} ds} \quad [1.6]$$

where α is the scattering efficiency, SCD_j the slant column density of the gas with index j , $\sigma_{\text{Ray}}(\lambda)$ and $\sigma_{\text{Mie}}(\lambda)$ are the scattering cross sections of Rayleigh scattering molecules (e.g. primarily air molecules, molecular nitrogen N_2 and oxygen, O_2) and Mie scattering particles (e.g. aerosol particles), $\text{SCD}(\text{Ray})$ and $\text{SCD}(\text{Mie})$ are the corresponding slant columns of Rayleigh and Mie

scatterers. As Rayleigh and Mie scattering efficiency varies smoothly with wavelength, they can be approximated by low order polynomials. This results in the following approximation:

$$\ln \frac{I_o(\lambda)}{I(\lambda)} = \sum_j \sigma_j(\lambda) \text{SCD}_j - \sum_p b_p \lambda^p \quad [1.7]$$

where b_p are the coefficients of the polynomial. It should be stated that the DOAS method can be applied to other platforms as well (e.g. instruments on ships, cars and stationary buildings). Figure 1.10 shows a DOAS fit performed for BrO with the settings we applied in this thesis:

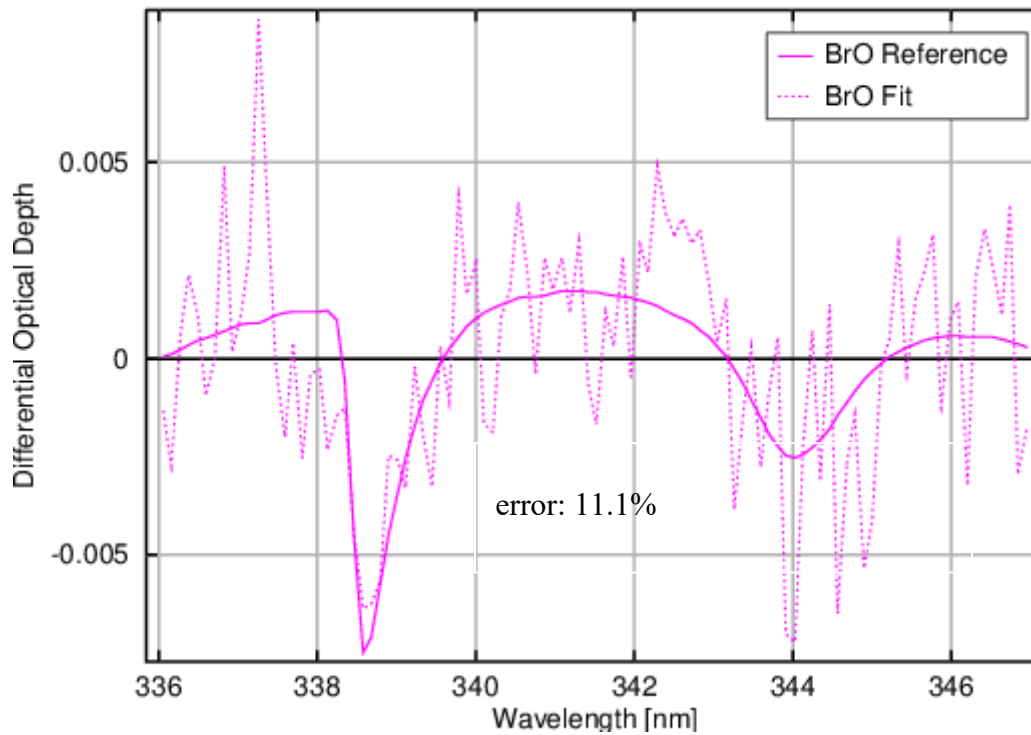


Figure 1.10: Examples of a typical DOAS fit for BrO with the settings used in this thesis.

1.5.2 Instruments

The GOME (Global Ozone Monitoring Experiment) (Burrows et al., 1999) instrument was launched in 1995 on ERS-2. It was a nadir viewing scanning spectrometer, observing solar back-scattered radiation upwelling from the Earth's surface and atmosphere. It measured continuously in four spectral channels from 240 to 790 nm, with a spectral resolution between 0.2 and 0.4 nm. For 27 days per month, the spatial resolution of the forward scans was $40 \times 320 \text{ km}^2$, and the swath was 960 km. For approximately three days per month, the instrument operated in narrow swath mode with a swath width of 240 km and ground scenes having a spatial resolution of $40 \times 80 \text{ km}^2$. ERS-2 was in a Sun-synchronous orbit with a 10:30 local time equator overpass in the descending node. GOME was the first satellite instrument, which measured vital tropospheric gases that have weaker absorption lines than ozone: examples being NO_2 , BrO, HCHO and SO_2 (Burrows et al., 1999). The instrument was launched in July 1995 and lost its global coverage in

2003 due to data rate limitation (the onboard storage capability of the instrument was disabled, and as a result, data could only be transmitted directly to ground stations) (Bracher et al., 2005).

SCIAMACHY (SCanning Imaging Absorption SpectroMeter for Atmospheric CHartography) (Bovensmann et al., 1999; Burrows et al., 1995) was a satellite spectrometer on board Envisat. It was launched into space in 2002. The main advantage of SCIAMACHY compared to GOME was its broader spectral coverage, ranging from 210 nm to 2380 nm, allowing the observation of many trace gases in the near-infrared (0.75 to 1.4 μm) and short wave infrared (1.4 to 3 μm) spectral regions. SCIAMACHY’s spectral resolution was 0.2 nm to 0.5 nm, and its spatial resolution in the spectral region used for BrO retrievals was 30x60 km^2 , with a 960 km swath width in nadir. The overpass of Envisat over the equator was at 10:00 local time. SCIAMACHY observed the Earth in nadir, limb and occultation geometries, providing a wealth of trace gas data of the atmosphere from the surface to the upper atmosphere (Bovensmann et al., 1999). In April 2012, Envisat lost contact with the ground station, and as a result, the mission was terminated.

The series of GOME-2 (Global Ozone Monitoring Experiment–2) Callies et al. (2000) instruments were developed as the successors of GOME. There are currently three instruments in orbit, one launched on board Metop-A in 2006, one on Metop-B in 2012, and one on Metop-C in 2018. Here, we use data from GOME-2A and GOME-2B. All GOME-2 instruments share the same attributes and sense the Earth’s backscattered radiance and extra terrestrial solar irradiance in the ultraviolet and visible part of the spectrum (240 nm to 790 nm). They have a spectral resolution between 0.2 nm and 0.4 nm, while the footprint size is 80x40 km^2 and the swath is much wider (1920 km) than for the previous instruments. However, GOME-2A changed its swath to 960 km and footprint to 40x40 km^2 in June 2013. The GOME-2 instruments are crossing the equator at 09:30 local time (Callies et al., 2000). All three instruments are currently in operation. Table 1.3 summarizes the instruments used in this thesis and their attributes:

Table 1.2: Satellite instruments used in this study and their attributes.

Instrument	Platform	Period	Footprint	Equatorial Overpass	Swath
GOME	ERS-2	1996 – 2003	320x40 km^2	10.30 LT	960 km
SCIAMACHY	Envisat	2002 – 2012	30x60 km^2	10.00 LT	960 km
GOME-2A	MetOp – A	2007 – present	80x40 km^2 40x40 km^2 (since June 2013)	09.30 LT	1920 km 960 km (since June 2013)
GOME-2B	MetOp – B	2012 – present	80x40 km^2	09.30 LT	1920 km

Space-borne optical instruments often suffer from a decrease in throughput in the ultraviolet spectral region, which arises from the deposition of absorbing layers on the optical surfaces such as mirrors, lenses or gratings. This results in a variety of effects, such as loss of throughput and changing etalons in the instrument. The quality of the retrieved BrO data produced from the weak

absorption signal in the UV region is influenced by these degradations. The GOME, SCIAMACHY and GOME-2 teams identify any degradation in the reflectances and correct where appropriate and possible. For example, organic compounds and water emitted by the spacecraft are photochemically transformed by UV-B and vacuum UV from the Sun and most likely form long chain polymers, which have low vapor pressure and are adsorbed on the mirrors. In this context, Tanzi et al. (2000) showed that the GOME sensor experienced degradation in all wavelength regions but in particular in the UV, consistent with degradation of the scan mirror. Krijger et al. (2007) compared the degradation of GOME to SCIAMACHY with respect to reflectivity. Most of the degradation effects on the sensors are identified and documented in the literature and, where possible, are accounted for (Munro et al., 2016). MetOp-A has started to drift in orbit, and there are periods during which solar measurements are no longer feasible for GOME-2A.

1.6 Artificial Neural Network

Artificial Neural Networks are computing systems inspired by biological neural networks similar to those in the human brain (Wang, 2003). They are part of artificial intelligence and machine learning algorithms. Artificial intelligence is the section of computer science that deals with the design and implementation of programs capable of imitating human learning behaviours, showing characteristics that are commonly attributed to humans, such as problem solution, conclusion extraction, recognition through vision, natural language processing. It is a rapidly evolving research area in a broad spectrum of fields (Vlahavas et al., 2011). Machine learning is a mechanism that allows the addition of new knowledge in the database of the system. We could say that it is the creation of information from the processing mechanism using the existing knowledge in the database (data). Machine learning is split into two major categories. In supervised learning, the learning process is achieved based on some rules and labels of the data. In unsupervised learning, the mechanism defines new rules and patterns using the existing data and its correlations (Vlahavas et al., 2011; Haykin, 2009).

Artificial neural networks provide a mathematical representation of the human mind. An artificial neural network comprises many independent processing units (neurons) connected and structured in a hidden layer, where the processing of the connections between the input and the output layer is performed to interpret complex systems. It acquires knowledge through training. Some of the many advantages are that they can extract hidden knowledge from highly complex data, either by supervised or unsupervised learning and that this is generally a fast approach (Zurada, 1992).

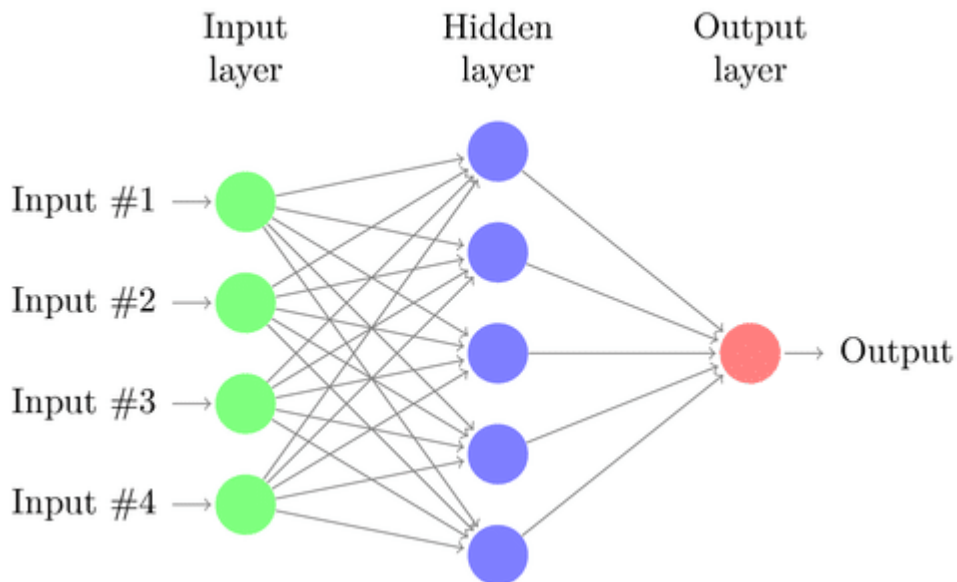


Figure 1.11: A schematic of a typical neural network.

Machine learning, especially neural networks, is often used to tackle non-linear problems (Zurada, 1992). Implementations of neural networks in atmospheric research include weather prediction (Rasp and Lerch, 2018), ozone forecasting (Comrie, 1997), remote sensing (Blackwell and Chen, 2005; Müller et al., 2002), air quality (Hooyberghs et al., 2005, p.1) and OH modeling (Nicely et al., 2019).

2. METHODS, ALGORITHMS AND DATASETS

In this chapter, the practical implementation of the theory will be discussed in order to investigate the retrieval settings for the satellite remote sensing of BrO for the Arctic region. This chapter is separated into two sections. The first includes the methods and algorithms used to derive the consistent long-term BrO dataset, apply the stratospheric separation of BrO, obtain the tropospheric vertical column density, and develop the artificial neural network to identify enhanced BrO plumes. The second section addresses the various additional datasets we used, either for technical reasons (e.g. stratospheric separation, flagging of scenes, training of the neural network) or for scientific analysis and interpretation (comparisons to the long-term tropospheric BrO dataset). At the end of this chapter, all the technical details concerning the results shown in the following chapters will be covered. For all the figures, which include results from different satellite instruments, GOME will be shown in red, SCIAMACHY in blue, GOME-2A in green and GOME-2B in brown color.

2.1 Satellite Retrieval

In this section, the approach followed to create the consolidated long-term BrO dataset is described. This includes the procedure of the final cross sections and fitting windows selected, together with the criteria evaluated for each of the set of settings applied. Afterwards, some of the sensitivity tests performed to assess each satellite sensor's final settings will be presented, together with a short sub-section about the OMI instrument.

2.1.1 Approach

As discussed in the introduction, the first immediate output of applying the DOAS method to satellite remote sensing is the Slant Column Density (SCD), which describes the concentration of the trace gas of interest along the entire light path. Since the central area of interest is the Arctic, we decided to select the retrievals in the region from 70.0° N to 85.0° N latitude and from 180° W to 180° E longitude. This is based on sea ice covered scenes (that is why we set the southern limit to 70.0° N) and that all instruments provide measurements over the same area so that our results are consistent (that is why we set the northern limit to 85.0° N). The maximum Solar Zenith Angle (SZA) was set to 80 degrees to ensure good sensitivity for tropospheric BrO. To retrieve accurate BrO SCDs, an optimal selection of the spectral window, which maximises the

information content concerning the BrO absorption, and the selection of corresponding cross sections of other trace gases absorbing in the same spectral window is the first step. We chose to use temperature dependent cross sections of ozone (dominant absorber in the UV) by Serdyuchenko et al. (2014) at 223K and 243K and a BrO cross section (Fleischmann et al., 2004) at 223K. Figure 2.1 shows the BrO cross section used, as a function of wavelength, before the convolution with the instrument's slit function.

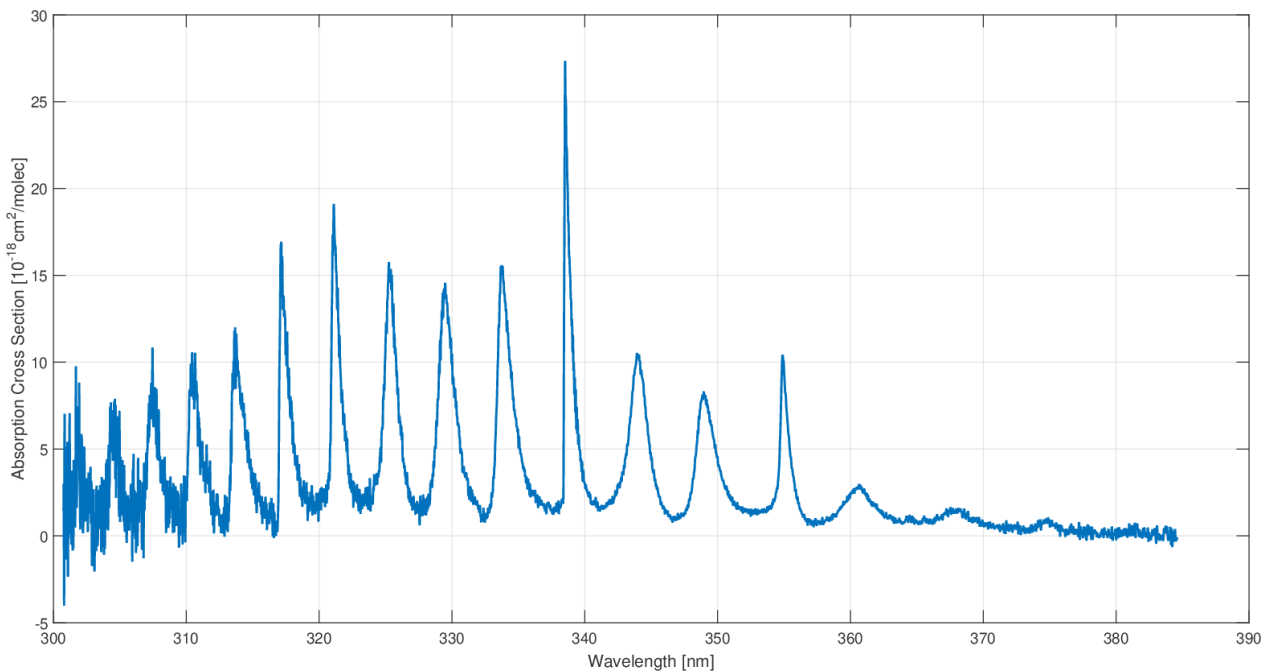


Figure 2.1: The absorption cross section of BrO used in this work in vacuum at 223 Kelvin (Fleischmann et al., 2004).

In addition, a pseudo cross section is used for simulating the filling-in of Fraunhofer lines by Raman scattering known as the Ring effect (Vountas et al., 1998), and another pseudo cross section, which deals with spectral undersampling (Chance et al., 2005), was included in the fitting for all instruments. The high spectral resolution absorption cross sections were convolved by the slit function of each instrument. The impact of using different combinations of trace gas absorption cross sections in the fit of BrO SCD was investigated. It was found that the omission of the explicit fitting of NO_2 and SO_2 has a minimal impact on the fit of the BrO SCD north of 70° N. The differences in BrO SCD between fits with and without NO_2 or SO_2 in the selected spectral ranges were typically less than 1% of the BrO SCD. Consequently, we decided to use only the cross sections of the dominant absorber O_3 in this region and of the trace gas of interest itself, BrO, in the non-linear least squares SCD fitting. The differences between fits of BrO SCD using fourth and fifth order polynomials were small, and the quality of the fit improved significantly for a fourth order compared to a third order polynomial fit. These results led to the selection of the use of the fourth order polynomial in our retrieval. The selection of parameters used in this study is appropriate for BrO columns in the region defined as the Arctic.

As BrO is a relatively weak absorber, small changes in the input parameters and especially of the fitting window of the retrieval lead to significant changes in the quality of the fit. Although there are many good practices developed for the DOAS fitting window selection for an absorber (e.g. it must include at least two absorption peaks from the trace gas of interest, no large Fraunhofer lines, little interference from other species), there is no precise and agreed methodology to determine the optimal selection. Consequently, different spectral fitting windows for BrO retrievals have been used in previous studies. For example, Richter et al. (1998) used a 345 – 359 nm wavelength region for GOME, Afe et al. (2004) used a 336 - 347 nm fitting window for SCIAMACHY, while Theys et al. (2009) used a 336 to 359 nm fitting window for GOME-2A. Each of the sensors has slightly different instrumental characteristics, and each of them shows different degradation behavior. Consequently, we chose the optimal spectral fitting window for each of the sensors using the following set of selection criteria: a) smallest root mean square error (RMSE) of the fit, b) minimal trend of BrO SCDs over a clear Pacific reference region, where no strong trend in BrO is expected and c) good agreement between retrievals from the different sensors for periods of overlapping measurements. The RMSE of the fit in absolute units is defined as:

$$\text{RMSE} = \sqrt{\sum_{i=1}^N \frac{\left(\ln\left(\frac{I_0(\lambda_i)}{I(\lambda_i)}\right) - \sum_j \sigma_j(\lambda_i) \text{SCD}_j - P(\lambda_i) \right)^2}{N}} \quad [2.1]$$

where N is the number of spectral points, and $P(\lambda)$ is the low order polynomial. The RMSE was averaged over all the scenes in the region of interest (i.e. the Arctic from 70.0° N to 85.0° N latitude, 180° W to 180° E longitude, the Pacific reference region from 50.0° S to 10.0° N latitude and 90.0° W to 125.0° W longitude and the Hudson Bay from 50.0° N to 66.0° N latitude and 264.0° W to 284.0° W longitude).

Figure 2.2 shows the SCDs of BrO and the RMSE of the fit over the Pacific reference region for the final set of settings.

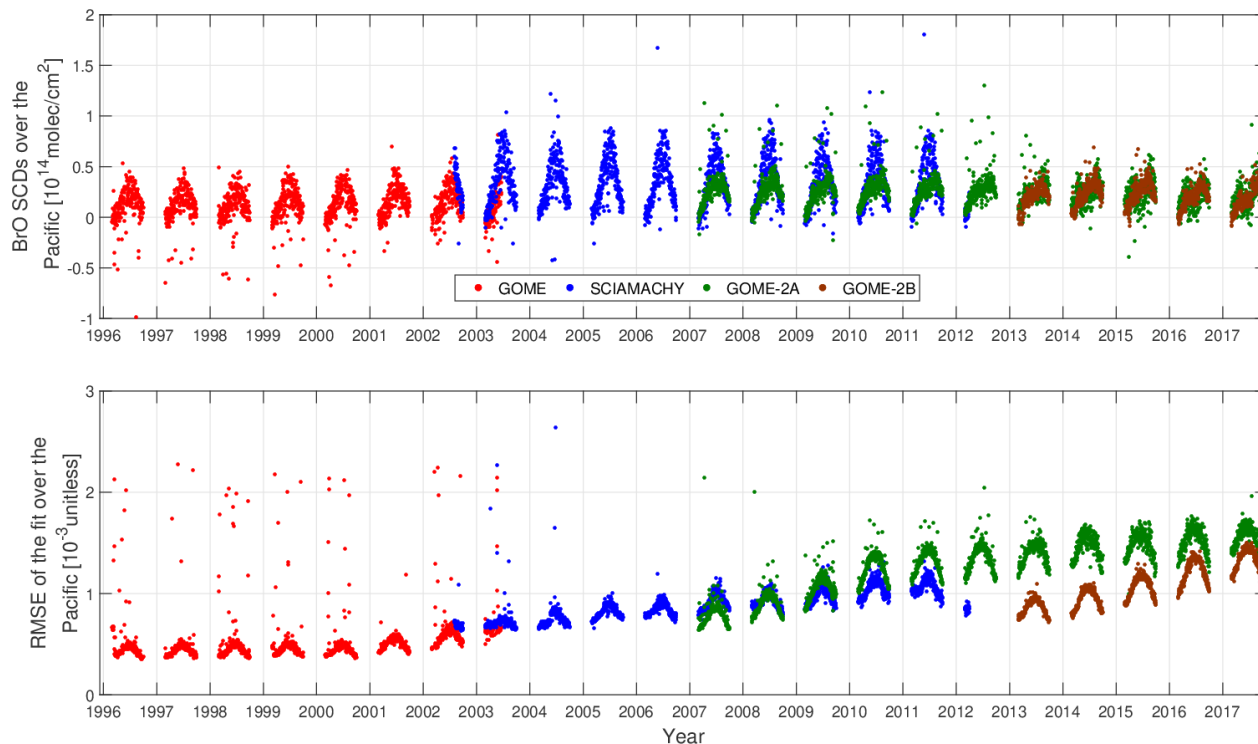


Figure 2.2: Evaluation criteria for the retrievals. Top: SCDs of BrO over the Pacific reference area. Bottom: the RMSE of the fit for the same region (50.0° S to 10.0° N latitude and 90.0° W to 125.0° W longitude).

The RMSE for the Pacific region shows similar behavior for GOME-2A and GOME-2B, as both increase strongly with time. GOME appears to have lower RMSE values on average than the GOME-2A and GOME-2B instruments, presumably because of the lower spatial resolution, but the RMSE shows large variability. Generally, daily mean RMSE values are below 2.0×10^{-3} for all instruments. There is no clear trend in the SCD of BrO over the Pacific region for any of the instruments.

Figure 2.3 shows the RMSE of the fit over the Arctic region and the Hudson Bay for the final set of settings.

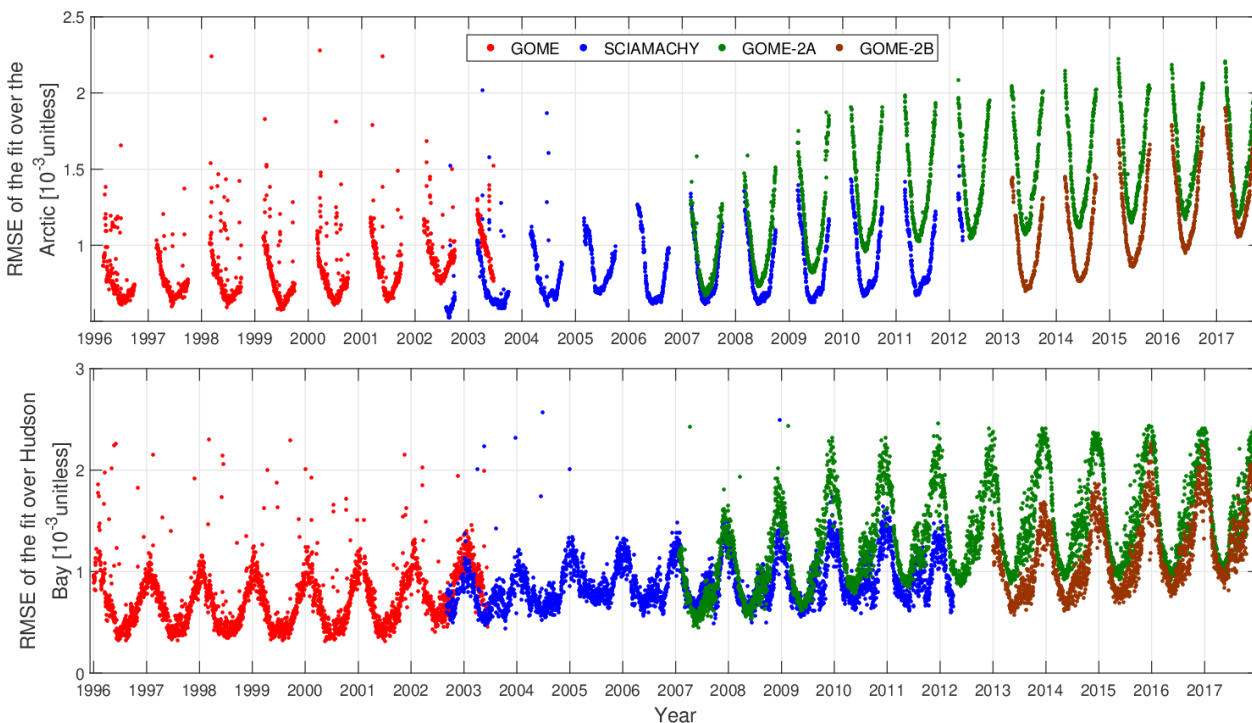


Figure 2.3: Evaluation criteria for the retrievals. Top: RMSE of the fit over the Arctic region (70.0° N to 85.0° N latitude, 180° W to 180° E longitude). Bottom: RMSE of the fit for the Hudson Bay (50.0° N to 66.0° N latitude and 264.0° W to 284.0° W longitude).

The annual cycle in the fitting RMSE for the Arctic results from changes in the Sun's position and its impact on the upwelling radiance. In spring and autumn, when the solar zenith angle is larger, the scattering and attenuation increase, and as a result, the radiance signal is low. In the Arctic, SCIAMACHY has the lowest fitting RMSE of all instruments. GOME-2A shows a rapid increase in RMSE up to 2009 and a more minor upward trend in the following years. A similar systematic increase in RMSE occurs for GOME-2B. The seasonality of the RMSE is similar for the Hudson Bay, except that there we have values throughout the entire year. We see that SCIAMACHY is stable, with an absence of a trend, and much lower RMSE errors, from both GOME (i.e. 2003 the only overlapping year) and GOME-2A (i.e. from 2007 to 2012).

The use of a reference area over the Pacific as background spectrum is an alternative to solar irradiance measurements, which removes systematic errors arising from interfering instrumental structures in the solar irradiance measurements. The region of the Pacific is selected because of its relatively small annual cycle of BrO (Richter et al., 2002). In this way, the quality of the fit improves as problems in the radiances mainly cancel out. Consequently, the Pacific background spectrum has been used instead of the Sun background spectrum for all instruments in the present study. Although trends over the clean Pacific background region resulting from instrumental degradation were minimised, residual trends had to be accounted. This has been achieved by applying an additional Pacific correction to each instrument separately. The normalization method computes the average BrO SCD in a small Pacific area ($0.0^\circ \pm 10.0^\circ$ latitude, $180.0^\circ \pm 20.0^\circ$ longitude) and then subtracts this average from every pixel of the BrO SCD on a daily

basis. To compensate the negative bias imposed by the method, a constant offset of 7×10^{13} molecules/cm² was added for every day (Richter et al., 2002; Sihler et al., 2012). This correction tackles offset errors that occur for weak absorbers and are due to instrumental degradation (Alvarado et al., 2014). Figure 2.4 shows the impact of such a correction on some early GOME-2A retrievals (old settings). We compare the application of the Pacific correction to the final retrieval settings that we applied (new settings) to point out that solid trends were already excluded.

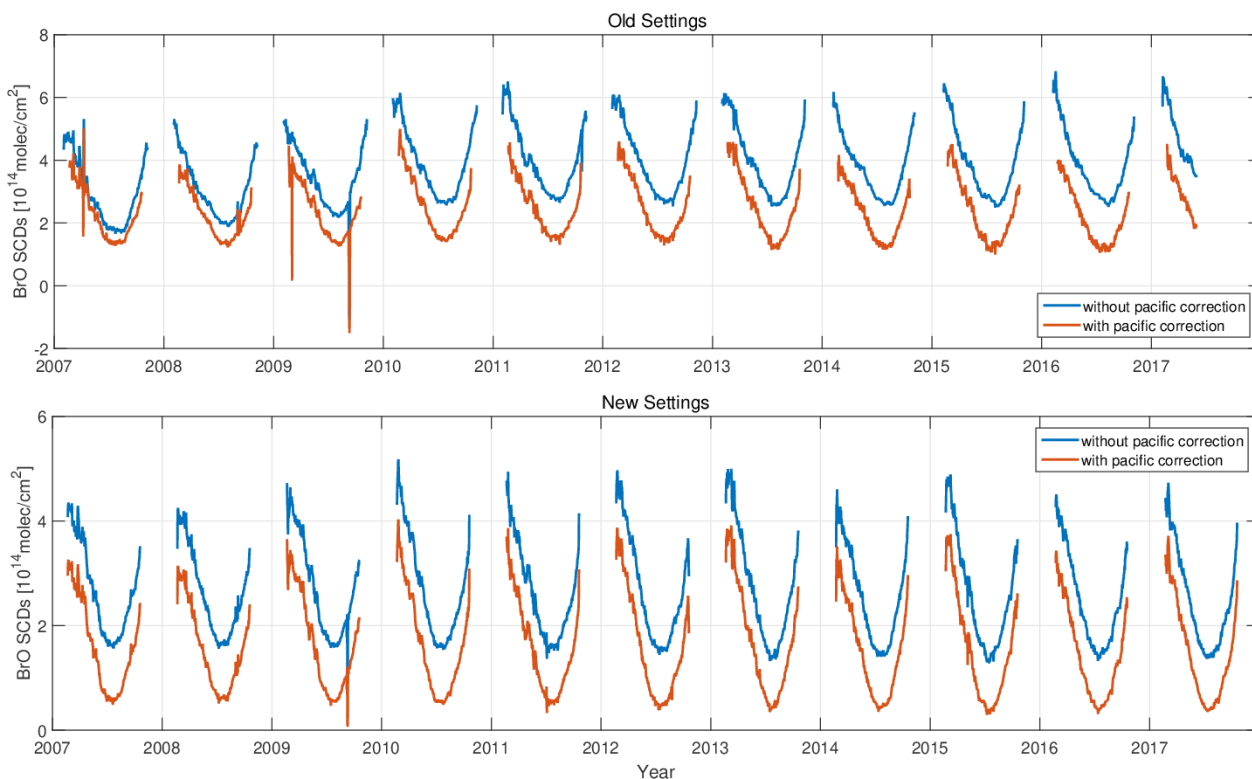


Figure 2.4: Two examples of the application of the pacific correction on GOME-2A retrieval settings. Top: old settings, where the correction has an impact. Bottom: new settings, where the correction can be described as an offset. Both plots are showing BrO SCDs for the Arctic region.

In the old settings, there is a clear trend without the application of the pacific correction. However, as the trend vanishes with its application, it is safe to conclude that it is artificial and not produced by geophysical phenomena. In the new settings, though, there is no obvious trend without the application of the pacific correction, something that verifies the improvement on the quality of the retrieval settings.

The final step of the methodology for the satellite retrieval is to derive the geometric BrO VCD, which includes only the vertical concentration of BrO. This is done by dividing the BrO SCD with a simple stratospheric air mass factor (AMF), which considers the scattering at the surface but ignores the impact of scattering within the atmosphere. Consequently, the geometric VCD differs from the sum of the tropospheric and stratospheric columns.

The empirically determined sets of parameters used in the fitting of BrO in the spectral windows are reported in Tables 2.1 and 2.2.

Table 2.1: Final parameter selection for all instruments.

Parameters	Cross sections - Application Selection
Ozone, O₃	(Serdyuchenko et al., 2014), 223K and 243K
BrO	(Fleischmann et al., 2004), 223 K
Ring effect	Ring cross section calculated by SCIATRAN model
Under-sampling correction	Yes
Fraunhofer lines	Chance and Kurucz (Chance et al., 2010)
Background spectrum	Pacific area (50.0° S to 10.0° N lat., 90.0° W to 125.0° W lon.)
Degree of the polynomial	4 th

Table 2.2: Fitting windows used for the different instruments.

Instrument	Fitting Window [nm]
GOME	336.8 - 358
SCIAMACHY	336 - 347
GOME-2A	337.5 - 357
GOME-2B	338 - 360

2.1.2 Sensitivity Tests

As mentioned before, although there are many empirical suggestions on how to perform a retrieval of a trace gas of interest, there is no established precise algorithm on how to perform it. Since the long-term agreement between the sensors was an additional criterion that we applied, it was not valuable to perform sensitivity tests for single days (or short periods) and then evaluate the produced retrieval using the metrics described above (i.e. SCD over the pacific and RMSE over the areas of interest). Therefore, we have performed several sensitivity tests, spanning the whole period of the dataset we want to derive (i.e. 1996 – 2013 for GOME, 2003 – 2012 for SCIAMACHY, 2007 to 2017 for GOME-2A and 2013 – 2017 for GOME-2A). In total, 33 sensitivity tests were performed for GOME, 23 for SCIAMACHY, 55 for GOME-2A and 93 for GOME-2B. The two parameters that mostly influenced the produced retrievals were the fitting window and the cross section selections. Consequently, we will present some of the sensitivity tests we performed to justify the final set of settings introduced in tables 2.1 and 2.2.

In the first sensitivity test, an older BrO cross section (Wahner et al., 1988) is used, while the fitting window for all instruments is set to 336 – 347 nm, except for GOME (334.7 – 359 nm).

Figure 2.5 shows the SCD of BrO over the Pacific reference area, the RMSE of the fit for the same area, and the RMSE for the Arctic region:

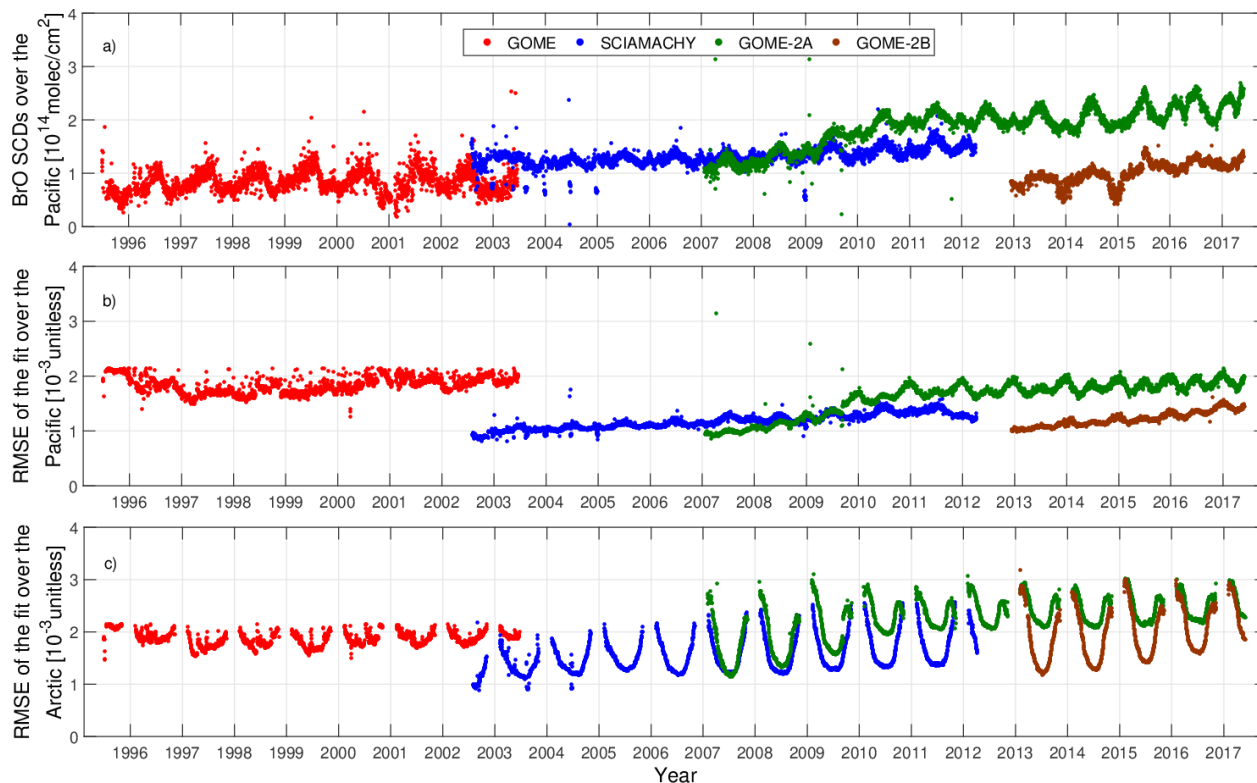


Figure 2.5: Evaluation of early retrieval settings. a) SCDs of BrO over the Pacific reference region. b) RMSE of the fit for the Pacific reference region. c) RMSE of the fit for the Arctic region.

The SCD of BrO over the Pacific region shows an upward trend for all instruments (in contrast to Figure 2.2 top). The trend is pronounced for GOME-2A and GOME-2B. Also, the RMSE of the fit for the Pacific shows higher values when compared with Figure 2.2 bottom, especially for the GOME instrument. Similar conclusions can be drawn by comparing Figure 2.5c with Figure 2.3 top. The improvement of the final set of settings is evident.

The agreement of the geometric BrO VCDs between the different sensors for their overlapping periods was another metric that we applied. Although we have not shown the geometric BrO VCDs for the final set of settings yet (i.e. Figure 3.3 top), it is shown for the initial set of settings in Figure 2.6.

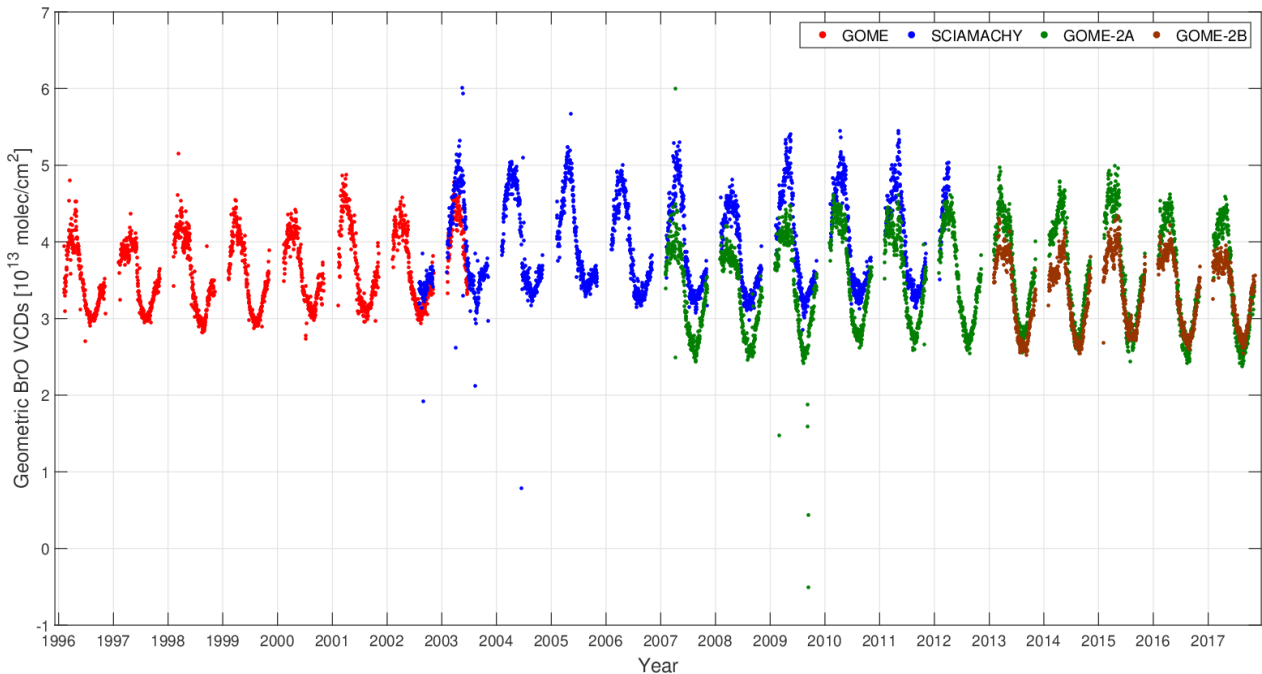


Figure 2.6: Geometric BrO VCDs for the initial set of settings.

The agreement between the instruments is far from satisfactory (for example, the difference between GOME-2A and GOME-2B during polar spring is approximately 1.0×10^{13} molecules/cm²). The columns during summer (i.e. background BrO, when bromine explosions do not occur) should be approximately on the same level. However, for GOME-2A and GOME-2B, the summer columns are much lower than those for GOME and SCIAMACHY (i.e. approximately 0.5×10^{13} molecules/cm²). These differences are more pronounced when we compare Figure 2.6 to Figure 3.3 top.

In Figure 2.7, we investigate the quality and agreement of another set of settings for each instrument. For each sensor, we used the settings in Table 2.1, while the fitting window for GOME, GOME-2A and GOME-2B was 338 – 355nm, while for SCIAMACHY 336 – 347 nm.

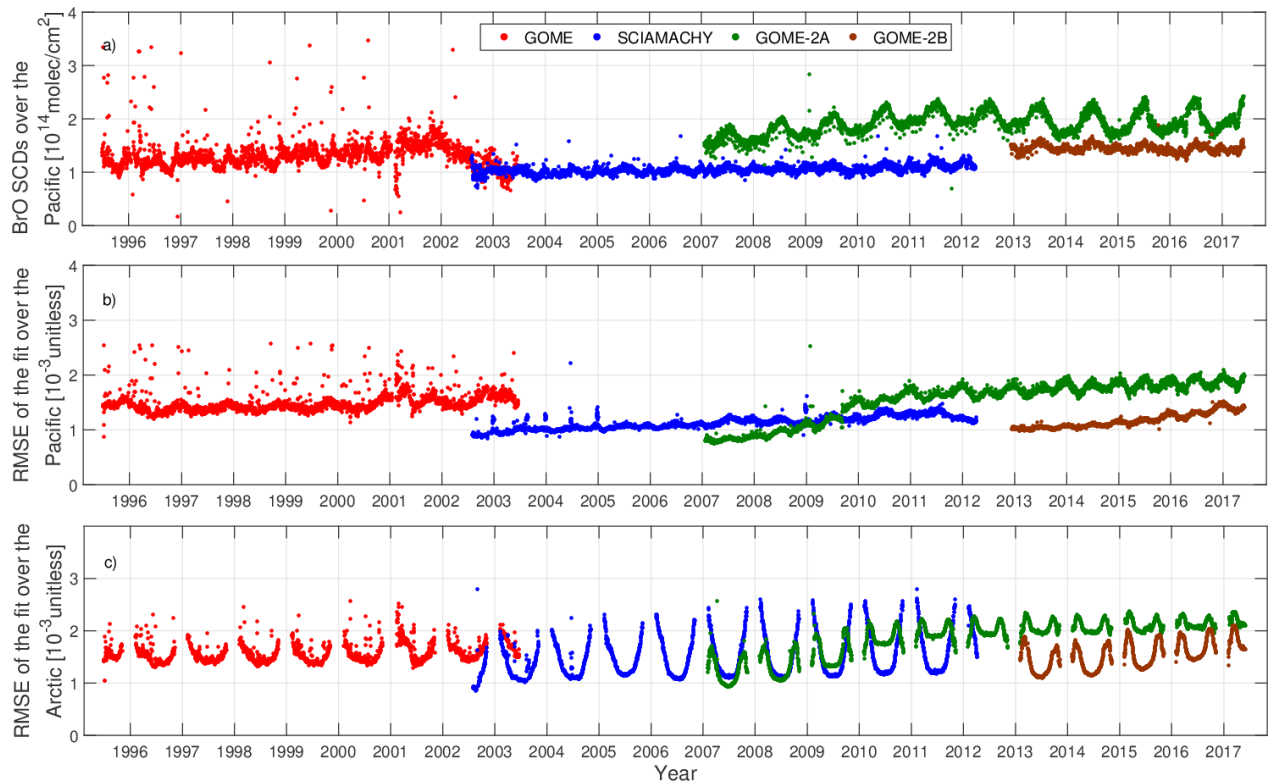


Figure 2.7: Sensitivity test with the final cross sections, but not fitting windows. a) SCDs of BrO over the Pacific reference region. b) RMSE of the fit for the Pacific reference region. c) RMSE of the fit for the Arctic region.

We infer that all panels of Figure 2.7 improved when compared with the corresponding plots of Figure 2.5. The trends of BrO SCDs over the Pacific region became less pronounced, and the RMSE values for both the Pacific and the Arctic decreased for each instrument. However, compared to Figures 2.2 and 2.3, we see that this set of settings still lacks quality for all three criteria.

Figure 2.8 shows the geometric BrO VCDs for the Arctic for the set of settings we presented in Figure 2.7.

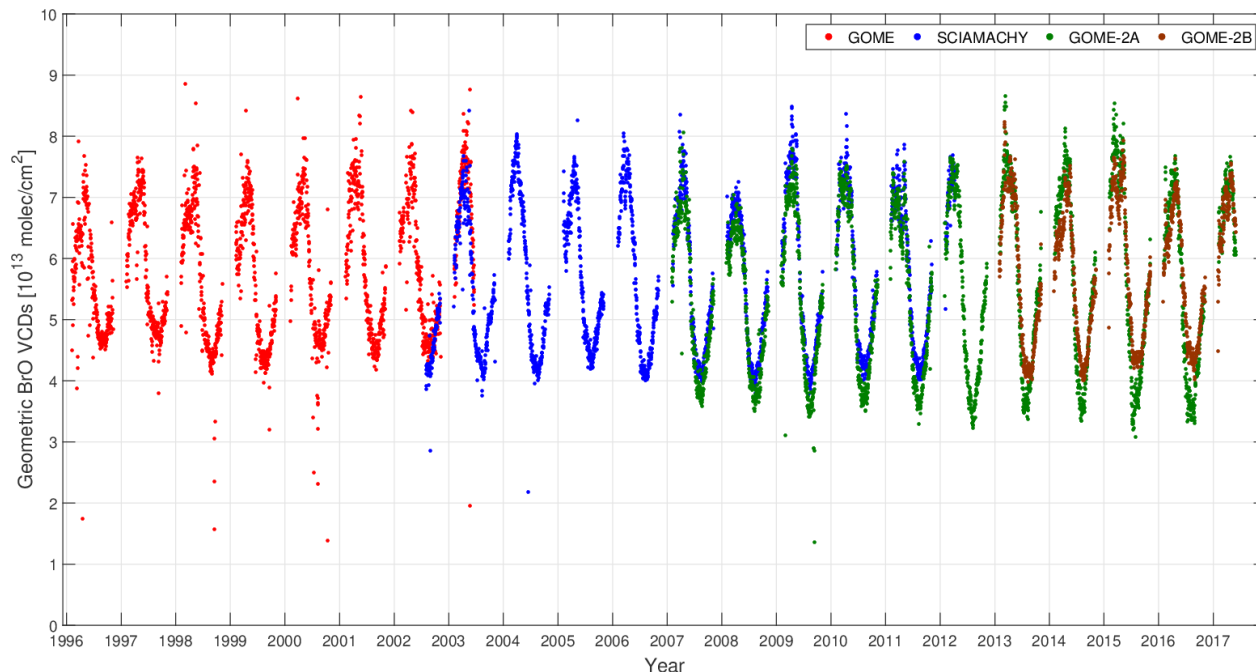


Figure 2.8: Geometric BrO VCDs for the set of settings with the final cross sections, but not fitting windows.

Similar to the other criteria, there is a significant improvement in the agreement between the sensors during their overlapping periods. However, the summer columns vary significantly (i.e. in some cases, even 1.0×10^{13} molecules/cm²), and the general agreement is not satisfactory (especially when compared to Figure 3.3 top).

The investigation of the optimal retrieval settings is a complex and intriguing process, which requires many sensitivity tests. The following example is for GOME, where we slightly modified the fitting window (i.e. from 338 – 355 nm that we saw in the previous example to 337 – 355 nm) to indicate the immense impact the fitting window has in the retrieval of BrO.

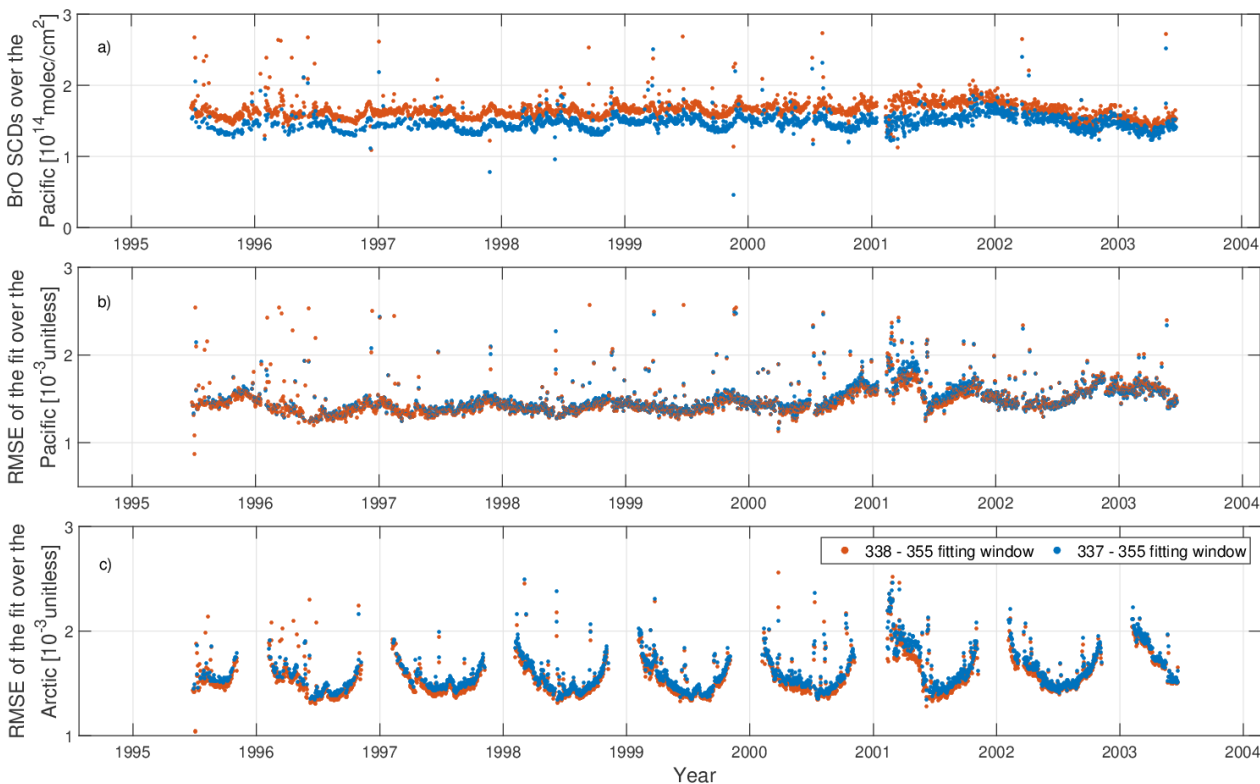


Figure 2.9: Sensitivity test for GOME, with 1nm change of the fitting window (338 – 355 nm (brown) against 337 – 355 nm (blue)). a) SCDs of BrO over the Pacific reference region. b) RMSE of the fit for the Pacific reference region. c) RMSE of the fit for the Arctic region.

Although we might expect that the differences from the 1nm change would be negligible, we can see clearly that the change affects the fit, with the 338 – 355 nm fitting window yielding slightly better results. A similar difference is also observed in the geometric VCD, where we are primarily interested in small fluctuations affecting the agreement between the sensors. A large number of sensitivity tests to derive a set of fitting parameters that minimize the RMSE of the fit, the trend of BrO SCD over the pacific and achieve an agreement between the instruments is justified.

2.1.3 OMI

The OMI instrument was launched on satellite Aura in 2004. It is a spinoff from GOME and SCIAMACHY. It has a much better spatial resolution in nadir ($13 \times 24 \text{ km}^2$) and an even broader swath (2600 km). It has a spectral resolution of about 0.5 nm, while the light entering the instrument is split into two channels: the ultraviolet (270 nm to 380 nm) and the visible (350 nm – 500 nm). The instrument has a local afternoon equatorial overpass at 13.30. It is still in orbit, monitoring the changing global climate (Levelt et al., 2018). OMI suffers from row anomaly (Kroon et al., 2011): Starting in June 2007, some detector rows were blocked by a thermally insulating material. As a result, the incoming light is blocked and scattered, creating errors in level 1b data and consequently on the retrieval of SCDs. Initially, only two rows were affected.

However, as the years passed, and especially after January 2011, the problems grew; more rows were affected (approximately one-third of the total sixty). The row anomaly problem appears dynamically, meaning that the affected rows change over time. A flag for pixels affected by the row anomaly is inserted in level 1b data (i.e. the instrument's data upon which the retrieval is performed). On the left side of Figure 2.10, we see one OMI orbit for 2005, on the right side the same for 2017; both figures display the SCD of the retrieved BrO, while the pixels affected by the row anomaly are excluded:

Starting from 2011, the orbits of the instrument looked similar to the right side of Figure 2.10

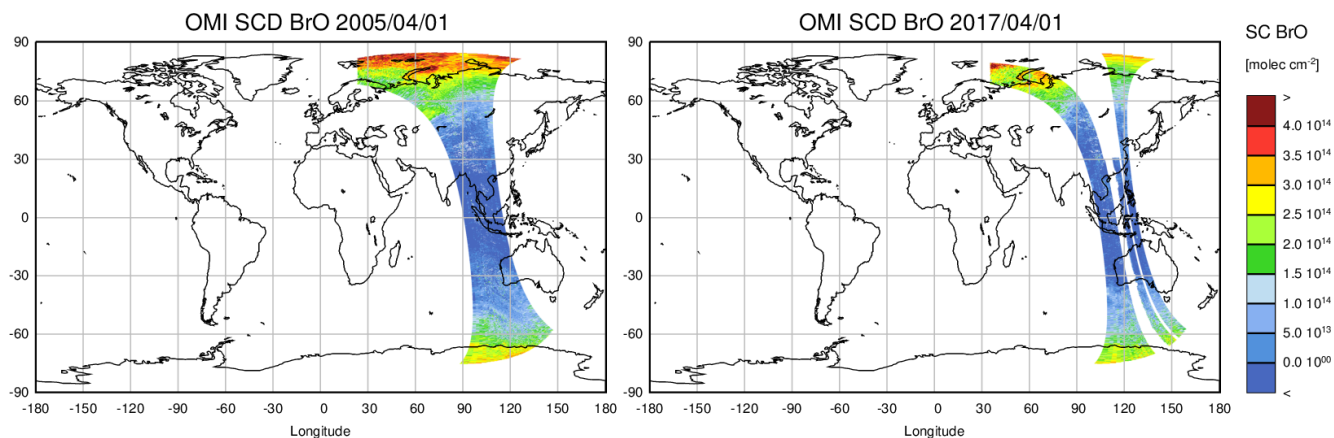


Figure 2.10: Operational orbit rows of the OMI instrument. Left: An orbit from the year 2005. Right: An orbit from 2017. The missing rows on the right figure are due to the row anomaly.

(2017). As a result, for sampling issues, we decided to exclude all the middle rows (21 to 54) from all years (and keep the row anomaly flagging as well), as they do not contribute signal for the Arctic region, from 2011 and onwards. However then, we have encountered another problem, which is shown in Figure 2.11 (monthly mean BrO VCDs for April 2011):

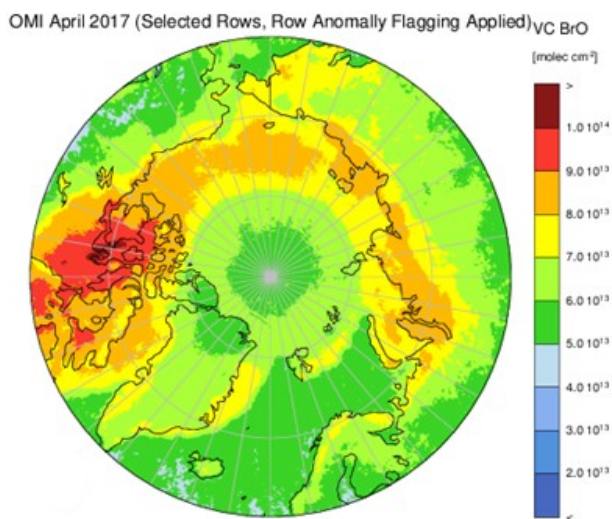


Figure 2.11: Geometric BrO VCDs from OMI for April 2007.

Abnormally low values for high latitudes appear for BrO VCDs. Figure 2.12 shows the amount (counts) of signal contributing to the plotted quantity for April 2005. On the left side, the case using the row anomaly mask (but including all rows) is shown, while on the right side, the selection of rows (excluding rows 21 to 54, but still using the mask, as described before) is applied for the northern hemisphere:

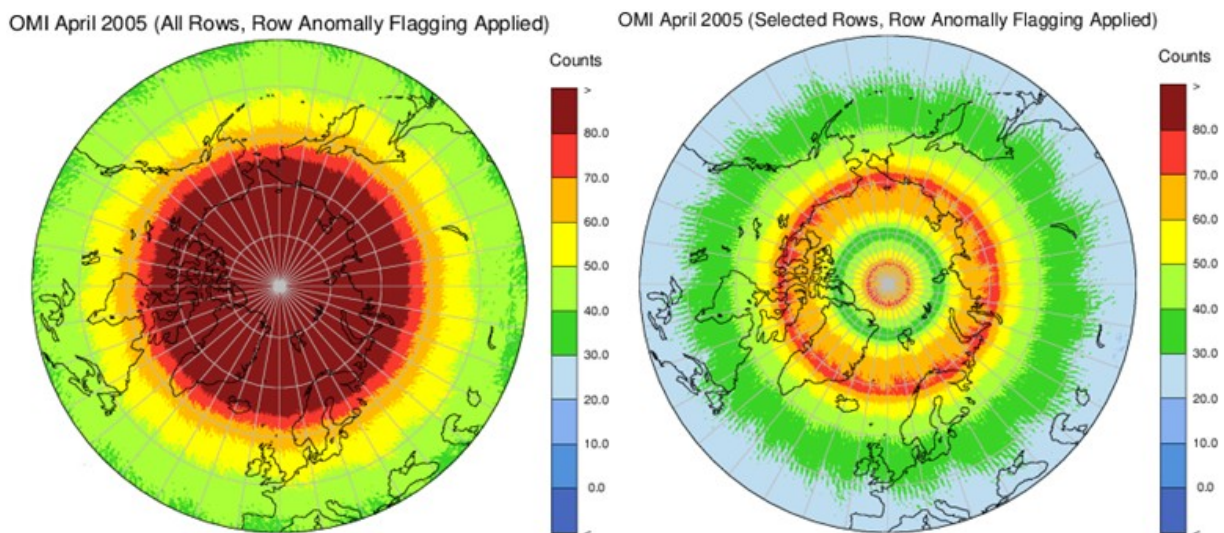


Figure 2.12: Counts of OMI instrument for April 2005. Left: Selection of all available rows. Right: Selection only of rows that contribute for all years (2005 – 2017).

We see clearly that this selection of rows has a negative effect, as unphysical coverage patterns are formed (especially in the region around 80.0° of latitude). However, if we repeat the same test for 2011, we get two similar figures:

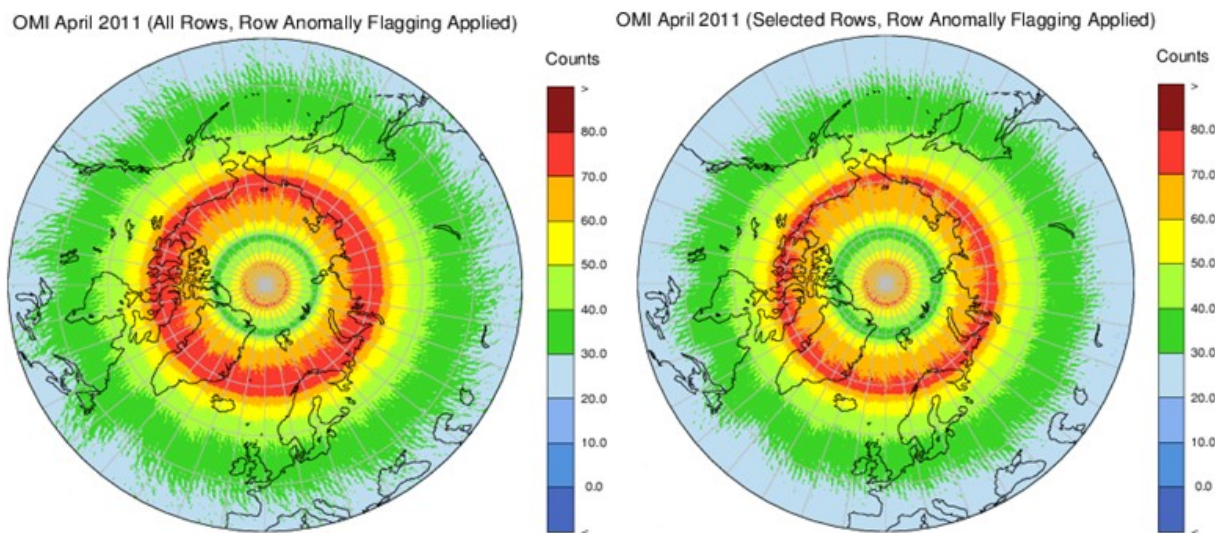


Figure 2.13: Counts of OMI instrument for April 2011. Left: Selection of all available rows. Right: Selection only of rows that contribute for all years (2005 – 2017).

From 2011, it does not matter whether one applies the row anomaly flagging or additionally exclude the rows, which do not contribute any signal. The amount of the received signal is reduced significantly for the Arctic, with strange patterns appearing (although minor differences are observed in the figure above, the two maps eventually end up being identical in 2017). We have performed various tests, with different cross sections, different fitting windows, even with retrievals that included other weak UV absorbers (e.g. O_4 , HCHO). In all cases, we saw the same unphysical patterns in the contributing counts and an underestimation in the values of the retrieved trace gas, from 80.0° N onwards. We have performed similar tests for absorbers (e.g. NO_2 and CHOCHO) in the visible part of the spectrum, and it seems that the problem is not that pronounced. As a result, and although OMI is in orbit since 2005, covering 13 years, with the highest resolution from all other instruments we used, we decided not to include its data in our analysis.

2.2 Stratospheric Contribution

In order to derive the tropospheric BrO VCD from the retrieved SCD of BrO, the method of Theys et al. (2009) was used. Briefly, this method uses a stratospheric BrO climatology, derived with the BASCOE model (Errera and Fonteyn, 2001) and requires year, latitude, tropopause height, O_3 and NO_2 columns as input. This approach has been applied successfully in previous studies (e.g. Begoin et al., 2010; Theys et al., 2011; Blechschmidt et al., 2016; Choi et al., 2018). In the present study, satellite retrieved O_3 VCDs from Weber et al. (2018), stratospheric NO_2 VCDs from the QA4ECV project (Boersma et al., 2018), and from the Tropospheric Emission Monitoring Internet Service (TEMIS), (Boersma et al., 2004) and tropopause heights retrieved from NCEP reanalysis (Kalnay et al., 1996) data were used as input. In Theys et al. (2009), a correction factor was applied to account for the long-term reduction of bromine emissions in the stratosphere. This factor was determined using zenith-sky measurements of BrO over Harestua (Hendrick et al., 2008). Here, this factor was excluded, as the long-term development of stratospheric BrO VCDs of the model without applying the correction factor comes to a closer qualitative agreement with updated measurements of BrO over Harestua (from F. Hendrick, BIRA-IASB, personal communication). In Figure 3.4, the multiplication factor, together with the impact it has on the stratospheric and tropospheric BrO time-series is shown. The time-series of NO_2 , O_3 and tropopause height are shown in Figure 2.14.

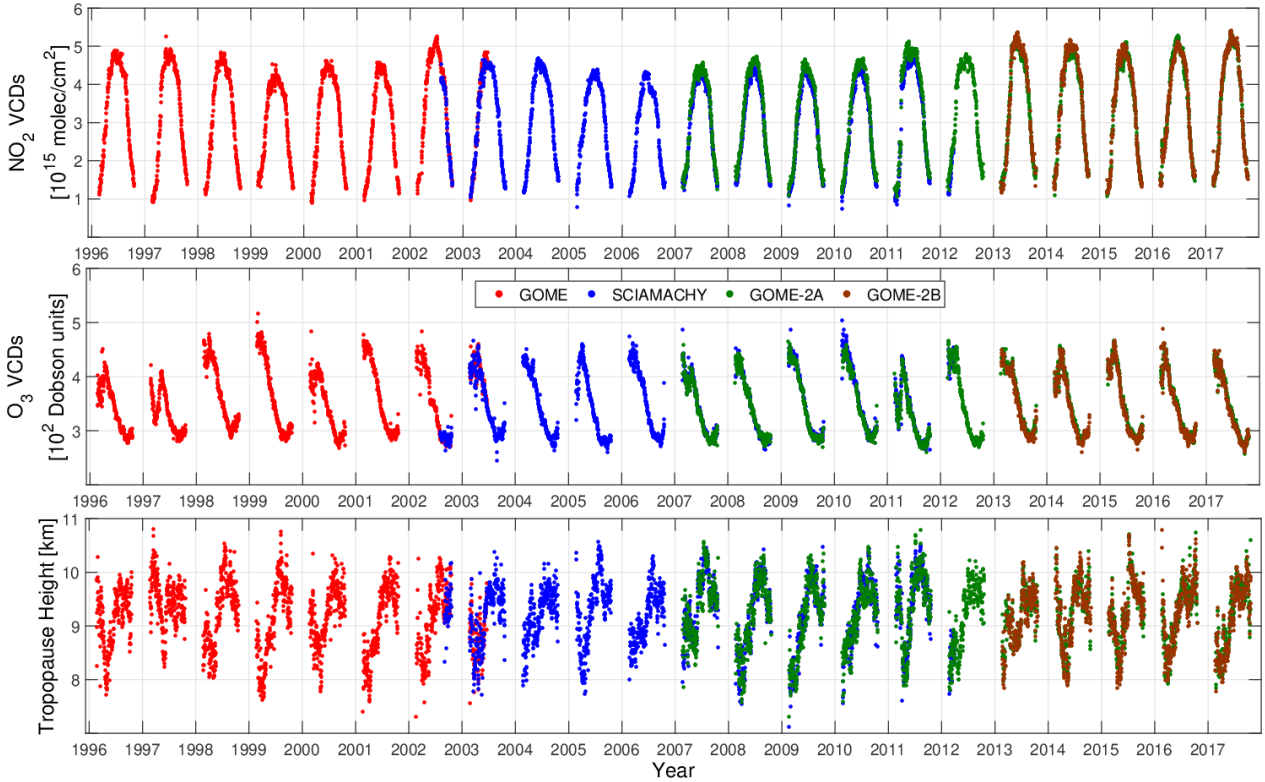


Figure 2.14: Time-series of daily averaged input data over the Arctic used for deriving stratospheric BrO VCDs: Top: stratospheric NO₂ VCDs [molecules/cm²] from QA4ECV (GOME, SCIAMACHY and GOME-2A) and TEMIS (GOME-2B). Middle: O₃ VCDs [DU] from Weber et al. (2013). Bottom: Tropopause height [km] from NCEP reanalysis data. Data for the GOME instrument is colored in red, SCIAMACHY in blue, GOME-2A in green and GOME-2B in brown. All three time-series show daily averages over the Arctic region.

The following formula (Theys et al., 2009) is used to derive the tropospheric VCD of BrO:

$$\text{VCD}_{\text{tropo}} = (\text{SCD}_{\text{total}} - \text{VCD}_{\text{strato}} \times \text{AMF}_{\text{strato}}) / \text{AMF}_{\text{tropo}}, \quad [2.2]$$

where $\text{SCD}_{\text{total}}$ is the slant column of BrO retrieved by the DOAS method, $\text{VCD}_{\text{strato}}$ corresponds to the stratospheric BrO VCD retrieved from the Theys et al. (2009) climatology, $\text{AMF}_{\text{strato}}$ is a stratospheric air mass factor, $\text{AMF}_{\text{tropo}}$ is a tropospheric air mass factor. For the latter, as in Begoin et al. (2010) and Blechschmidt et al. (2016), a surface albedo of 0.9 has been assumed above sea ice and that all tropospheric BrO is well mixed within the boundary layer extending to 400m altitude. Note that the stratospheric BrO VCD column is independent of the BrO SCD retrieved by the DOAS method and depends on the Theys et al. (2009) climatology and its inputs.

2.3 Datasets used in this Study

In this section, the external datasets that were used to compare them to the tropospheric BrO dataset we derived, and extract geophysical relationships between them, are presented. The sea ice age dataset was used to identify the satellite scenes over sea ice covered regions. This is

consistent with the settings used in the tropospheric AMF (i.e. a surface albedo of 0.9). Also, all external datasets (except the one about cyclones) were spatially and temporally interpolated to each satellite orbit to provide data only where and when tropospheric BrO was retrieved from the satellite sensor observations.

2.3.1 Sea Ice Age

In order to study the connection between tropospheric BrO and sea ice under the impact of Arctic warming, long term sea ice data (starting from 1996) is required. In addition, since the tropospheric AMF applied for the retrieval of tropospheric BrO (see section 2.2) assumes a surface albedo of 0.9, the sea ice data was used to remove data with no sea ice cover from the BrO data. For this purpose, the sea ice age dataset from Tschudi et al. (2019) was used. It is retrieved from different passive microwave satellite remote sensing instruments (AMSR-E, AVHRR, SMMR, SSM/I, SSMIS) and drifting buoys and has a high spatial resolution of $12.5 \times 12.5 \text{ km}^2$, while its temporal resolution is seven days. Its temporal coverage is from 01.01.1984 until 31.12.2019.

2.3.2 Meteorological Parameters – Sea Ice Thickness

For the meteorological parameters involved in the formation of enhanced tropospheric BrO plumes (i.e. air temperature, wind speed and direction, mean sea level pressure, boundary layer height and vertical wind velocity), we have used reanalysis data from two sources. ERA-5 data from ECMWF (European Center for Meso-scale Weather Forecast) and ASR-2 (Arctic System Reanalysis). ERA-5 data (Hersbach et al., 2020) is provided in 0.25×0.25 degrees resolution and has an hourly temporal resolution. We have downloaded ERA-5 data from (<https://cds.climate.copernicus.eu/#/search?text=ERA5&type=dataset>) and ASR-2 data from (<https://rda.ucar.edu/datasets/ds631.1/>) and used them with a timestamp of three hours, and then interpolated them to the satellite orbits. Their temporal coverage is from 1979 to the present. ASR-2 (Arctic System Reanalysis version 2, 2017) provides the same parameters mentioned above (except boundary layer height), with a temporal resolution of 3 hours and a spatial resolution of $15 \times 15 \text{ km}^2$. The temporal coverage of the dataset is from 2000 to 2016. In addition to the parameters mentioned above, ASR-2 provided data for sea ice thickness. The surface level was selected for the vertical wind velocity, as it is provided for different altitudes (based on pressure).

2.3.3 Cyclones

The dataset describing the cyclonic activity (radius of the cyclone, intensity, pressure) in the Arctic is presented in Akperov et al. (2019). The data was provided by M. Akpevov, A.M. Obukhov Institute of Atmospheric Physics through personal communication. They have simulated cyclones using meteorological data from climate models. Although many useful

cyclonic parameters are included in the dataset (i.e. radius, intensity and frequency), the dataset is not gridded to a specific spatial resolution. Therefore, it was not interpolated to the satellite orbits, as it is quite sparse and not suitable to be interpolated to a pre-defined grid.

2.4 Artificial Neural Network

In order to successfully implement an artificial neural network, sensitivity tests regarding the architecture of the network, the selection of an appropriate training dataset and input parameters should be performed. The goal is to successfully predict the appearance and magnitude of enhanced tropospheric BrO plumes during polar spring in order to forecast the formation of future tropospheric BrO plumes. For this purpose, we have used all the external datasets mentioned in section 2.3. Most of the parameters discussed in 2.3 act either as a source location for bromine release (i.e. sea ice age) or as parts of a mechanism in the formation of enhanced BrO (i.e. meteorological parameters). No spatial (i.e. latitude or longitude) or temporal (i.e. day, hour) information was used as input parameters, as we wanted to investigate the impact of sea ice and meteorology on the formation of tropospheric BrO plumes. After tests with all the available parameters, we have concluded using sea ice age, 2m air temperature, mean sea level pressure, 10m wind speed and wind direction, and boundary layer height from ERA-5 (as it covers the whole period) as input parameters. The targets (i.e. quantity that the neural network tries to model) were the satellite retrievals of tropospheric BrO.

Regarding the architecture, the most critical parameter is the number of hidden neurons, where the calculations and the assignment of the weights for each input parameter are performed. Although there are many approaches to choose the number of hidden neurons, the final choice is ambiguous and depends on the specific dataset and the number of input parameters (Hornik, 1991). If the number of neurons is too large, then the so-called “over-fitting” occurs (i.e. the neural network learns by heart the training dataset but does not perform well on samples outside the training ones). If the number is too small, then the network is too simplistic and cannot achieve its maximum potential in prediction. This study used the simple shallow cascade neural network architectures (Warsito et al., 2018) with 30 hidden neurons. During the training process, the dataset is randomly split into 70% for training, 15% for evaluation and 15% for testing. The training data are used to accurately adjust the weighting factors of each input in order to get a close approximation of the target. The validation set is used to determine an appropriate stopping training point (i.e. when the generalization error increases). In this way, over-fitting is avoided, and the model becomes more flexible in adapting to new datasets. The final testing set was used to evaluate the model by comparing neural network outputs to measurements without re-adjusting the weighting factors. After the training procedure and the steps described, we have re-constructed the whole time-series with the neural network to assess its performance. Figure 2.15 shows the neural network architecture of the neural network created.

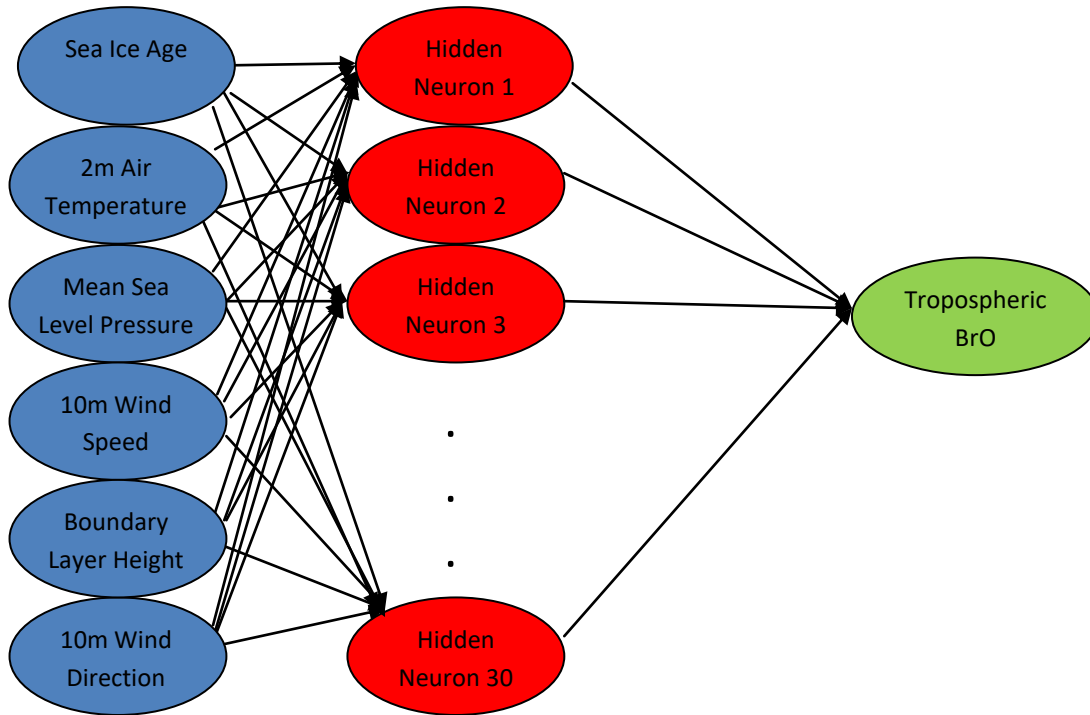


Figure 2.15: Schematic representation of the neural network.

As a first test, individual neural networks, one for every single day were employed. Every day was remodeled by its own neural network. The purpose of this test was not to create a model which predicts tropospheric BrO and extrapolate its predictions to different years (as the training set is too small, i.e. one day, it is not reasonable to expect from such a neural network to model tropospheric BrO of other days robustly). The reason is to investigate the level of agreement between the targets (measurements of tropospheric BrO) and inputs (i.e. sea ice age and meteorology), whether it is acceptable and if it shows deviations over time. In Figure 2.16, the yearly averaged correlation coefficients and root mean square errors between the neural network outputs and tropospheric BrO measurements are shown.

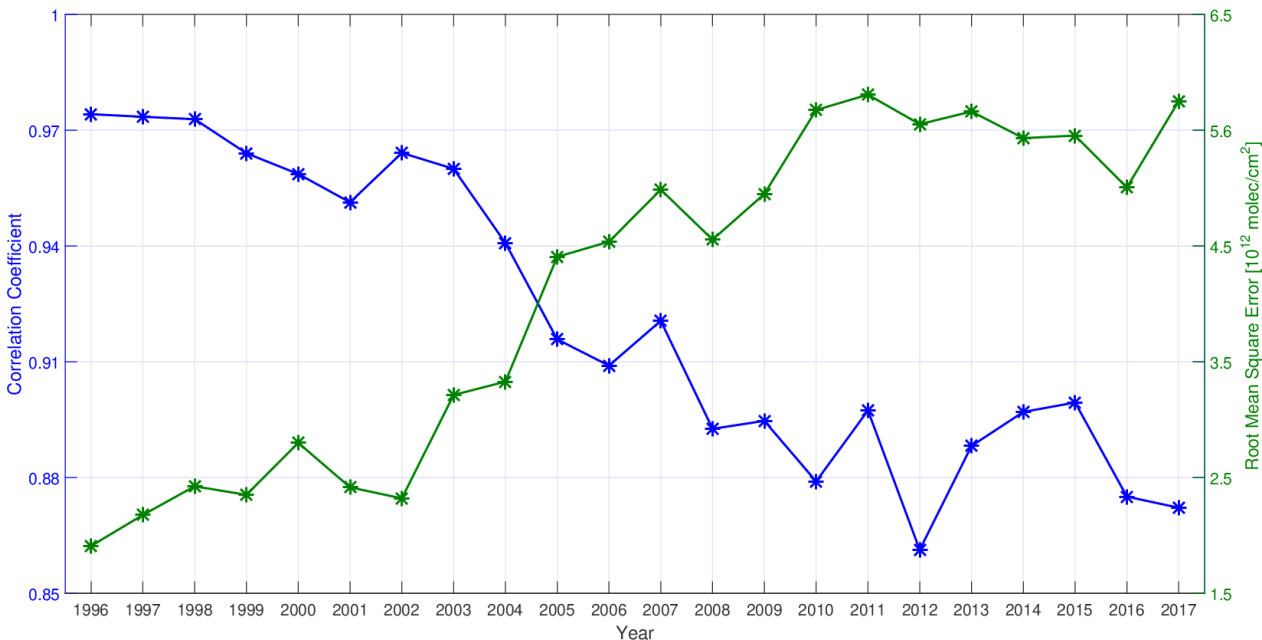


Figure 2.16: Polar spring averaged correlation coefficients, and root mean square errors between neural network outputs and tropospheric BrO measurements (sensor merged for the overlapping years).

Both the correlation coefficients and the root mean square errors show good agreement between the modeled and the measured tropospheric BrO VCDs. This could be an indication that a neural network could be actually employed in order to predict tropospheric BrO VCDs successfully. Degradation in both quantities is seen as the years pass by. Despite the many sensitivity tests (i.e. different selection of input parameters, different architecture and amount of hidden neurons), the result we were getting was always similar to Figure 2.15. The only possible explanation could be that the well-established relationship between inputs and targets that we see in the early years is being diminished. Consequently, this potentially means degradation in either the input parameters or the targets. Since the targets dataset was the only quantity that remained stable during every test, the reason for this decrease in quality could be related to the instrumental degradation of the satellite sensors. Another geophysical explanation could be that there is a change in the bromine explosion events, which cannot be explained by the input parameters used.

Bearing this in mind, we proceeded to an optional training set selection. Ideally, we would investigate all the days where there is an obvious relationship between the input parameters and targets (e.g. enhanced tropospheric BrO appearing over low temperatures and first year sea ice). However, this would create a biased, subjective selection. Therefore, we performed sensitivity tests, in which we chose each year separately as the training dataset. By calculating the correlation coefficient between modeled and measured tropospheric BrO, we evaluated each of the 22 neural networks. Afterwards, we have re-constructed the entire tropospheric BrO time-series, by using the best neural network and calculated the correlation coefficients and root mean square errors for each year's modeled and measured tropospheric BrO VCDs. These findings are shown in Figure 2.17.

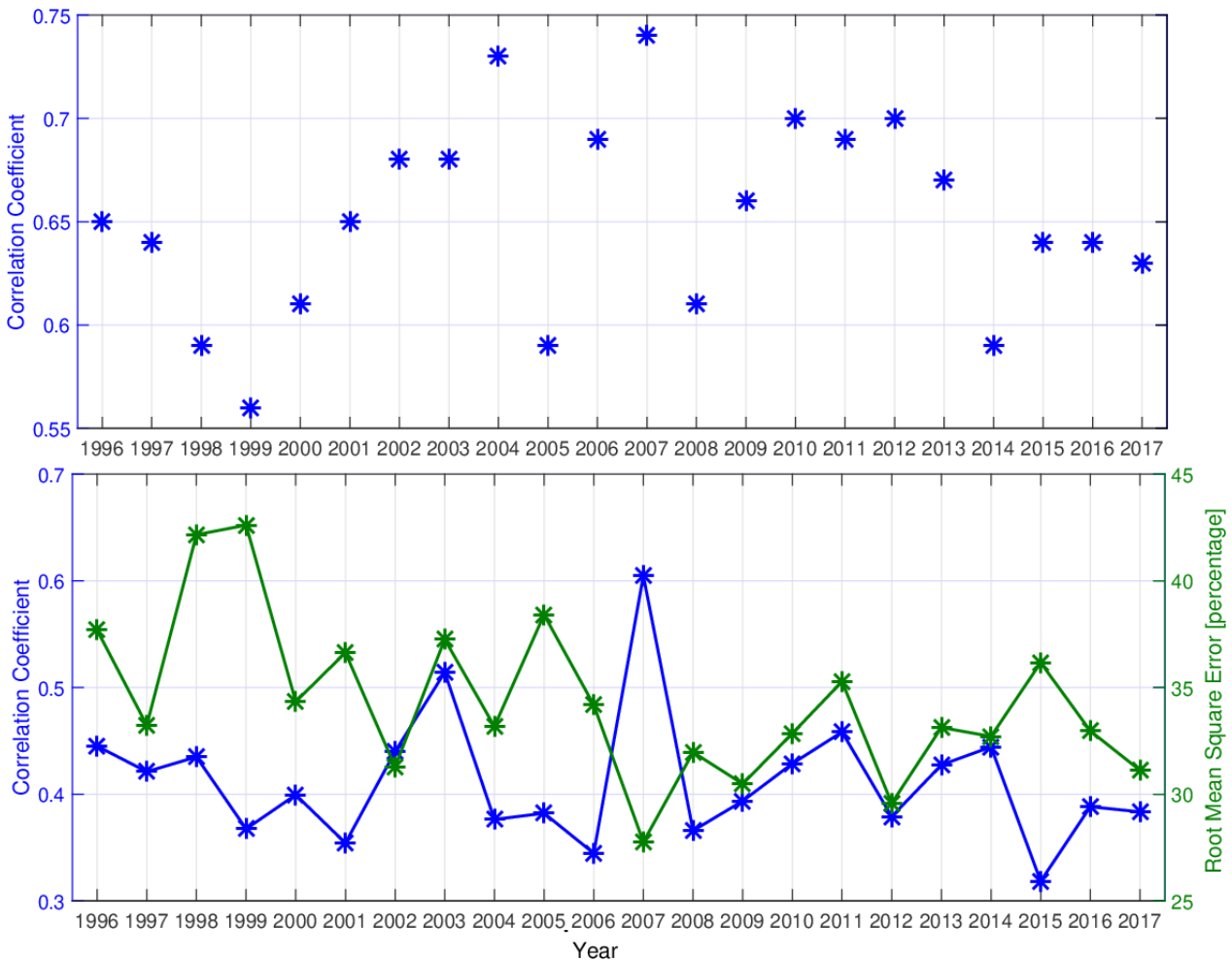


Figure 2.17: Top: Polar spring averaged correlation coefficients between tropospheric BrO measurements and neural network outputs for each training year. Bottom: Polar spring averaged time-series of correlation coefficients, and root mean square errors (in percentage) between tropospheric BrO measurements and neural network outputs using the best neural network (i.e. 2007) to reconstruct the entire time-series.

Figure 2.17 top does not depict a continuous time-series. Instead, it shows the correlation coefficient achieved by each sensitivity test, which used the corresponding year as a training dataset. We can infer that 2007 yields the best results, with 2004 being slightly worse. In Figure 2.17, bottom the quality assessment of the neural network trained with 2007 as a training dataset is seen. With this neural network, the entire time-series of tropospheric BrO VCD was reconstructed, and then for each year, the correlation coefficients and root mean square errors were calculated between modeled and measured tropospheric BrO VCDs. Apart from a higher correlation and lower root mean square error for 2007 (which is to be expected), the error percentage is around 35% of the measured tropospheric BrO VCDs, while the correlation coefficients are around 0.4, values that are considered adequate.

Another way to evaluate the selected neural network is to plot linear spatial correlations between the input parameters and the satellite measurements for each year and then plot the exact same figure, but this time between the input parameters and neural network outputs. Although the

actual correlations between tropospheric BrO VCD and its driving mechanisms are not linear, these plots provide a comparison between the level of agreement of inputs and measured – modeled tropospheric BrO VCDs.

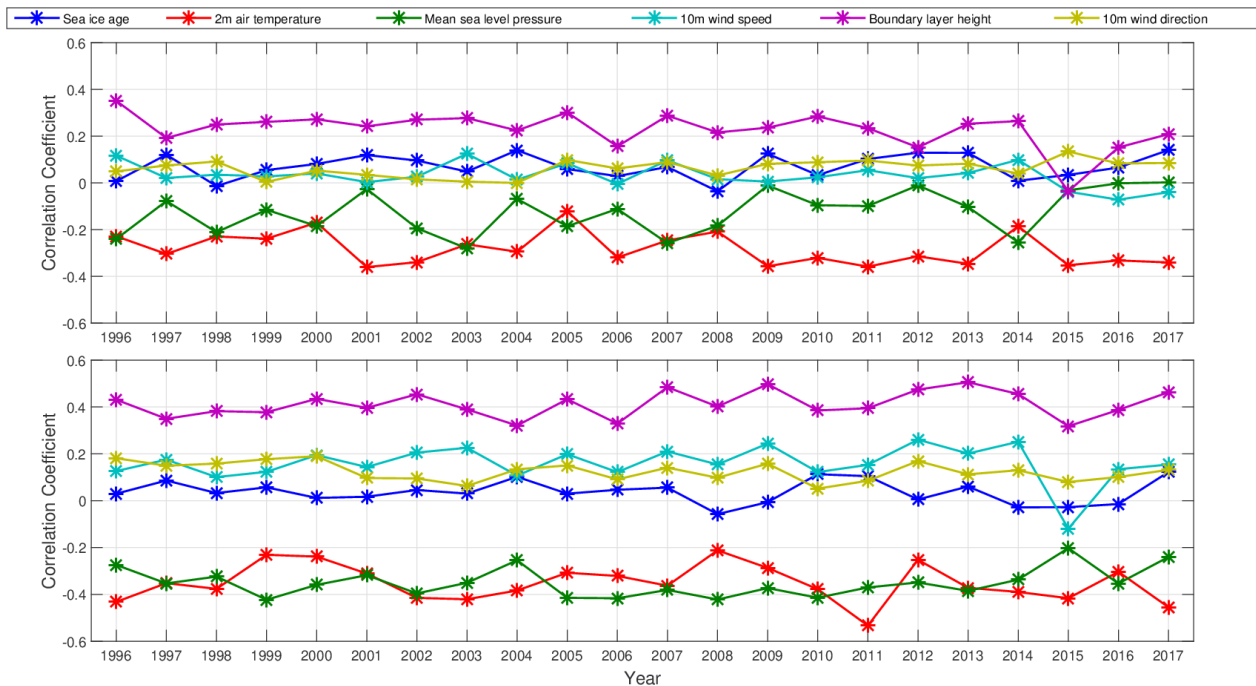


Figure 2.18: Polar spring averaged spatial correlation coefficient time-series. Top: Correlation coefficient time-series between each input parameter and measured tropospheric BrO VCDs. Bottom: Correlation coefficient time-series between each input parameter and modeled tropospheric BrO VCDs using the best neural network (i.e. 2007).

Figure 2.18 (top) shows the polar spring averaged spatial correlation coefficients between each input parameter and tropospheric BrO VCD. We see that 2m air temperature has the most significant absolute values correlation with tropospheric BrO VCD, with a negative sign. Mean sea level pressure also has a negative correlation, although the correlation coefficient is zero for some years (e.g. 2009). Boundary layer height, on the other hand, has the strongest positive correlation to tropospheric BrO measurements. Sea ice age, 10m wind speed and direction do not seem strongly correlated to tropospheric BrO VCD measurements. We infer from Figure 2.18 bottom that the same conclusions can be drawn by plotting the spatial correlation coefficients of the input parameters and modeled tropospheric BrO VCDs. Both 2m air temperature and mean sea level pressure negatively correlate to modeled tropospheric BrO VCD, while boundary layer height has the strongest positive one. The other three parameters do not seem to correlate with modeled tropospheric BrO significantly. Although there are differences between the two plots (e.g. the fluctuations that can be seen on almost every input parameter are much more pronounced in the top plot), the general picture is similar. This verifies that the neural network trained with the measurements of 2007 is suitable for extrapolating and re-constructing the entire time-series of tropospheric BrO VCD.

3. BRO COLUMN DENSITIES AND TRENDS

The retrieval methodology, together with the stratospheric separation and the datasets used, were described in Chapter 2. This chapter presents the results from the DOAS retrieval algorithm for the Arctic region (i.e. from 70.0° N to 85.0° N latitudes and 180° W to 180° E longitudes) and the Hudson Bay (i.e. 50.0° N to 66.0° N latitudes and 264.0° E to 284.0° E longitudes). For both regions, comparisons of geometric, stratospheric and tropospheric BrO vertical column densities (VCDs) time-series and maps for the different sensors are shown. Our purpose is to verify the agreement between them for the overlapping periods. For both regions, the temporal evolution of tropospheric BrO, for both the magnitude and spatial distribution, is given. The chapter closes with a summary and conclusions, where the most significant findings of the assessment of the impact of Arctic Amplification of tropospheric BrO VCDs are discussed. In all time-series where multiple sensors are displayed, the data from GOME is plotted in red, that from SCIAMACHY in blue, that from GOME-2A in green and that from GOME-2B in brown color. The largest solar zenith angle (SZA) used is 80°, and the gridding resolution was set at 0.125x0.125 degrees.

3.1 Arctic

The Arctic region (70.0° N to 85.0° N) was the focus of interest and the region where the quality assessment of the retrieval process was performed. Latitudes smaller than 70.0° N were not included in the long-term analysis because the proportion of sea ice covered areas is decreasing significantly there. The extension of the region to latitudes above 85.0° N may result in inconsistency, as not all the sensors have the same coverage and measuring capabilities. All the results shown in this sub-section are from 70.0° to 85.0° N latitudes and 180° W to 180° E longitudes. Figure 3.1 shows this Arctic area (without any plotted data).

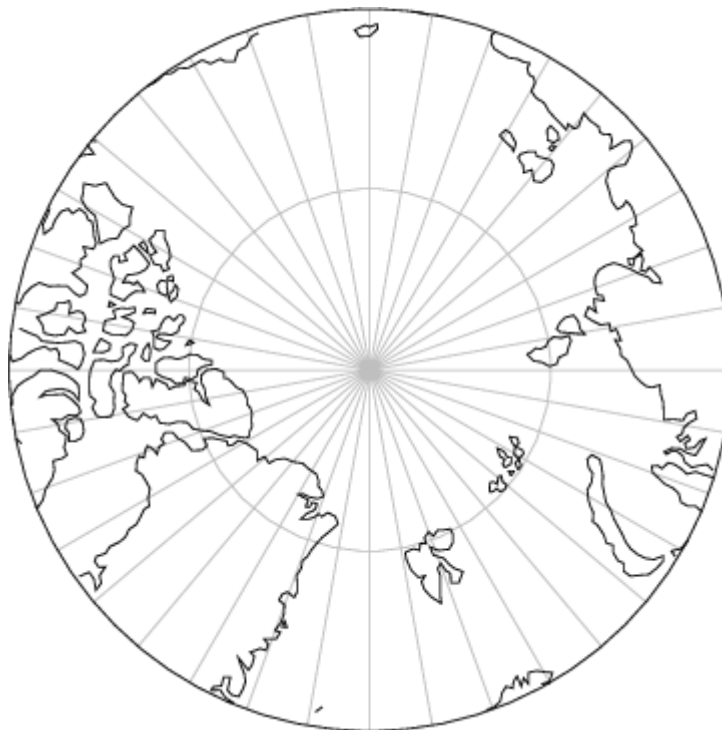


Figure 3.1: The area defined as "Arctic".

As there is no light and therefore no satellite retrieval is possible in this region from October to February, only results from March until September for every year are shown. For the time-series figures shown in the following sections, every data point is a daily average of BrO column density of the region described above. Finally, a small section is devoted to the discussion regarding the implementation of the multiplication factor on the stratospheric separation method, comparing the tropospheric and stratospheric BrO time-series, with and without the application of the factor, as mentioned in chapter 2.

3.1.1 Time-series

The primary data product of the DOAS retrieval method, as described in chapter 2, is the BrO SCD. The SCD depends on the path of the electromagnetic radiation through the atmosphere, i.e. the viewing geometry of the sensors. The SCD was used neither to verify the agreement between the sensors nor for scientific conclusions. Figure 3.2 shows the SCDs of the four instruments for the Arctic region (70.0° N to 85.0° N).

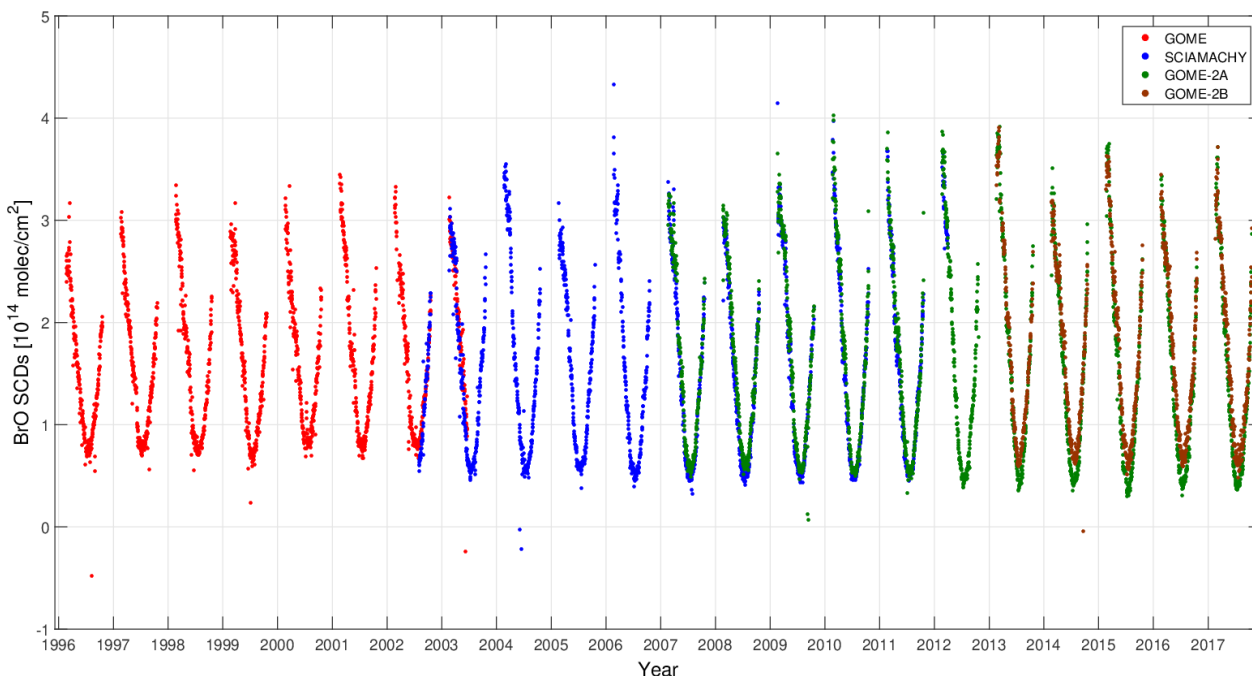


Figure 3.2: Time-series of average daily Slant Column Densities of BrO over the Arctic from multiple satellite sensors.

We observe that the seasonality of the SCDs is similar to the RMS figure for the Arctic (Figure 2.7c). This is mainly due to the light path, which is longer during the beginning and the end of each year. In addition, the seasonality of BrO columns also plays a role. Although the SCDs are dominated by the light path, high values of SCD are found on some days in springs (for example, in 2006 and 2009). These are days where there was a bromine explosion event.

The quantity that was used for verifying the agreement was the geometric Vertical Column Density (VCD). In order to obtain them, we divided the SCDs with a simple stratospheric air mass factor (AMF), which corrects for the length of the stratospheric light path by taking into account the scattering at the surface. It necessarily differs from the summation of the stratospheric and the tropospheric column. This is why we used the term “geometric” instead of the “total” column. The stratospheric BrO VCDs were used only as an intermediate step to extract the tropospheric VCDs. All these three VCDs (geometric, stratospheric and tropospheric) are presented in Figure 3.3.

3. BrO Column Densities and Trends

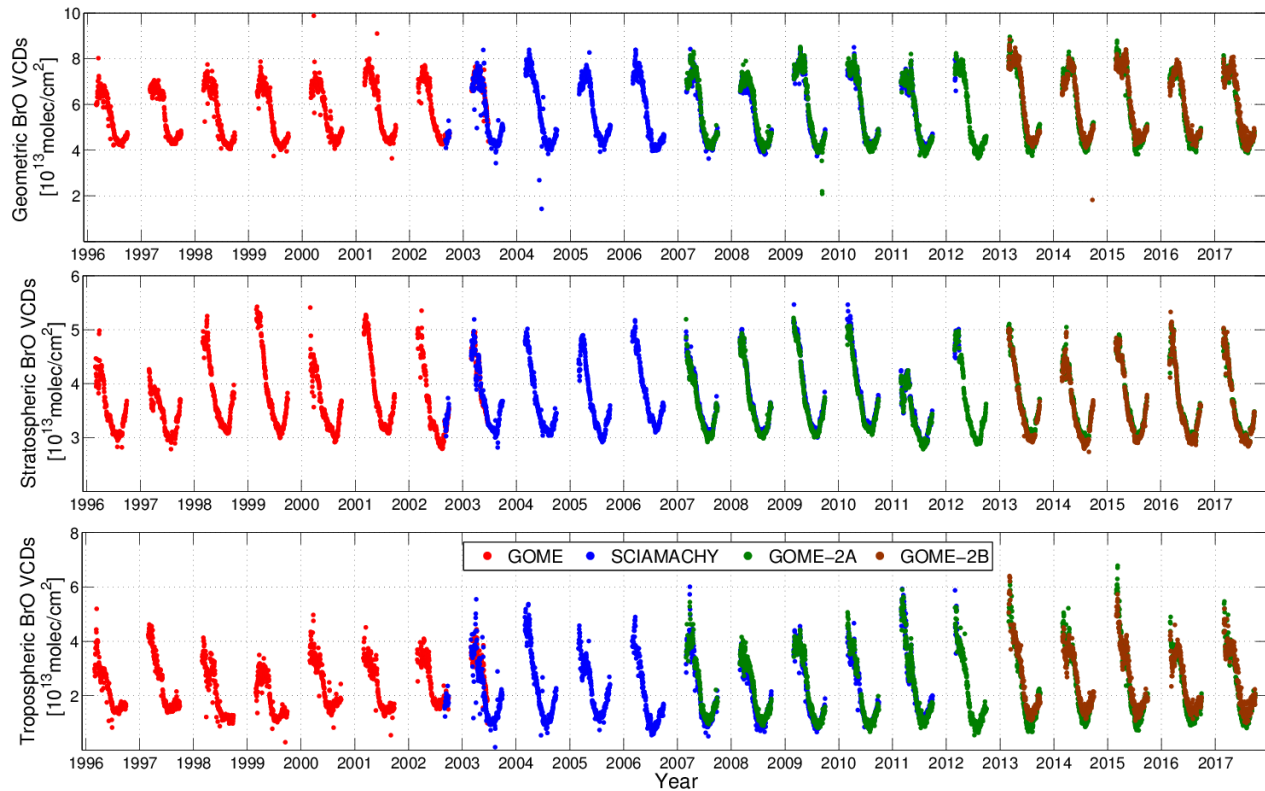


Figure 3.3: Long-term time-series of daily average BrO VCDs over the Arctic region. Top: Daily geometric BrO VCDs. Middle: Daily stratospheric BrO VCDs. Bottom: Daily tropospheric BrO VCDs. GOME data is coloured in red, SCIAMACHY in blue, GOME-2A in green and GOME-2B in brown.

The geometric VCDs account for the expected differences between the different viewing geometries of the satellite sensors to a good first order. For periods of overlapping measurements, there is a satisfactory agreement between the different sensors (GOME and SCIAMACHY from August 2002 to June 2003, SCIAMACHY and GOME-2A from March 2007 to March 2012 and GOME-2A and GOME-2B from March 2013 to September 2017). A quantitative comparison is provided in Figures 3.5 to 3.8. Another criterion that we checked to verify the quality of the retrievals, apart from the agreement, is the stability of the summer BrO VCDs, where we may generally expect an absence of a trend, due to the absence of inorganic bromine explosions, due to the melting of sea ice and the increased temperatures. There is a release of bromine compounds from organic sources found in open water, but the oxidation of these compounds is relatively slow compared to the release of bromine during springtime (Salawitch, 2006, and references therein).

The stratospheric VCDs show a good agreement, which, however, is not related to the satellite retrievals. The stratospheric BrO estimations are produced independently from the retrieval algorithm. The stratospheric BrO time-series is similar to the ozone time-series, with 1996, 1997 and 2011 being significantly lower than the rest. A slight upward trend is observed from 1996 to

2001, with a slight decrease afterwards. These trends are in agreement with stratospheric BrO measurements from the Harestua station (Hendrick et al., 2008).

Comparing tropospheric BrO VCD time-series for periods of overlap between the different instruments shows a similar level of agreement as to the geometric VCDs. The seasonality of the tropospheric time series is also similar to the geometric one. We attribute this seasonality mainly to the inorganic release of Br₂ and BrCl from sources, which depend on sea ice and meteorological parameters. As described in the introduction, in polar spring, the combination of low-temperature conditions and the presence of first-year sea ice, as it has sufficient brine, trigger the release of Br₂ and BrCl into the troposphere. This condition prevails in spring, moving slowly northwards with the solar zenith angle. During July and August, the temperature reaches its maximum. In September, the minimum sea ice extent is observed. The release of organobromine compounds from the oceanic biosphere is highest in summer and early autumn. As noted, this provides a biogenic source of bromine, but the oxidation of organic-bromine-containing compounds is relatively slow compared to the release of BrO from bromine explosion events. During summer and early autumn, tropospheric BrO VCDs reach their minimum values of the year. A slight increase is observed each September. The origin of this increase is not yet identified. Potential candidate explanations include inaccuracies in the stratospheric BrO VCD calculation or potentially lower temperature accelerating the inorganic release of bromine from brine without reaching the threshold for an explosion.

At this point, the application of the multiplication factor used during the stratospheric separation process is introduced. The method initially included the implementation of a multiplication factor, as the BASCOE model simulations by Theys et al. (2009) did not include the decrease of bromine compounds due to the implementation of the Montreal protocol. This “forcing” of a downward trend on the stratospheric BrO estimations impacts the tropospheric BrO time-series as well. The method by Theys et al. (2009) was introduced in 2009. However, comparison to more recent measurements of stratospheric BrO from Harestua (from F. Hendrick, BIRA-IASB, personal communication) shows that, by excluding the multiplication factor, the estimated stratospheric BrO VCDs are closer to the updated measurements than the estimations with the multiplication factor. Figure 3.4 shows the exact value of the multiplication factor that was applied for every year, the stratospheric BrO estimations and the tropospheric BrO VCDs after the application of the multiplication factor.

3. BrO Column Densities and Trends

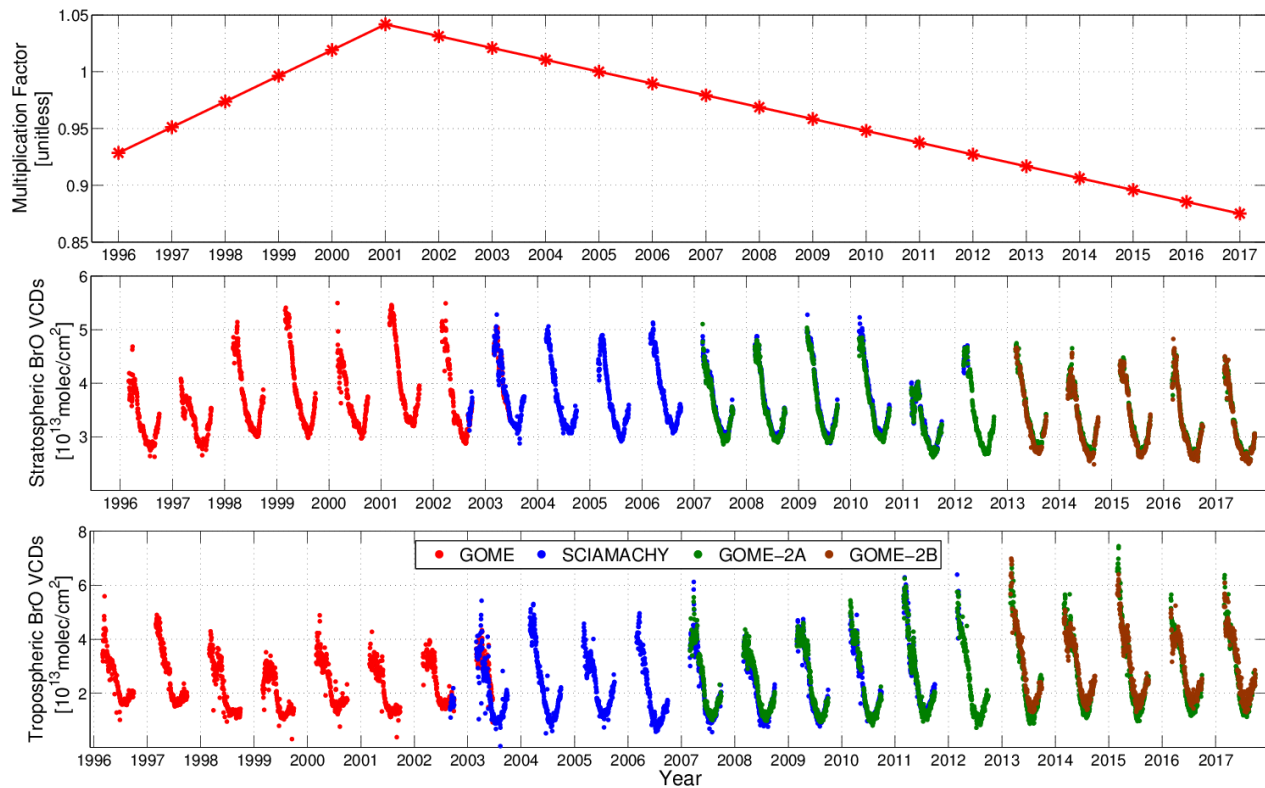


Figure 3.4: The multiplication factor and its effect on stratospheric and tropospheric BrO VCDs time-series. Top: the actual value of the multiplication factor for every year of the dataset. Middle: The stratospheric BrO estimations with the application of the multiplication factor. Bottom: The tropospheric BrO measurements with the application of the multiplication factor.

We see that the multiplication factor follows the conclusions from Hendrick et al. (2008). The yearly values of the factor increase until 2001 and decrease afterwards. The impact of the factor is clearly seen on the stratospheric BrO estimations, where especially the late years show a significant downward trend (compared with Figure 3.3 middle). Also, the early years (until 2001) show a much more substantial increase. An increase is also evident in Figure 3.3 middle, but without the application of the multiplication factor is not as pronounced. Consequently, the tropospheric BrO VCDs time-series is also affected by the factor. Especially for the latest years, the increase of the tropospheric columns is much more evident than the one in Figure 3.3 bottom (without the factor). Moreover, a potential extension of the time-series will lead to a more potent “forced” positive trend as the factor continues to decrease. The stratospheric BrO estimations without the factor (Figure 3.3 middle) come to a closer qualitative agreement with the updated measurements from the Harestua station (from F. Hendrick, BIRA-IASB, personal communication, 2019). Consequently, we decided to proceed without applying the factor. Consequently, all results shown in the following will be based on data as shown in Figure 3.3.

Another way to verify the agreement of the BrO time-series for the different sensors and check their seasonality is to compare the climatological seasonal cycles. Of course, sensors that have no overlapping period (e.g. GOME and GOME-2B) are expected to be more different from each

other. Figure 3.5 provides the annual cycles of geometric, stratospheric and tropospheric BrO VCDs:

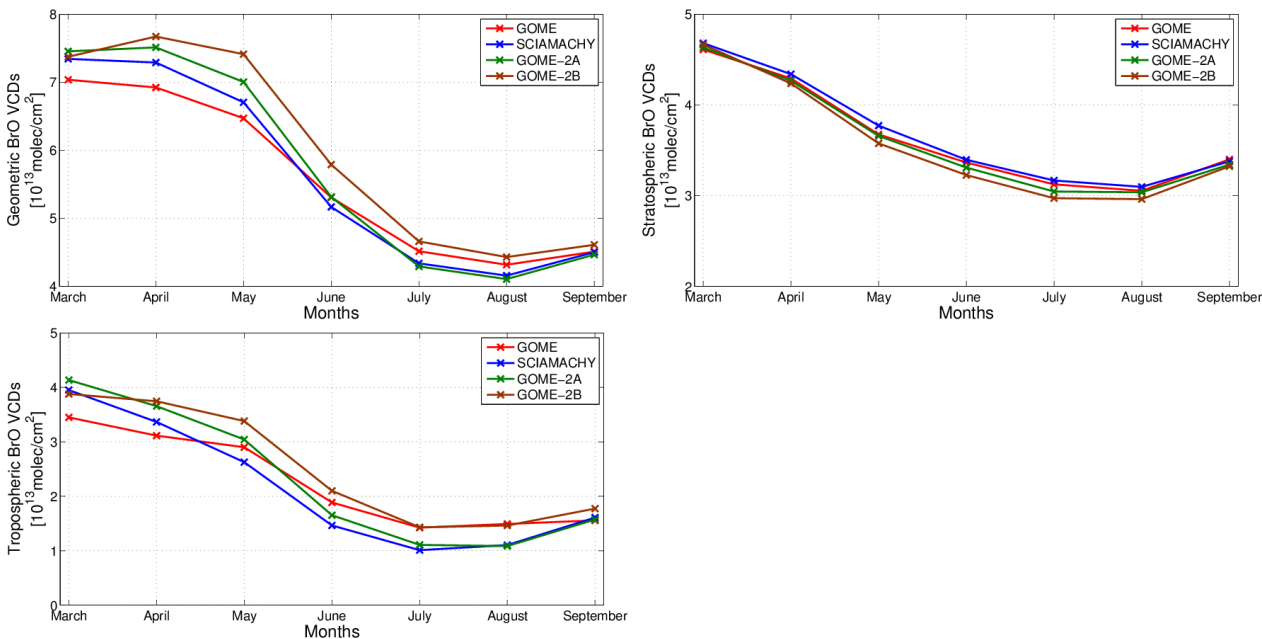


Figure 3.5: Climatological seasonal cycles of BrO VCDs in the Arctic derived from different satellite instruments.

The seasonal cycles of all three plots are similar. The peak of the cycle every polar spring (i.e. March to May) is when bromine explosions occur. Then, as the sea ice melts and temperature increases, BrO decreases subsequently. We infer that GOME-2B has the highest monthly average columns for the geometric BrO VCDs (as it spans over the last years of the dataset). GOME-2A has the second highest, especially for polar springs. GOME appears to have higher monthly average columns for July and August from SCIAMACHY and GOME-2A, in contrast to March and April. The stratospheric BrO VCD annual cycles are similar for all instruments. The tropospheric columns are similar to the geometric cycles. GOME has the lowest monthly averages for polar springs (as it covers the beginning of the time-series), while there is a satisfactory agreement for the instruments with overlapping periods.

Scatter plots of BrO VCDs can also be used to identify the agreement level between the sensors' overlapping periods. The plot of daily average BrO VCDs is used to verify the agreement of the BrO retrievals. Figure 3.6 presents geometric, and tropospheric BrO VCD scatter plots for the instruments during overlapping periods, together with the reference line. The best fitting line, its equation, the correlation coefficient of the scattered points, and the root mean square errors (RMSE) between the points and the best fitting line of each plot are shown. Statistical values were calculated using daily averaged columns.

3. BrO Column Densities and Trends

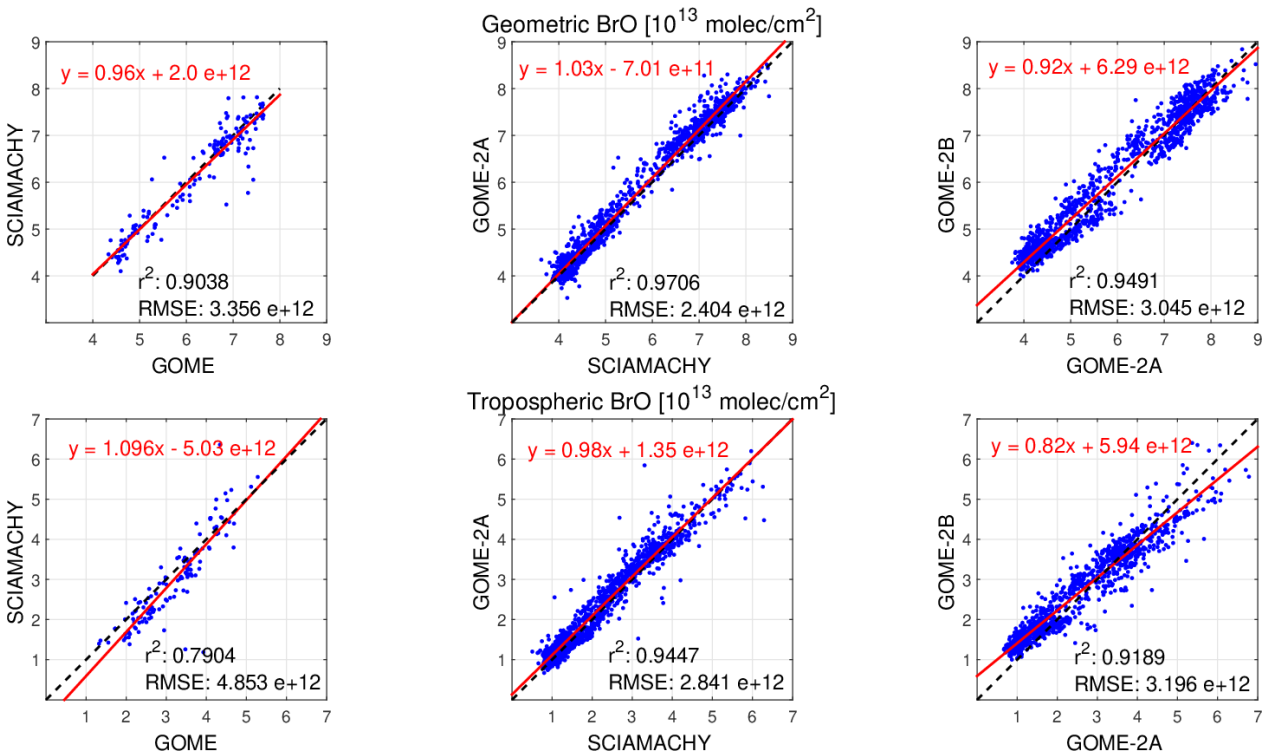


Figure 3.6: Scatter plots of geometric and tropospheric BrO VCDs. The upper row shows geometric BrO VCDs, the lower row tropospheric ones. The first column is GOME – SCIAMACHY, the second column SCIAMACHY – GOME-2A and the third column GOME-2A – GOME-2B. The red line is the best fitting line, while the black dashed line is the 1-1. The r^2 is the correlation coefficient between the two instruments, while the RMSE is the root mean square error between the points and the best fitting line.

For all three instrumental pairs, the comparisons of geometric VCDs show better statistical results, i.e. higher correlations and lower RMSEs than the corresponding tropospheric ones. This is attributed to the additional uncertainty that the stratospheric separation introduces. However, in all cases, the slope of the best fitting line is close to 1. The best agreement is seen for SCIAMACHY – GOME-2A (01.2007 – 03.2012) for both geometric and tropospheric columns. The most preliminary agreement is for GOME – SCIAMACHY (09.2012 – 06.2003), especially for the tropospheric BrO VCD comparison. Nevertheless, the agreement of all scatter plots is considered satisfactory.

3.1.2 Maps

Figure 3.7 shows geometric monthly (March) average maps, one for every year with two instruments in operation.

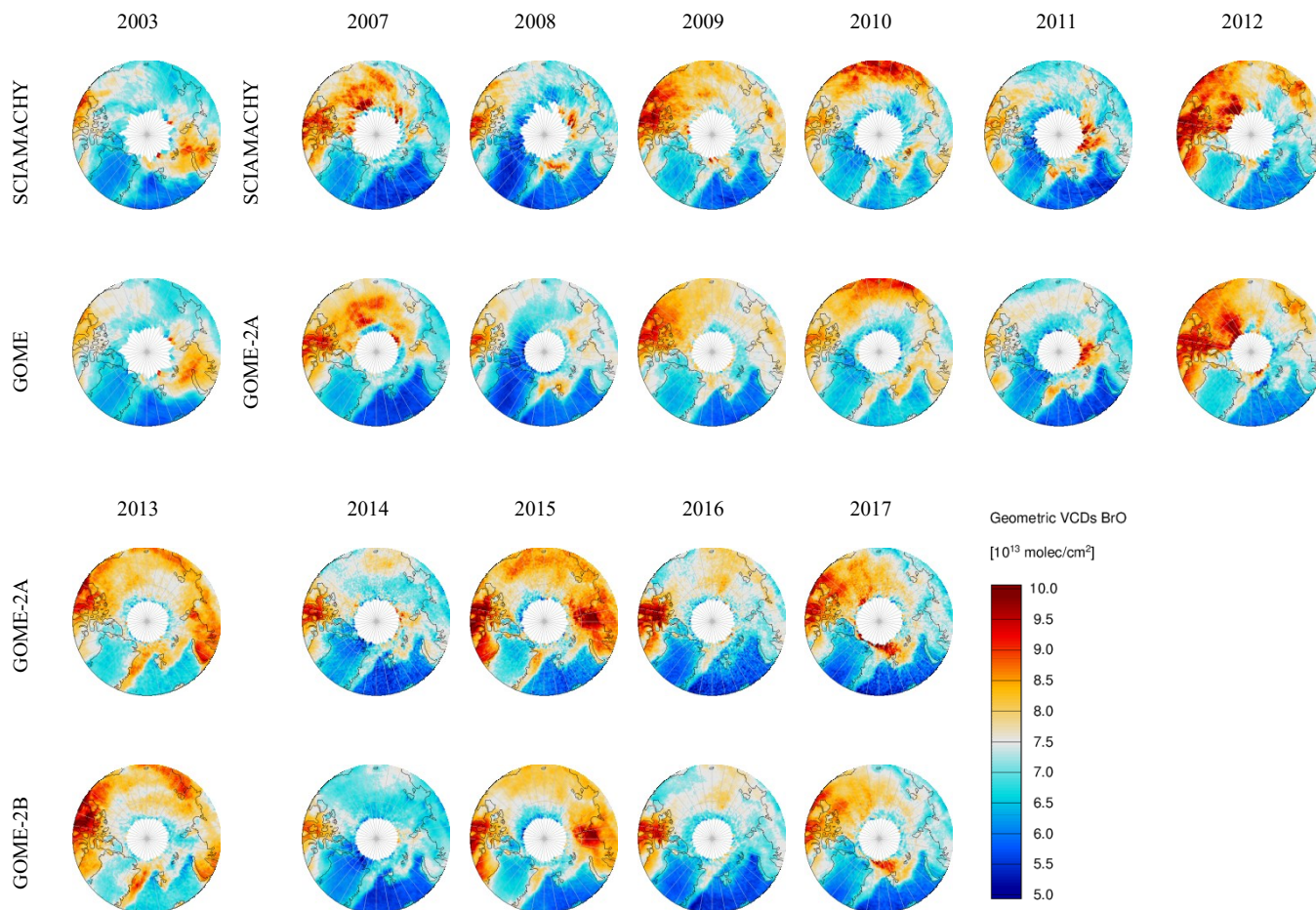


Figure 3.7: Geometric March BrO VCD maps for the Arctic region. Rows indicate different sensors, and columns refer to different years of overlapping periods.

The March of 2003 is the only month when measurements from both GOME and SCIAMACHY are available. The pair SCIAMACHY – GOME-2A has six overlapping years, while the pair GOME-2A – GOME-2B has 5. The enhanced BrO VCDs appear over the same areas and approximately with the same magnitude in all cases. Minor differences are seen between the instruments. They are attributed to different observation times, footprints, viewing geometries and instrumental degradation.

Figure 3.8 shows maps of tropospheric BrO VCDs for one bromine explosion event for each instrumental pair, spanning over four days (starting from the genesis of the BrO plume to the end or dissolving state). Since three different bromine explosion events are shown, each one is presented with an individual color scale.

3. BrO Column Densities and Trends

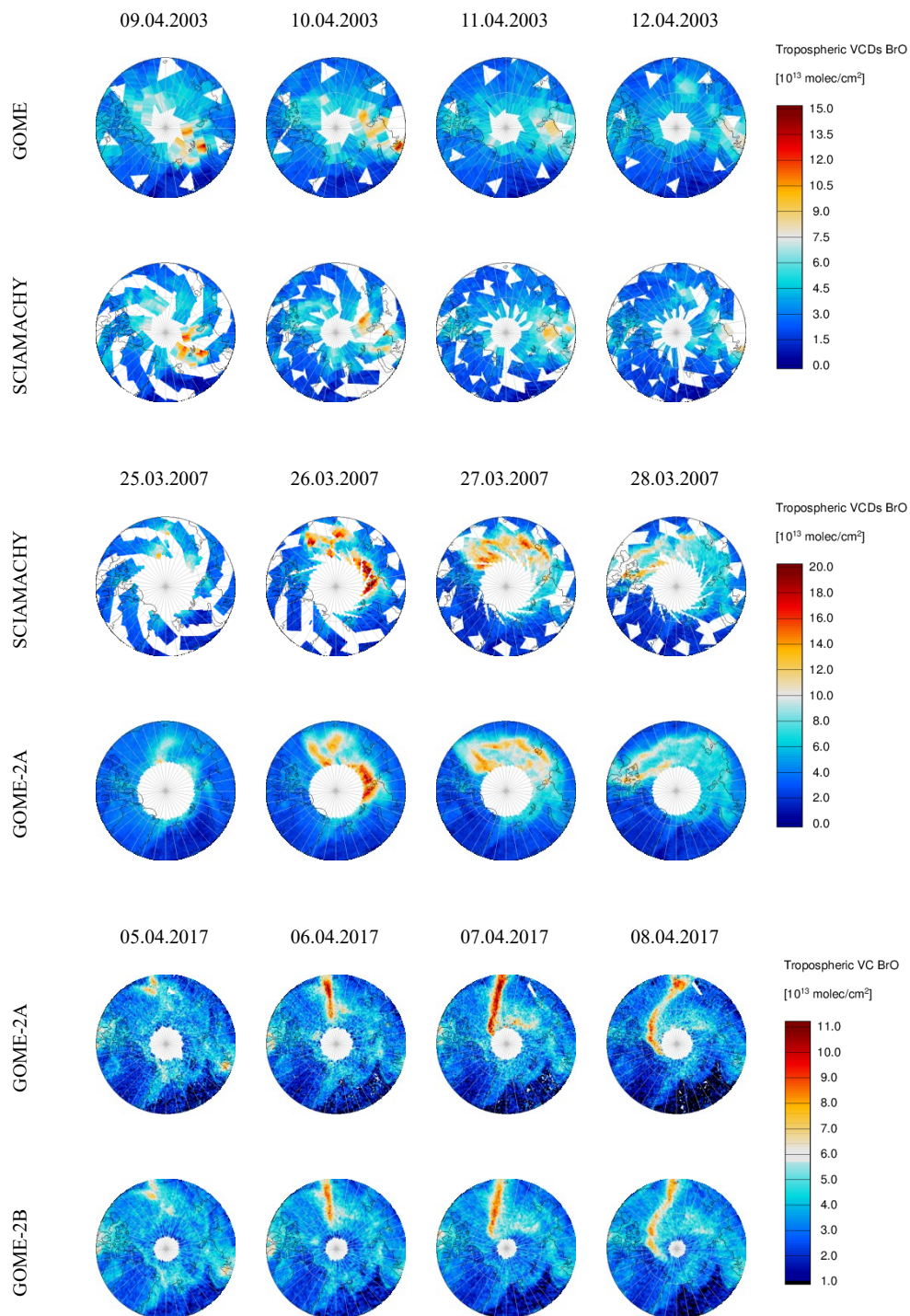


Figure 3.8: Polar Projection of the tropospheric BrO VCD for bromine explosion events retrieved from the observations of two instruments. Rows indicate the instrument for each case, while columns the date. For each case, four consecutive daily average maps of tropospheric BrO VCDs are shown.

Bromine explosion events are characterized by high values of tropospheric BrO VCDs, which occur every polar spring. The agreement between the tropospheric BrO VCDs retrieved from the

different sensors for each bromine explosion case is good, with BrO plumes appearing over the same areas and with similar magnitudes of tropospheric BrO VCDs. The times of observations are similar but not identical, and we have not identified evidence of this influencing the comparison of tropospheric BrO VCDs.

3.2 Hudson Bay

The Hudson Bay is the second region of interest for which the BrO dataset is investigated. This region is a well known tropospheric BrO hotspot. Some of the first satellite retrievals of BrO were investigated there (Richter et al., 1998; Chance, 1998). In this study, the Hudson Bay is defined as -96.0° E to -76.0° E longitudes and 50.0° N to 66.0° N latitudes. The land around the Bay was excluded from all results by applying a land mask filtering. As the region is at comparatively lower latitudes, the coverage is high throughout the whole year. Figure 3.9 shows the area of interest.

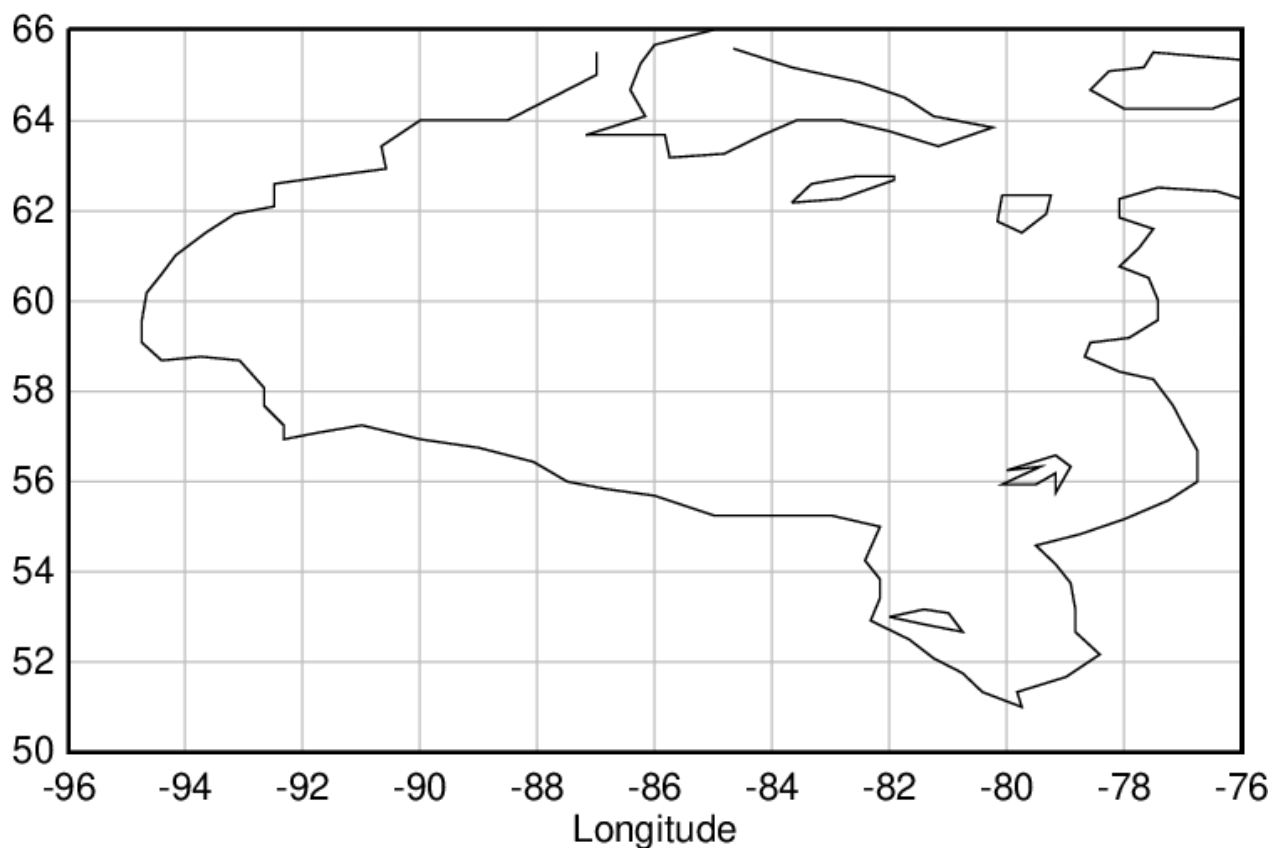


Figure 3.9: The area defined as Hudson Bay.

Time-series and maps of the Hudson Bay for the 22 years of the research will be shown to investigate the agreement between the retrieved BrO VCDs for the overlapping periods of the sensors.

3.2.1 Time-series

For the Hudson Bay, geometric, stratospheric and tropospheric BrO VCDs are investigated in the following and shown in Figure 3.10.

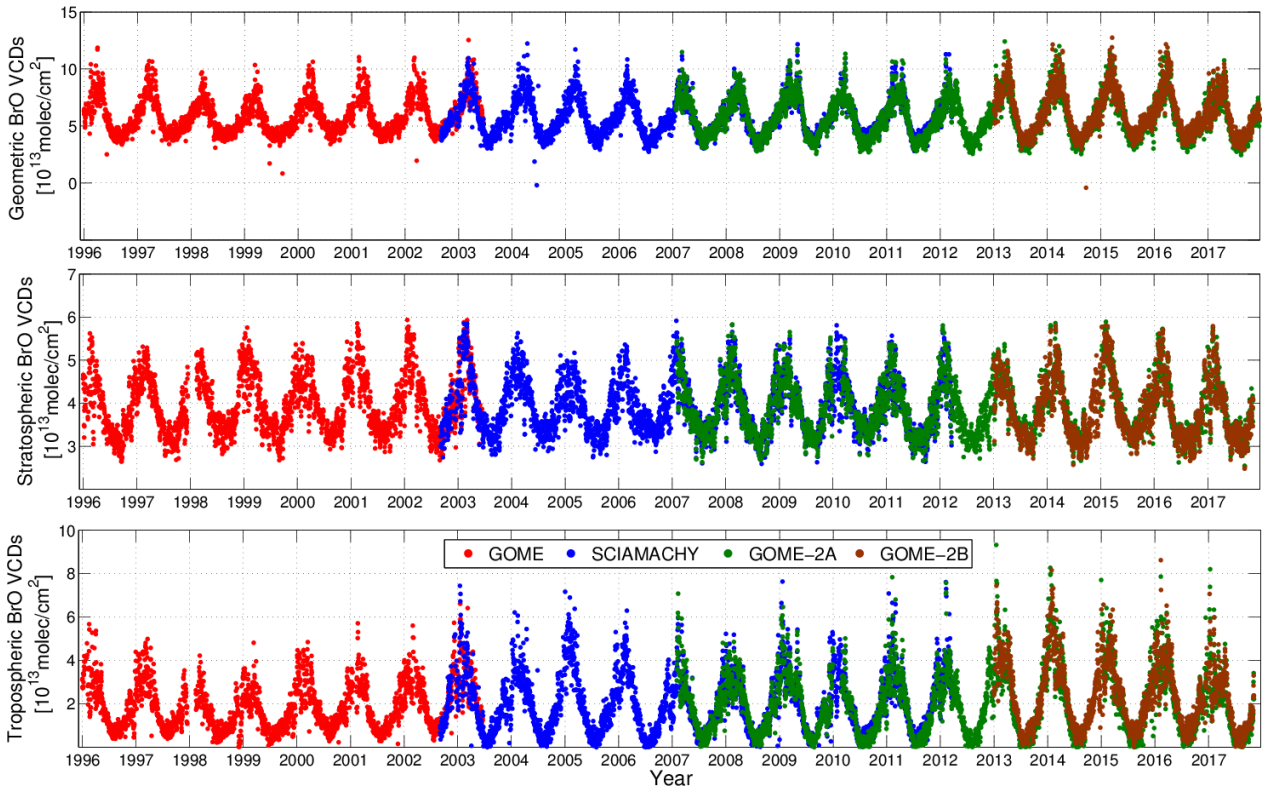


Figure 3.10: Long-term BrO VCD time-series over the Hudson Bay region.

The consistency is evident for the overlapping periods of measurements of BrO VCDs retrieved from different instruments. The coverage is good throughout the whole year. Consequently, the time-series is continuous from one year to another. The seasonality is similar; the peaks of every year occur during December – February when there is a combination of solar radiation and low temperatures. The stratospheric BrO estimations show a remarkable agreement. In the tropospheric time-series many days with much larger values than the rest of the time-series, associated with bromine explosion events are observed. It is also clear that the earlier years (when GOME was in operation) are lower than the later years (when GOME-2A and GOME-2B provide measurements), especially for the peaks of each year. This will be discussed in the trend section. The seasonality of the tropospheric time-series is also similar to the Arctic tropospheric time-series. The peak of every year is during December – February, while in the Arctic during March – April. A decrease until the end of the summer as the air temperature increases, and a re-increase afterwards is seen for both regions.

In Figure 3.11, 12 months are averaged and presented for geometric, stratospheric and tropospheric BrO VCDs.

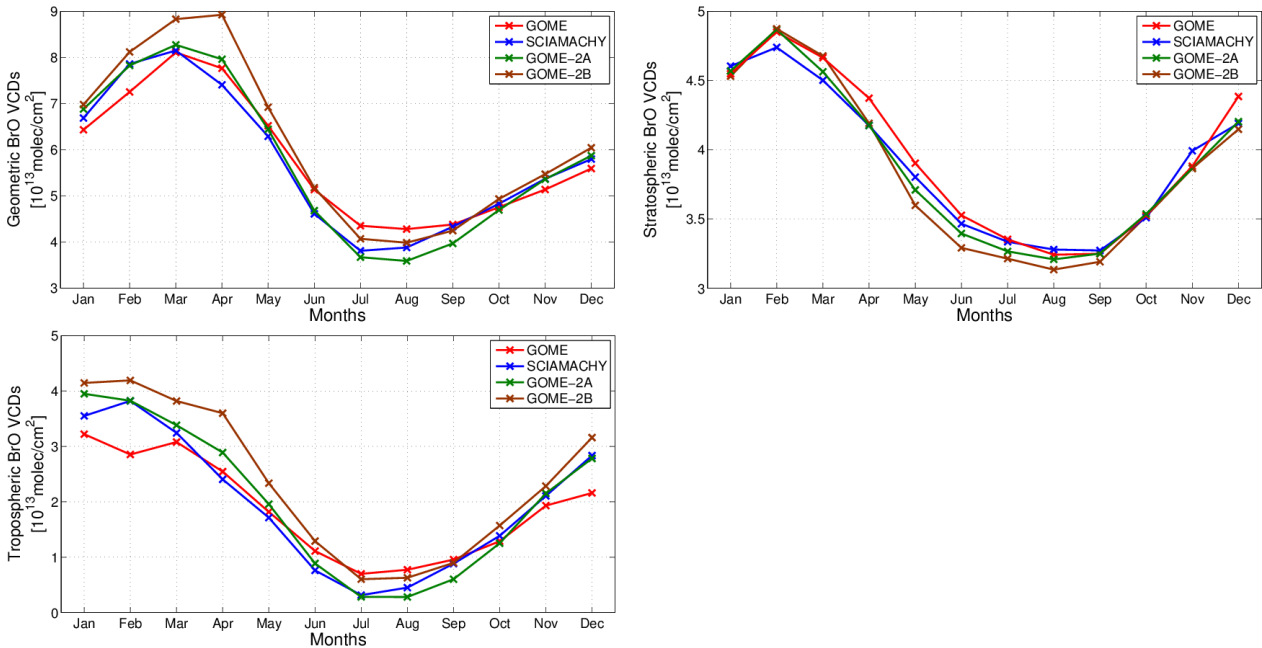


Figure 3.11: Climatological seasonal cycles of BrO VCDs over the Hudson Bay.

The GOME-2B geometric BrO VCD climatological means are higher than the rest of the sensors, especially for the first five months. We see that from 2013 onwards, the geometric columns are significantly higher (even compared to GOME-2A, starting at 2007). Generally, though, a satisfactory agreement is seen here. Regarding the annual tropospheric cycles, we still see GOME-2B being higher until May for the same reason. GOME seems to be lower, especially for the three winter months (December, January and February). We infer that indeed, there are not so many daily averages for GOME, during which a bromine explosion event may have happened (peaks in the time-series with significantly larger tropospheric BrO VCDs compared to the rest of the time-series). 2001 and 2002 seem to have few such days, but especially compared to the later years and the other sensors (for example, 2005, 2009 and 2013), they are fewer. Therefore, the smaller winter climatological means for GOME are justified. By comparing the climatological seasonal cycles over the Hudson Bay with the ones over the Arctic region, similar patterns regarding seasonality are seen. However, some differences are observed in the magnitude of tropospheric BrO VCDs during April and May. This may result from the higher temperatures in the Hudson Bay during these months.

In Figure 3.12, scatter plots for the geometric and tropospheric BrO VCDs over the Hudson Bay are shown (as in Figure 3.6 for the Arctic region). For GOME and SCIAMACHY have five overlapping months for the Arctic region, while for the Hudson Bay, there are ten. Another difference is that the daily tropospheric averages go down to zero. This happens during July and

August. It is not visible in the GOME – SCIAMACHY tropospheric scatter plot, as their overlapping period is from September 2002 to June 2003.

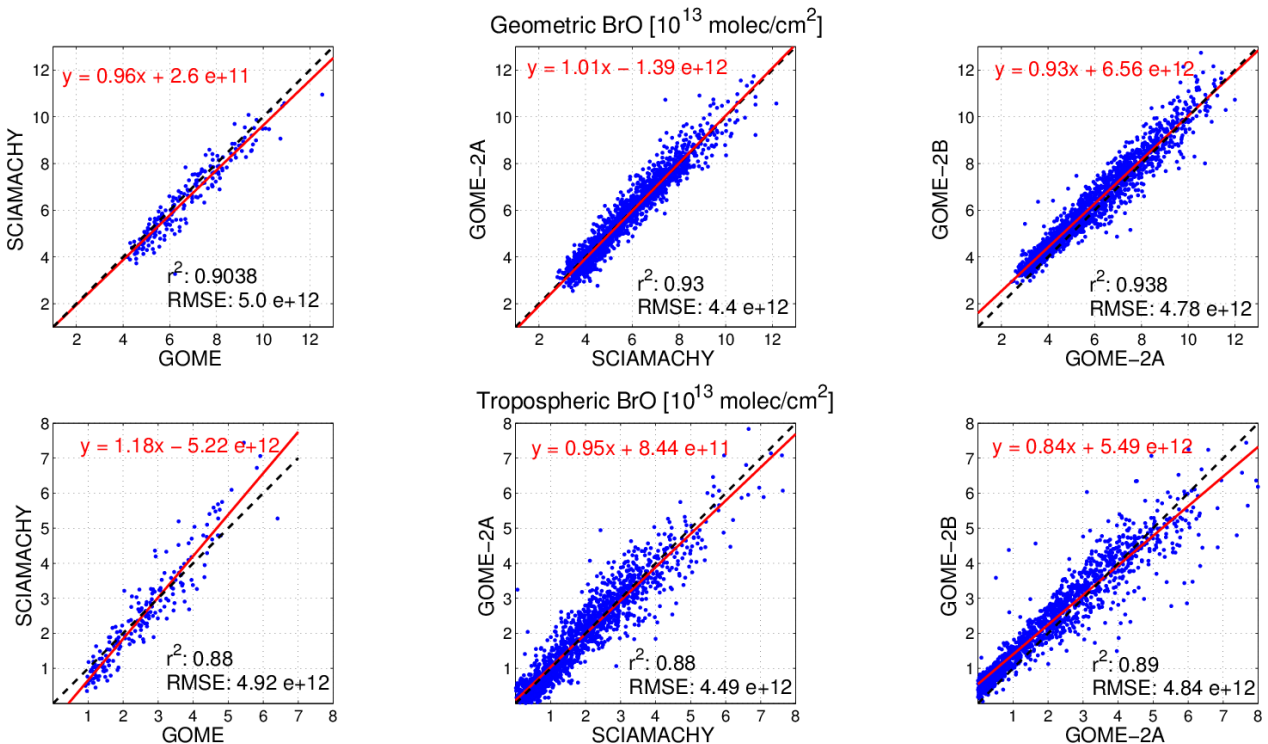


Figure 3.12: Scatter plots of BrO VCDs over the Hudson Bay.

By comparing these scatter plots with the ones for the Arctic region (Figure 3.6), we see that apart from the GOME – SCIAMACHY pair (especially for the tropospheric case), the Arctic time-series are in better agreement than the ones for the Hudson Bay, despite the more challenging retrieval (higher latitude, longer lightpath) and the smaller number of overlapping days. For example, the correlation coefficient for the tropospheric VCDs between SCIAMACHY and GOME-2A for the Arctic is 0.94, while for the Hudson Bay is 0.88. This difference is not yet explained. Nevertheless, the agreement for the Hudson Bay is equally satisfactory. One difference here is that we do not see significant variations between the different instrumental pairs (GOME – SCIAMACHY, SCIAMACHY – GOME-2A and GOME-2A – GOME-2B). In all three cases, the agreement in the tropospheric BrO VCDs is similar, while for the Arctic, the SCIAMACHY – GOME-2A pair was more consistent than the others.

3.2.2 Maps

In this sub-section, and similar to the one for the Arctic (3.2.1), we will investigate the agreement of the different sensors for the Hudson Bay by comparing geometric and tropospheric BrO VCD maps.

3. BrO Column Densities and Trends

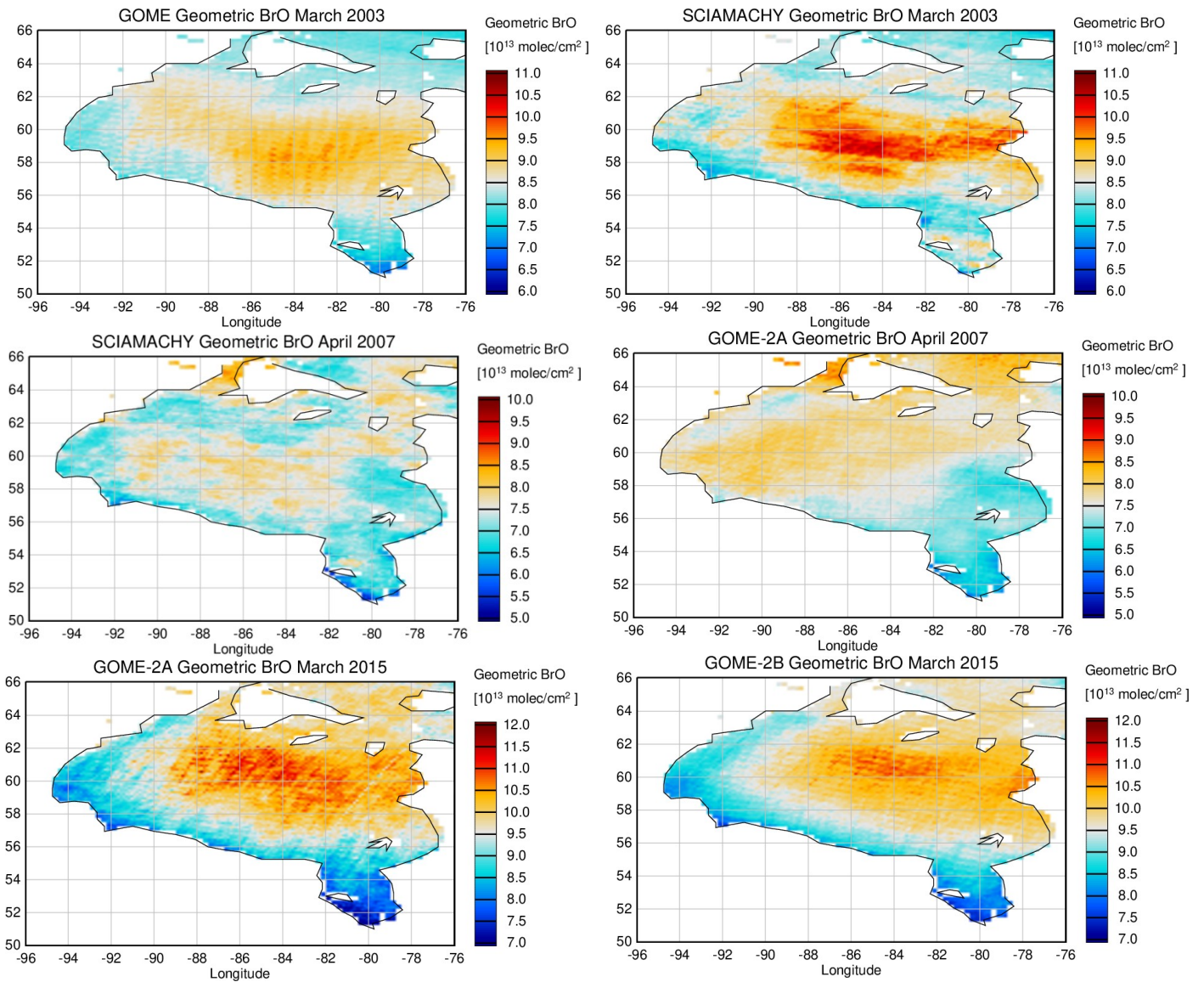


Figure 3.13: Geometric BrO VCDs of overlapping periods between the sensors for the Hudson Bay.

Similar to the scatter plots, we see that the agreement between the different sensors is not as consistent as for the Arctic region (70.0° N to 85.0° N). These differences in the magnitude of geometric BrO VCDs are evident by visual inspection, while this is not the case in Figure 3.7. However, the enhanced geometric BrO VCDs appear over the same regions for all cases.

In Figure 3.14, maps of tropospheric BrO VCDs for selected bromine explosion events (similar to Figure 3.8 for the Arctic) are compared. We show one figure per instrumental pair only.

3. BrO Column Densities and Trends

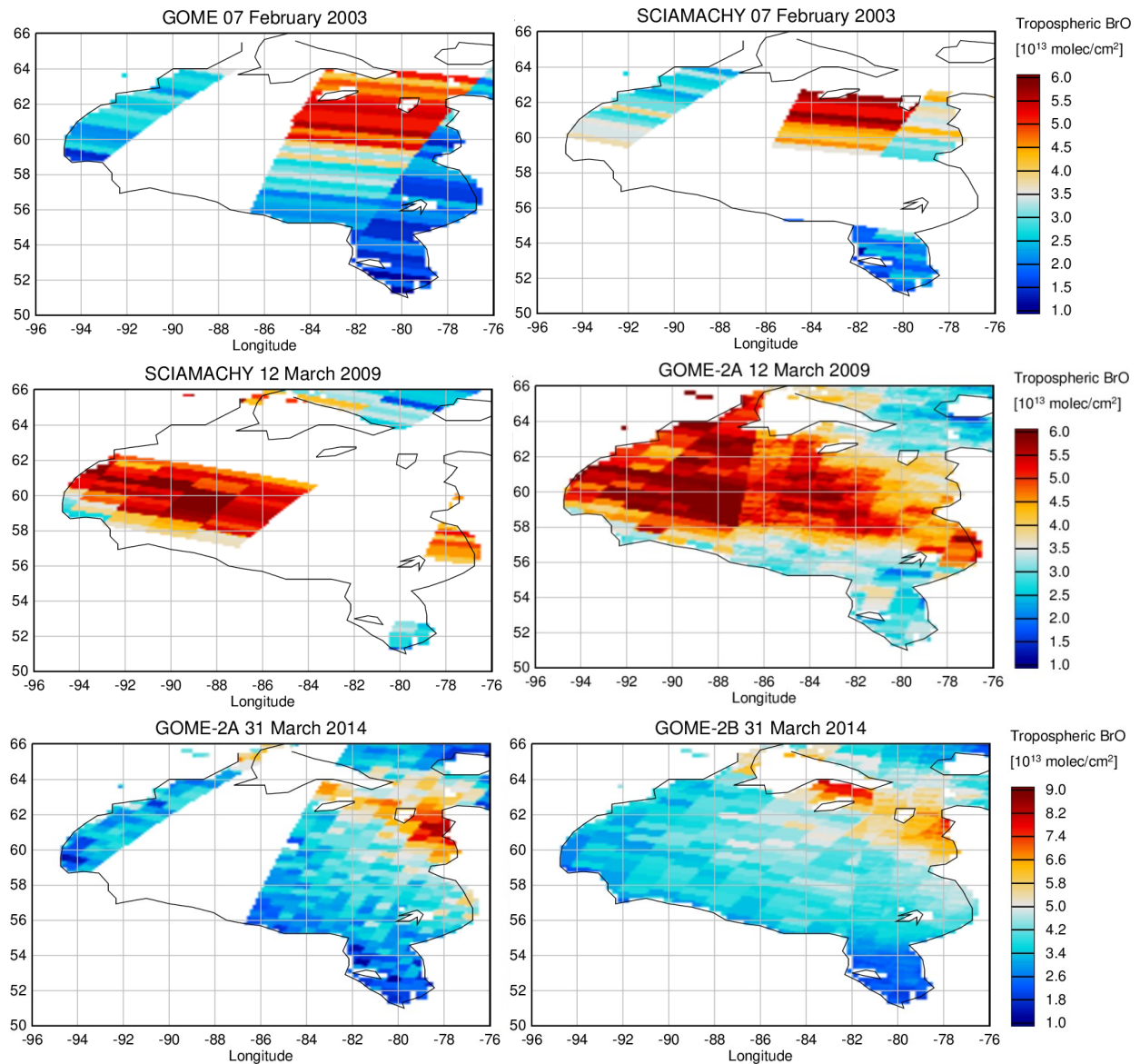


Figure 3.14: Tropospheric BrO VCDs of overlapping periods between the sensors for the Hudson Bay.

Due to the nature of the satellite orbit, there are many days where a full coverage (unlike for the Arctic region) is not achieved (e.g. Figure 3.14 top left, GOME for 07.02.2003, where only two orbits provide measurements). Still, we see that the enhanced BrO plumes are appearing over the same areas for the selected days and with similar magnitude. As before, the agreement may not be as consistent as for the Arctic region, but it is considered satisfactory.

3.3 Trends of tropospheric BrO

In this section, trends in the tropospheric BrO datasets for the Arctic and the Hudson Bay are presented. For the Arctic, the objective is to identify the impact of Arctic Amplification on tropospheric BrO plumes, while for the Hudson Bay, it will be investigated how bromine release evolved over the last 22 years. In order to be concise, the trends calculated for the Arctic used the

tropospheric dataset over sea ice covered surfaces only. The reason for this was discussed in chapter 2 (the usage of the tropospheric AMF). This dataset and the flagging process are described thoroughly in chapter 4. Also, for both regions, a merged tropospheric BrO dataset was derived, where all the overlapping days between the different sensors were averaged. For both areas, the tropospheric BrO VCDs time-series show a seasonality, with a maximum every polar spring (for the Arctic), or winter (for the Hudson Bay) and a minimum every summer. Consequently, a model that combines a linear trend and seasonal variation was selected, similar to previous studies (Georgoulias et al., 2019; Hendrick et al., 2008b). Trends were calculated using the equation:

$$d(t) = At + B + \sum_{i=1}^3 \left\{ C_i \cos\left(\frac{2\pi}{M}(t)\right) + D_i \sin\left(\frac{2\pi}{M}(t)\right) \right\} \quad [3.1]$$

where A is the slope, B the intercept, $d(t)$ is the modeled value of BrO VCD on a given day, t is the day of the dataset (expressed in fractional years), and M is the period in years. The number of harmonic functions was chosen using the minimization of the residuals between the model and the dataset. The error of the trend was calculated as in Weatherhead et al. (1998):

$$\sigma_B = \left[\frac{\sigma_M}{M^{3/2}} \sqrt{\frac{1+\varphi}{1-\varphi}} \right] \quad [3.2]$$

where σ_M is the standard deviation of the residuals between the model and the time-series, M is the period in years (22), and φ is the autocorrelation of the residuals. Finally, for the trends appearing in the individual months (i.e. Figure 3.15 middle) and for the area of the BrO VCDs associated with bromine explosions (i.e. Figure 3.15 bottom), the trend model with harmonics was not used, but instead the linear equation:

$$d(t) = At + B \quad [3.3]$$

3.3.1 Arctic

As mentioned before, the Arctic time-series were flagged for ice-covered scenes, and only these were selected in the trend calculations. The extent of the areas where the merged tropospheric BrO VCDs over sea ice exceeded a certain threshold (7.0×10^{13} molecules/cm²) was calculated and included in the trend analysis. Figure 3.15 shows the datasets used in the trend analysis.

3. BrO Column Densities and Trends

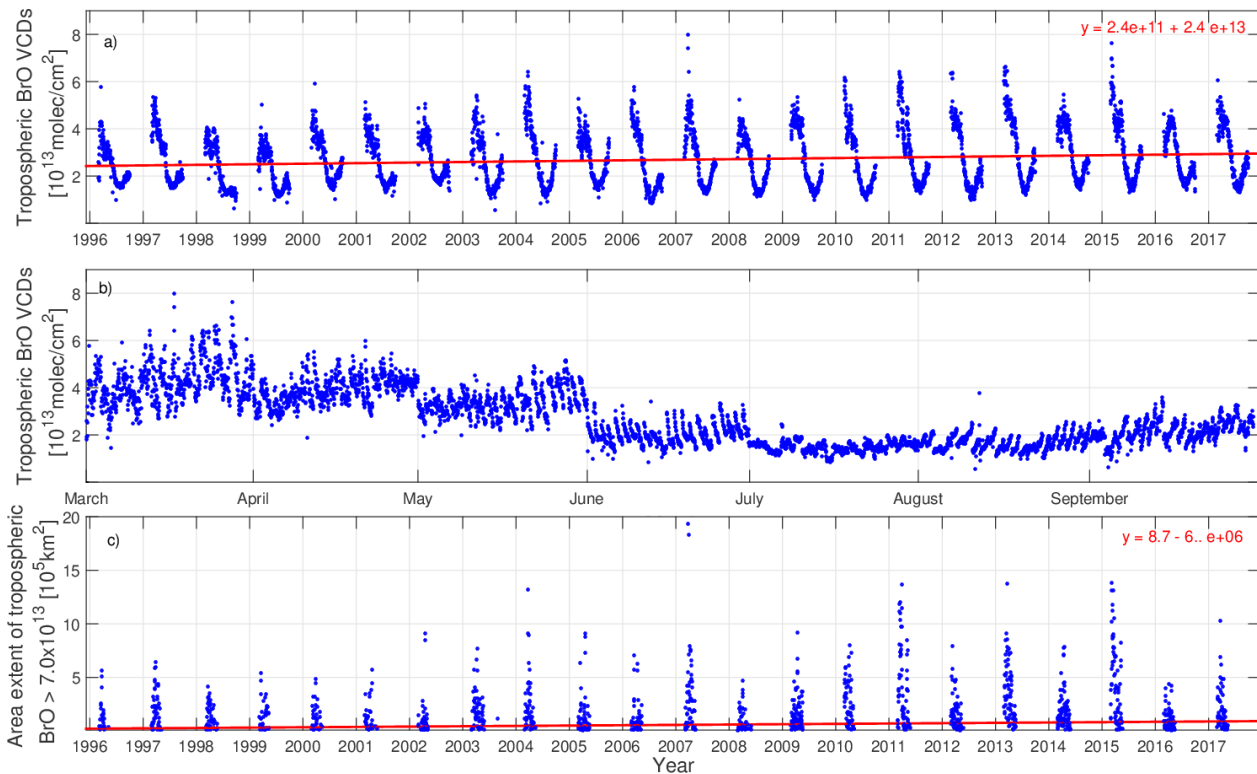


Figure 3.15: From top to bottom: a) time-series of daily averages of tropospheric BrO VCDs over sea ice in the Arctic region, b) The same, but plotted month-wise, c) the extent of the area where tropospheric BrO VCDs exceeded the threshold of 7.0×10^{13} molecules/cm². The best fitting line is plotted for sub-Figures 3.15a and 3.15c.

A slight positive trend is observed for the total tropospheric BrO dataset, although the two last years (2016 and 2017) show a decrease and closer resemblance to the early years. When we look at the evolution of tropospheric BrO VCDs on a monthly basis (e.g. for March, starting from March 1996 and taking under consideration only the March values of each year, until 2017), we see that the most vital trends are occurring during the polar spring month (March, April and May). This is interesting, as this period is also when bromine explosions appear. Positive trends also appear during June and September, while very weak trends can be seen for July and August. By checking individual maps, no significant BrO plumes can be seen for June and September, as the sea ice has decreased significantly. The positive trends for these two months are mainly attributed to changes in background BrO. Finally, the extent of the area where enhanced tropospheric BrO (i.e. above 7.0×10^{13} molecules/cm²) has also increased (especially during 2011, 2013 and 2015). However, this positive trend is also insignificant.

The table below summarizes the trends calculated in Figure 3.15; for every trend its error was calculated, the percentage of the trend based on the first year of the dataset (1996), and whether it is significant or not. A trend is considered significant if the ratio between it and its error is greater than 2 (Weatherhead et al., 1998):

Table 3.1: Trends of tropospheric BrO VCDs for the Arctic region.

Quantity	Trend	Error in trend	Trend	Significant
BrO VCD [molec/cm²] (Figure 3.15a)	+ 2.4x10 ¹¹	1.1x10 ¹¹	+ 0.99	Yes
March BrO VCD [molec/cm²] (Figure 3.15b)	+ 5.2x10 ¹¹	8.5x10 ¹⁰	+ 1.50	Yes
April BrO VCD [molec/cm²] (Figure 3.15b)	+ 4.9x10 ¹¹	5.0x10 ¹⁰	+ 1.60	Yes
May BrO VCD [molec/cm²] (Figure 3.15b)	+ 3.9x10 ¹¹	5.0x10 ¹⁰	+ 1.30	Yes
June BrO VCD [molec/cm²] (Figure 3.15b)	+ 1.5x10 ¹¹	4.3x10 ¹⁰	+ 0.74	Yes
July BrO VCD [molec/cm²] (Figure 3.15b)	+ 2.9x10 ¹⁰	2.2x10 ¹⁰	+ 0.18	No
August BrO VCD [molec/cm²] (Figure 3.15b)	+ 4.5x10 ¹⁰	3.1x10 ¹⁰	+ 0.26	No
September BrO VCD [molec/cm²] (Figure 3.15b)	+ 2.8x10 ¹¹	4.3x10 ¹⁰	+1.43	Yes
Area of BrO plumes [km²] (Figure 3.15c)	+ 896	2280	+ 0.06	No

We see that all trends (except for July, August and the extent of the area where enhanced BrO plumes appear) are significant. The positive upward trend of the entire tropospheric dataset (i.e. Figure 15a) is around 1%. However, this increase becomes much more robust for the polar spring periods, where the increase is around 1.5%. A further and more detailed analysis of the polar spring period will follow in the following pages.

In order to better investigate the trends appearing in the full tropospheric BrO VCD dataset, it is valuable to investigate the evolution of the rate of change of tropospheric BrO VCD from any starting year to any other. For example, is the trend different if calculated for data after 1998 only, or how did tropospheric BrO VCDs change during the last four years of the dataset? Therefore, a heat map figure, in which the x-axis indicates the starting year for the trend calculation, while the y-axis shows the ending year, was created. All trends in this figure were calculated by using equation 3.3, starting from the same date in a year for both the starting and the ending years (i.e. end of March):

3. BrO Column Densities and Trends

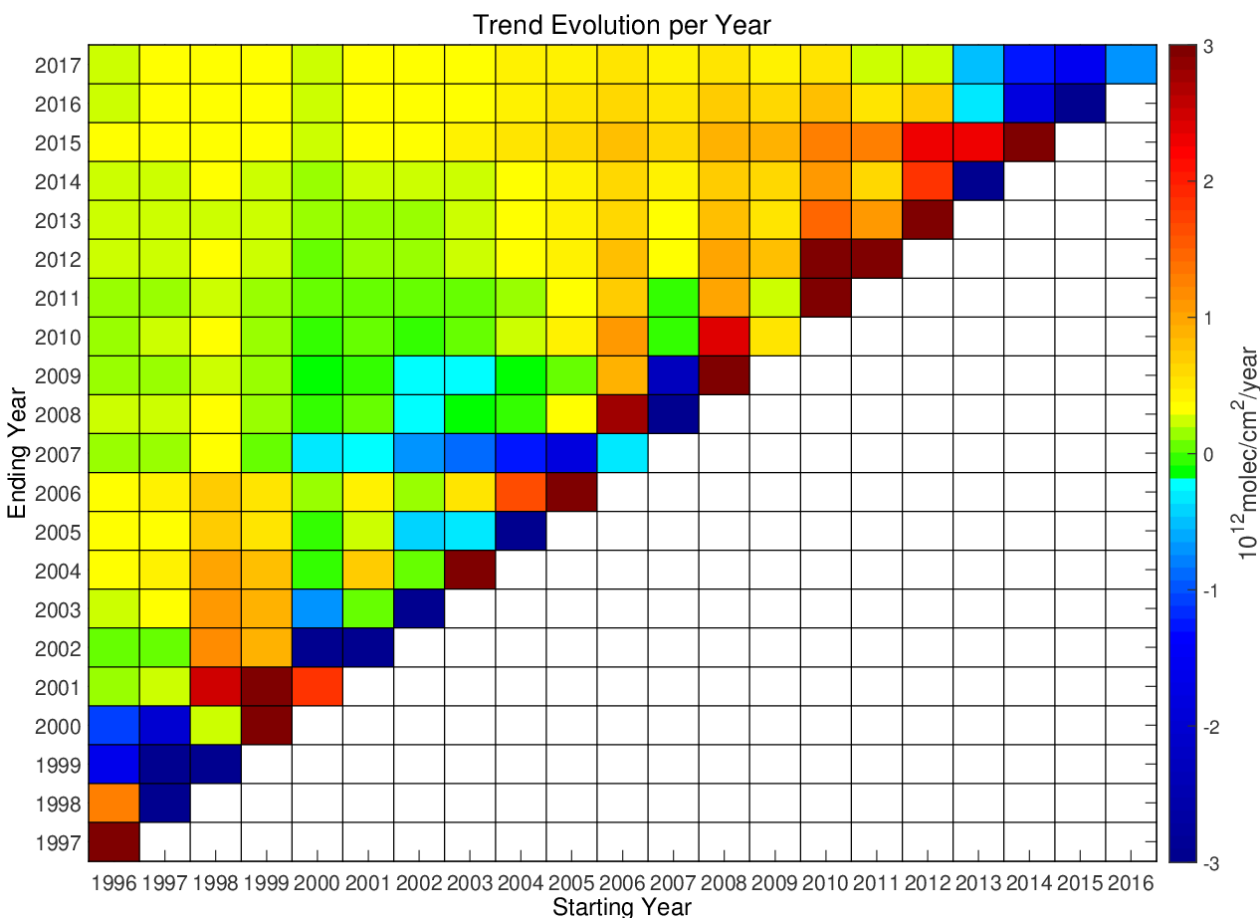


Figure 3.16: Linear trends of tropospheric BrO VCDs over different periods. The x-axis shows the starting year, and the y-axis is the ending year of the period.

Linear trends calculated by starting in one year and ending in the next one (e.g. from 1996 to 1997) are in agreement with the development of BrO VCD shown in Figure 3.15c (for example, the significant positive change from 2014 to 2015, or the decrease from 1997 to 1998). Trends over short periods are dominated by inter-annual variability. The positive linear trends are most prominent when the later years are included. We see that the strongest longer-term (here regarded as periods covering at least ten years) positive trends occur when we choose a starting point between 2006 – 2008 and as ending point the year 2017.

The polar spring is the season where the majority of bromine explosions occur. Consequently, a heat map has been generated for the BrO VCD in spring (Figure 3.17).

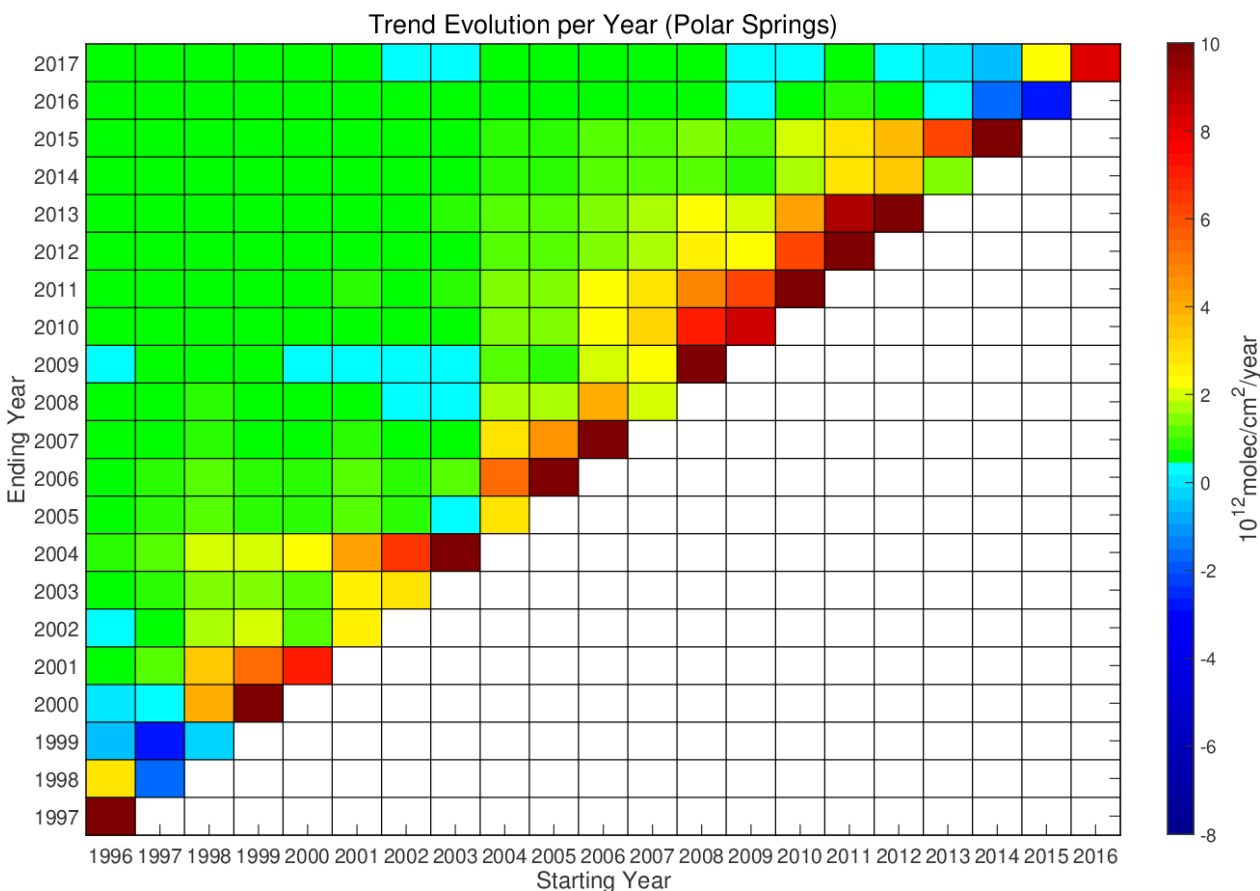


Figure 3.17: Linear trends of tropospheric BrO VCDs over different periods based on data for polar spring only. The x-axis shows the starting year, and the y-axis is the ending year of the period.

Similar to Figure 3.16, positive trends are observed for almost all cases. The short-term linear trends in this figure are calculated using only a small number of observations (92 polar spring days for each year). Therefore, it is more valuable to focus on long-term trends (i.e. five or more years). Positive trends of the magnitude of $4.0 \times 10^{11} - 1.0 \times 10^{12}$ molecules/cm²/year are observed. This is more pronounced than the corresponding trends of the entire dataset (around $2.0 \times 10^{11} - 4.0 \times 10^{11}$ molecules/cm²/year).

The positive trends appearing during the polar spring periods require a more thorough investigation. For this purpose, the polar spring BrO VCDs dataset is separated into three sub-sets: one with values greater than 7.0×10^{13} molecules/cm², one with the values between 3.0×10^{13} and 7.0×10^{13} molecules/cm² and one with values below 3.0×10^{13} molecules/cm². For each sub-set, the trends are calculated daily. Trends are provided for the number of counts that each value in each sub-set appears. Figure 3.18 provides the time-series of the three sub-sets on a polar spring average base. For each year, we have averaged both the values of tropospheric BrO and the number of observations (counts).

3. BrO Column Densities and Trends

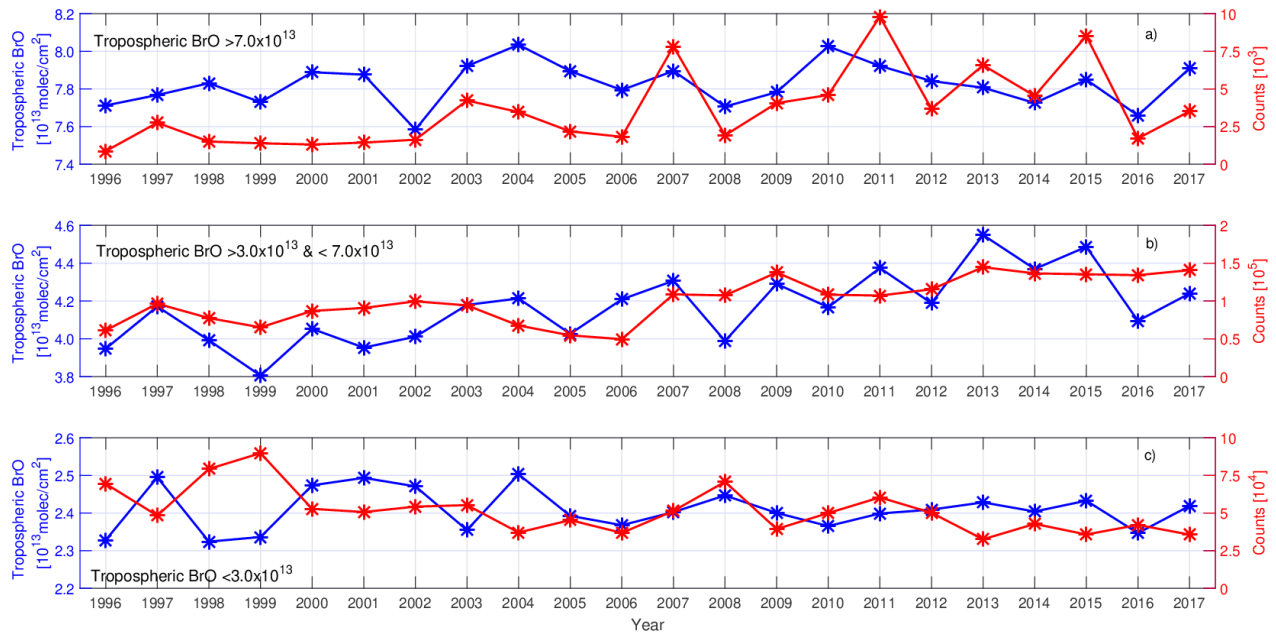


Figure 3.18: Subsets of the polar spring tropospheric BrO VCD dataset. a) tropospheric BrO VCDs above 7.0×10^{13} molecules/cm². b) tropospheric BrO VCDs between 3.0×10^{13} and 7.0×10^{13} molecules/cm². c) tropospheric BrO below 3.0×10^{13} molecules/cm².

One inference from Figure 3.18a is that the high tropospheric BrO VCDs (which are related to bromine explosion events) have not drastically changed in magnitude (i.e. the magnitude of enhanced BrO plumes has not increased over the 22 years). However, the number of times that a value $> 7.0 \times 10^{13}$ molecules/cm² was found has increased, especially since 2007. This means that the number of bromine explosion events increases, but not their intensity. From Figure 3.18b, we see that both the magnitude and the number of tropospheric BrO VCDs between 3.0×10^{13} and 7.0×10^{13} molecules/cm² have increased, meaning that we have more cases of tropospheric BrO which occur in this value range, but also that the magnitude of these medium-range cases has increased over time. Figure 3.18c shows the ambient tropospheric BrO VCD. We see that the number of such cases has slightly decreased over time, while their magnitude remains constant.

Table 3.2 presents the trends appearing in these three sub-sets. All trends were calculated on a daily basis (i.e. the polar spring days of each year, for both the magnitude of tropospheric BrO VCD and the counts):

Table 3.2: Trends of the subsets of tropospheric BrO during polar springs.

Quantity	Trend [units/yea]	Error in trend [units/year]	Trend percentage	Significant
Tropospheric BrO > 7.0x10¹³ [molec/cm²]	- 3.5x10 ⁰⁹	1.1x10 ¹¹	- 0.004	No
Counts of tropospheric BrO > 7.0x10¹³	292	78.4	+ 3.3	Yes
Tropospheric BrO > 3.0x10¹³ & < 7.0x10¹³ [molec/cm²]	+ 1.9x10 ¹¹	5.0x10 ¹⁰	+ 1.60	Yes
Counts of tropospheric BrO > 3.0x10¹³ & < 7.0x10¹³	3543	632.5	+ 5.8	Yes
Tropospheric BrO < 7.0x10¹³ [molec/cm²]	- 2.5x10 ⁰⁹	2.0x10 ¹⁰	- 0.001	No
Counts of tropospheric BrO < 7.0x10¹³	-1315	490	- 1.90	Yes

The only non-significant trends are the magnitude of tropospheric BrO VCD above 7.0x10¹³ molecules/cm² and the magnitude of tropospheric BrO VCD below 3.0x10¹³ molecules/cm². However, for these two subsets, the number of grid cells changed in a significant way (for the case above 7.0x10¹³ molecules/cm², it increased by 292 counts per year or +0.33% per year, while for the case below 3.0x10¹³ molecules/cm², it decreased by 1315 counts per year or -1.90% per year). For the subset of tropospheric BrO VCD below 7.0x10¹³ molecules/cm² and above 3.0x10¹³ molecules/cm², both the magnitude of the tropospheric BrO VCD and their counts increased significantly (+1.6% per year and +5.8% per year accordingly). During the 22 years of the dataset, the magnitude of enhanced tropospheric BrO plumes did not change significantly. However, their frequency increased significantly over the recent years, i.e. more bromine explosions occurred. In addition, there are more cases of “moderate” tropospheric BrO VCDs. The magnitude of tropospheric BrO VCD in this range has increased.

The trend analysis performed so far did not include any spatial information, i.e. where do enhanced BrO plumes appear and how did their distribution change spatially over time. The sources and driving mechanisms of bromine release and BrO formation are also changing irregularly (i.e. sea ice age increases in some Arctic regions but decreases in others; Wang et al., 2020). Also, the frequency of cyclones changes from region to region (Rinke et al., 2017). Therefore, it is meaningful to include spatial information in our trend analysis to identify the “hotspot” areas where enhanced BrO plumes develop and how the location of hotspots changed over the years. The anomaly maps in Figure 3.19 show the polar spring average of tropospheric

3. BrO Column Densities and Trends

BrO VCDs for every year, minus the long-term 22-year average, which is also shown on the bottom right of the figure. It should be stated again that all maps are flagged and show only data over sea ice covered regions (the process is explained in chapter 4).

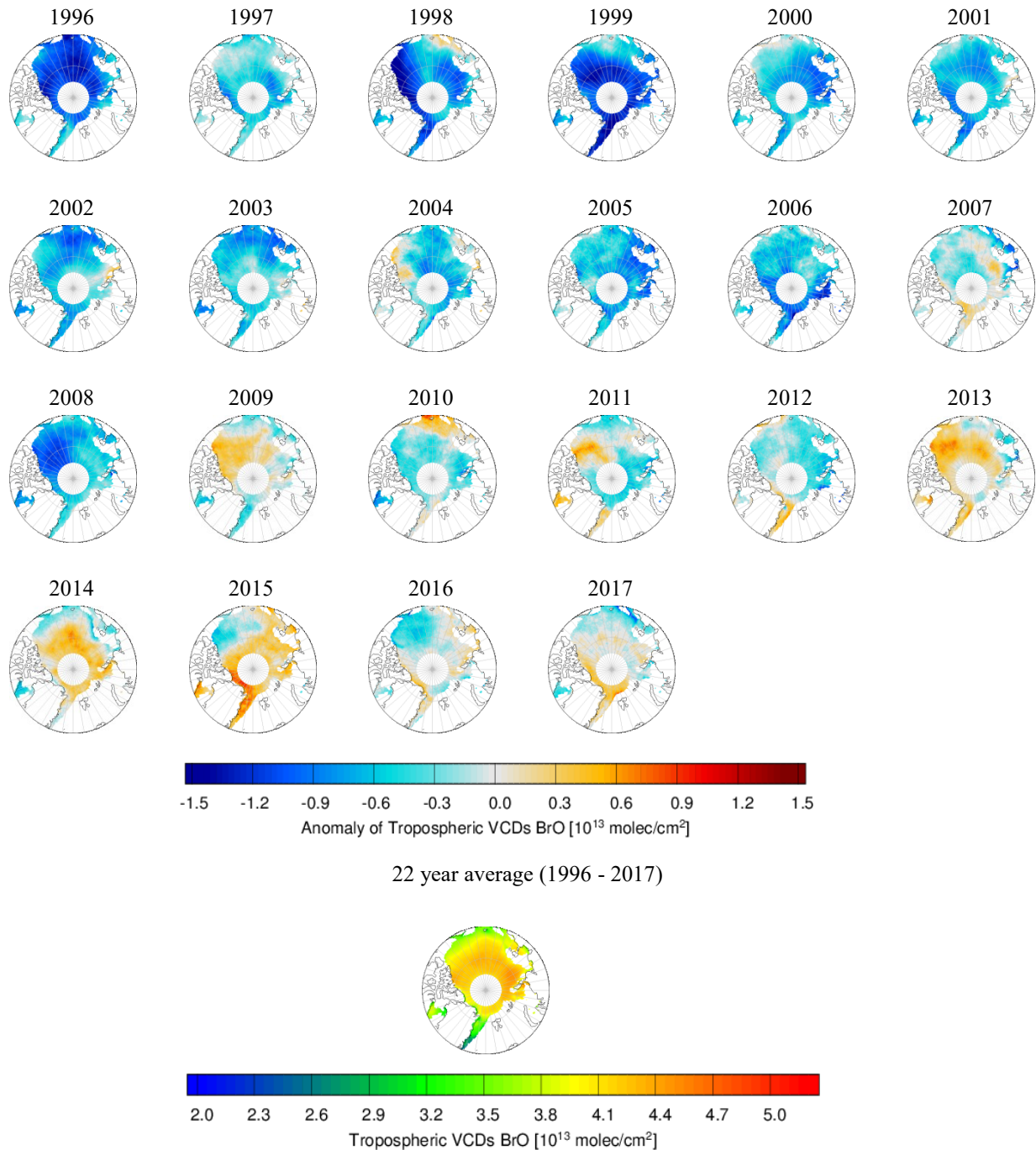


Figure 3.19: Polar spring anomaly maps of tropospheric BrO VCDs [molecules/cm²]. For every map, the long-term 22 year average (shown at the bottom right map) has been subtracted from the average of the corresponding year.

Negative values and blue colors (i.e. lower columns compared to the long-term average) dominate in most regions and years until 2008, with a few exceptions (e.g. in 1998 over the East Siberian Sea or 2004 over the Beaufort Sea). However, starting from 2009, positive anomalies (i.e. tropospheric BrO VCD higher than the long-term average) appear more frequently and in more regions (e.g. in the North-East of Greenland from 2013 onwards, or over the Canadian archipelago and in the Arctic Ocean in years 2009, 2013 and 2015). Consequently, it is inferred that tropospheric BrO VCDs change not only in magnitude but also spatially. In order to identify how tropospheric BrO VCDs change in every grid cell in time, the slope of the best fitting line for every grid cell was calculated. The corresponding spatial trend map is shown in Figure 3.20.

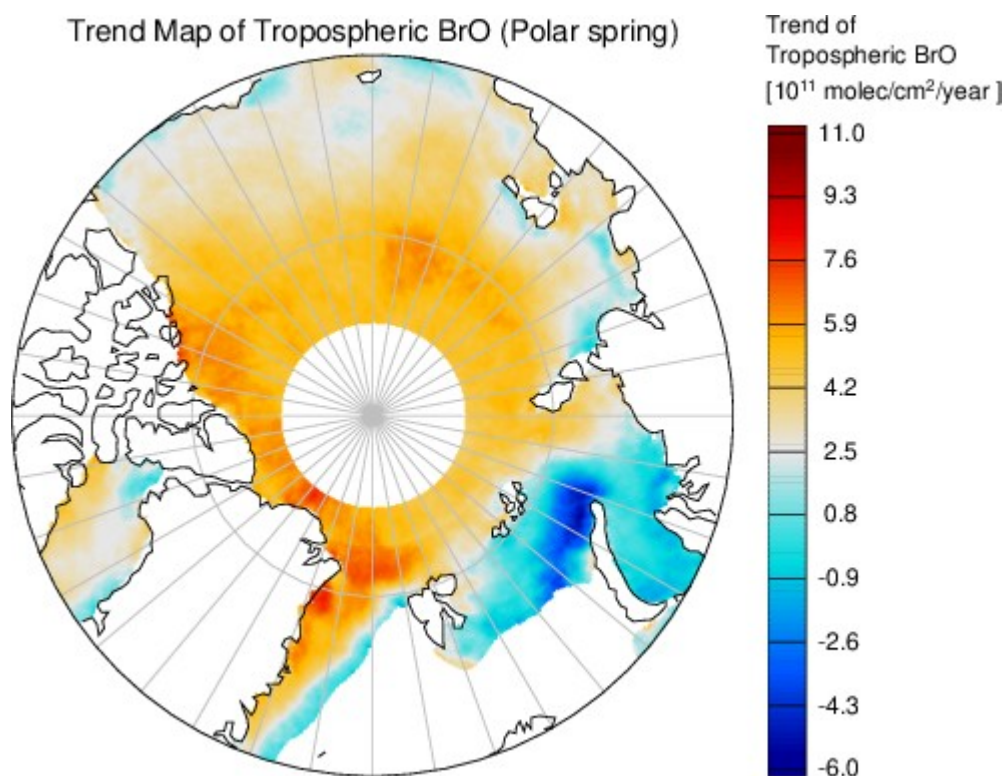


Figure 3.20: Spatial trend map of tropospheric BrO VCDs.

In most regions, an increase of tropospheric BrO VCDs during polar spring is observed. However, there are some areas where a decrease is found, the most profound being the Barents Sea and the Kara Sea, especially to the North-West of Severny island. We observe the most significant increases to the North-East of Greenland, where tropospheric BrO VCDs increased with a rate of around 10.0×10^{11} molecules/cm² per year. These changes will be compared with the corresponding changes in sea ice conditions and meteorological conditions favourable for bromine explosions in chapter 4.

3.3.2 Hudson Bay

3. BrO Column Densities and Trends

Further analysis of BrO VCD trends over the Hudson Bay will follow. As mentioned before, we did not perform a sea ice coverage flagging on the tropospheric BrO VCDs. Additionally, there is sufficient coverage over winter for the analysis over this session. Figure 3.21 is similar to Figure 3.15, but for the Hudson Bay region, showing the total merged tropospheric BrO VCD time-series and the best fitting line, the same dataset plotted per month and the extent of the areas in the Hudson Bay where tropospheric BrO VCD exceeded the threshold of 7.0×10^{13} molecules per cm^2 .

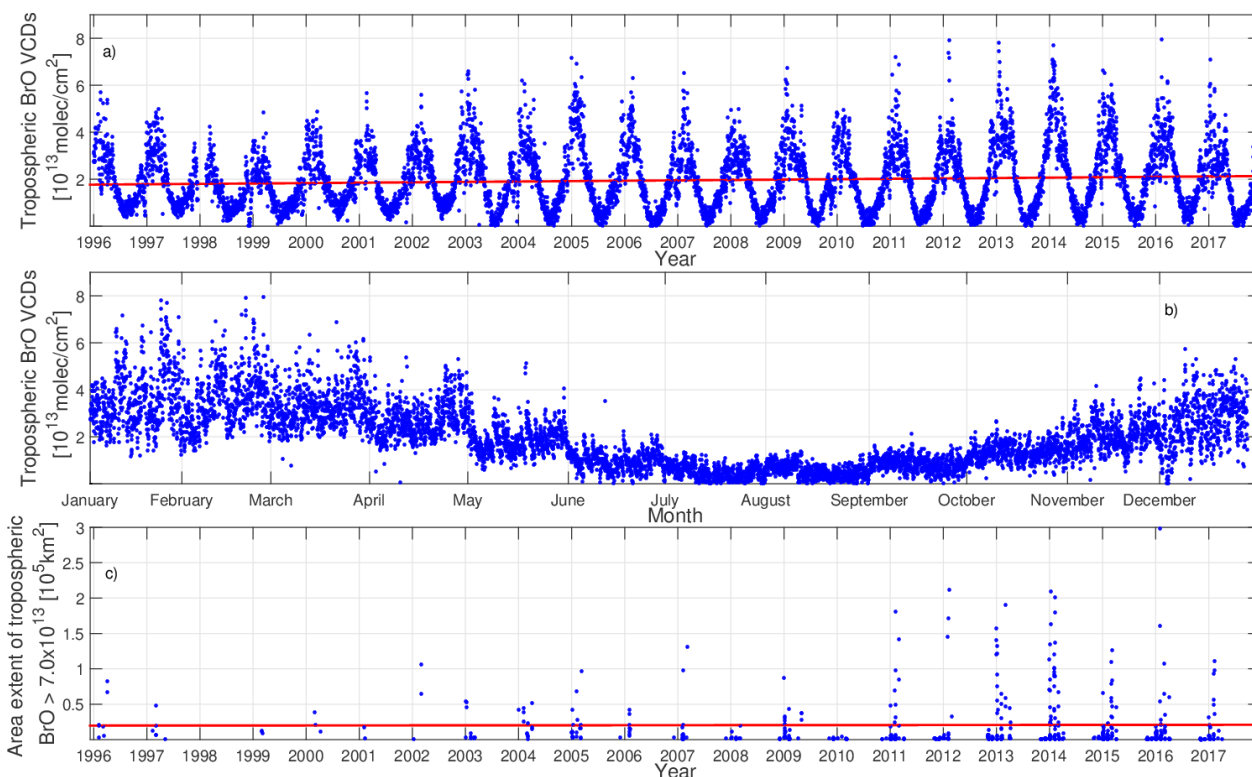


Figure 3.21: From top to bottom: a) time-series of daily averages of tropospheric BrO VCDs based on the sensor merged dataset for the Hudson Bay region, b) the same, but plotted monthly-wise, c) the extent of the area where tropospheric BrO VCDs exceeded the threshold of 7.0×10^{13} molecules/ cm^2 . The best fitting line is plotted for sub-figures 3.21a and 3.21c.

At first glance, we observe that the trend of the total merged tropospheric BrO VCDs for the Hudson Bay is smaller than the one for the Arctic region. Another difference to Figure 3.15a is that the background tropospheric BrO reaches zero during the summer months. Overall, we see higher tropospheric BrO VCD over the recent years. However, the maximum values of tropospheric BrO VCD occur during different years compared to those in the Arctic, i.e. 2012, 2013 and 2014. In the second panel, the trends that appear over the months when bromine explosions occur (spring and winter months here) are equal or even more robust than those appearing over the Arctic region. A similar response is observed for the summer months, where there are minimal bromine explosion events over Hudson Bay. For the areas of enhanced BrO plumes, both the magnitude of their extent and their frequency are lower than in the Arctic. In

1998 no single daily average tropospheric BrO VCD was above 7.0×10^{13} molecules/cm². The best fitting line also reveals no significant trend.

The trends appearing in the Hudson Bay tropospheric BrO time-series are listed in table 3.3, (similar to table 3.1).

Table 3.3: Trends of tropospheric BrO time-series for the Hudson Bay.

Quantity	Trend [units/year]	Error in trend	Trend percentage	Significant
Merged BrO VCD [molec/cm²] (Figure 3.21a)	+ 1.6×10^{11}	1.5×10^{11}	+ 0.88	No
January BrO VCD [molec/cm²] (Figure 3.21b)	+ 4.2×10^{11}	1.46×10^{11}	+ 1.24	Yes
February BrO VCD [molec/cm²] (Figure 3.21b)	+ 6.7×10^{11}	1.34×10^{11}	+ 2.43	Yes
March BrO VCD [molec/cm²] (Figure 3.21b)	+ 2.6×10^{11}	1.0×10^{11}	+ 0.81	Yes
April BrO VCD [molec/cm²] (Figure 3.21b)	+ 4.1×10^{11}	8.6×10^{10}	+ 1.40	Yes
May BrO VCD [molec/cm²] (Figure 3.21b)	+ 1.6×10^{11}	7.1×10^{10}	+ 0.69	Yes
June BrO VCD [molec/cm²] (Figure 3.21b)	- 2.7×10^{10}	5.4×10^{10}	- 0.02	No
July BrO VCD [molec/cm²] (Figure 3.21b)	- 1.6×10^{11}	3.8×10^{10}	- 2.22	Yes
August BrO VCD [molec/cm²] (Figure 3.21b)	- 2.1×10^{11}	3.2×10^{10}	- 2.63	Yes
September BrO VCD [molec/cm²] (Figure 3.21b)	- 1.4×10^{11}	4.0×10^{10}	- 1.68	Yes
October BrO VCD [molec/cm²] (Figure 3.21b)	+ 7.8×10^{10}	4.6×10^{10}	+ 0.69	No
November BrO VCD [molec/cm²] (Figure 3.21b)	+ 2.4×10^{11}	7.4×10^{10}	+ 1.26	Yes
December BrO VCD [molec/cm²] (Figure 3.21b)	+ 6.4×10^{11}	1.2×10^{11}	+ 3.57	Yes
Area of BrO plumes [km²] (Figure 3.21c)	+ 185	138.5	+ 0.59	No

The first significant difference compared to the Arctic region is that the entire merged tropospheric BrO VCD dataset (Figure 3.21a) has no significant trend (according to the significance test we performed). Although we see a slight increase of around 0.88% in the tropospheric BrO VCD, the error is quite large (1.5×10^{13} molecules/cm²/year). Strong trends appear over the winter months (with December being the highest, with an increase of 3.57% per year) and in April (with an increase of 1.4% per year). Another interesting difference to the Arctic trends is that July, August and September show significant negative trends above the Hudson Bay (with August being the strongest by absolute magnitude, with -2.63% per year). In

3. BrO Column Densities and Trends

the Arctic region, September had a significant positive trend. Finally, the areas of enhanced BrO plumes show here a non-significant trend, similarly to the Arctic region.

Similar to the Arctic, a trend heat map for the Hudson Bay (Figure 3.22) provides valuable insights about the dependency of the trend on the period for the tropospheric BrO VCD dataset. Since both seasons of interest show significant trends (winter and spring), we will provide separate trend heat maps for both of them in Figure 3.23 and Figure 3.24.

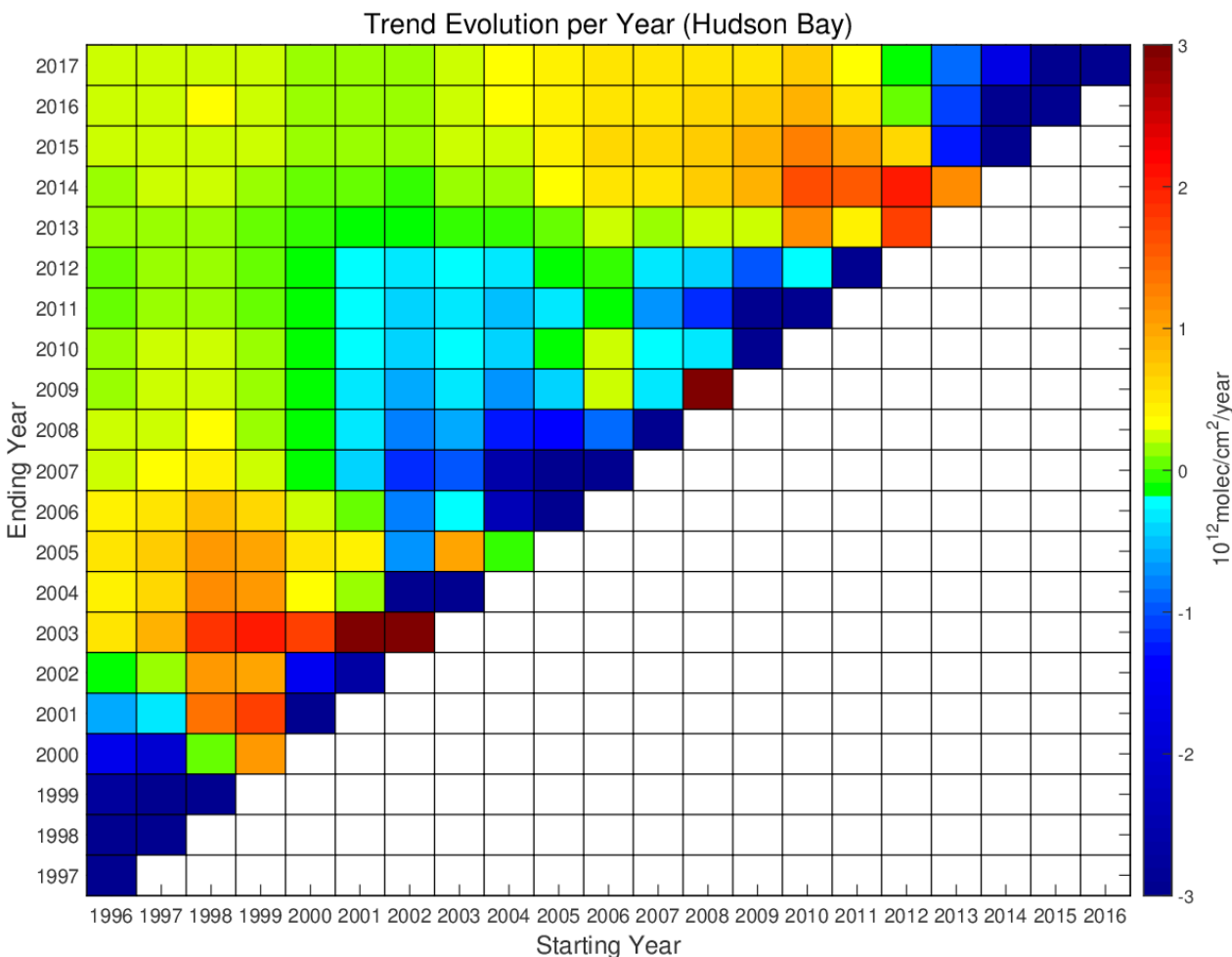


Figure 3.22: Linear trends of tropospheric BrO VCDs over different periods over the Hudson Bay. The x-axis shows the starting year, and the y-axis is the ending year of the period.

The x-axis denotes the starting year, while the y-axis is the ending year of the reference period of the corresponding trends. The color scale is the same for the two heat maps. There are positive trends when the ending year selected is one of the most recent years (as for the Arctic). However, more negative trends appear for shorter periods (e.g. starting in 2004 and ending in 2012). Every trend is calculated from the same starting and ending day of a year (i.e. start of February). The trends correspond to the data shown in Figure 3.21a. Trends covering short periods (i.e. from one year to another) are dominated by interannual variability.

The same heat maps for the seasons of interest (winter and spring) are valuable and yield meaningful information. Figure 3.23 shows the trend evolution for the Hudson Bay during the winter months (i.e. December, January and February) only.

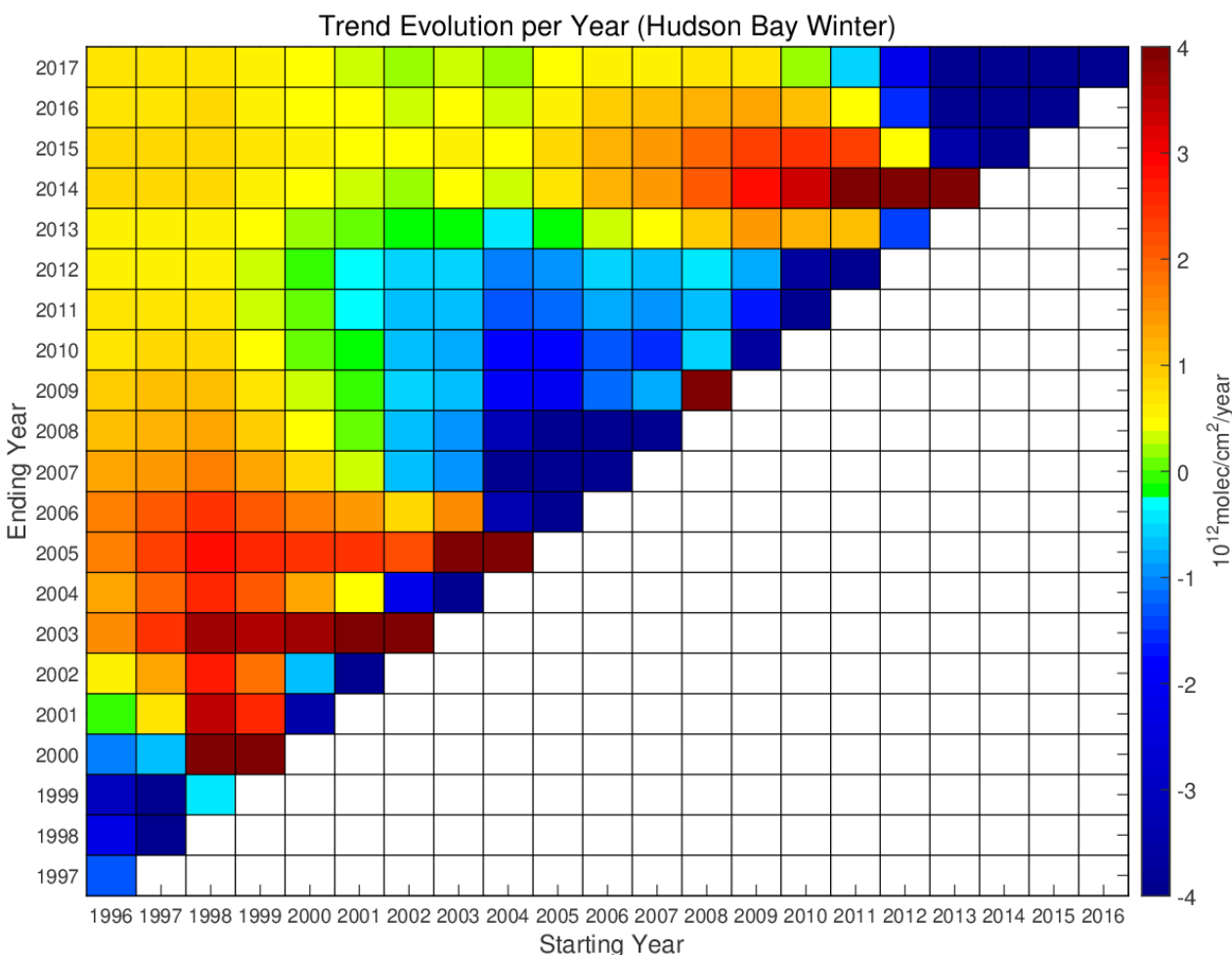


Figure 3.23: Linear trends of tropospheric BrO VCDs for the Hudson Bay over different periods based on data for winter only. The x-axis shows the starting year, and the y-axis is the ending year of the period.

The first difference between the total tropospheric BrO VCDs for the Hudson Bay (i.e. Figure 3.22) and the one for the winter months is that more robust trends (both positive and negative) are observed during winter. The two heat maps are similar, and trends that appear positive in the total tropospheric BrO VCD dataset appear positive also here (especially the long-term trends, i.e. ten years of duration). The winter months strongly influence the trend heat map (as we have seen from table 3.3, the most robust trends appear for winters for the Hudson Bay).

Figure 3.24 provides the trend heat map for the Hudson Bay during the spring months.

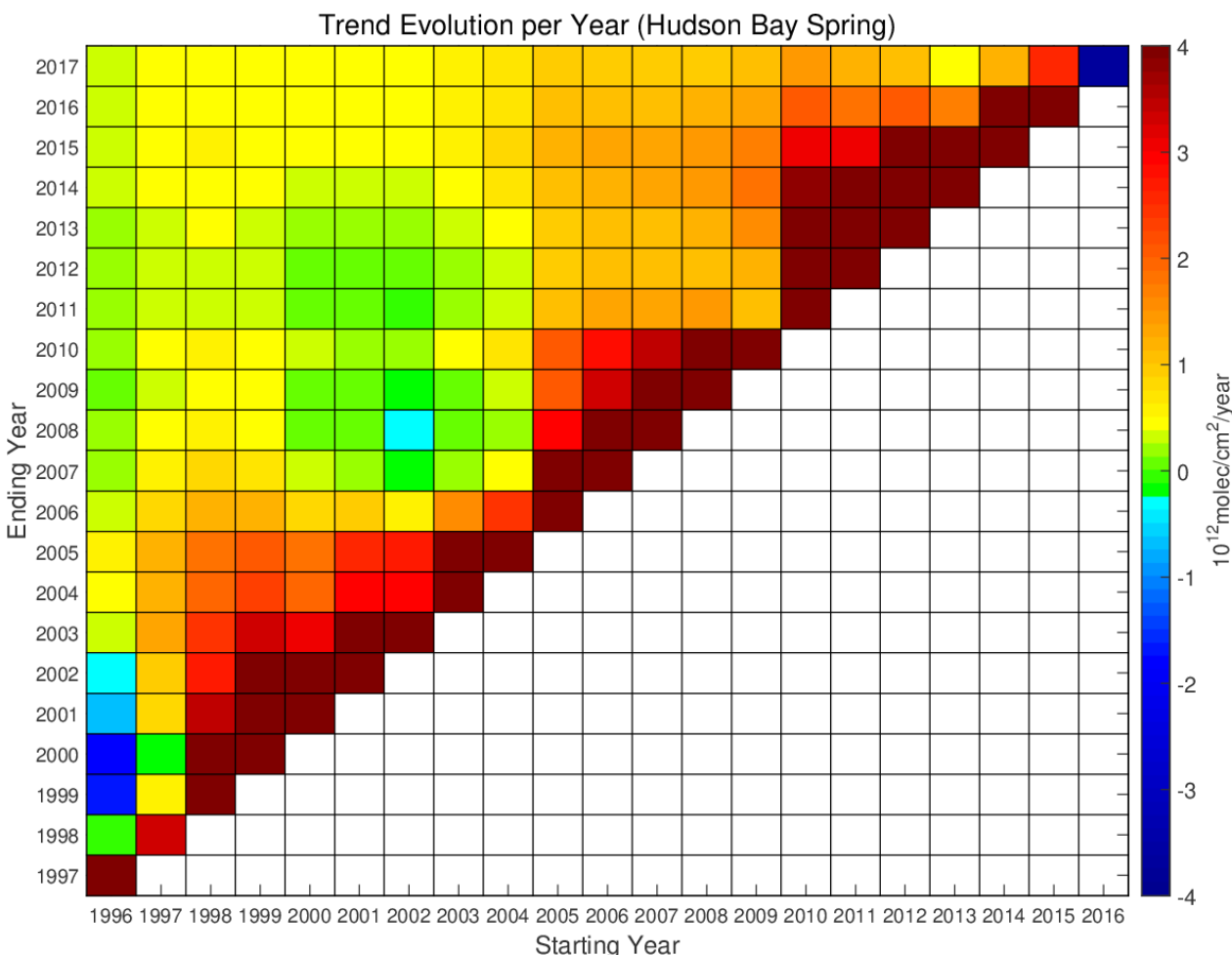


Figure 3.24: Linear trends of tropospheric BrO VCDs for the Hudson Bay over different periods based on data for spring only. The x-axis shows the starting year, and the y-axis is the ending year of the period.

The heat map differs from the one in Figure 3.23 in that primarily positive trends, with very few negative ones, are observed. The most robust positive trends are seen when the covered time-span is short (e.g. one year). These trends are dominated by seasonality. When focusing on long-term trends (i.e. starting from an early year and ending in one of the last years), positive trends, similar to the ones seen in Figures 3.22 and 3.23, are observed.

Figure 3.25 shows the trend analysis on the individual subsets of tropospheric BrO VCDs over the Hudson Bay for winter and spring, based on the magnitude of the tropospheric BrO VCD (i.e. above $7.0 \times 10^{13} \text{ molecules/cm}^2$, between $7.0 \times 10^{13} \text{ molecules/cm}^2$ and $3.0 \times 10^{13} \text{ molecules/cm}^2$ and below $3.0 \times 10^{13} \text{ molecules/cm}^2$):

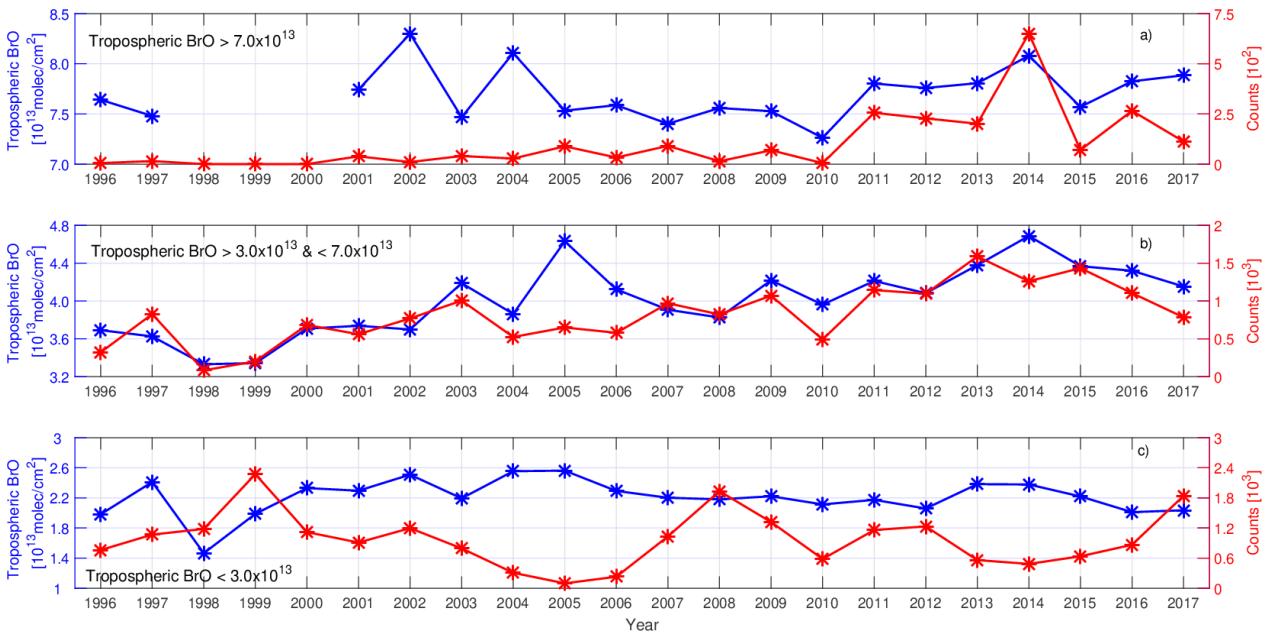


Figure 3.25: Subsets of the Hudson Bay winter tropospheric BrO dataset. a) tropospheric BrO VCDs above 7.0×10^{13} molecules/cm². b) tropospheric BrO VCDs between 3.0×10^{13} and 7.0×10^{13} molecules/cm². c) tropospheric BrO below 3.0×10^{13} molecules/cm². From 1998 to 2000 there were no scenes with tropospheric BrO above 7.0×10^{13} molecules/cm².

For tropospheric BrO VCD above 7.0×10^{13} molecules/cm², the average winter tropospheric BrO VCDs are slightly lower than those of polar springs for the Arctic region (Figure 3.18a). For three consecutive years (i.e. 1998 to 2000), there was no single grid cell with a value above 7.0×10^{13} molecules/cm². Although the magnitude of tropospheric BrO VCD seems to be stable with no significant trend, the number of observations has increased significantly since 2011. In Figure 3.25b, we see that both the magnitude of tropospheric BrO plumes between 3.0×10^{13} molecules/cm² and 7.0×10^{13} molecules/cm² and their counts increased over the years, while for Figure 3.25c (tropospheric BrO grid cells below 3.0×10^{13} molecules/cm²), neither the magnitude nor the counts show a strong trend. Table 3.4 shows the trends calculated (similarly to table 3.2).

3. BrO Column Densities and Trends

Table 3.4: Trends of the subsets of tropospheric BrO during winter months for the Hudson Bay.

Quantity	Trend [units/yea]	Error in trend [units/year]	Trend percentage	Significant
Tropospheric BrO > 7.0x10¹³ [molec/cm²]	+1.9x10 ¹¹	0.5x10 ¹¹	+ 0.24	Yes
Counts of tropospheric BrO > 7.0x10¹³	+13	5.4	+ 9.44	Yes
Tropospheric BrO > 3.0x10¹³ & < 7.0x10¹³ [molec/cm²]	+ 3.8x10 ¹¹	7.3x10 ¹⁰	+ 1.00	Yes
Counts of tropospheric BrO > 3.0x10¹³ & < 7.0x10¹³	+74.56	26.5	+ 6.1	Yes
Tropospheric BrO < 3.0x10¹³ [molec/cm²]	- 2.3x10 ¹⁰	6.2x10 ¹⁰	- 0.11	No
Counts of tropospheric BrO < 3.0x10¹³	-11.42	18.9	- 1.20	No

The trend for the magnitude of enhanced BrO VCDs above 7.0x10¹³ molecules/cm² is significant, but the increase per year is still small (+0.24%). The opposite occurs for the counts of enhanced BrO VCDs above 7.0x10¹³ molecules/cm², as there the increase is much more potent (+9.44% per year). A potential reason for this increase could be the spike in 2014 and the fact that 0 such grid cells occurred for some early years. For the second panel, positive and significant trends are seen, but moderate in magnitude (1.0% per year for the magnitude of the tropospheric BrO VVCD between 3.0x10¹³ molecules/cm² and 7.0x10¹³ molecules/cm² and +6.1% per year for the corresponding counts). Finally, we see negative but not significant trends for the trends appearing on the subset with tropospheric BrO VCD below 3.0x10¹³ molecules/cm².

The analysis of tropospheric BrO VCD for the spring months for the Hudson Bay and the corresponding time-series are shown in Figure 3.26.

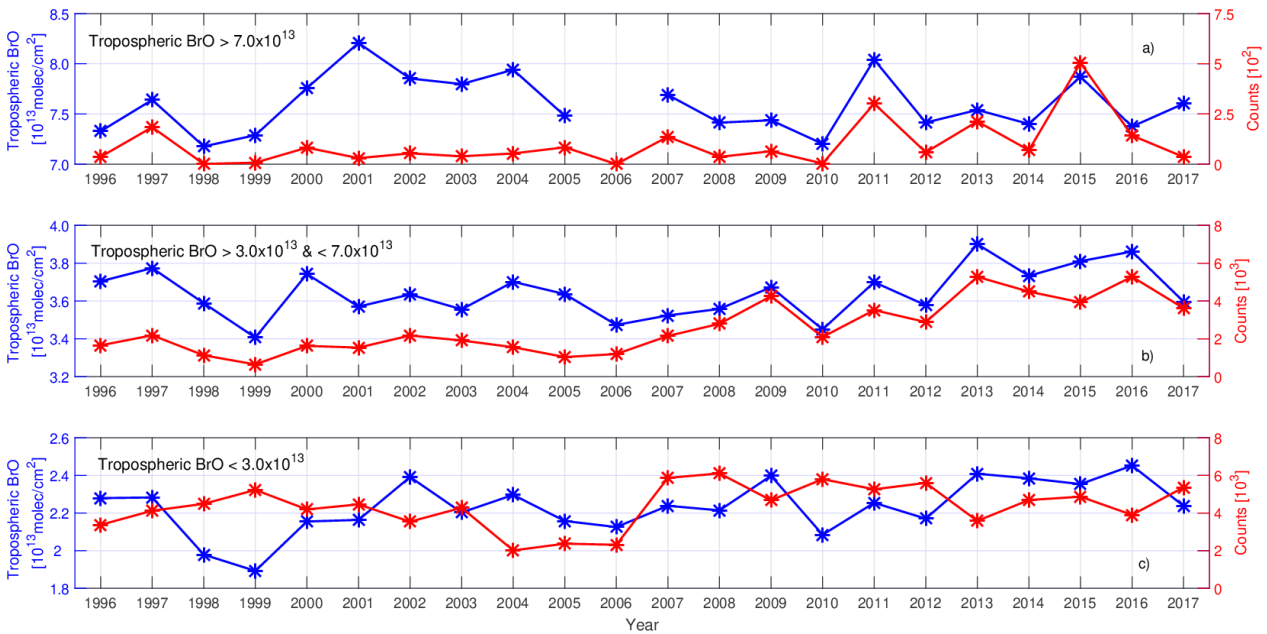


Figure 3.26: Subsets of the Hudson Bay spring tropospheric BrO dataset. a) tropospheric BrO VCDs above 7.0×10^{13} molecules/cm². b) tropospheric BrO VCDs between 3.0×10^{13} and 7.0×10^{13} molecules/cm². c) tropospheric BrO below 3.0×10^{13} molecules/cm². For 2006 there were no scenes with tropospheric BrO above 7.0×10^{13} molecules/cm².

For values of tropospheric BrO VCD above 7.0×10^{13} molecules/cm², the behaviour is similar to that in the winter months: no visible trend for the magnitude of the enhanced tropospheric BrO VCD is observed, while the number of observations has increased. In 2006, not a single grid cell of tropospheric BrO VCD above 7.0×10^{13} molecules/cm² occurred. The same conclusions are made for the subset of tropospheric BrO VCD between 3.0×10^{13} molecules/cm² and 7.0×10^{13} molecules/cm²: both their magnitude and counts increase over time, although a prevalence of higher magnitudes over the first years of the dataset is observed. The magnitude and the number of observations of tropospheric BrO VCDs below 3.0×10^{13} molecules/cm² do not seem to change over time.

Table 3.5 summarizes the trends appearing in Figure 3.26:

3. BrO Column Densities and Trends

Table 3.5: Trends of the subsets of tropospheric BrO during spring months for the Hudson Bay.

Quantity	Trend [units/yea	Error in trend [units/year]	Trend percentage	Significant
Tropospheric BrO > 7.0x10¹³ [molec/cm²]	- 2.5x10 ¹⁰	6.6x10 ¹⁰	- 0.03	No
Counts of tropospheric BrO > 7.0x10¹³	+ 4	3.8	+ 0.99	No
Tropospheric BrO > 3.0x10¹³ & < 7.0x10¹³ [molec/cm²]	+ 5.8x10 ¹¹	6.3x10 ¹⁰	+ 0.15	Yes
Counts of tropospheric BrO > 3.0x10¹³ & < 7.0x10¹³	+ 167	30.7	+ 6.5	Yes
Tropospheric BrO < 3.0x10¹³ [molec/cm²]	+ 1.0x10 ¹¹	4.6x10 ¹⁰	+ 0.44	Yes
Counts of tropospheric BrO < 3.0x10¹³	+ 55.37	35.53	+ 1.37	No

The magnitude of the enhanced tropospheric BrO VCD above 7.0x10¹³ molecules/cm² during spring has decreased. The number of observations has increased, but the trend is not significant (only four counts per year). Nevertheless, both trends are not significant. We infer significant but not robust in magnitude trends for the columns between 3.0x10¹³ molecules/cm² and 7.0x10¹³ molecules/cm², as the magnitude increased by 0.15% per year, while their counts 6.5% per year. In the last subset, we see that only the trend of the magnitude of tropospheric BrO VCD below 3.0x10¹³ molecules/cm² is significant (with a 0.44% increase per year), while the equivalent counts do not increase in a significant way (+1.37% per year). Overall, we see that the trends appearing over the winter months are more substantial than those over springs for the Hudson Bay region (higher trend values and more cases being significant).

In Figures 3.27 and Figure 3.28, pixel trend maps for the Hudson Bay region, during winter and spring months, similar to Figure 3.20 for the Arctic, are shown.

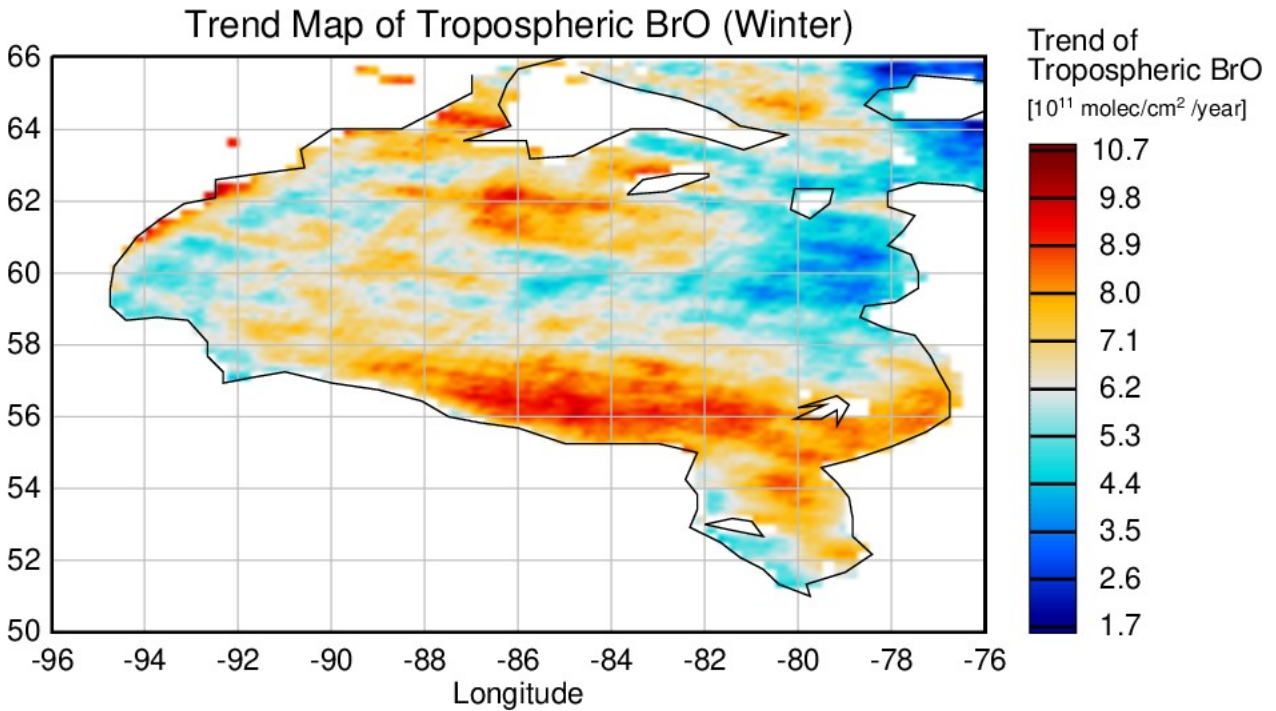


Figure 3.27: Spatial trend map of tropospheric BrO VCDs during winter months over the Hudson Bay.

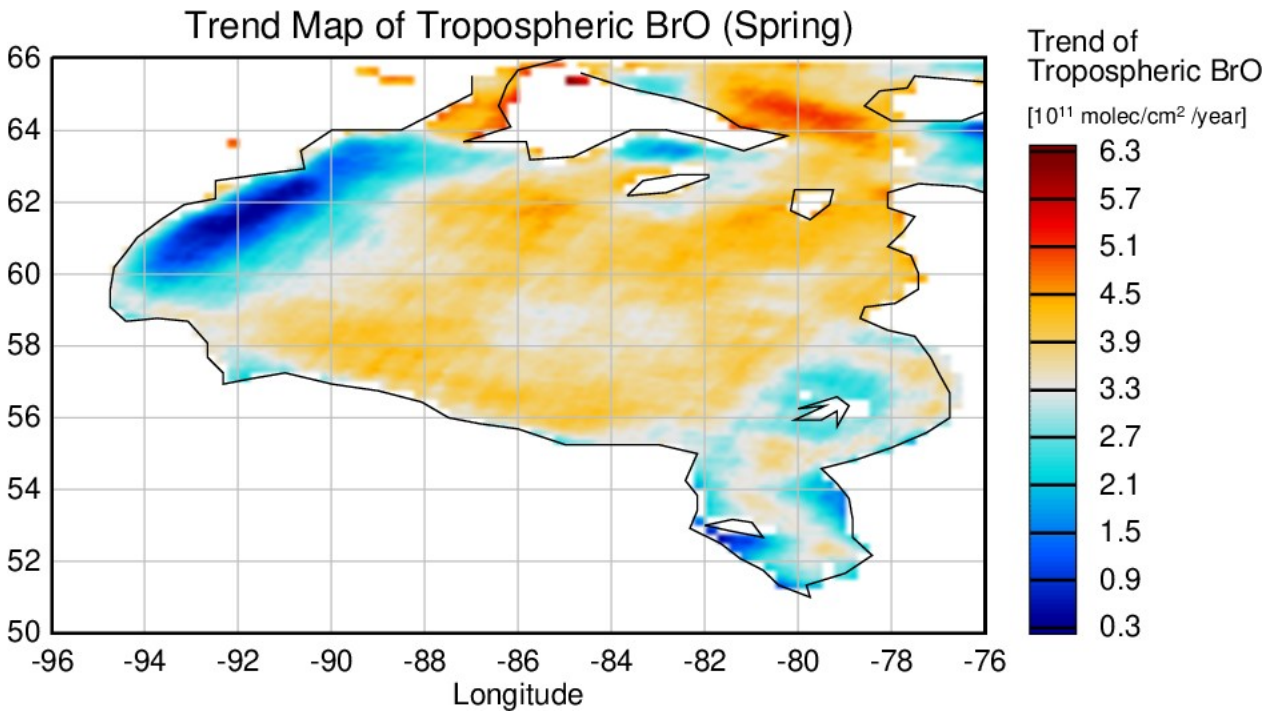


Figure 3.28: Spatial trend map of tropospheric BrO VCDs during spring months over the Hudson Bay.

A substantial increase of tropospheric BrO VCDs during winter for the Hudson Bay is observed. This increase is not uniformly distributed, as there are some areas, especially in the south of the Bay, where the increase is more pronounced. However, in contrast to the Arctic region, there is no single grid cell where the trend is negative. The same conclusion is drawn

from the trend map over the spring months. Although the increase here is weaker (and there is an area on the north-west of the Bay, where the trend is not robust), only increasing trends of tropospheric BrO VCD are seen, in contrast to the Arctic (Figure 3.20), where areas with negative trends of tropospheric BrO VCDs are showed.

3.4 Summary and Discussion

A unique long-term tropospheric BrO dataset was developed, using observations from four UV-VIS satellite instruments, providing information on the evolution of tropospheric BrO plumes for the Arctic region and the Hudson Bay. Hollwedel et al. (2004) studied total BrO VCD and derived six years of BrO data from the GOME instrument. Hörmann et al. (2016) derived a ten year tropospheric BrO dataset from two satellite instruments (OMI and GOME-2A), but for a different region (Rann of Kutch). The consistency of BrO VCD in the overlapping periods of the sensors was assessed and showed satisfactory agreement. The correlation coefficients were between 0.9 and 0.97 for the geometric columns, 0.79 to 0.94 for the tropospheric columns in the Arctic and 0.9 to 0.93 for the geometric and 0.88 to 0.89 for the tropospheric columns in the Hudson Bay. This good agreement in the tropospheric BrO VCDs from the different sensors was a prerequisite for investigating trends.

An increase of approximately 1.0% per year is estimated for the merged tropospheric BrO VCD for the Arctic region (70.0° N to 85.0° N). The increase is pronounced during polar spring, where it reaches 1.5% per year. The enhanced tropospheric BrO plumes (i.e. with magnitude above 7.0×10^{13} molecules/cm²) have not increased significantly, while the corresponding number of grid boxes did (about 3.3% per year). From a spatial trend analysis, the most robust increase in tropospheric BrO VCD appears to be in the Fram Strait, while the most substantial decrease is observed over the Barents and Karas seas.

For Hudson Bay, a significant change for the merged tropospheric BrO VCD is not observed. However, strong trends appear during the winter and spring months (the seasons when bromine explosions are expected). More specifically, an upward trend of 3.57% per year for December and 1.40% per year for April are the most robust monthly positive trends for these two seasons. A further trend investigation revealed that both the magnitude (trend of +0.24% per year) of enhanced tropospheric BrO VCD with magnitude above 7.0×10^{13} molecules/cm² and their number of observations (+9.44% per year) have increased for the winter months, while for springs neither the magnitude nor the counts of enhanced tropospheric BrO VCD have drastically changed. For the subset with tropospheric BrO VCD between 3.0×10^{13} molecules/cm² and 7.0×10^{13} molecules/cm², an increase is observed (+0.15% per year for the magnitude and + 6.5% per year for the corresponding counts). Finally, from the investigation of the trend maps of the Hudson Bay, we conclude that tropospheric BrO columns have increased all over the Bay for both seasons (with the increase being more pronounced during winter, especially in the south of the Bay).

Figure 3.29 summarizes the trends discussed in this chapter:

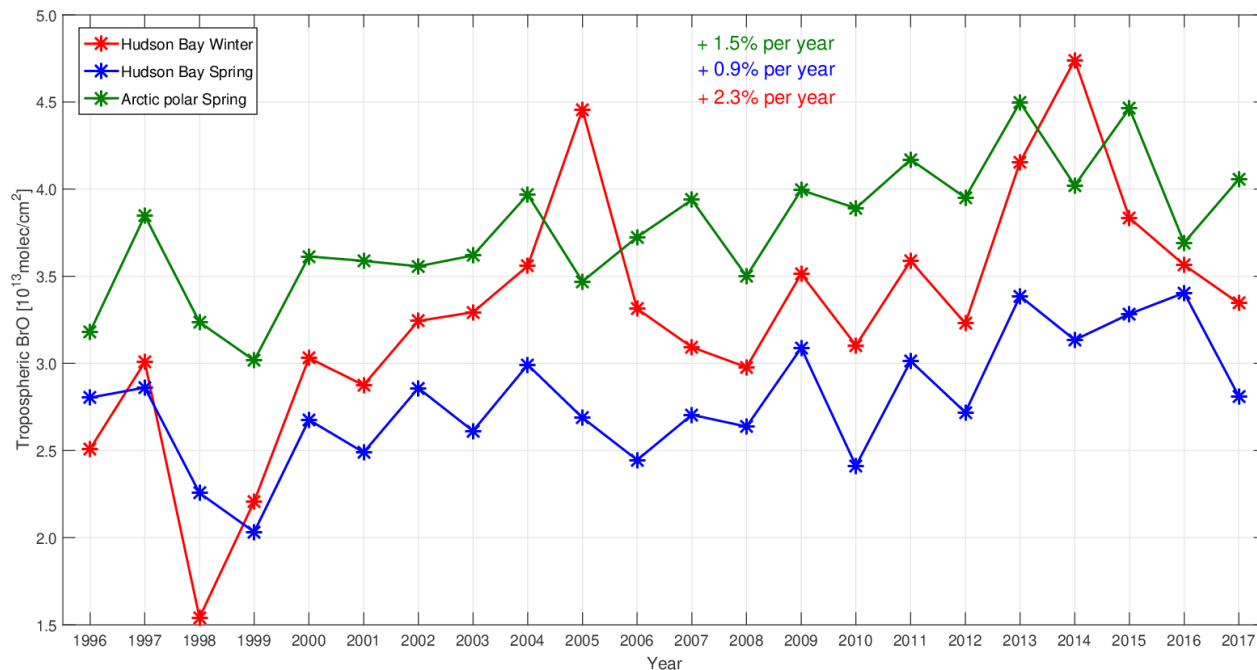


Figure 3.29: Summary of the trends of tropospheric BrO VCDs presented in the chapter. All trends are calculated on a daily basis. The Arctic polar spring curve is based on Figure 3.15b, while the Hudson Bay Winter and Spring in Figure 3.21b.

4. THE RELATIONSHIP BETWEEN TROPOSPHERIC BRO VCD, SEA ICE AND METEOROLOGICAL CONDITIONS

As discussed in chapter 1, it is well known from the literature that sea ice is the primary platform for the release of bromine molecules into the atmosphere (Wagner et al., 2001). Several studies have reported that specific meteorological parameters and conditions act as driving mechanisms and enhance, transport and recycle BrO (Blechschmidt et al., 2016; Jones et al., 2009). In this chapter, the results presented in chapter 3 (the time-series, maps and trends of tropospheric BrO VCDs for the Arctic and the Hudson Bay) are combined and linked to sea ice conditions and meteorological driving mechanisms. Significant changes in tropospheric BrO VCD occurred during polar springs in the Arctic region and winter and spring for the Hudson Bay. Consequently, the tropospheric BrO VCD and their dependence on external parameters will be investigated. Each parameter will have a dedicated subchapter, while the comparisons will be held for both the Arctic and the Hudson Bay. Sea ice age, sea ice thickness and cyclonic activity information are available for the Arctic region. For every parameter, time-series, maps, scatter plots, and pixel trend maps will be presented. Each parameter will be related to enhanced tropospheric BrO VCDs (i.e. above 7.0×10^{13} molecules/cm²). For the sea ice age, an individual sub-chapter is dedicated to the process of flagging. This is required to identify sea ice covered scenes. The essential parameters for enhanced BrO formation are identified at the end of the chapter.

4.1 Relationship of Tropospheric BrO VCD and Sea Ice Age

Sea ice age is a parameter of critical importance, as sea ice is considered the primary platform for the release of bromine molecules (Wagner et al., 2001). The sea ice dataset selected is available for the same period as the retrieved BrO VCDs, for the Arctic region, but not for the Hudson Bay (Tschudi, M. and Univ Of CO, 2019). Before proceeding to the relationship between sea ice age and trends in tropospheric BrO VCD, the procedure to flag the BrO dataset was followed.

4.1.1 Sea Ice Flagging

4. The Relationship between Tropospheric BrO VCD, Sea Ice and Meteorological Conditions

The advantage of measuring the trends in tropospheric BrO VCD over snow and ice is that the surface reflectivity is high. This does result in the exclusive of some scenes where bromine explosions occur, e.g. in the Canadian Archipelago. However, the identification of sea ice and the determination of trends of tropospheric BrO VCD are considered to be more accurate than in mixed surfaces. This flagging was applied already in the trend section discussed in chapter 3. In order to perform the flagging, the corresponding daily sea ice coverage map was spatially and temporally interpolated to the BrO VCDs satellite retrievals. Afterwards, only the scenes where we had information on sea ice coverage were selected for the analysis. This was applied daily, both on the maps and the time-series. Figure 4.1 shows an example of a daily tropospheric BrO map, before and after the flagging, together with the corresponding sea ice age daily map:

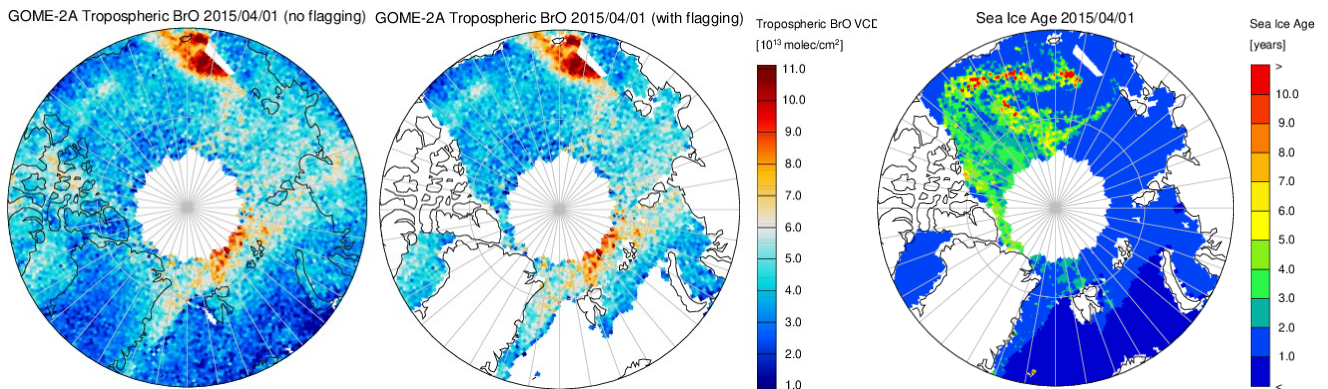


Figure 4.1: An example of sea ice flagging on tropospheric BrO VCDs maps. From left to right: a) A daily tropospheric BrO VCD map as seen from GOME-2A (01.04.2015), without sea ice flagging, b) the same day, but with the application of sea ice flagging, c) the corresponding sea ice age map for the same day.

Open water scenes (denoted by dark blue on Figure 4.1c) and all land scenes were excluded by the flagging. The same procedure was followed for the sea ice age so that these scenes were excluded from that dataset. The tropospheric BrO VCD used for all geophysical conclusions and interpretations included knowledge of the sea ice age. Figure 4.2 shows the daily sea ice extent for the Arctic, which was included in the sea ice dataset, together with the flagged tropospheric BrO dataset, per instrument and merged.

4. The Relationship between Tropospheric BrO VCD, Sea Ice and Meteorological Conditions

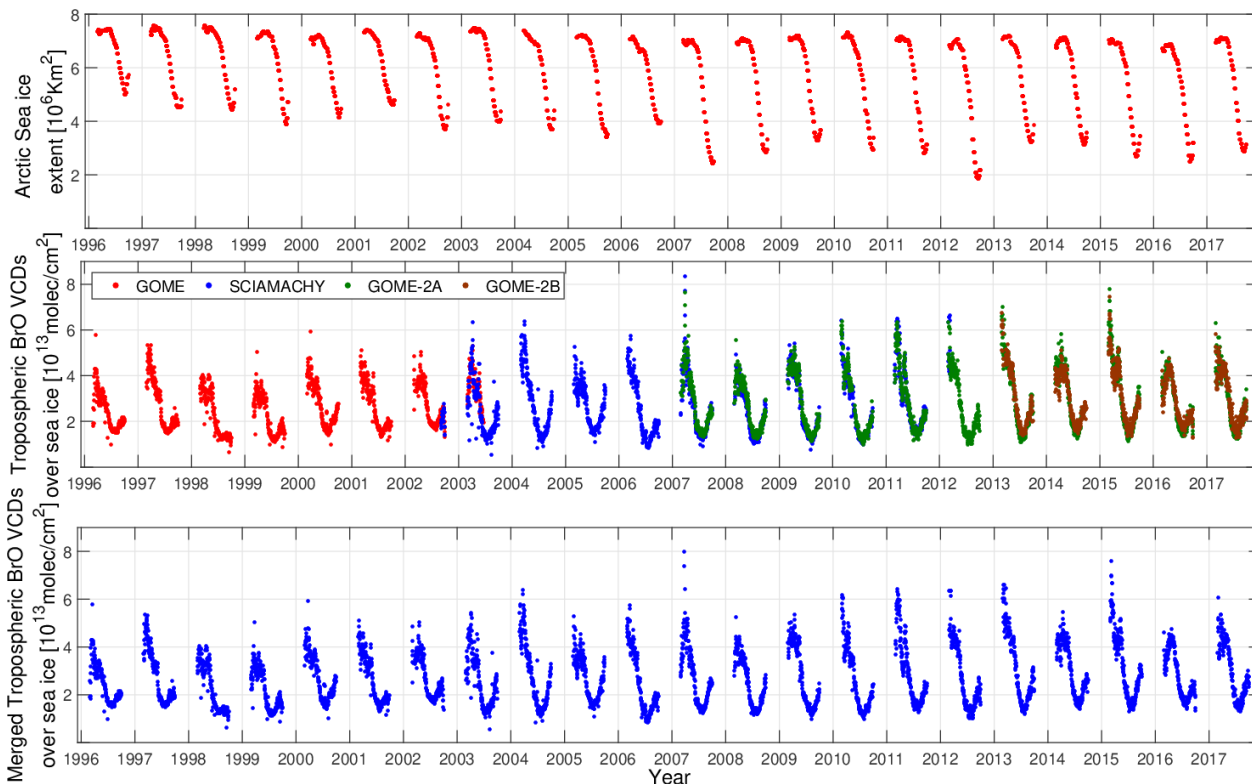


Figure 4.2: From top to bottom: a) Daily sea ice extent for the Arctic region (in 10^6 km^2), b) same as in Figure 3.3c, but flagged for scenes with sea ice coverage, c) the merged sea ice flagged tropospheric BrO VCDs dataset.

In Figure 4.2a, there are two minima in the sea ice extent time-series for the Arctic, which occurred in 2007 and 2012, respectively. The merged tropospheric BrO VCDs dataset over sea ice (Figure 4.2c) is used for all the geophysical analyses in this study and was already shown and discussed in chapter 3.

4.1.2 Arctic Region (70.0° N to 85.0° N)

The first relationship investigated is that between tropospheric BrO VCD and sea ice age. More specifically, the first year sea ice is of interest, as it is saltier than multi-year sea ice. It includes potentially more liquid brine and frost flowers (and therefore favours the release of bromine molecules into the atmosphere). From literature, the sea ice extent is decreasing in the Arctic (as shown in Figure 4.2a), and the extent of first year ice is increasing. This is due to the appearance of open water regions during the summer months when the temperature is high, and the sun is present. After September, when the temperature decreases and the sun slowly disappears, the open water regions transform into first year ice. This process repeats itself every year. The polar spring average time-series of tropospheric BrO over sea ice, together with the first year extent, and the corresponding daily scatter plot is shown in Figure 4.3. The areas with tropospheric BrO VCD exceeding the threshold of $7.0 \times 10^{13} \text{ molecules/cm}^2$, together with the extent of first year ice and the corresponding scatter plot, are also displayed:

4. The Relationship between Tropospheric BrO VCD, Sea Ice and Meteorological Conditions

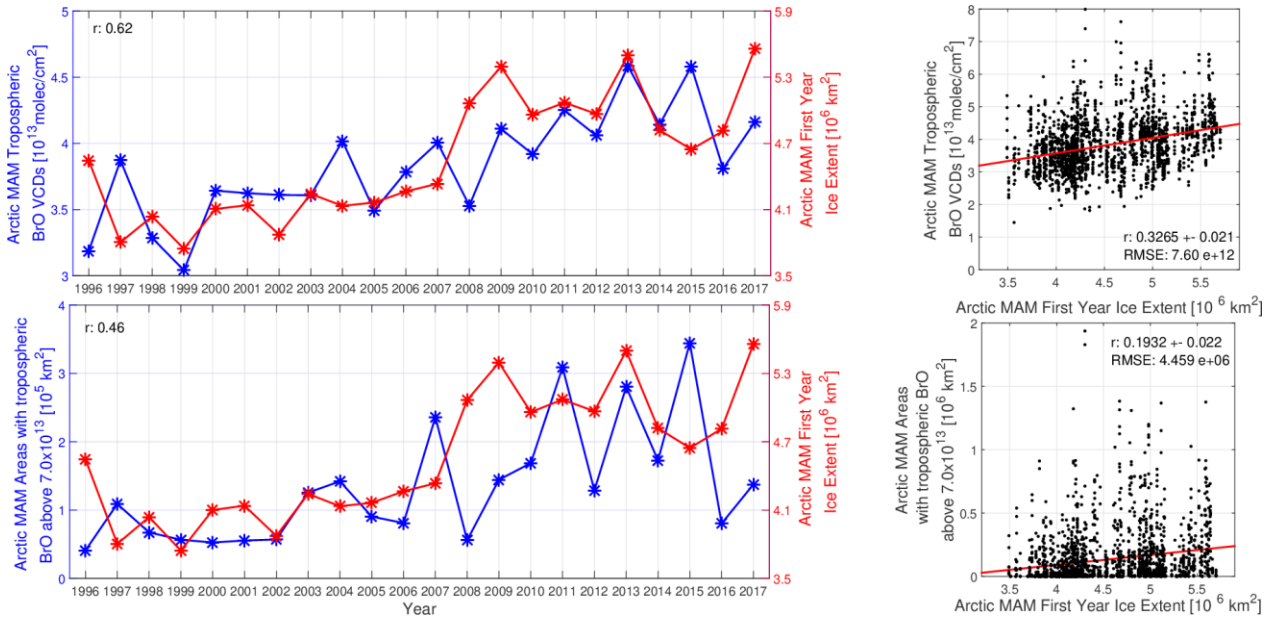


Figure 4.3: Relationship of tropospheric BrO to first year ice extent. Top left: polar spring average time-series of tropospheric BrO VCDs over sea ice and first year sea ice extent. Top right: daily polar spring scatter plot between tropospheric BrO VCDs over sea ice and first year sea ice extent. Bottom left: polar spring average time-series of areas where tropospheric BrO VCDs over sea ice exceeded the threshold of 7.0×10^{13} molecules/cm² and first year sea ice extent. Bottom right: daily polar spring scatter plot between areas where tropospheric BrO VCDs over sea ice exceeded the threshold of 7.0×10^{13} molecules/cm² and first year sea ice extent.

The red curves in the time-series of Figure 4.3 are the polar spring average of first year sea ice extent. The average polar spring tropospheric BrO VCDs are plotted in blue. There is an explicit long-term general agreement between the two quantities (with a +0.62 correlation coefficient). Although the agreement is not visible every year (e.g. in 2008, tropospheric BrO VCDs decreased, while the first year ice extent increased), there is a similar long-term evolution, especially from 2009 onwards. By checking the corresponding daily scatter plot of the two quantities (top right subplot), we get a moderate correlation coefficient of +0.32. However, it should be stated that sea ice extent does not change on a daily basis. The sea ice age dataset used is based on a weekly basis. In the bottom left time-series, the blue quantity is the area having tropospheric BrO VCDs above the threshold of 7.0×10^{13} molecules/cm². Here, the agreement is not as straightforward as in the comparison above. This finding is confirmed by the weak correlation coefficient (i.e. +0.19) of the corresponding scatter plot (bottom right subplot).

Although the extent of first year ice is the most valuable parameter to compare to, to investigate the relationship of tropospheric BrO VCD to first year sea ice, comparisons with the sea ice age are also of value. Figure 4.4 is similar to Figure 4.3, but we have substituted the extent of first year ice with average sea ice age:

4. The Relationship between Tropospheric BrO VCD, Sea Ice and Meteorological Conditions

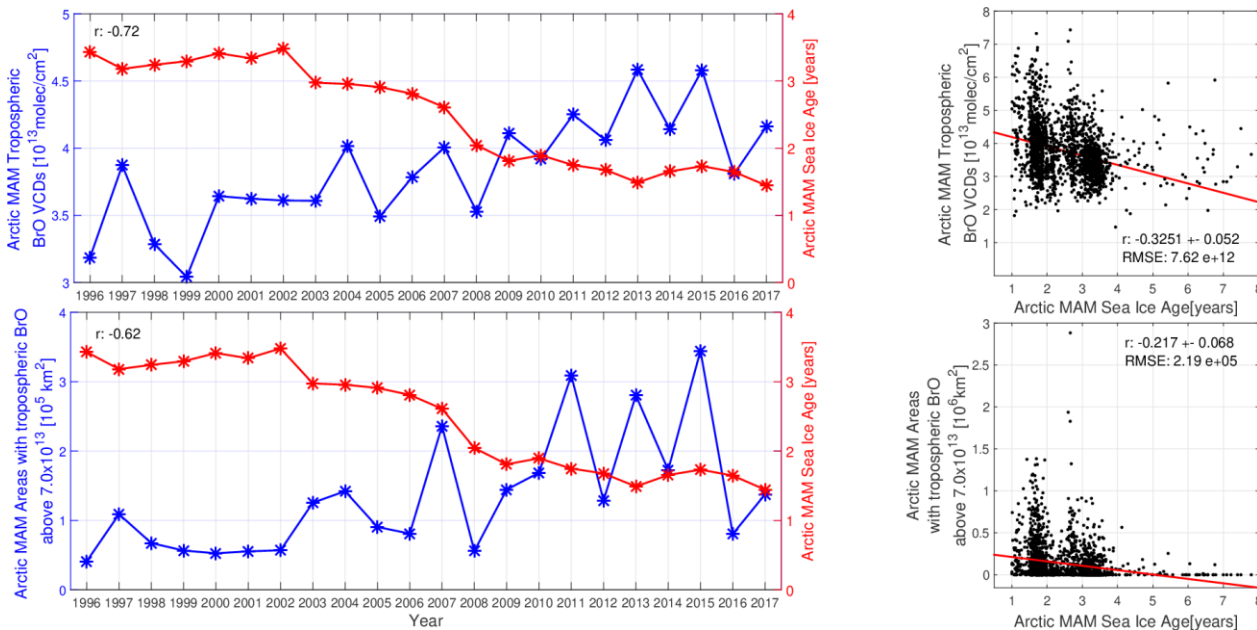


Figure 4.4: Relation of tropospheric BrO to sea ice age. Top left: polar spring average time-series of tropospheric BrO VCDs over sea ice and sea ice age. Top right: daily polar spring scatter plot between tropospheric BrO VCDs over sea ice and sea ice age. Bottom left: polar spring average time-series of areas where tropospheric BrO VCDs over sea ice exceeded the threshold of 7.0×10^{13} molecules/cm² and sea ice age. Bottom right: daily polar spring scatter plot between areas where tropospheric BrO VCDs over sea ice exceeded the threshold of 7.0×10^{13} molecules/cm² and sea ice age.

The general long-term agreement also holds for the time-series between polar spring averaged tropospheric BrO VCDs, and polar spring averaged sea ice age. Since 2009, all the tropospheric BrO VCDs have had a higher value than all the previous years, while after 2009, the sea ice age is the lowest to be reported, compared to the previous years. The correlation coefficient for the time-series is -0.72, slightly higher in absolute magnitude than the one between tropospheric BrO and first year ice extent. The top left scatter plot also shows a similar relationship, with a correlation coefficient of approximately -0.32. The highest daily averaged tropospheric BrO VCDs occur when the daily average sea ice age is between 1 and 2 years. Regarding the relationship between areas of enhanced tropospheric BrO VCD and sea ice age, a slightly higher absolute correlation (-0.62 for the time-series and -0.22 in bottom right subplot) compared to first year ice extent is observed (+0.46 for the time-series and +0.19 for the daily scatter plot). There is a long-term relationship between the increase of tropospheric BrO VCDs and the increase of first year sea ice extent (or consequently the decrease of the average sea ice age in the Arctic region). However, the average sea ice age decrease implies a decrease of the multi-year ice age (e.g. old ice that melted during one polar spring-summer and now became two or more years old, but less than the initiate age).

In Figure 4.5 and Figure 4.6, the relationship of first year sea ice extent and sea ice age to only enhanced tropospheric BrO scenes is investigated (i.e. scenes with a BrO column above 7.0×10^{13} molecules/cm²):

4. The Relationship between Tropospheric BrO VCD, Sea Ice and Meteorological Conditions

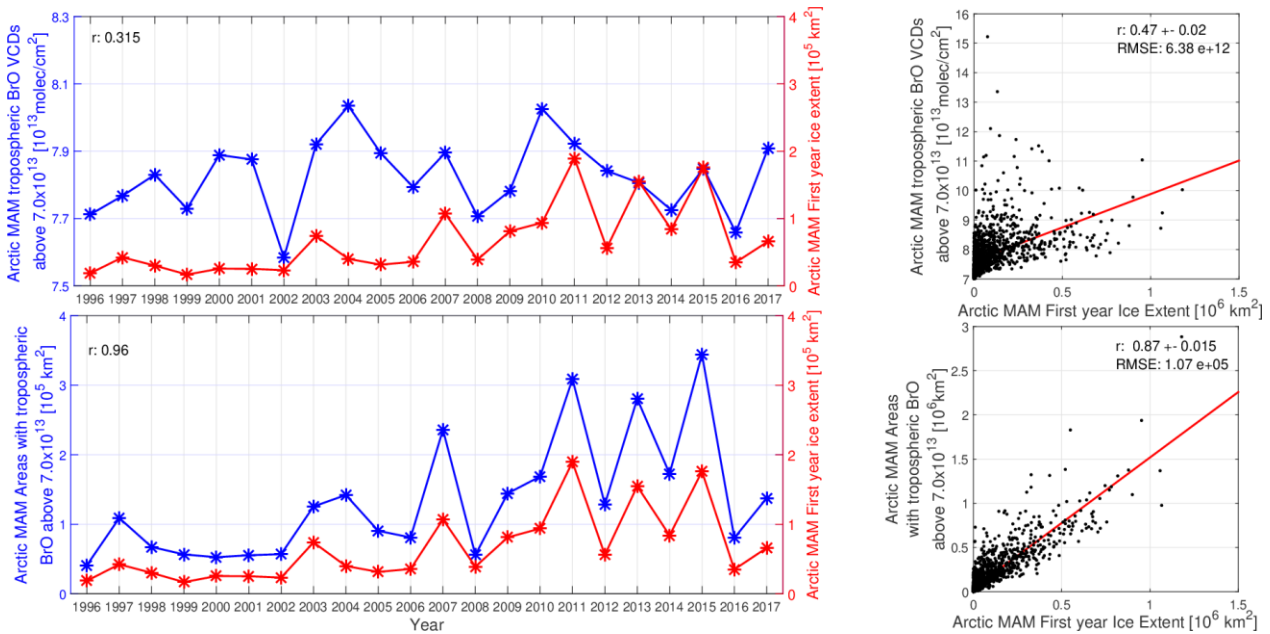


Figure 4.5: Same as Figure 4.3, but only for enhanced tropospheric BrO scenes (above 7.0×10^{13} molecules/cm²).

Although we see that the long-term agreement between enhanced tropospheric BrO VCD and the increase of first year ice extent is not as strong as the one for all tropospheric BrO columns (i.e. +0.315 compared to +0.62 for the top left time-series of Figure 4.3), the corresponding daily correlation improved (+0.47 to +0.32). This could imply that the increase of first year ice extent affects the daily release of enhanced bromine, but not its evolution (which does not show a significant trend, as discussed in Figure 3.18 and Table 3.2). However, as it seems, the bigger the first year ice extent is, the bigger the platform for a potential release of bromine in the Arctic atmosphere. This argument can also be assessed by the bottom left time-series, where the area with enhanced tropospheric BrO VCD is shown by the blue curve, while the area with enhanced tropospheric BrO and first year ice is shown by the red curve. We see that the two curves have almost identical evolution, with a correlation coefficient of +0.96, which can be seen from the corresponding (i.e. bottom right) scatter plot (correlation coefficient of +0.87). These results indicate that the first year ice does not play the most crucial role in the eventual magnitude of the tropospheric BrO VCDs, but is crucial for the number of incidents of high BrO that we will have and the area they will capture. As first year ice becomes more dominant in the Arctic, there is more potential for the release of bromine molecules, which can lead to more bromine explosion events.

In Figure 4.6, a similar comparison of enhanced tropospheric BrO, but this time to the averaged sea ice age and not to the first year ice extent, is shown:

4. The Relationship between Tropospheric BrO VCD, Sea Ice and Meteorological Conditions

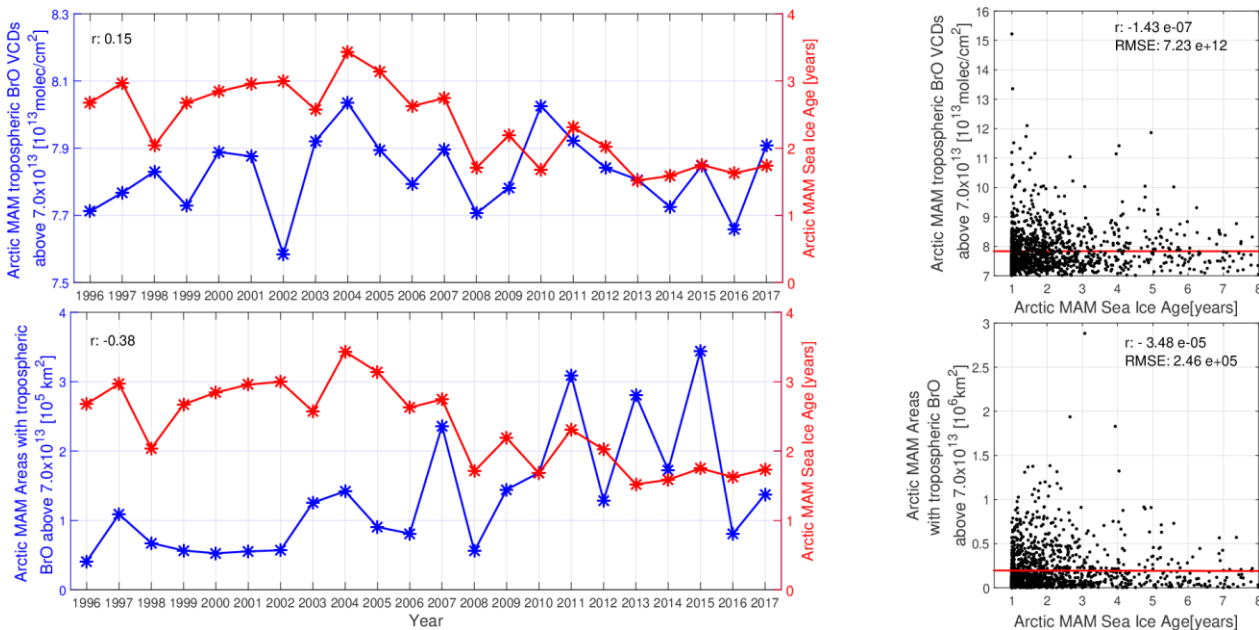


Figure 4.6: Same as Figure 4.3, but only for enhanced tropospheric BrO scenes (above 7.0×10^{13} molecules/cm²).

Significant correlations are not observed in either of the subplots. Sea ice age also decreases for the scenes where tropospheric BrO VCD is above 7.0×10^{13} molecules/cm², but this cannot lead to any solid scientific conclusions, as the averaged decrease of sea ice age implies a decrease of the multi-year ice age, but not necessarily an increase of first year ice.

As the sea ice age dataset is weekly, it is valuable to perform the investigations discussed above on weekly scatter plots. More specifically, the plot consists of the weekly tropospheric BrO VCDs and weekly first year ice extent; weekly tropospheric BrO VCDs and weekly averaged sea ice age; enhanced (above 7.0×10^{13} molecules/cm²) tropospheric BrO VCDs and the corresponding (selected only the equivalent scenes) weekly first year ice extent, and finally enhanced (above 7.0×10^{13} molecules/cm²) tropospheric BrO VCDs, and the corresponding (selected only the equivalent scenes) averaged sea ice age:

4. The Relationship between Tropospheric BrO VCD, Sea Ice and Meteorological Conditions

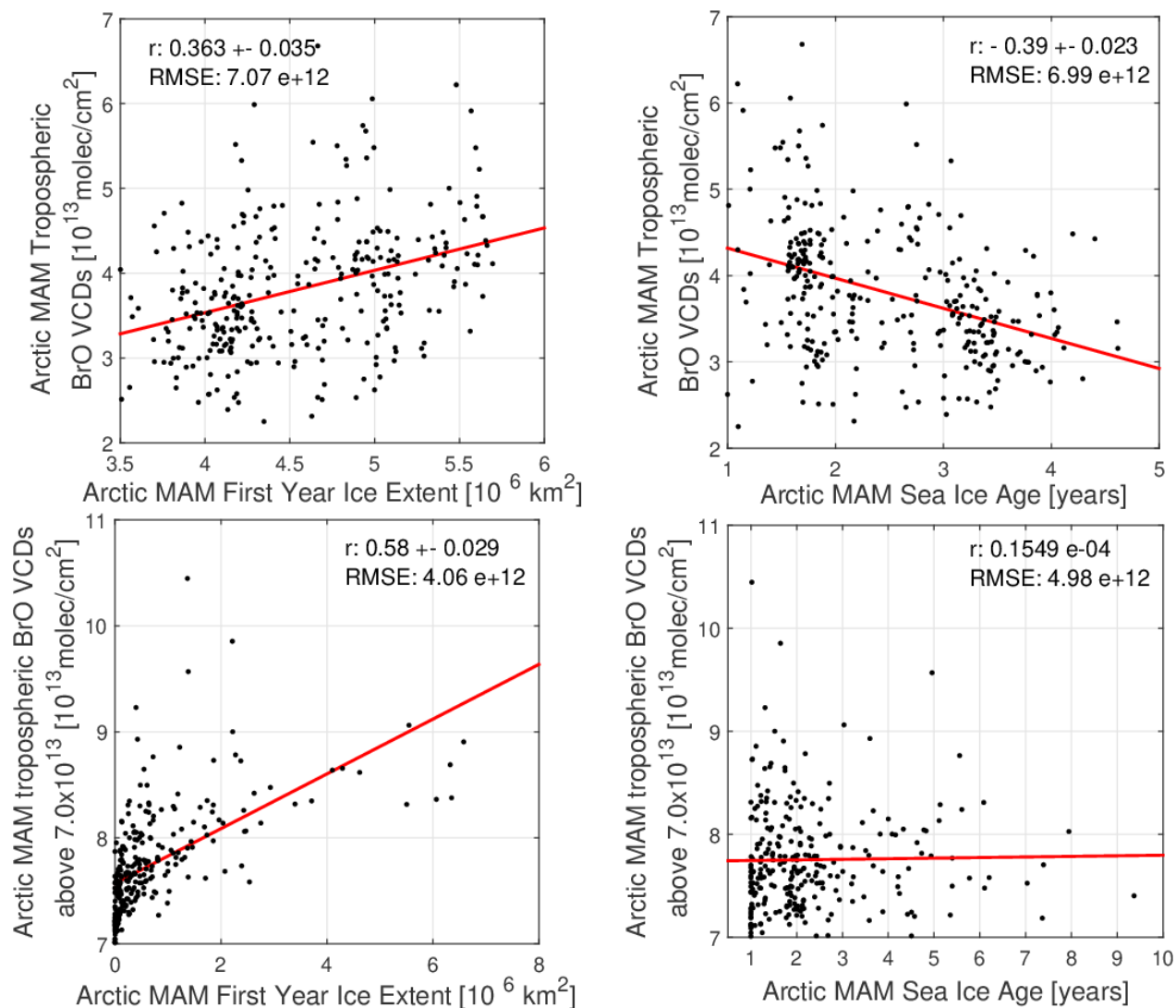
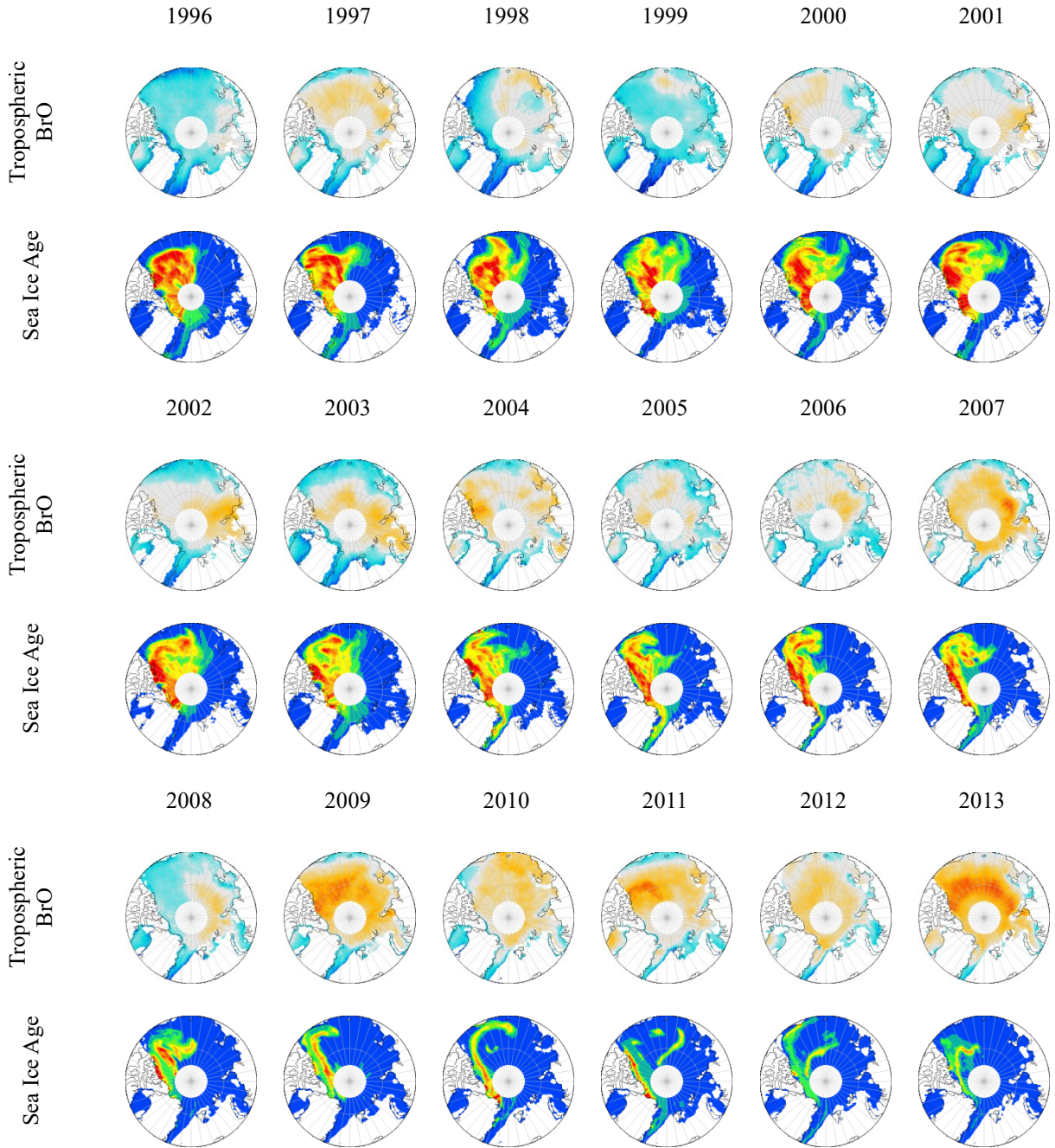


Figure 4.7: Scatter plots of weekly time-series between tropospheric BrO VCDs and sea ice age. Top left: weekly tropospheric BrO VCDs against weekly first year ice extent. Top right: weekly tropospheric BrO VCDs against weekly averaged sea ice age. Bottom left: enhanced (above 7.0×10^{13} molecules/cm 2) tropospheric BrO VCDs against the corresponding (selected only the equivalent scenes) weekly first year ice extent. Bottom right: enhanced (above 7.0×10^{13} molecules/cm 2) tropospheric BrO VCDs against the corresponding (selected only the equivalent scenes) averaged sea ice age. The best fitting line is plotted in every scatter plot.

A comparison of the top row of Figure 4.7 with Figure 4.3 (top right scatter plot) and Figure 4.4 (top right scatter plot) indicates that there are no differences between the daily and the weekly plots. The same conclusion can be drawn when the bottom row of Figure 4.7 is compared with the equivalent daily scatter plots (top right scatter plot of Figure 4.5 and top right of Figure 4.6). In total, the correlation coefficients improve, but not to a great extent. As the original sea ice dataset is weekly, weekly averages for the tropospheric BrO VCD are used. As the tropospheric BrO VCD is more dynamic than sea ice, it may be that some critical information is lost by averaging it on a weekly basis.

4. The Relationship between Tropospheric BrO VCD, Sea Ice and Meteorological Conditions

In Figure 4.8, yearly polar spring average maps of tropospheric BrO VCDs and sea ice age are shown. The first year ice is shown in dark blue color, so that it is easily distinguishable from the rest of the sea ice age values:



4. The Relationship between Tropospheric BrO VCD, Sea Ice and Meteorological Conditions

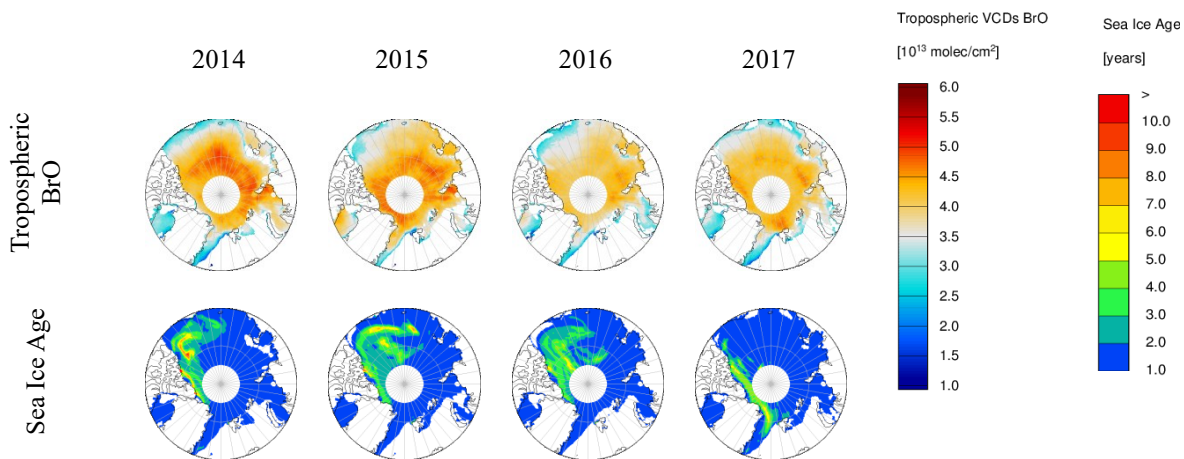


Figure 4.8: Polar spring average maps of tropospheric BrO VCDs [10^{13} molec/cm²] and sea ice age [years]. First year ice is denoted with dark blue color.

It is expected that high tropospheric BrO VCDs would appear over first year ice regions. Such a case appears, for example, in 2001, where the most enhanced tropospheric BrO VCD appears over Kara – East Siberian Sea, where first year sea ice was also evident. However, there are also cases, such as 2004, when high tropospheric BrO VCD appeared over the Canadian Archipelago, a region where multi-year ice is almost always found. However, first year ice seems to be associated with the increased frequency of enhanced tropospheric BrO VCD rather than with the magnitude of tropospheric BrO VCD. This implies that the increase of the first year sea ice covered regions (which started approximately from 2009 onwards) comes in general agreement with the increased area of high tropospheric BrO VCD regions. Although there were some years before 2009 (e.g. 2003), where high tropospheric BrO VCD was evident almost everywhere in the Arctic region, from 2009 onwards, for almost every year, the regions with enhanced tropospheric BrO VCD have increased and cover a much broader area, extending from the American to the European Arctic. In the same period, we can observe that first year ice has become more dominant in the Arctic, covering larger regions, while multi-year ice coverage has decreased mainly over the Canadian Archipelago. This implies that this increase in the extent of first year ice regions over the latest years impacts the increased appearance and frequency of enhanced tropospheric BrO VCDs.

Another way to investigate the evolution and relationship of the two quantities is to plot trend maps of tropospheric BrO (as in Figure 3.20) and corresponding trend maps of sea ice.

4. The Relationship between Tropospheric BrO VCD, Sea Ice and Meteorological Conditions

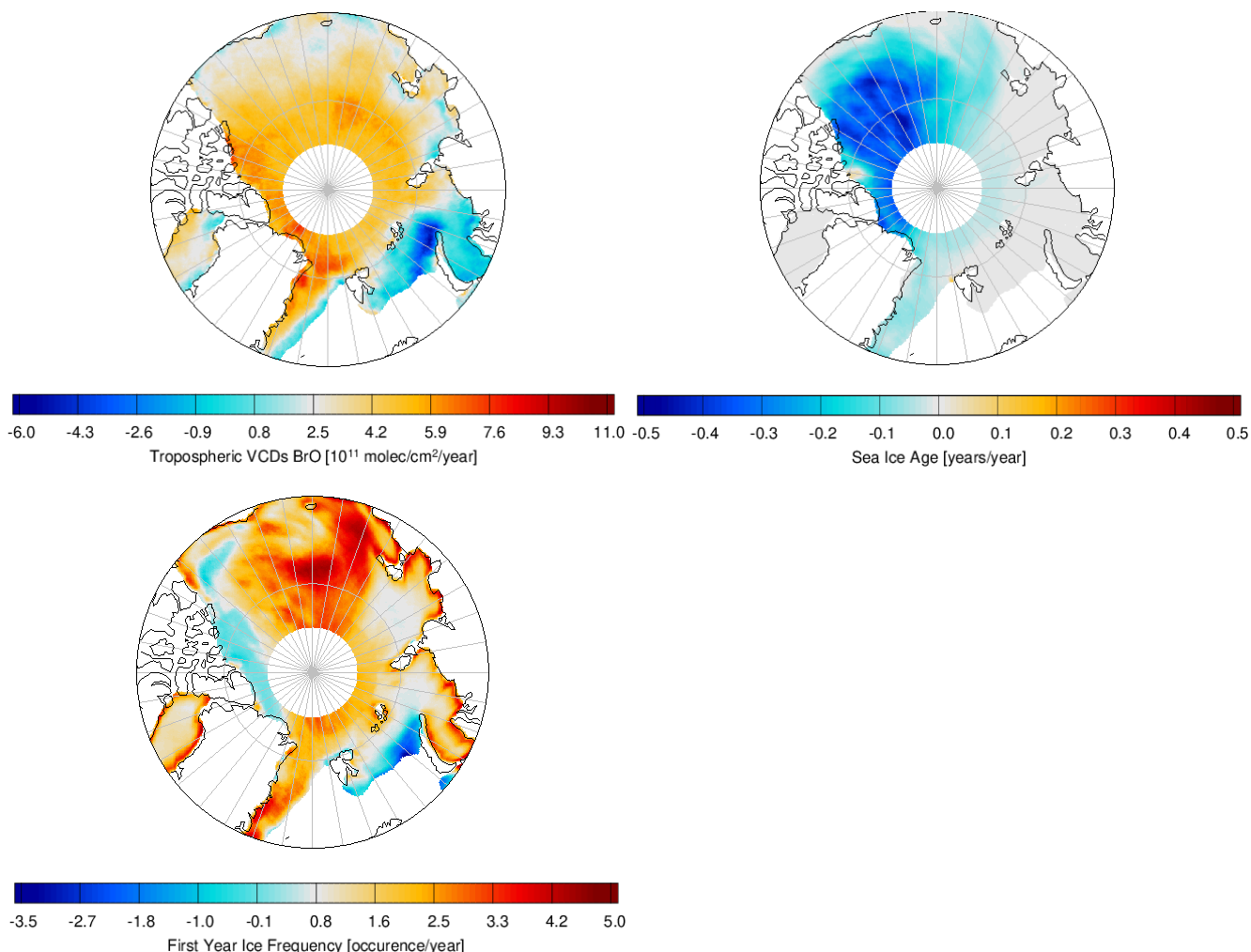


Figure 4.9: Pixel trend maps of tropospheric BrO VCDs (top left), sea ice age (top right) and first year ice frequency (bottom left).

The top left trend map is the same as that in Figure 3.20. By studying the sea ice age trend map, we see that the most significant decrease in sea ice age is observed over the Canadian Archipelago and Alaska, where multi-year ice was dominant over the first years of the dataset and has severely declined over the latest years. However, a decrease of sea ice age over the Fram Strait and the north of Greenland is found, where the most robust increase of tropospheric BrO VCDs occurs. If these findings are combined with the trend map of first year ice occurrence, an increase to the east of Greenland of first year ice over the latest years is observed. Therefore, the decrease of the sea ice age agrees with an increase of first year ice occurrence, which played a role in the increase of tropospheric BrO VCDs in the same region. However, the same cannot be said for the area north of Greenland and over Canada, where there is a sea ice age decrease and a decrease of first year ice. This is the region where multi-year ice has retreated recently, as it can also be seen in the individual yearly polar spring average sea ice age maps in Figure 4.8.

4.2 Relationship of Tropospheric BrO VCD and Air Temperature

As mentioned in chapter 1, it was shown, both in laboratory experiments and field campaigns, that there is a relationship between temperature and the speed of the autocatalytic chemical reaction cycle that recycles BrO in the troposphere. More specifically, once the temperature is high enough, the cycle halts. For air temperature, two datasets are used: ERA-5 and WRF ASR-2, which were described in chapter 2. WRF ASR-2 provides model simulations optimised explicitly for the Arctic region. For air temperature and all the following meteorological parameters, tropospheric BrO VCD time-series, scatter plots, polar spring average maps, trend maps, enhanced tropospheric BrO time-series and scatter plots to the corresponding data of each parameter will be compared.

4.2.1 Arctic Region (70.0° N to 85.0° N)

Air temperature is increasing at a rapid pace in the Arctic region. This increase is believed to have serious consequences for the Arctic ecosystem. It also affects the atmospheric chemistry and the trace gases appearing in it. The anti-correlation between temperature and BrO is well known. Therefore, it is expected that there will be some relationship between the two quantities. The first plot shows polar spring average time-series between tropospheric BrO VCDs and 2m air temperature from ERA-5 and ASR-2; one for all scenes and one where enhanced BrO (above 7.0×10^{13} molecules/cm²) occurred, together with the corresponding daily scatter plots from ERA-5 (as this reanalysis dataset covers the period of the tropospheric BrO dataset, i.e. 1996 – 2017).

4. The Relationship between Tropospheric BrO VCD, Sea Ice and Meteorological Conditions

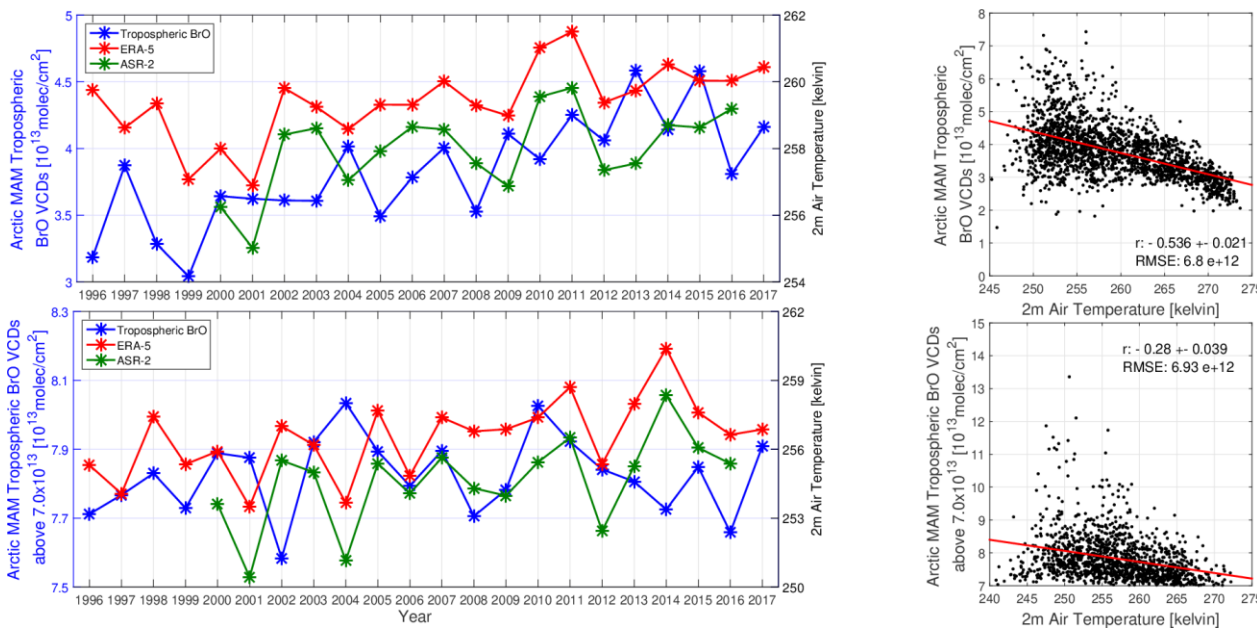


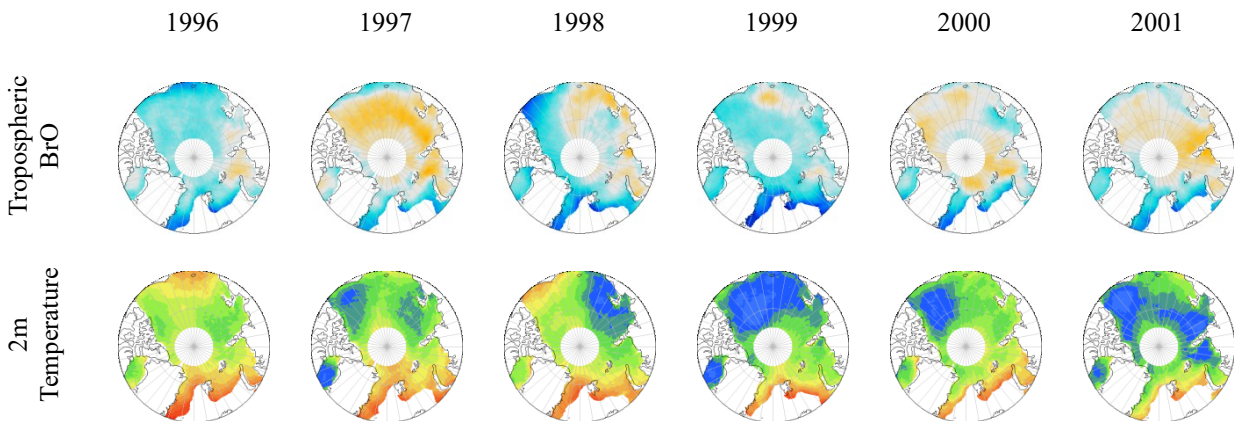
Figure 4.10: Time-series and scatter plots of tropospheric BrO VCDs and 2m air temperature. Top left: Polar spring averaged time-series of tropospheric BrO VCDs and 2m air temperature from reanalysis data. Top right: The corresponding daily scatter plot of tropospheric BrO (blue curve in the time-series) and ERA-5 2m air temperature (the red one). Bottom left: Polar spring averaged time-series of enhanced tropospheric BrO VCDs (above 7.0×10^{13} molecules/cm²) and 2m air temperature for the corresponding areas from reanalysis data. Bottom right: The corresponding daily scatter plot of enhanced tropospheric BrO (above 7.0×10^{13} molecules/cm², blue curve in the time-series) and ERA-5 2m air temperature (the red one).

ASR-2 only provides data from 2000 to 2016. This is also why ERA-5 was chosen for the scatter plots. The top left time-series in Figure 4.10 shows an anti-correlation between tropospheric BrO VCD and air temperature. There are some years, for example, from 1998 to 1999 or from 2010 to 2011, where the expected anti-correlation is not seen as both quantities increase or decrease together. Since air temperature is more dynamic and changes from day to day, it is expected that the polar spring yearly averaged time-series will provide a generalized image of the relationship between the two quantities and will not be able to capture correlations occurring on more minor time scales. The correlation coefficient between tropospheric BrO and ERA-5 2m air temperature in the time-series plot is +0.48, which does not depict the proper relationship between them (as it has a positive sign). When we focus on the corresponding scatter plot (top right) between tropospheric BrO VCD and ERA-5, we see that the correlation increases by absolute number and has a value of -0.536. This is much stronger than the correlation between tropospheric BrO VCD and sea ice on a daily basis (+0.325), indicating that air temperature is a more critical parameter on a daily basis. However, the interpretation of scatter plots and their relationships requires care, as there are hidden indirect correlations between tropospheric BrO VCD and other quantities included. For instance, as temperature increases, sea ice also melts, and that means a smaller area for a potential release of reactive bromine molecules into the Arctic atmosphere in the later years. Nevertheless, the information drawn from the scatter plot is

4. The Relationship between Tropospheric BrO VCD, Sea Ice and Meteorological Conditions

valuable and meaningful. The scatter plots do not include spatial correlations, as they show daily averages. We can also infer from the scatter plot an extensive range of tropospheric BrO VCD for temperatures below 260 Kelvin. However, as long as the temperature exceeds approximately this threshold, we see that tropospheric BrO VCD drop significantly, as only three daily averages exist with a temperature above 260 Kelvin and tropospheric BrO VCD above 5.0×10^{13} molecules/cm². The opposite does not necessarily apply (i.e. we see high and low BrO columns for low temperatures). By looking at the bottom subplots (i.e. only selected scenes with enhanced tropospheric BrO VCD above 7.0×10^{13} molecules/cm²), we see a general anti-correlation in the polar spring averaged time-series between tropospheric BrO VCD and temperature. There are some exceptions, for example, from 2009 to 2010, where both quantities increased. However, if we study the corresponding scatter plot, a smaller correlation coefficient than the one with all observations (-0.28 against -0.536) is inferred. This implies that temperature is not the most decisive parameter for forming enhanced BrO plumes (for comparison, the equivalent correlation coefficient between enhanced BrO and first year ice extent was + 0.47, from Figure 4.5). Therefore, one could conclude that first year ice extent plays a more critical role in the appearance of enhanced BrO plumes than air temperature (which, as it seems, matters on a “threshold” basis and halts the autocatalytic chemical cycle if it is too high, but does not accelerate it in the opposite case).

In Figure 4.11, and similar to Figure 4.8, yearly polar spring average maps of tropospheric BrO VCDs and 2m air temperature from ERA-5 are presented.



4. The Relationship between Tropospheric BrO VCD, Sea Ice and Meteorological Conditions

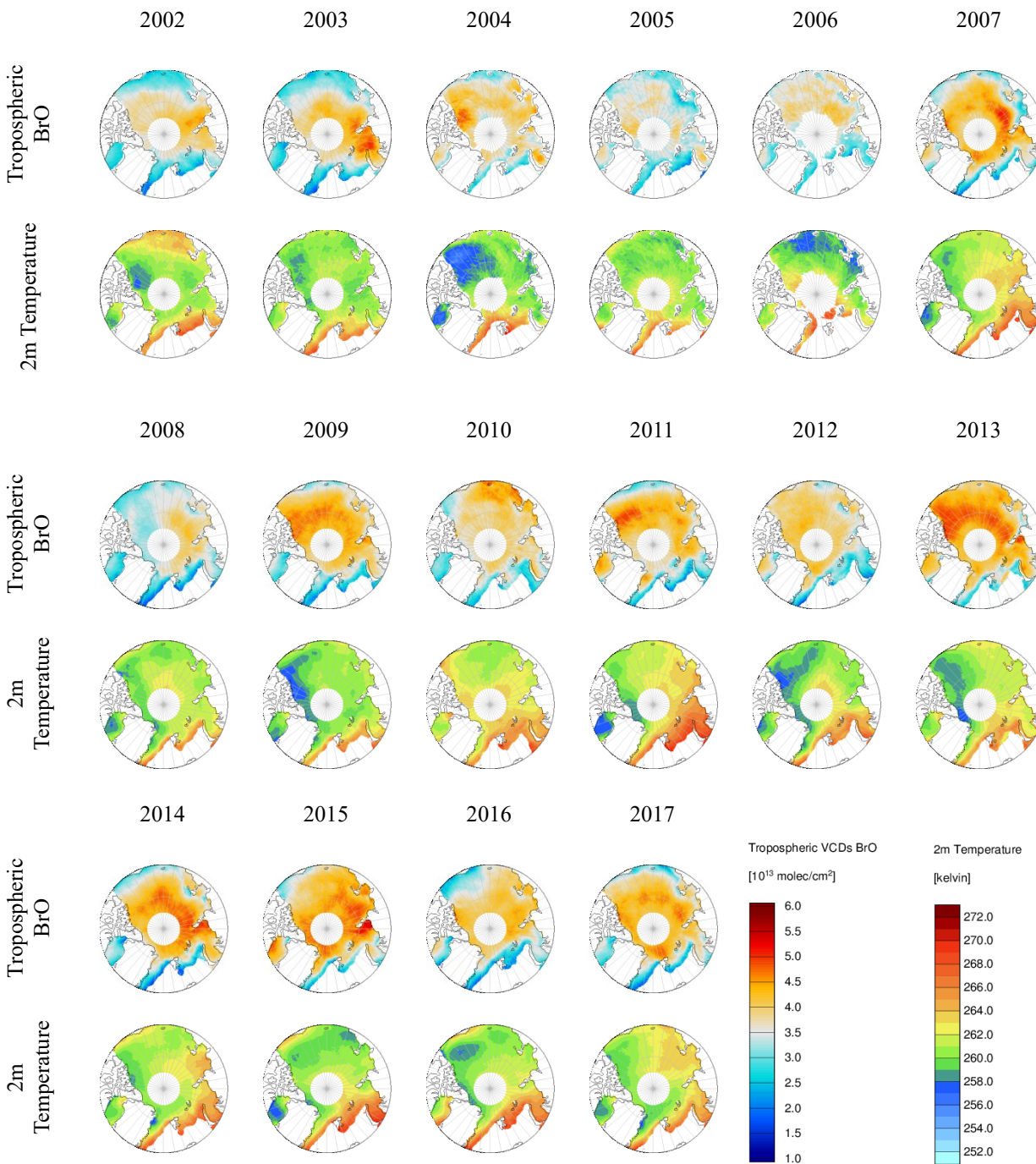


Figure 4.11: Polar spring average maps of tropospheric BrO VCDs [molec/cm^2] and ERA-5 2m air temperature [kelvin].

There are years when the highest BrO VCDs occurred at the lowest temperature (or low temperature, for example, 2004, 2001 and 1999), but this relationship does not appear in all years (especially the latest). However, long-term averages may not be the best way to compare a dynamic meteorological parameter as temperature to tropospheric BrO VCD. As the lower the

temperature does not necessarily imply the higher the BrO, the relationship between the two quantities is difficult to interpret. There are years (i.e. 2011 and 2013) where tropospheric BrO VCD appears over areas with widespread temperatures (i.e. from 258 to 265 Kelvin). However, we can see that tropospheric BrO is usually low when the temperature is high (e.g. 2002 on Beaufort and the East Siberian Sea).

In Figure 4.12, pixel trend maps of temperature (from ERA-5) and that of tropospheric BrO VCD are plotted:

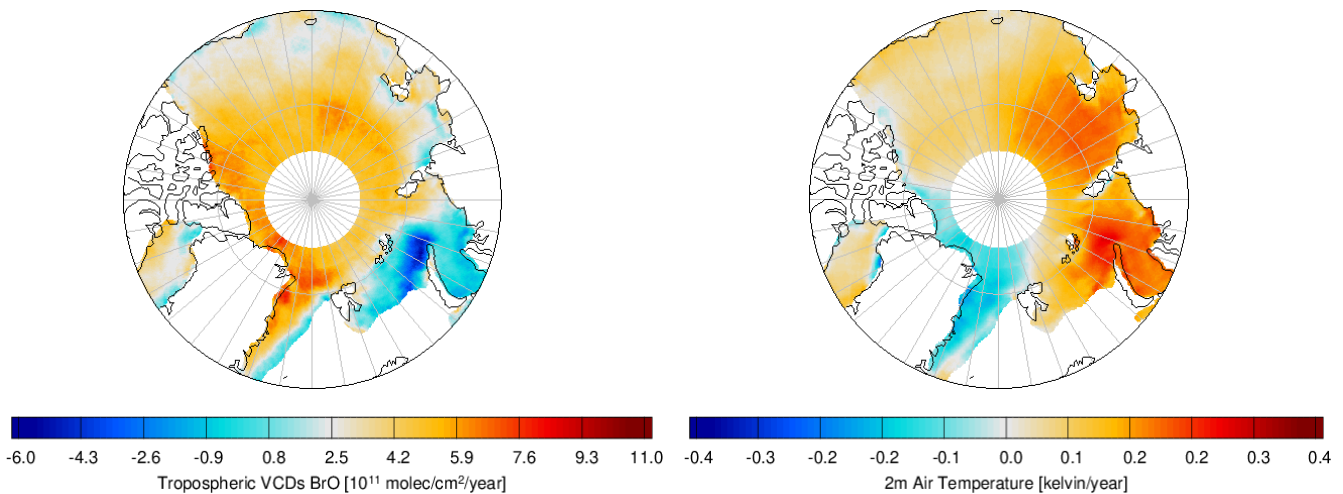


Figure 4.12: Spatial trend patterns of tropospheric BrO (left) and ERA-5 2m air temperature (right).

From this comparison, the evolution of tropospheric BrO VCDs in each grid box is in an excellent inverse agreement with the corresponding evolution of 2m air temperature. We see that in the area where the increase of tropospheric BrO VCDs was the most profound (i.e. north of Greenland and in the Fram Strait), the temperature decreased significantly, about -0.2 Kelvin per year. A similar anti-correlation is observed in the Kara Sea, where tropospheric BrO VCD strongly decreased. In the same region, the most robust increase of air temperature is observed. However, temperature could not explain the general long-term changes of tropospheric BrO from the time-series perspective (but also from the yearly polar spring averaged maps), a satisfactory and explanatory agreement in the grid box trend maps of temperature and tropospheric BrO for the Arctic region.

4.2.2 Hudson Bay

An analysis of tropospheric BrO VCD and air temperature is performed for both winter and spring periods. In Figure 4.13, similar to Figure 4.10, average winter time-series of tropospheric BrO VCD and 2m air temperature, the corresponding scatter plot, enhanced time-series, and the scatter plot of enhanced tropospheric BrO VCD against air temperature are plotted.

4. The Relationship between Tropospheric BrO VCD, Sea Ice and Meteorological Conditions

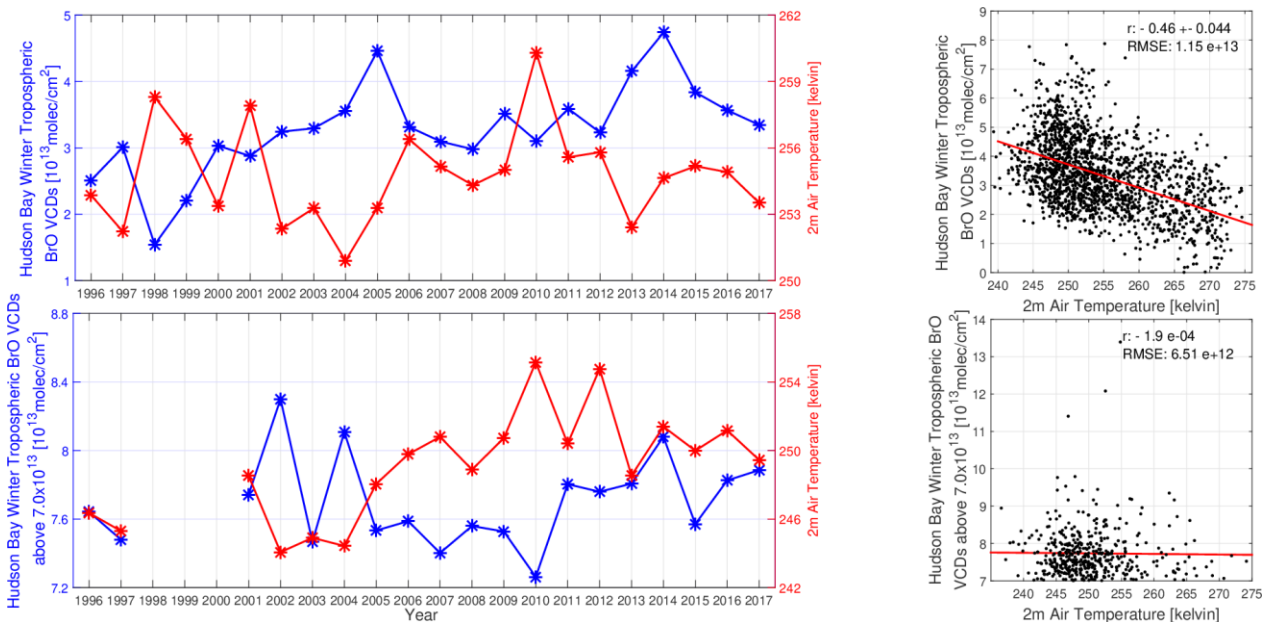


Figure 4.13: Time-series and scatter plots between tropospheric BrO VCDs and 2m air temperature for the Hudson Bay region during winters. Top left: Winter averaged time-series of tropospheric BrO VCDs and 2m air temperature from reanalysis data. Top right: The equivalent daily scatter plot between tropospheric BrO and ERA-5 2m air temperature. Bottom left: Winter averaged time-series of enhanced tropospheric BrO VCDs (above 7.0×10^{13} molecules/cm²) and 2m air temperature from this area from reanalysis data. Bottom right: The equivalent daily scatter plot between enhanced tropospheric BrO (above 7.0×10^{13} molecules/cm²) and ERA-5 2m air temperature.

The top-left time-series in Figure 4.13 show a good overall anti-correlation between tropospheric BrO VCD and air temperature. In most cases, when tropospheric BrO VCD increases (e.g. 1998), temperature decreases. The correlation coefficient for the time-series is -0.4, much higher than that for the two quantities in the Arctic region (Figure 4.10, where the correlation coefficient was positive). The anti-correlation is seen in the top right scatter plot as well, where daily averages of tropospheric BrO VCD and air temperature are plotted. The correlation coefficient is -0.46, slightly weaker than the one for the Arctic daily scatter plot (-0.53). However, the scatter of the measurements around the best fitting line is changing less with temperature, indicating that indirect hidden correlations between tropospheric BrO VCD and other quantities may not occur to such an extent. If we focus on the enhanced tropospheric BrO scenes (i.e. above 7.0×10^{13} molecules/cm², bottom subplots), we see that in the time-series, the general anti-correlation between tropospheric BrO VCD and air temperature holds (e.g. 2010). However, on a daily basis, the correlation coefficient drops significantly, similar to the Arctic (the value of the correlation coefficient on Figure 4.10, bottom right subplot did not drop sharply but is much smaller than that of Figure 4.10, top right).

A similar figure follows, but this time for the spring months:

4. The Relationship between Tropospheric BrO VCD, Sea Ice and Meteorological Conditions

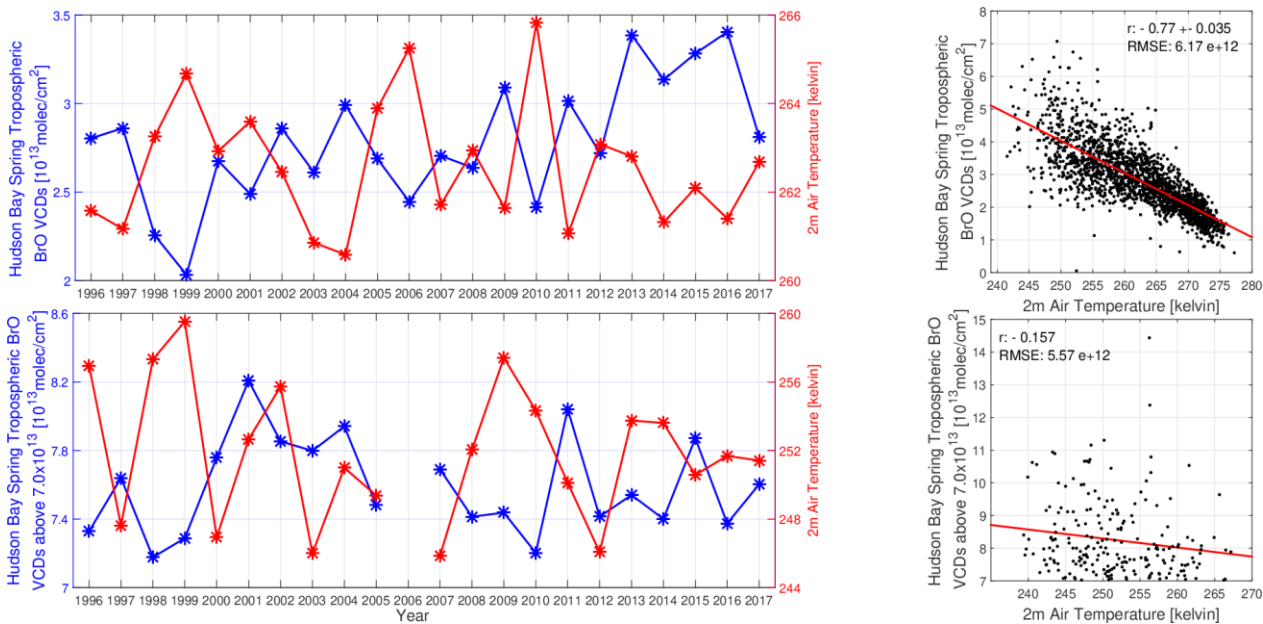


Figure 4.14: Time-series and scatter plots between tropospheric BrO VCDs and 2m air temperature for the Hudson Bay region during springs. Top left: Spring averaged time-series of tropospheric BrO VCDs and 2m air temperature from reanalysis data. Top right: The corresponding daily scatter plot between tropospheric BrO and ERA-5 2m air temperature. Bottom left: Spring averaged time-series of enhanced tropospheric BrO VCDs (above 7.0×10^{13} molecules/cm²) and 2m air temperature from reanalysis data. Bottom right: The corresponding daily scatter plot between enhanced tropospheric BrO (above 7.0×10^{13} molecules/cm²) and ERA-5 2m air temperature.

The top left time-series of Figure 4.14 shows an anti-correlation, with a correlation coefficient of -0.63. The two quantities are anti-correlated (e.g. 1999, 2006, 2009 and 2010). The correlation coefficient is also higher than the equivalent one for the winter periods. The daily scatter plot (top-right) shows a very strong anti-correlation of -0.77, much higher than the -0.46 of the winter period. The scatter of the points around the best fitting line is prominent for lower temperatures (similar to the polar spring scatter plot for the Arctic region, Figure 4.10, top right subplot). Although temperatures are comparable with those during the winter periods (i.e. Figure 4.13, top right scatter plot), the points are much closer to the best fitting line (i.e. in the winter periods, tropospheric BrO VCD is in the range of 0 to almost 5 molecules/cm², for temperatures between 265 and 270 Kelvin, while in spring and the same temperature interval, tropospheric BrO VCD ranges from 1.5 to 3 molecules/cm²). Temperature does not look like a threshold parameter in that case, as an overall linear relationship can be seen. Regarding the enhanced BrO VCDs during springs, the correlation drops, both for the time-series (from -0.63 to -0.42) and the daily scatter plots (from -0.77 to -0.15) compared to all the BrO VCDs values. The number of days where tropospheric BrO VCD exceeds the threshold of 7.0×10^{13} molecules/cm² decreases (number of data values in the bottom right scatter plot).

4. The Relationship between Tropospheric BrO VCD, Sea Ice and Meteorological Conditions

Figure 4.15 shows the trend maps of tropospheric BrO and temperature for the Hudson Bay area, both for the winter and spring periods.

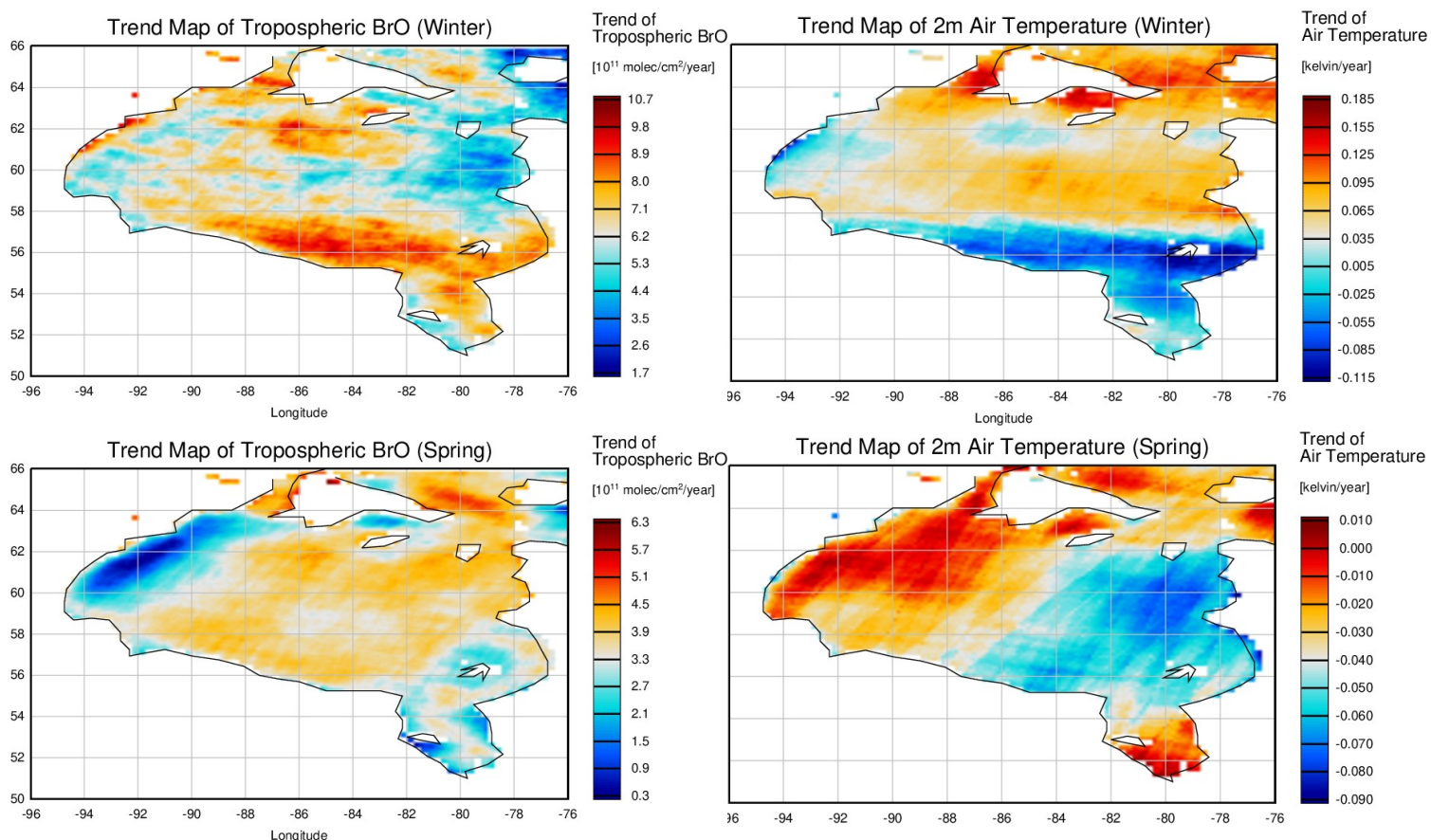


Figure 4.15: Trend maps of tropospheric BrO and air temperature for the Hudson Bay. Top left: trend map of tropospheric BrO during the winter period. Top right: trend map of air temperature during the winter period. Bottom left: trend map of tropospheric BrO during the spring period. Bottom right: trend map of air temperature during the spring period.

The comparisons of the trend maps of tropospheric BrO VCD and air temperature for the winter period show significant anti-correlation patterns. A strong anti-correlation with air temperature is observed in areas where an intense change in tropospheric BrO VCD occurs. A good example is the increase of tropospheric BrO VCD on the southeast of the Bay, which is mirrored by a substantial decrease of temperature in the same region. The opposite behaviour is seen on the northeast of the Bay, where temperature increased. The anti-correlation between tropospheric BrO VCD and air temperature is not as apparent as over the Arctic region. The trend maps of spring show anti-correlation in some areas, but not as pronounced as for winter. The weakest increase of tropospheric BrO VCD occurs on the northwest of the Bay, where there is a substantial increase in temperature. However, the changes in temperature during springs do not vary much. Temperature trends range from -0.09 to +0.01 Kelvin per year. Since tropospheric

BrO VCD did not decrease anywhere in the Bay for both winter and spring, the relationship to air temperature is not easy to interpret.

4.3 Relationship of Tropospheric BrO VCD and Mean Sea Level Pressure

From the literature, it is known that low pressure systems can contribute to the formation of enhanced tropospheric BrO VCD in combination with low wind speeds (“closed reaction chamber”) (Jones et al., 2009). However, tropospheric BrO VCDs appear also in the region of high pressure systems (e.g. through transport and blowing snow). Therefore, the comparison between tropospheric BrO VCD and mean sea level pressure is not expected to yield as precise results as the one with temperature. Nevertheless, we expect to see an anti-correlation between the two quantities, as the low pressure systems, together with the combination of other meteorological parameters that are associated with them, are linked to an enhancement of tropospheric BrO VCD.

4.3.1 Arctic Region (70.0° N to 85.0° N)

In the Arctic, it is known that low pressure systems occur over the European and Russian parts of the Arctic, and then, through the appearance and move of cyclones, high pressure systems occur over the Canadian Archipelago (Serreze and Barrett, 2010). Figure 4.16 shows time-series between tropospheric BrO VCD and mean sea level pressure, the corresponding scatter plot and the same results for enhanced tropospheric BrO VCD scenes.

4. The Relationship between Tropospheric BrO VCD, Sea Ice and Meteorological Conditions

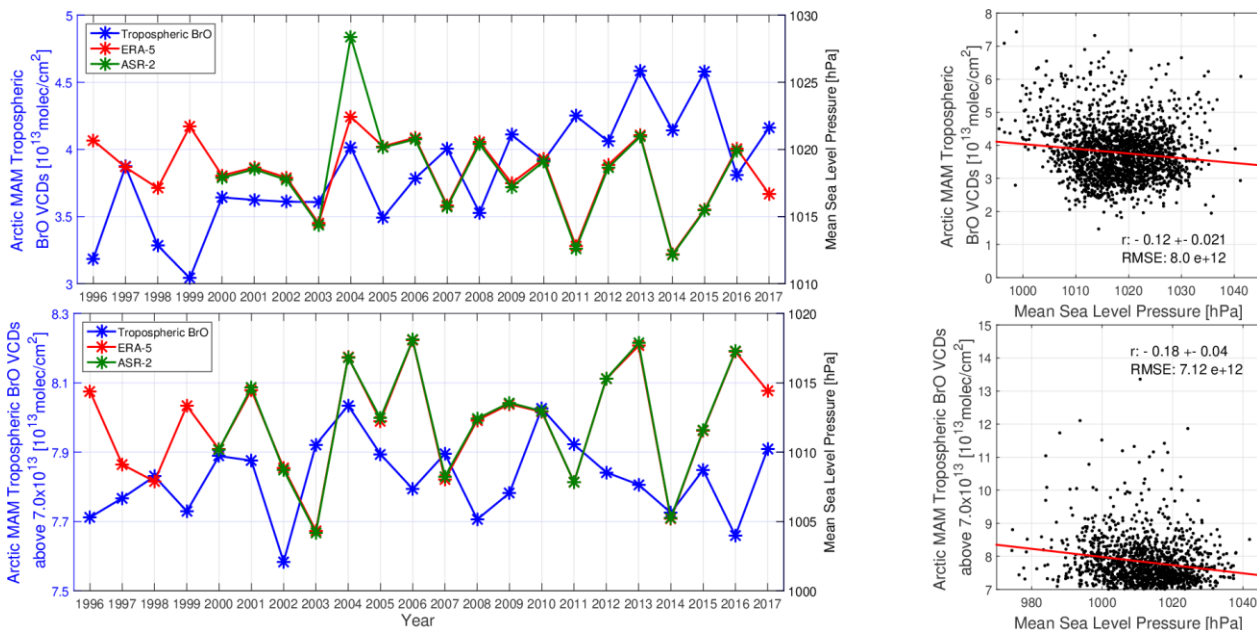
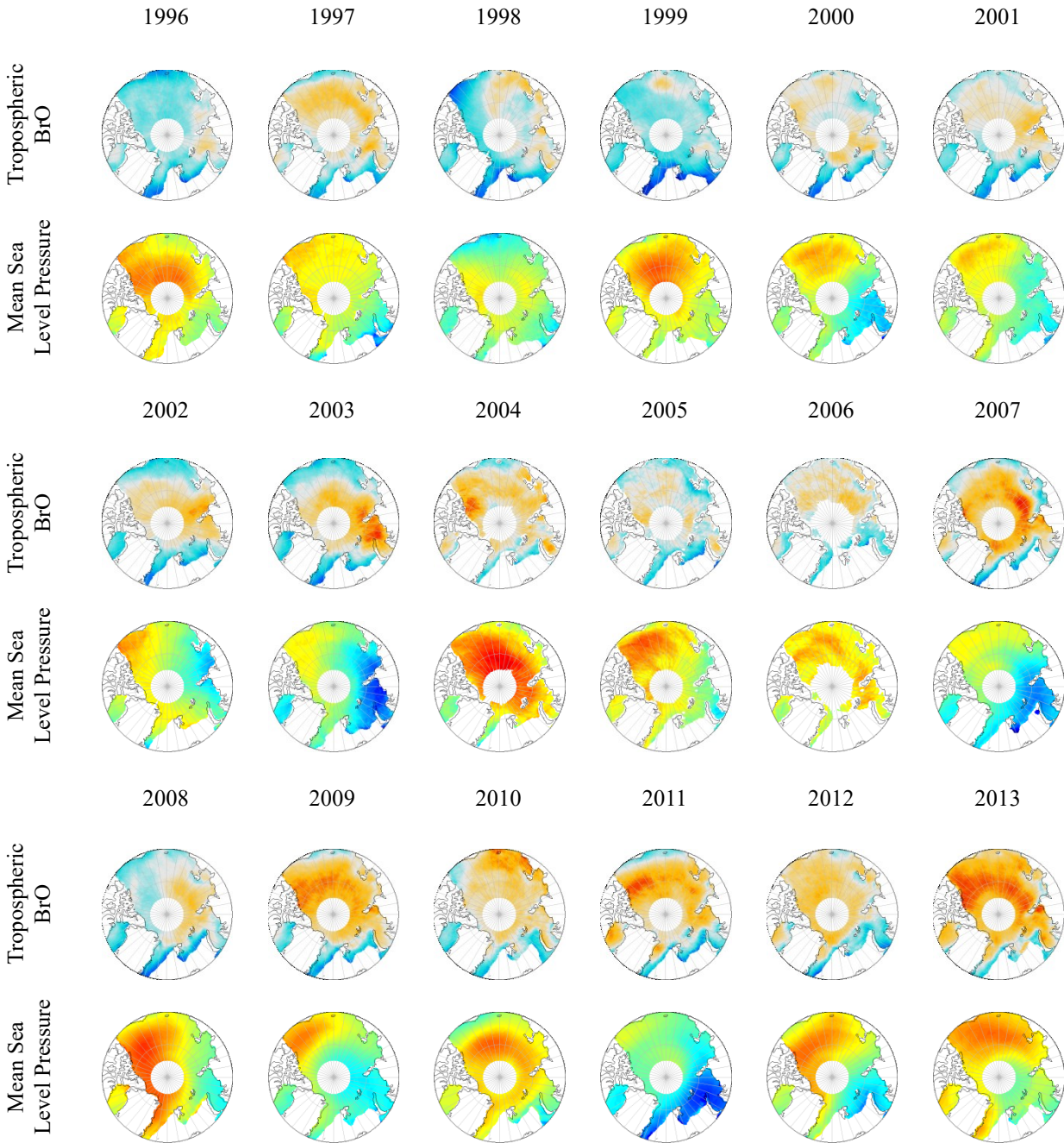


Figure 4.16: Time-series and scatter plots of the tropospheric BrO VCDs and mean sea level pressure. Top left: Polar spring averaged time-series of tropospheric BrO VCDs and mean sea level pressure from reanalysis data. Top right: The equivalent daily scatter plot between tropospheric BrO VCDs (blue curve in the time-series) and ERA-5 mean sea level pressure (the red one). Bottom left: Polar spring averaged time-series of enhanced tropospheric BrO VCDs (above 7.0×10^{13} molecules/cm²) and mean sea level pressure from reanalysis data. Bottom right: The equivalent daily scatter plot between enhanced tropospheric BrO VCDs (above 7.0×10^{13} molecules/cm², blue curve in the time-series) and ERA-5 mean sea level pressure (the red one).

Some anti-correlations are observed in the top left time-series, between tropospheric BrO VCD and mean sea level pressure. The correlation coefficient is -0.35 and can be seen in many years (e.g. 2007 to 2008). Meteorological parameters have a high dynamic range and change daily. Still, a high correlation between tropospheric BrO VCD and mean sea level pressure in polar spring averages is not expected. The daily scatter plot of tropospheric BrO VCD and mean sea level pressure show an anti-correlation of -0.12. Similar weak correlations are seen from the two bottom subplots (time-series of scenes with enhanced tropospheric BrO VCD), and the equivalent scatter plot. Although pressure as a quantity itself does not seem to play a dominant role in the bromine explosion and the generation of enhanced tropospheric BrO VCD, its value is associated with conditions that favour the bromine explosion (e.g. low pressure systems and the condition of wind speed, boundary layer height, and cyclones).

In Figure 4.17, similar to Figure 4.11, annual polar spring average maps of tropospheric BrO VCD and mean sea level pressure for the Arctic region are shown.

4. The Relationship between Tropospheric BrO VCD, Sea Ice and Meteorological Conditions



4. The Relationship between Tropospheric BrO VCD, Sea Ice and Meteorological Conditions

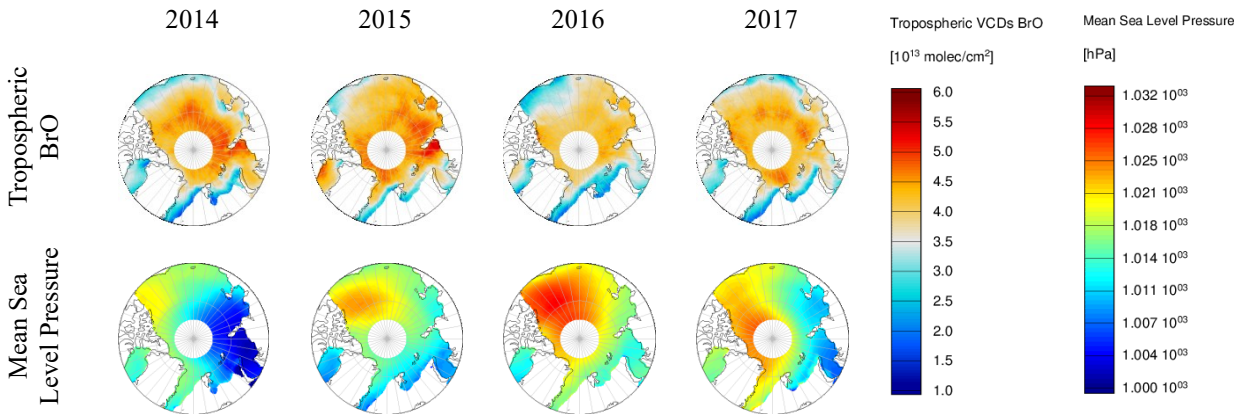


Figure 4.17: Polar spring average maps of tropospheric BrO VCDs [molec/cm^2] and ERA-5 mean sea level pressure [hPa].

Almost every year, the spatial distribution of pressure is similar; lower pressures occur over the European – Asian Arctic, while high pressures are found around the American Arctic. For some years, the highest tropospheric BrO VCD is found in areas having low pressure (e.g. 2003 and 2007). In other years (e.g. 2004), enhanced tropospheric BrO VCD occurred under high pressure. The recent increase of tropospheric BrO VCD (both in magnitude and spatial extent) does not correlate strongly with mean sea level pressure. Due to the dynamic nature of mean sea level pressure and the complex relationship to other meteorological drivers, it is found that tropospheric BrO VCD is not strongly correlated to mean sea level pressure.

In Figure 4.18, the trend maps for tropospheric BrO VCD and mean sea level pressure for the Arctic region are plotted.

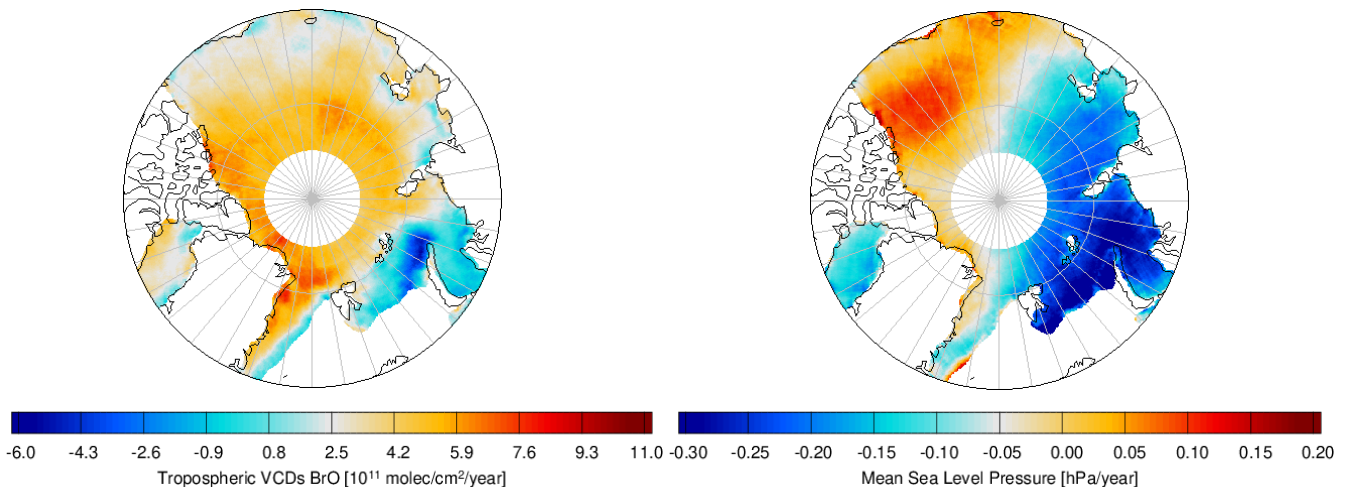


Figure 4.18: Spatial trend patterns for tropospheric BrO (left) and mean sea level pressure (right) for the Arctic region.

The spatial distribution of trend values of pressure is similar to average polar spring spatial distributions of mean sea level pressure in the previous figure. It seems that the high pressure

4. The Relationship between Tropospheric BrO VCD, Sea Ice and Meteorological Conditions

systems over the American Arctic and the lower pressure areas over the European – Asian Arctic intensified over the 22 years of our dataset. These changes are small and can be considered negligible. Overall, we do not see a clear relationship between the trend maps. Over the area where tropospheric BrO VCD has greatly increased (northeast of Greenland), mean sea level pressure shows a slight increase, while in the region, where tropospheric BrO shows the most profound decrease (Kara Sea), pressure also shows the most robust decrease.

4.3.2 Hudson Bay

Figure 4.19 shows the time-series of all scenes and those with enhanced tropospheric BrO VCD and the corresponding scatter plots of tropospheric BrO and mean sea level pressure for the Hudson Bay during the winter period:

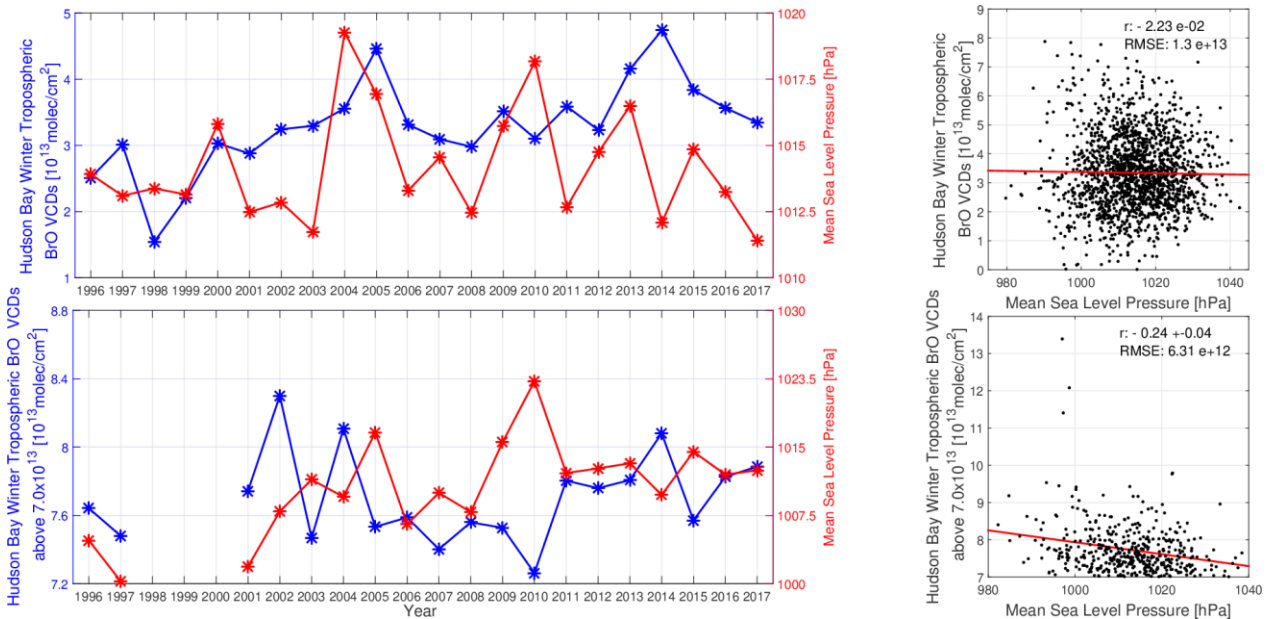


Figure 4.19: Time-series and scatter plots between tropospheric BrO VCDs and mean sea level pressure for the Hudson Bay region during winters. Top left: Winter averaged time-series of tropospheric BrO VCDs and mean sea level pressure from reanalysis data. Top right: The equivalent daily scatter plot between tropospheric BrO VCD and ERA-5 mean sea level pressure. Bottom left: Winter averaged time-series of enhanced tropospheric BrO VCDs (above 7.0×10^{13} molecules/cm²) and mean sea level pressure from reanalysis data. Bottom right: The equivalent daily scatter plot between enhanced tropospheric BrO (above 7.0×10^{13} molecules/cm²) and ERA-5 mean sea level pressure.

Although there are some years in the top left time-series where the expected anti-correlation between tropospheric BrO VCD and mean sea level pressure (e.g. 2014) is seen, the calculated correlation coefficient is +0.2. In the equivalent scatter plot (top right subplot), we see also a close to zero correlation between the two quantities. When we focus on the enhanced tropospheric BrO scenes, we get -0.23 for the long-term time-series correlation and -0.24 for the daily values. Still, the correlations are low, similar to what we saw for the Arctic region.

A similar figure, but for the spring months follows:

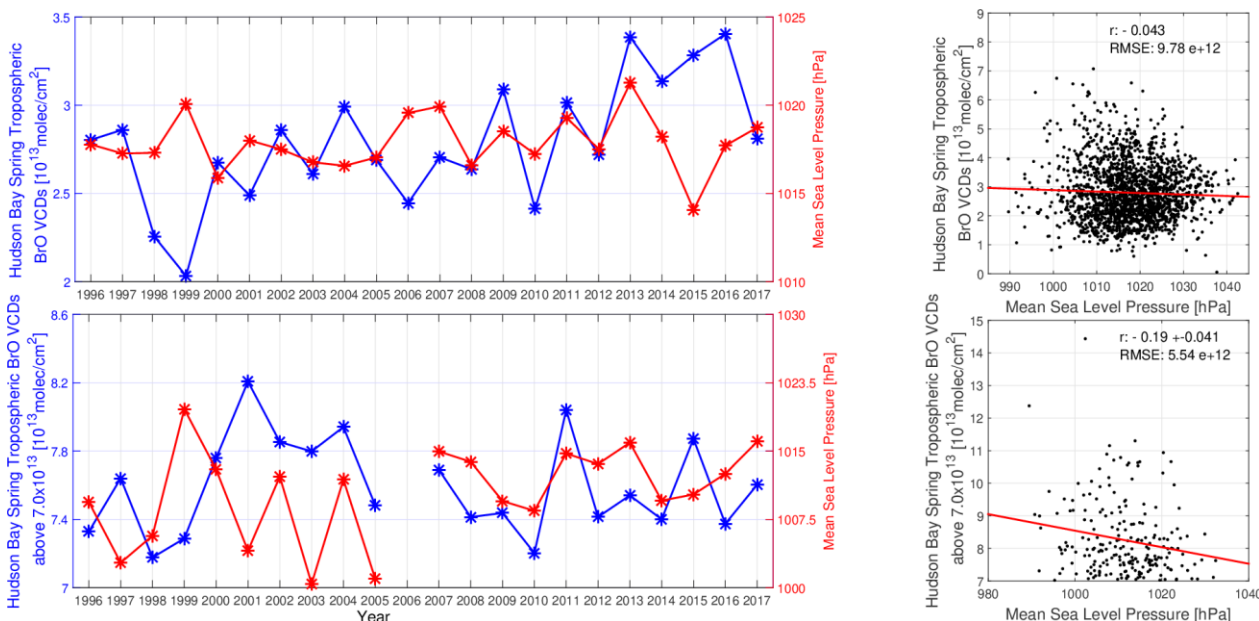


Figure 4.20: Time-series and scatter plots between tropospheric BrO VCDs and mean sea level pressure for the Hudson Bay region during springs. Top left: Winter averaged time-series of tropospheric BrO VCDs and mean sea level pressure from reanalysis data. Top right: The equivalent daily scatter plot between tropospheric BrO and ERA-5 mean sea level pressure. Bottom left: Spring averaged time-series of enhanced tropospheric BrO VCDs (above 7.0×10^{13} molecules/cm²) and mean sea level pressure from reanalysis data. Bottom right: The equivalent daily scatter plot between enhanced tropospheric BrO (above 7.0×10^{13} molecules/cm²) and ERA-5 mean sea level pressure.

Similar behaviour is observed: low correlation coefficients for both the time-series and the scatter plot (-0.07 and -0.043, respectively). However, the absolute value of the correlation coefficients increases very slightly when we focus only on the enhanced tropospheric BrO VCD scenes (bottom subplots), where the correlation coefficient for the time-series is -0.23, while for the scatter plot -0.19. Still, these are low correlations, as for all other comparisons between tropospheric BrO VCD and mean sea level pressure for both the Arctic and the Hudson Bay.

In Figure 4.21, a comparison between the trend maps of tropospheric BrO VCD and mean sea level pressure for both winter and spring periods is shown.

4. The Relationship between Tropospheric BrO VCD, Sea Ice and Meteorological Conditions

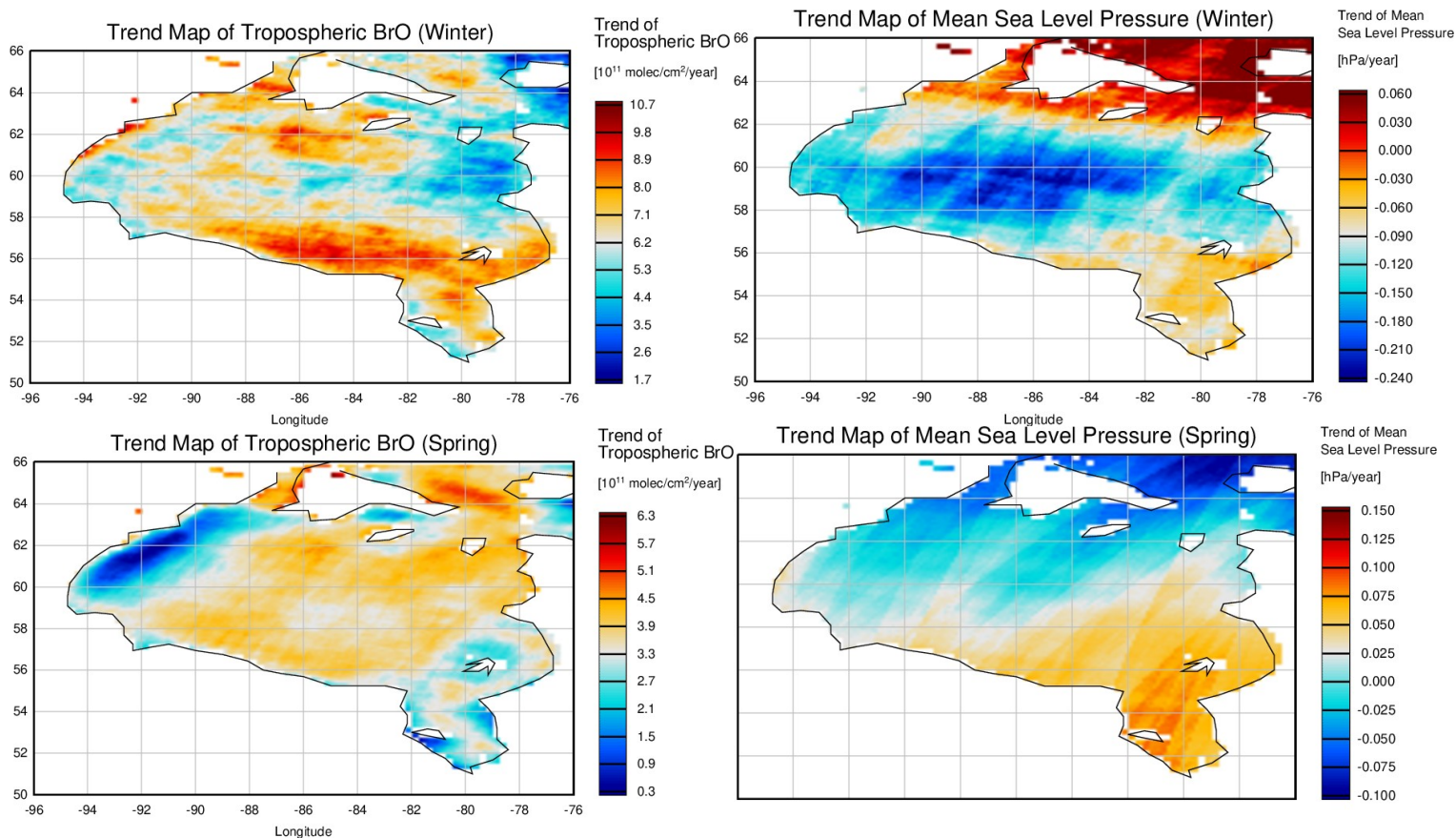


Figure 4.21: Spatial trend patterns of tropospheric BrO and mean sea level pressure for the Hudson Bay. Top left: trend map of tropospheric BrO during the winter period. Top right: trend map of mean sea level pressure during the winter period. Bottom left: trend map of tropospheric BrO during the spring period. Bottom right: trend map of mean sea level pressure during spring.

Although the time-series and scatter plots showed a slightly higher correlation between tropospheric BrO VCD and mean sea level pressure during spring months than winter, a stronger spatial anti-correlation during winters is inferred from the trend maps. The most profound decrease of mean sea level pressure occurred in the middle and south of the Bay, where we have the most robust tropospheric BrO VCD increase. However, the agreement is not one to one. No direct relationship can be found by the comparison of the trend maps of the spring months. Therefore, we follow that the trend maps of tropospheric BrO VCD and mean sea level pressure do not show a strong correlation in addition to the previous results.

4.4 Relationship of Tropospheric BrO VCD and Wind Speed

The following parameter discussed is horizontal wind speed, which was calculated from u and v component vectors of 10 meter wind from the reanalysis data. The relationship between tropospheric BrO VCD and 10 meters wind speed will be investigated. It is known from the

literature that both high and low wind speeds can influence the formation of enhanced BrO plumes (high wind speeds by transporting and re-cycling BrO on blowing snow, low wind speeds by stable inversion and a constant release of bromine molecules from a saline surface) (Jones et al., 2009).

4.4.1 Arctic Region (70.0° N to 85.0° N)

Similar to the previous driving mechanisms that we examined, Figure 4.22 shows time-series of tropospheric BrO VCD and wind speed for the spring months, the corresponding daily scatter plots, time-series with only the enhanced tropospheric BrO VCD scenes (above 7.0×10^{13} molecules/cm²), and the equivalent scatter plot of the daily values:

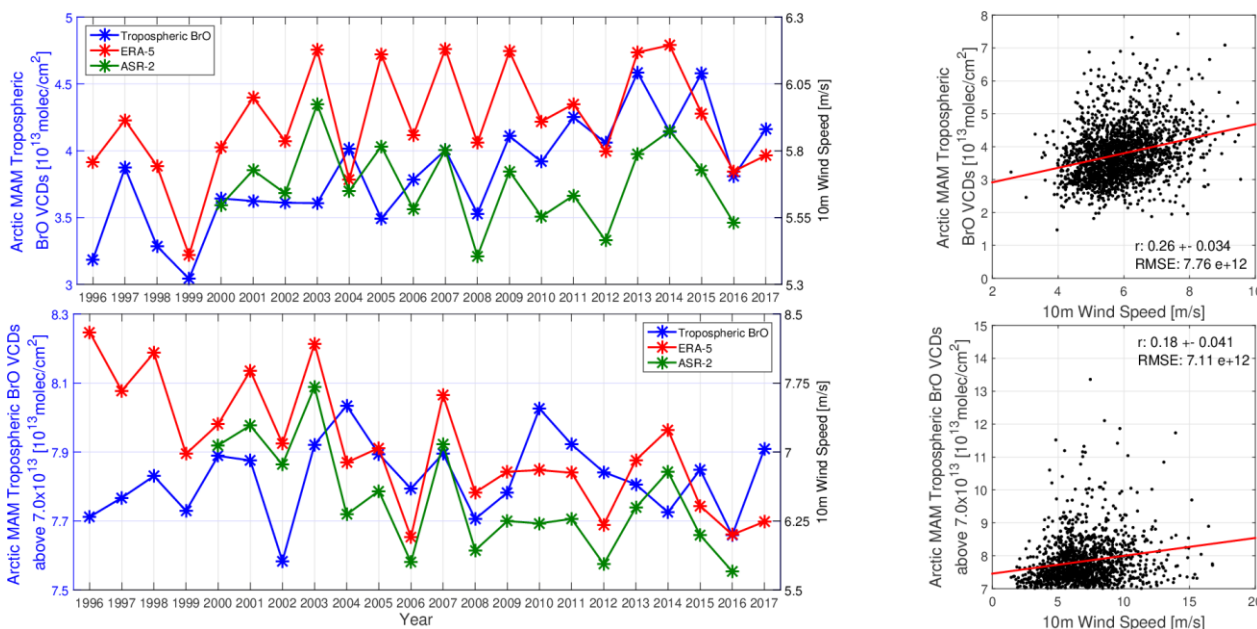


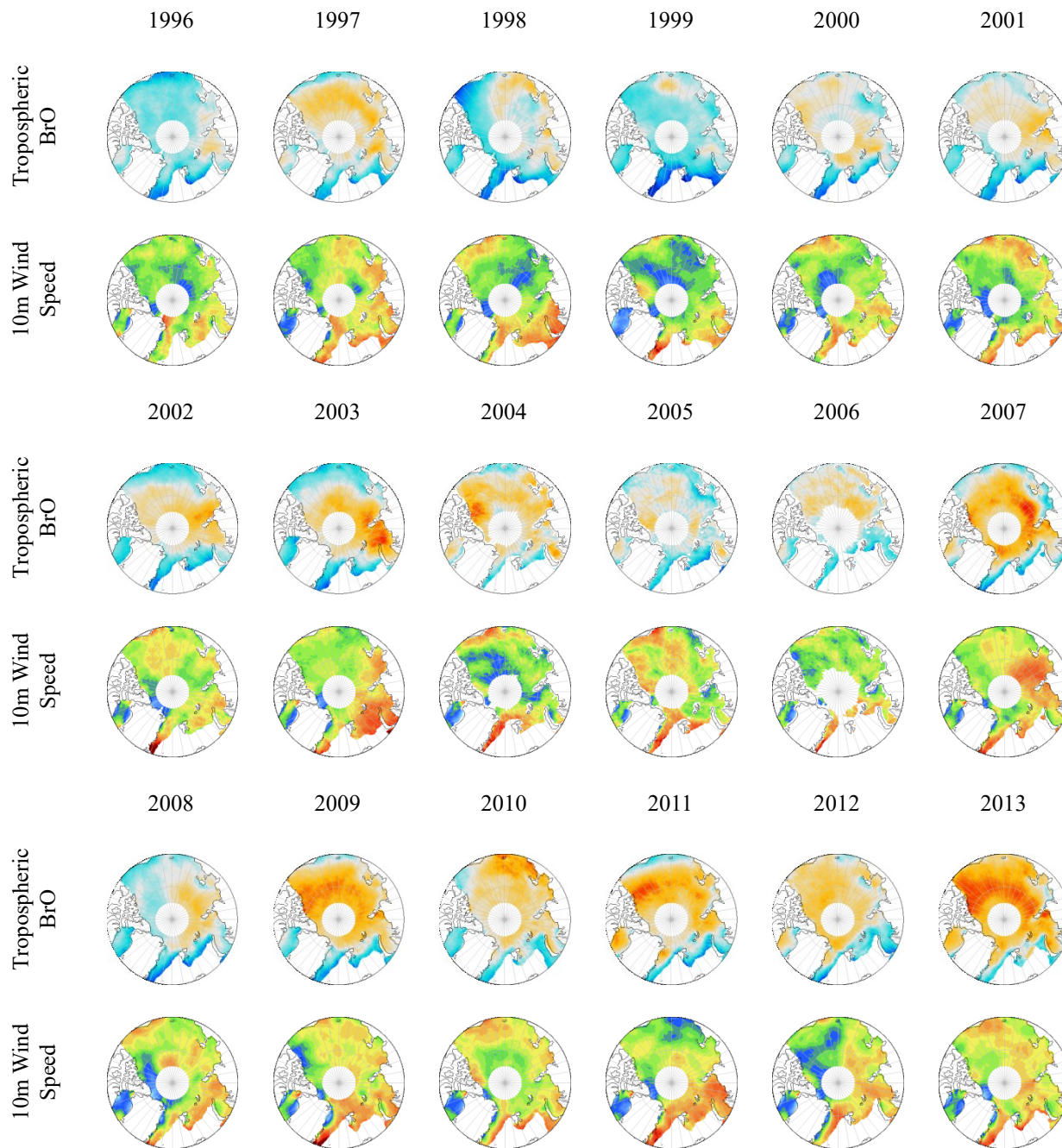
Figure 4.22: Time-series and scatter plots between tropospheric BrO VCDs and 10m wind speed. Top left: Polar spring averaged time-series of tropospheric BrO VCDs and 10m wind speed from reanalysis data. Top right: The equivalent daily scatter plot between tropospheric BrO (blue curve in the time-series) and ERA-5 10m wind speed (the red one). Bottom left: Polar spring averaged time-series of enhanced tropospheric BrO VCDs (above 7.0×10^{13} molecules/cm²) and 10m wind speed from reanalysis data. Bottom right: The equivalent daily scatter plot between enhanced tropospheric BrO (above 7.0×10^{13} molecules/cm², blue curve in the time-series) and ERA-5 10m wind speed (the red one).

All four correlation coefficients are positive, meaning that the increase observed in the wind speed over the Arctic region agrees with the evolution of tropospheric BrO VCD. By examining the top left time-series, for most years (e.g. from 2007 to 2008, or from 1996 to 1999), a similar evolution between the two quantities is observed. However, both the correlation coefficients for the top panels indicate moderate correlations (+0.49 for the time-series and +0.26 for the daily scatter plot). These values are slightly lower than the equivalent ones for first year ice extent and much higher than those for mean sea level pressure. When we focus on the enhanced

4. The Relationship between Tropospheric BrO VCD, Sea Ice and Meteorological Conditions

tropospheric BrO VCD scenes (bottom subplots), we see that the correlation is lower for both subplots (+0.04 for the time-series, +0.18 for the scatter plot). The increase in wind speed in the Arctic region shows a moderate positive correlation with tropospheric BrO VCDs' increase.

Figure 4.23 shows yearly polar spring averaged maps of tropospheric BrO and 10m wind speed:



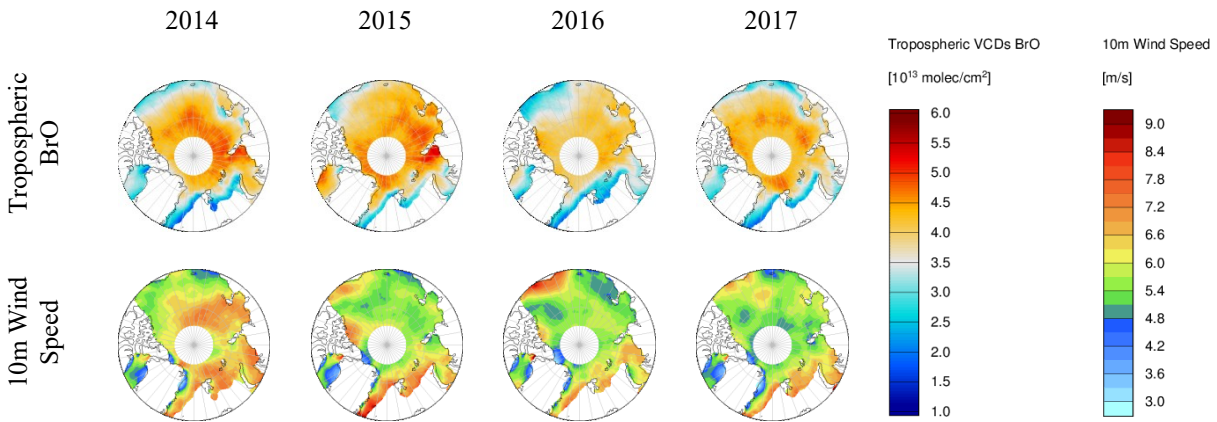
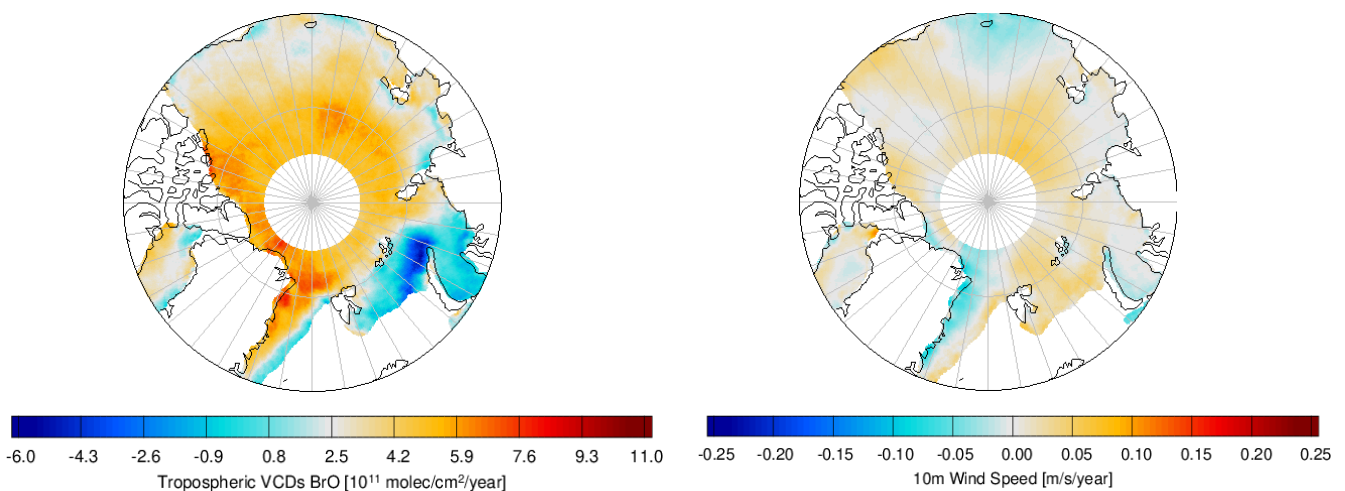


Figure 4.23: Polar spring average maps of tropospheric BrO VCDs [molec/cm^2] and ERA-5 10m wind speed [m/s].

The wind speed maps resemble those of mean sea level pressure, as high wind speeds are developing on the European side of the Arctic (low pressure in the pressure maps), while low wind speeds appear over high pressure. This agreement is not straightforward (e.g. 2005). From the comparison of tropospheric BrO VCD maps to wind speed, there are years (e.g. 2003, 2007, 2014) where high tropospheric BrO VCD occurred in conjunction with high wind speeds. However, there are also years (e.g. 2015, 2004, and 1998) where the highest tropospheric BrO VCD appeared over regions with low – mean wind speeds. This is expected, as both meteorological wind speed conditions can favour enhanced tropospheric BrO VCD. There is a satisfactory agreement when the yearly polar spring averaged maps of the two quantities are compared. Not all the enhanced tropospheric BrO plumes can be interpreted by wind speed. For instance, in the year 2015, the most profound tropospheric BrO occurred over average wind speeds.

Figure 4.24 shows the trend maps of tropospheric BrO and wind speed:



4. The Relationship between Tropospheric BrO VCD, Sea Ice and Meteorological Conditions

Figure 4.24: Spatial trend patterns of tropospheric BrO (left) and 10m wind speed (right) for the Arctic region.

From comparing the two trend maps, we infer that in the region where we see the most significant increase of tropospheric BrO VCDs (northeast of Greenland), the wind speed seems to have slightly decreased over the 22 years. Over the Canadian Archipelago, the increase of tropospheric BrO VCD occurs in conjunction with a slight increase in wind speed. The decrease in wind speed does not necessarily imply low wind speeds. By checking the maps of Figure 4.23, in this region, high average wind speeds (i.e. around 7 m/s) occur. In the same region, tropospheric BrO VCD does not take its maximum value.

4.4.2 Hudson Bay

In the first panel of Figure 4.25, time-series of tropospheric BrO VCDs and 10m wind speed for the winter season, for both all and enhanced (i.e. above 7.0×10^{13} molecules/cm²) scenes of tropospheric BrO are shown:

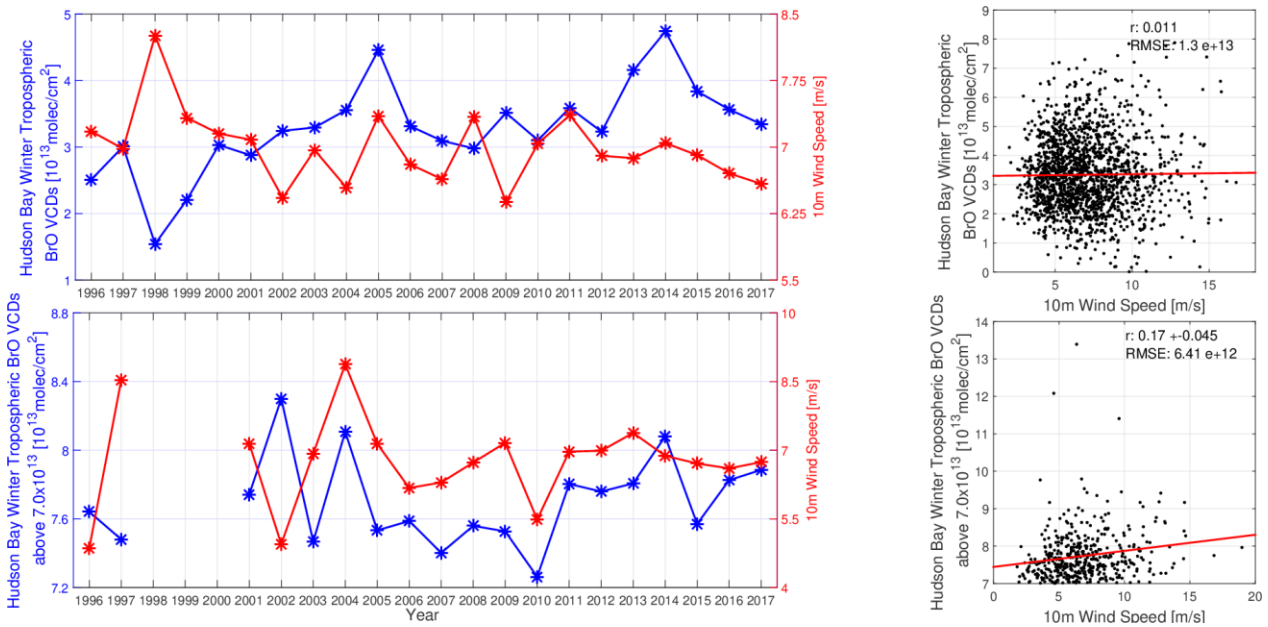


Figure 4.25: Time-series and scatter plots of tropospheric BrO VCDs and 10m wind speed for the Hudson Bay region during winters. Top left: Winter averaged time-series of tropospheric BrO VCDs and 10m wind speed from reanalysis data. Top right: The equivalent daily scatter plot between tropospheric BrO and ERA-5 10m wind speed. Bottom left: Winter averaged time-series of enhanced tropospheric BrO VCDs (above 7.0×10^{13} molecules/cm²) and 10m wind speed from reanalysis data. Bottom right: The equivalent daily scatter plot between enhanced tropospheric BrO (above 7.0×10^{13} molecules/cm²) and ERA-5 10m wind speed.

A significant difference is seen in the top panels of Figure 4.25, compared to the equivalent plots for the Arctic (i.e. Figure 4.22). The correlations were much more robust (e.g. +0.26 for the daily scatter plot), while here, the same scatter plot gives a correlation coefficient of 0.011. The top left time-series show a weaker correlation, but with a negative sign (-0.45 compared to +0.49 for the Arctic). The situation does not change when we focus on the enhanced BrO scenes

4. The Relationship between Tropospheric BrO VCD, Sea Ice and Meteorological Conditions

(bottom subplots of Figure 4.25). The correlation coefficient for the time-series is +0.05 (much lower and with a different sign than the top left time-series), while the correlation of the scatter plot increases to +0.17. Wind speed does not play a significant role in the formation of tropospheric BrO plumes in the Hudson Bay during winters.

A similar figure, but for the spring months follows:

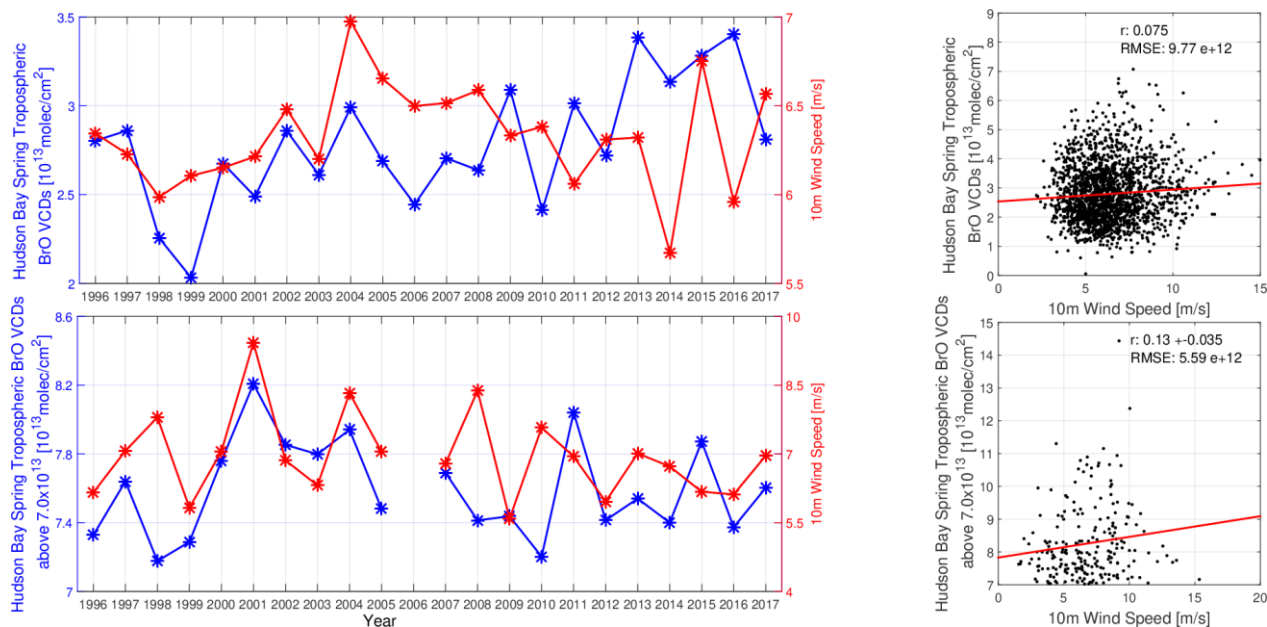


Figure 4.26: Time-series and scatter plots of tropospheric BrO VCDs and 10m wind speed for the Hudson Bay region during springs. Top left: Winter averaged time-series of tropospheric BrO VCDs and 10m wind speed from reanalysis data. Top right: The equivalent daily scatter plot between tropospheric BrO and ERA-5 10m wind speed. Bottom left: Spring averaged time-series of enhanced tropospheric BrO VCDs (above 7.0×10^{13} molecules/cm²) and 10m wind speed from reanalysis data. Bottom right: The equivalent daily scatter plot between enhanced tropospheric BrO (above 7.0×10^{13} molecules/cm²) and ERA-5 10m wind speed.

Similar conclusions for the relationship between tropospheric BrO VCD and 10m wind speed can be extracted from the spring figure. The correlation coefficients are low in all cases (+0.043 for the top left time-series, +0.075 for the equivalent daily scatter plot, +0.36 for the bottom left time-series, and +0.13 for the bottom right scatter plot). As a result, we can infer that wind speed does not play a significant role in forming tropospheric BrO plumes in the Hudson Bay. A possible explanation for these results and the differences between the Arctic and Hudson Bay could be that cyclones, which can transfer and recycle enhanced BrO by blowing snow and aerosols, are primarily seen in the Arctic and not inside the Hudson Bay.

The trend maps of tropospheric BrO VCD and 10m wind speed for both winter and summer periods are presented in Figure 4.27.

4. The Relationship between Tropospheric BrO VCD, Sea Ice and Meteorological Conditions

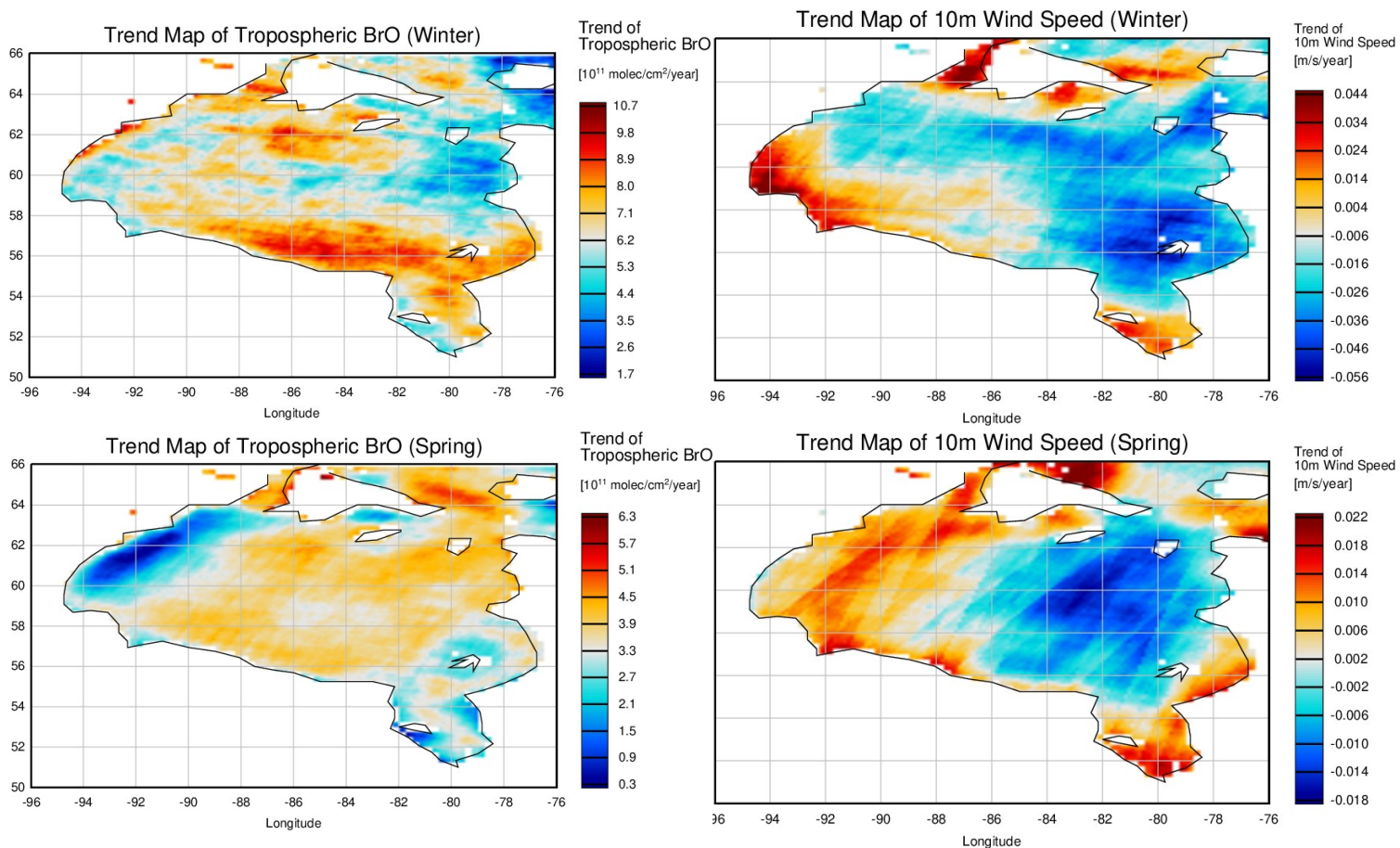


Figure 4.27: Spatial trend patterns of tropospheric BrO VCD and 10m wind speed for the Hudson Bay. Top left: trend map of tropospheric BrO VCD during the winter period. Top right: trend map of 10m wind speed during the winter period. Bottom left: trend map of tropospheric BrO VCD during the spring period. Bottom right: trend map of 10m wind speed during the spring period.

Although from the time-series and scatter plots comparison, a strong correlation between tropospheric BrO VCD and 10m wind speed was not seen, when we compare the trend maps for the winter periods, a slight correlation between them is observed. In the southeast area of the Bay, the increase of tropospheric BrO VCD is more pronounced and occurs in conjunction with a slight decrease in wind speed. Similar patterns can be seen in the middle-north of the Bay. However, the changes in wind speed are insignificant and can be considered negligible. Regarding the spring maps, the changes in wind speed are even weaker, so any spatial correlation of tropospheric BrO and wind speed cannot be considered significant.

4.5 Relationship of Tropospheric BrO VCD and Boundary Layer Height

Only the ERA-5 reanalysis data provides values for boundary layer height. As a hypothesis, it can be suggested that the higher the boundary layer height, the more tropospheric BrO the

satellite will see. However, a low boundary layer height implies conditions that favour the accumulation of bromine molecules released to the Arctic atmosphere (i.e. “closed reaction chamber”, as described in the introduction). In addition, tropospheric BrO can also be present above the boundary layer through upward winds under low pressure systems.

4.5.1 Arctic Region (70.0° N to 85.0° N)

In Figure 4.28, data from ERA-5 boundary layer height is compared to tropospheric BrO VCD. No ASR-2 data is shown.

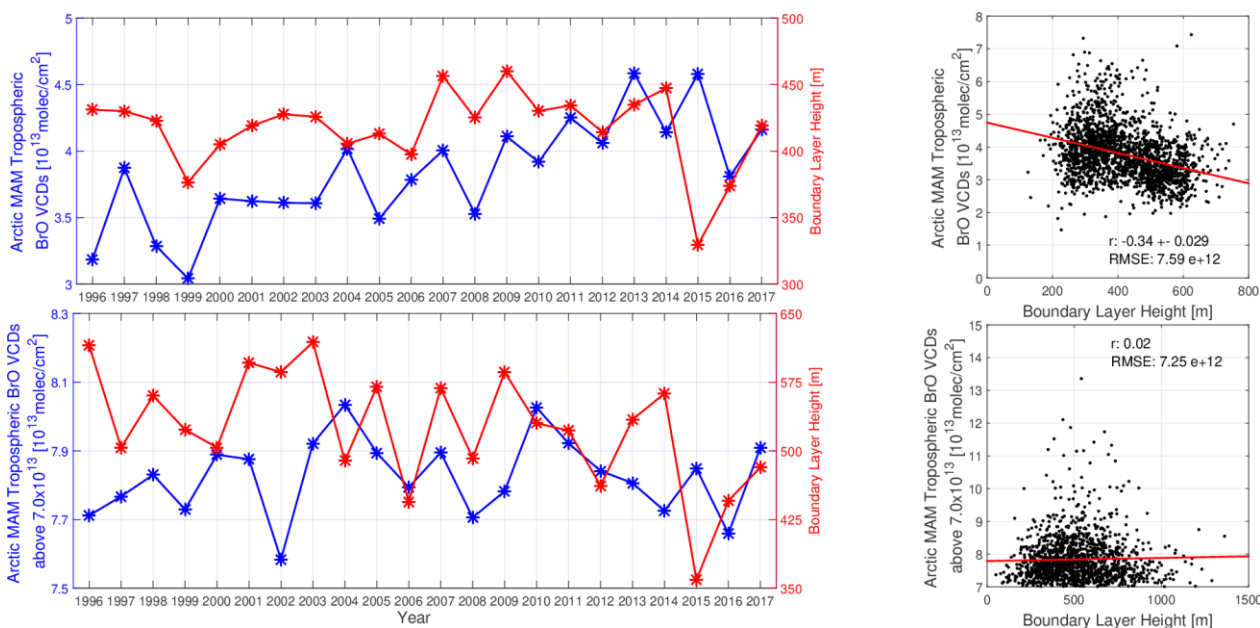
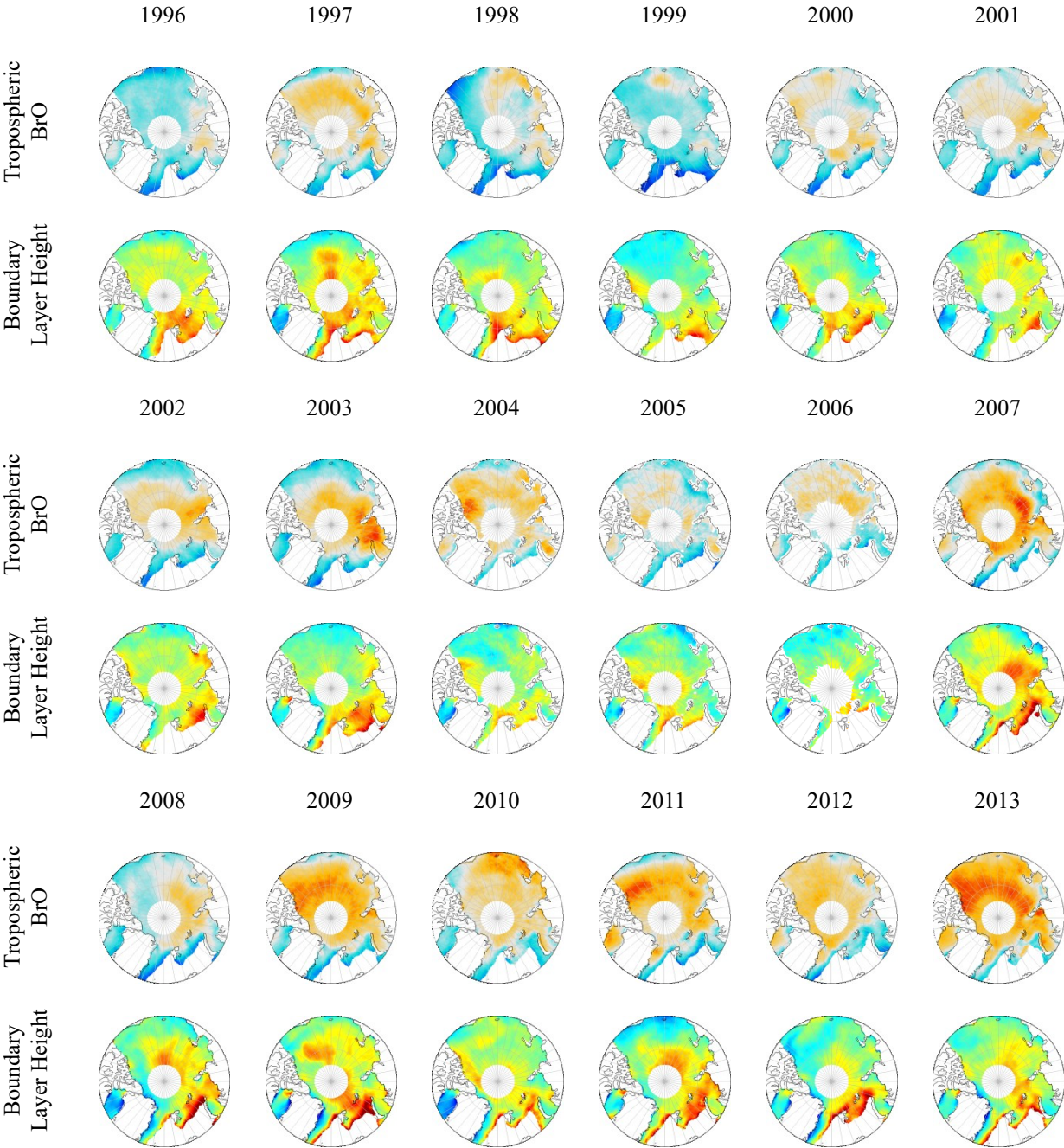


Figure 4.28: Time-series and scatter plots between tropospheric BrO VCDs and boundary layer height. Top left: Polar spring averaged time-series of tropospheric BrO VCDs and boundary layer height from ERA-5 reanalysis data. Top right: The equivalent daily scatter plot between tropospheric BrO and boundary layer height. Bottom left: Polar spring averaged time-series of enhanced tropospheric BrO VCDs (above 7.0×10^{13} molecules/cm²) and boundary layer height from ERA-5 reanalysis data. Bottom right: The equivalent daily scatter plot between enhanced tropospheric BrO (above 7.0×10^{13} molecules/cm²) and boundary layer height.

In the top left panel of Figure 4.28, there are some years where a positive correlation between tropospheric BrO VCD and boundary layer height can be seen (e.g. from 2007 to 2009). In the top right panel of Figure 4.28, a moderate anti-correlation of -0.34 is seen. This is the biggest by absolute values correlation after 2m air temperature for the Arctic region. The correlations drop for the bottom panels (-0.053 for the enhanced time-series and +0.02 for the scatter plot), the correlation coefficient of the top right scatter plot shows that boundary layer height can play an essential role in the formation of tropospheric BrO plumes.

In Figure 4.29, the relationship between polar spring averaged maps of tropospheric BrO VCDs, and boundary layer height is investigated:

4. The Relationship between Tropospheric BrO VCD, Sea Ice and Meteorological Conditions



4. The Relationship between Tropospheric BrO VCD, Sea Ice and Meteorological Conditions

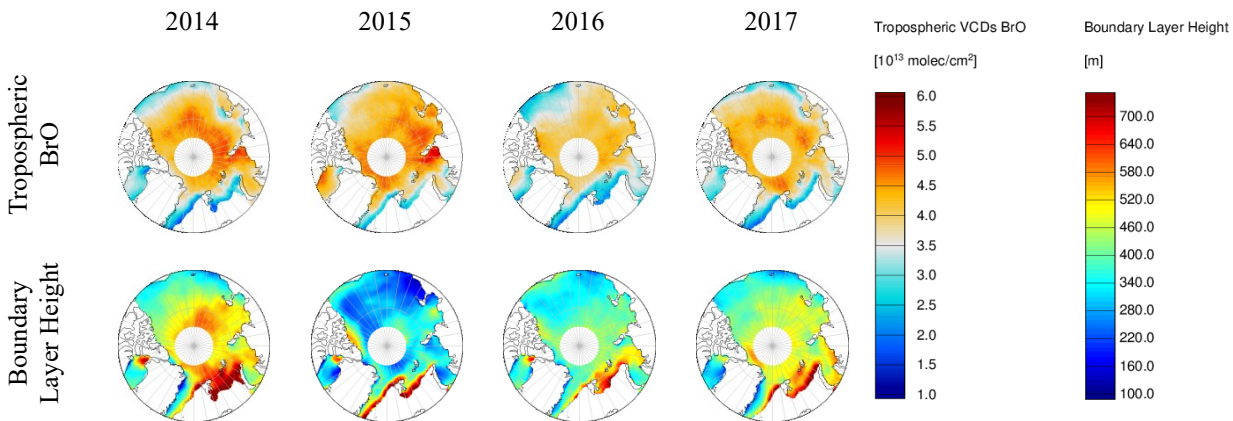


Figure 4.29: Polar spring average maps of tropospheric BrO VCDs [molec/cm^2] and ERA-5 boundary layer height [m].

In contrast to the previous results, where the daily scatter plot of all scenes indicated a negative correlation between tropospheric BrO VCD and boundary layer height, the polar spring months suggest that in many cases, enhanced BrO appeared over regions of high boundary layer (e.g. 2007, 2008, and 2009). There are also years where high tropospheric BrO VCD appeared over mean values of boundary layer height (e.g. 2013, 2004). 2015 is a unique year, as shallow boundary layer conditions in the Arctic were observed. The boundary layer height plays a role in the formation of enhanced tropospheric BrO VCD. However, the complexity of bromine explosion, together with the deep interaction of meteorological parameters, makes the task of isolating the effect of boundary layer height as a driving mechanism of bromine explosions a difficult one.

Figure 4.30 shows the relationship between tropospheric BrO and boundary layer height through trend maps:

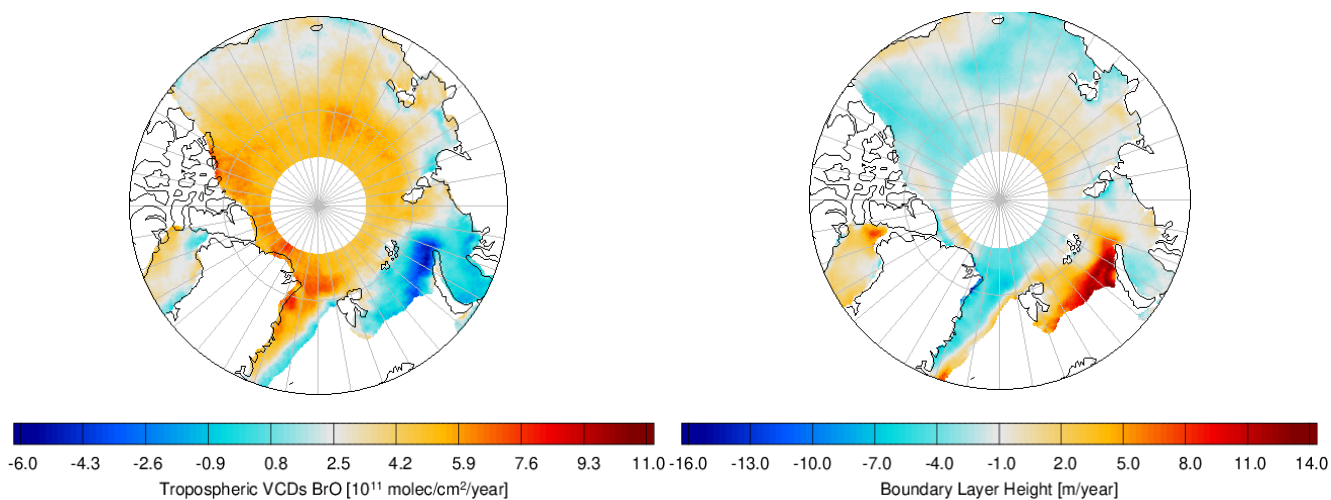


Figure 4.30: Spatial trend patterns of tropospheric BrO (left) and boundary layer height (right) for the Arctic region.

4. The Relationship between Tropospheric BrO VCD, Sea Ice and Meteorological Conditions

Over the Fram Strait, where the increase of tropospheric BrO VCD is more pronounced, the boundary layer height shows a decreasing trend of around 7 meters per year. To the north of Greenland and the west, a slight decrease of boundary layer height of 1 meter per year is seen. In the region where tropospheric BrO VCD strongly decreased, boundary layer height shows its most robust increase (the Kara Sea, approximately 13 to 14 meters per year). In the other region where tropospheric BrO VCD increased (inside the Arctic Ocean), boundary layer height shows a slight increase of 2 meters per year. Therefore, we could conclude that the analysis of the role of boundary layer height in the formation of enhanced BrO plumes is complicated as tropospheric BrO VCD formation also depends on other parameters.

4.5.2 Hudson Bay

Figure 4.31 shows tropospheric BrO VCD time-series and boundary layer height for the winter season, for both all and enhanced (i.e. above 7.0×10^{13} molecules/cm²) scenes of tropospheric BrO.

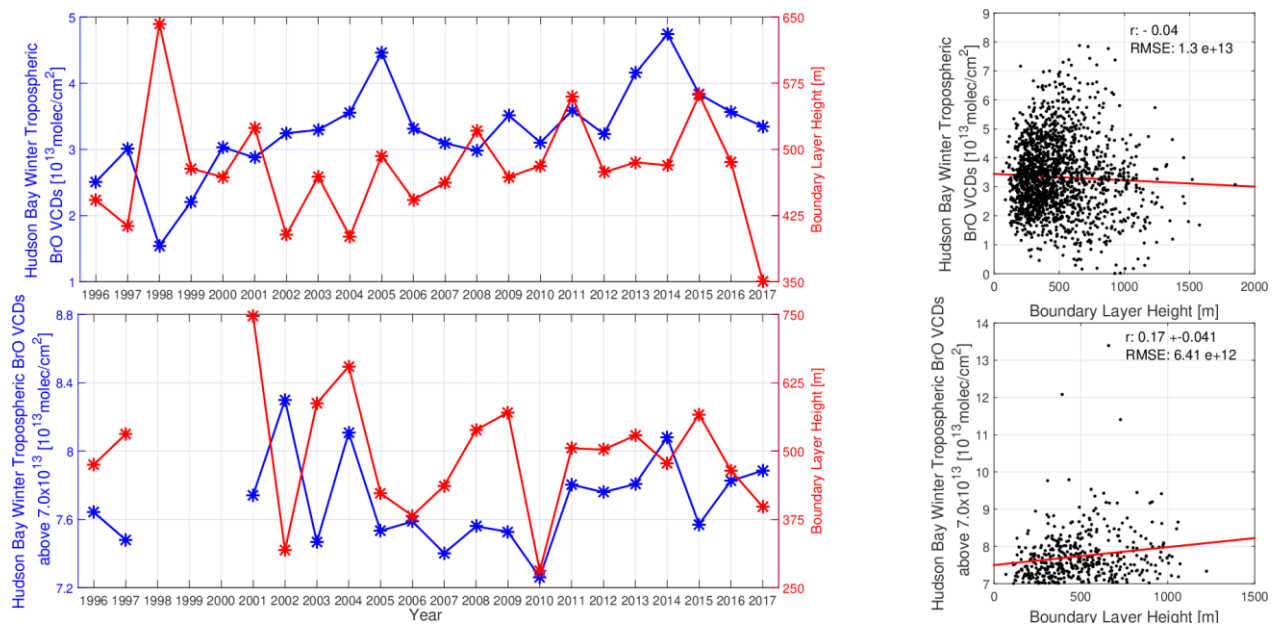


Figure 4.31: Time-series and scatter plots of tropospheric BrO VCDs and boundary layer height for the Hudson Bay region during winters. Top left: Winter averaged time-series of tropospheric BrO VCDs and boundary layer height from reanalysis data. Top right: The equivalent daily scatter plot between tropospheric BrO and ERA-5 boundary layer height. Bottom left: Winter averaged time-series of enhanced tropospheric BrO VCDs (above 7.0×10^{13} molecules/cm²) and boundary layer height from reanalysis data. Bottom right: The equivalent daily scatter plot between enhanced tropospheric BrO (above 7.0×10^{13} molecules/cm²) and ERA-5 boundary layer height.

A weak anti-correlation of -0.217 is inferred from the top left time-series. There are some years where this anti-correlation is evident (e.g. 1998). Overall, the two quantities do not strongly relate. The same conclusion is made from the equivalent daily scatter plot (top right), where the correlation coefficient is almost zero (-0.04). The situation does not change for the bottom

subplots (enhanced tropospheric BrO VCD scenes), where the correlation for the time-series is +0.047, while for the scatter plot +0.17. The boundary layer height is a more critical parameter for tropospheric BrO VCD in the Arctic than for the Hudson Bay, at least for the winter period.

In Figure 4.32, the same results will be presented, but for the spring months:

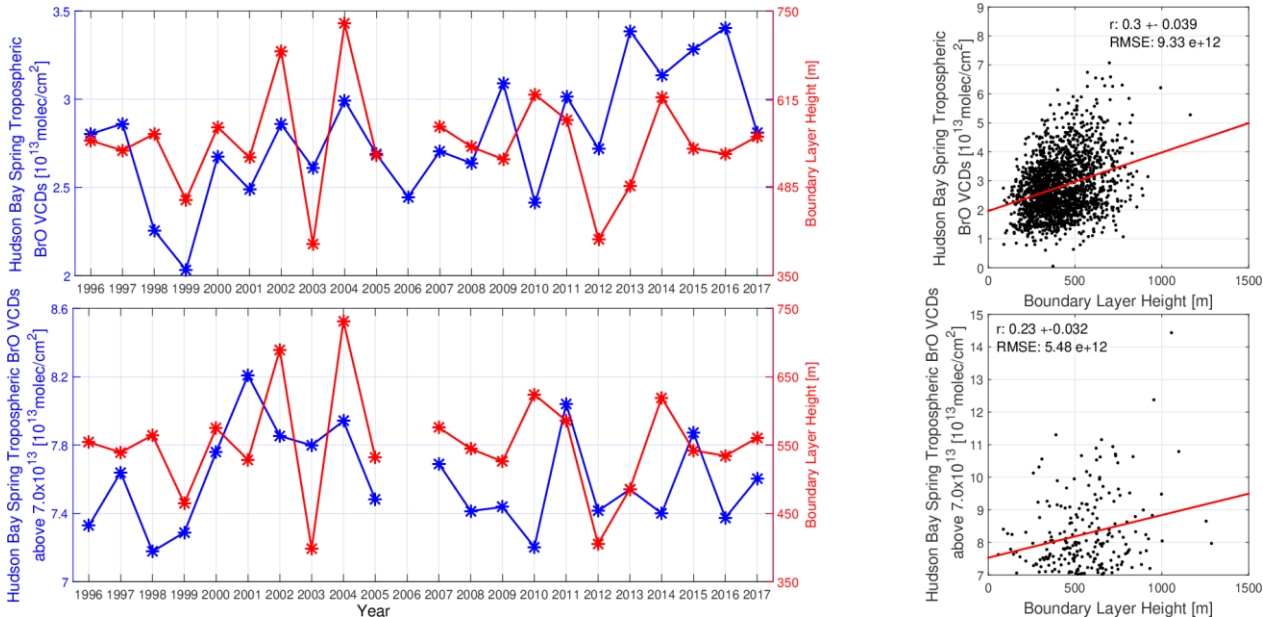


Figure 4.32: Time-series and scatter plots between tropospheric BrO VCDs and boundary layer height for the Hudson Bay region during springs. Top left: Spring averaged time-series of tropospheric BrO VCDs and boundary layer height from reanalysis data. Top right: The equivalent daily scatter plot between tropospheric BrO and ERA-5 boundary layer height. Bottom left: Spring averaged time-series of enhanced tropospheric BrO VCDs (above 7.0×10^{13} molecules/cm²) and boundary layer height from reanalysis data. Bottom right: The equivalent daily scatter plot between enhanced tropospheric BrO (above 7.0×10^{13} molecules/cm²) and ERA-5 boundary layer height.

Here, the correlations improve; for the top left time-series, a positive correlation of +0.62 is seen. For most of the years (e.g. 2002 to 2004), the two quantities follow the same evolution pattern. The correlation coefficient for the corresponding daily spring scatter plot is moderate and comparable with the Arctic polar spring (+0.3 here, -0.34 for the Arctic). The sign is different, indicating a different dependence on the boundary layer height due to the differences in the geographical characteristics of the two regions. The correlation drops for the bottom left time-series (enhanced BrO scenes), at +0.23, for the equivalent scatter plot. Therefore, we follow that the correlation between tropospheric BrO VCD and boundary layer height is stronger during spring.

In Figure 4.33, comparisons of the trend maps of tropospheric BrO VCD and boundary layer height for both winter and spring for the Hudson Bay are shown:

4. The Relationship between Tropospheric BrO VCD, Sea Ice and Meteorological Conditions

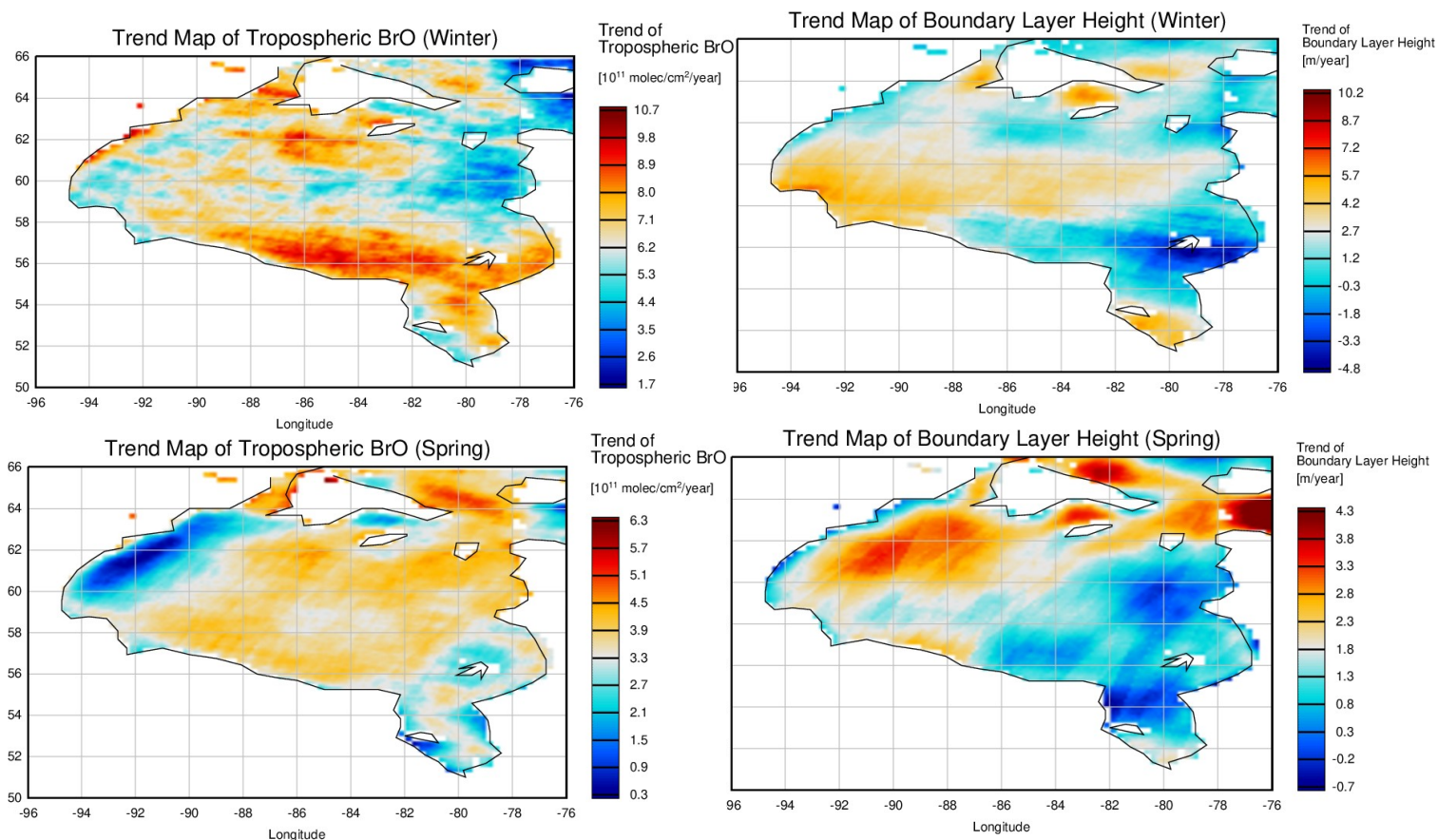


Figure 4.33: Spatial trend patterns of tropospheric BrO VCD and boundary layer height for the Hudson Bay. Top left: trend map of tropospheric BrO during the winter period. Top right: trend map of boundary layer height during the winter period. Bottom left: trend map of tropospheric BrO VCD during the spring period. Bottom right: trend map of boundary layer height during the spring period.

In the two central regions where the most profound increase of tropospheric BrO is seen (in the southeast and north of the Bay), there is a decrease of boundary layer height of around 1 meter per year. This can be seen even in the small region on the west edge of the Bay. A similar agreement can be seen for the spring months as well. The difference is that here, as also mentioned in the time-series (Figure 4.32), the spatial correlation is positive. In the west of the Bay, where the slowest increase of tropospheric BrO VCD occurred, the boundary layer height shows one of its most robust increases, of approximately 3.5 meters per year. Similar conclusions can also be made in the top east area of the Bay and on the north of it (precisely between Southampton and Coats Islands). Therefore, we conclude that spatial trend patterns of boundary layer height are correlated to spatial trend patterns of tropospheric BrO plumes. However, the magnitude and the sign of the correlation are not straightforward and depend on the season (for the Hudson Bay) and other meteorological parameters.

4.6 Relationship of Tropospheric BrO VCD and Other Parameters

In this section, the relationship of some other parameters to the formation of tropospheric BrO VCD will be discussed. The reason they are presented all together in a sub-chapter is that either their relationship is not that strong (both from previous literature research and from our results), or because the coverage and the technical attributes of the datasets (e.g. resolution) do not fully match the ones of the tropospheric BrO VCD dataset.

4.6.1 Sea Ice Thickness

The first parameter of this section will be sea ice thickness, which may be another indication of the salinity of sea ice. From literature, we know that multi-year ice is thicker than first year ice, which is more fragile and, in many cases, breaks every polar summer, giving its place to open water (Kaleschke et al., 2004). The dataset which provides sea ice thickness measurements is the ASR-2 reanalysis data. Therefore, its temporal span is from 2000 to 2016. Also, data is available only for the Arctic region. In Figure 4.34, the time-series and scatter plot between polar springs between tropospheric BrO VCD and sea ice thickness is shown for all scenes available and the enhanced ones (i.e. tropospheric BrO above 7.0×10^{13} molecules/cm²):

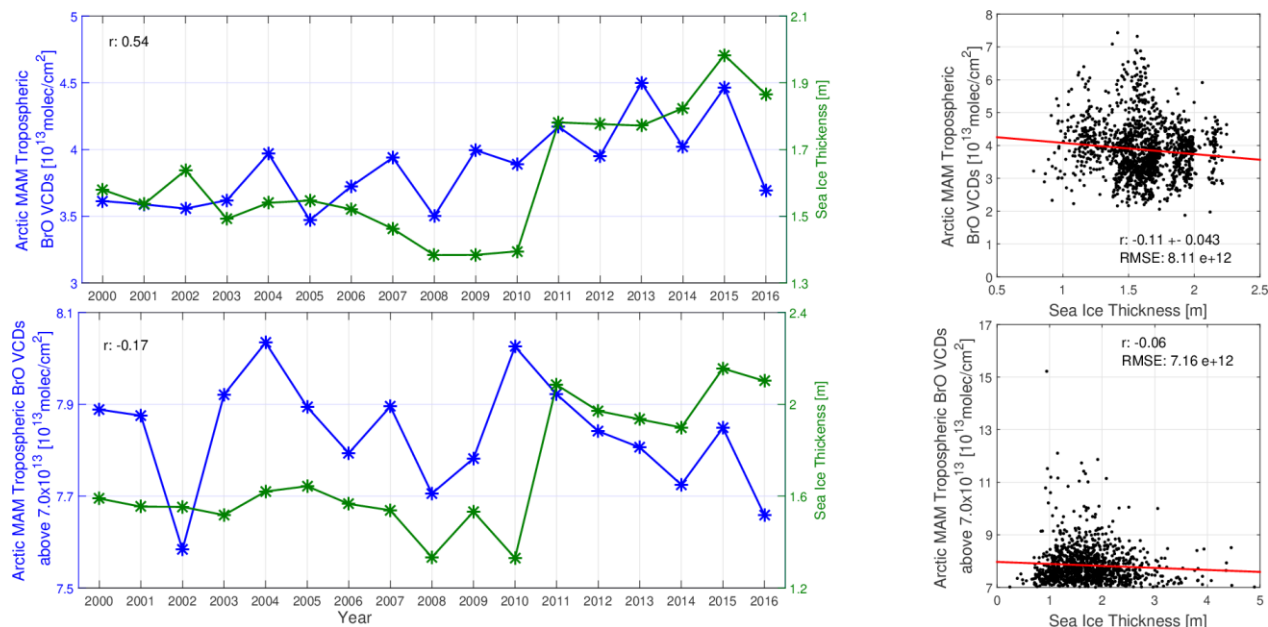


Figure 4.34: Time-series and scatter plots of tropospheric BrO VCDs and sea ice thickness. Top left: Polar spring averaged time-series of tropospheric BrO VCDs and sea ice thickness from ASR-2 reanalysis data. Top right: The equivalent daily scatter plot between tropospheric BrO and sea ice thickness. Bottom left: Polar spring averaged time-series of enhanced tropospheric BrO VCDs (above 7.0×10^{13} molecules/cm²) and sea ice thickness from ASR-2 reanalysis data. Bottom right: The equivalent daily scatter plot between enhanced tropospheric BrO (above 7.0×10^{13} molecules/cm²) and sea ice thickness.

4. The Relationship between Tropospheric BrO VCD, Sea Ice and Meteorological Conditions

There is a general agreement in the long-term time-series (top left) between tropospheric BrO VCD and sea ice thickness (+0.54 correlation coefficient). Similar to the first year ice extent (Figure 4.3), there is an increase in sea ice thickness from 2011 onwards. This can be attributed to the fact that thinner ice grows faster than thicker, more insulated ice. The increase of first year ice extent increases sea ice thickness. When we focus on the top right scatter plot, we see that the correlation drops significantly (and changes sign, -0.11). No clear conclusion can be drawn. Both correlations drop for the bottom subplots (the time-series have a correlation coefficient of -0.17, while the corresponding daily data scatter plot is -0.06). First year ice extent better explains the changes of tropospheric BrO VCD, while the sea ice thickness is a similar quantity and does not add new conclusions.

In Figure 4.35, the trend maps of tropospheric BrO VCD and sea ice thickness for the Arctic region are presented. It should be noted that the tropospheric BrO VCD trend map is different from the ones present before (e.g. in Figure 4.9), as here the calculation period is limited to the availability of ASR-2 data, i.e. from 2000 to 2016:

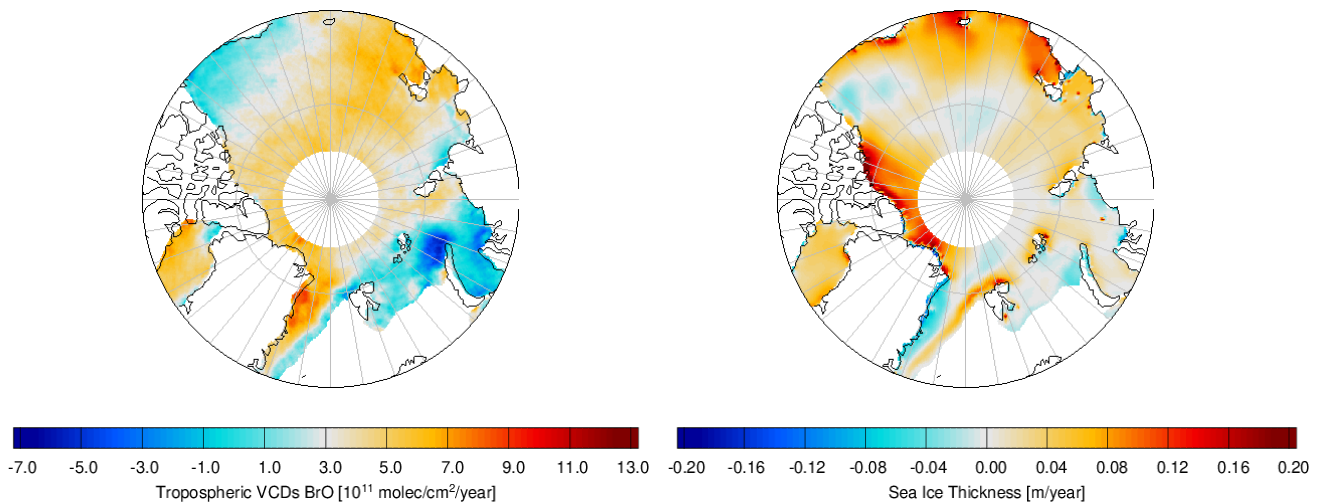


Figure 4.35: Spatial trend patterns of tropospheric BrO VCD (left) and sea ice thickness (right) for the Arctic region.

The sea ice thickness trend map resembles the one of first year ice frequency (Figure 4.9). The area where the most profound increase of tropospheric BrO VCD occurred (east of Greenland) is where the sea ice thickness decreased (and consequently, first year occurrence increased). Sea ice thickness increased over the north of Greenland and the Canadian Archipelago, where tropospheric BrO VCD shows a slight increase. It seems that the sea ice thickness dataset does not add any new information regarding the appearance of enhanced tropospheric BrO plumes, especially since the comparison with sea ice age and first year ice extent has been already made.

4.6.2 Vertical Wind Velocity

4. The Relationship between Tropospheric BrO VCD, Sea Ice and Meteorological Conditions

The next meteorological parameter discussed is the vertical wind velocity. This variable is included in the ERA-5 reanalysis dataset and is provided on many pressure levels. Here, we selected the surface level to determine whether the movement of air masses at the surface in the regions with larger values of tropospheric BrO VCD has an upward or downward direction. This movement may reveal upward or downward movement of enhanced tropospheric BrO. This variable can be considered “supportive” and not one of the main ones that influence enhanced tropospheric BrO plumes. Since the values of vertical wind velocity can be both negative and positive, calculating long-term averages can draw us to wrong conclusions. As the vertical wind speed is given in pressure coordinates, negative values of vertical velocity indicate upward motion. The same figures as before for the sea ice thickness will be presented. Figure 4.36 includes time-series and scatter plots of all scenes and those with enhanced tropospheric BrO VCD:

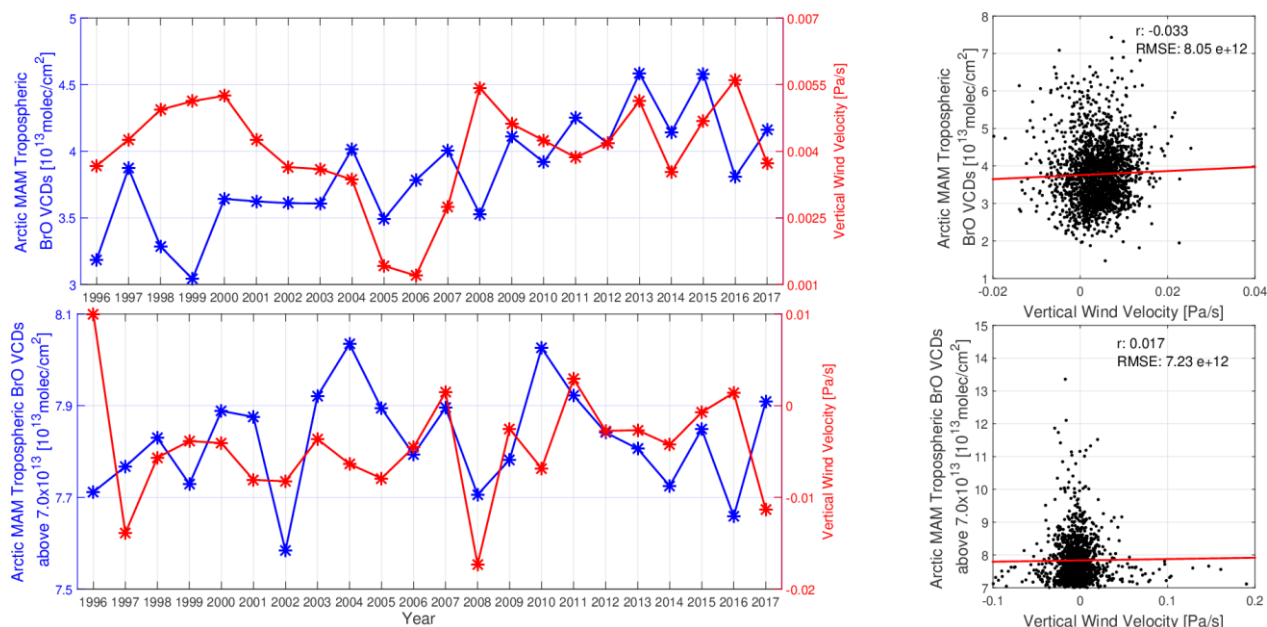


Figure 4.36: Time-series and scatter plots of tropospheric BrO VCDs and vertical wind velocity. Top left: Polar spring averaged time-series of tropospheric BrO VCDs and vertical wind velocity from ERA-5 reanalysis data. Top right: The equivalent daily scatter plot between tropospheric BrO VCD and vertical wind velocity. Bottom left: Polar spring averaged time-series of enhanced tropospheric BrO VCDs (above 7.0×10^{13} molecules/cm²) and vertical wind velocity from ERA-5 reanalysis data. Bottom right: The equivalent daily scatter plot between enhanced tropospheric BrO VCD (above 7.0×10^{13} molecules/cm²) and vertical wind velocity.

There is practically no correlation between tropospheric BrO VCD and vertical wind velocity. The correlation coefficients between all four subplots are close to zero and therefore negligible. Both positive and negative values of vertical wind velocity make the long-term averaging of them a difficult task.

In Figure 4.37, the trend maps of tropospheric BrO VCD and vertical wind velocity for the Arctic region are shown:

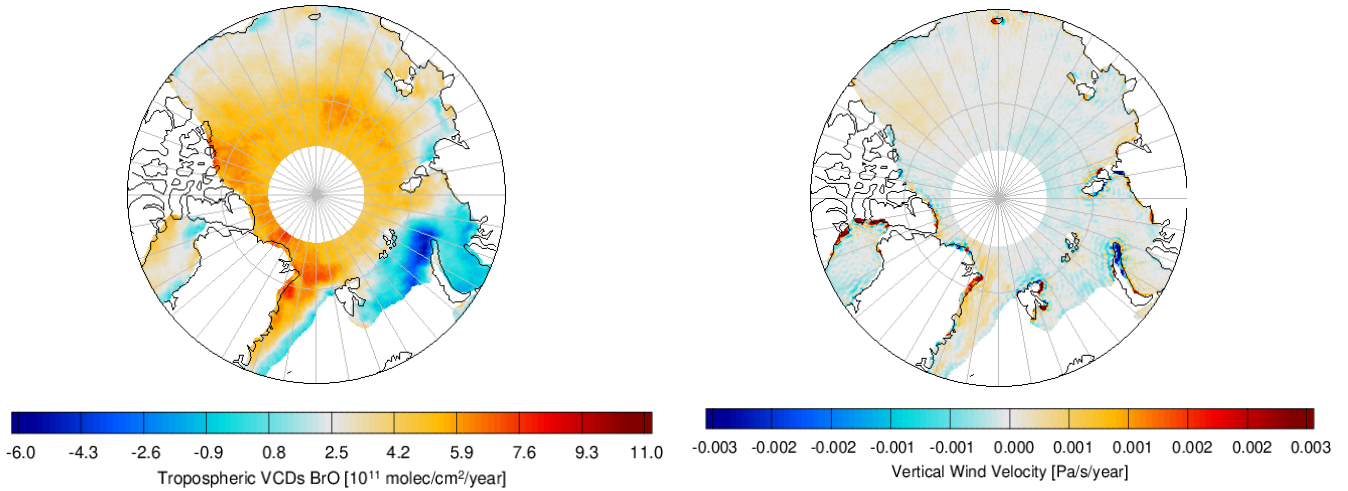


Figure 4.37: Spatial trend patterns of tropospheric BrO VCD (left) and vertical wind velocity (right) for the Arctic region.

The vertical velocity fluctuations are minimal, and the small changes that are occurring can be considered negligible. In the region where we have the most profound increase of tropospheric BrO VCDs (northeast of Greenland), the vertical wind velocity shows a minimal upward trend. Since the quantity includes negative values, it is challenging to infer whether this positive trend means less uplifting (as negative values indicate an upward movement of air masses) or more downward movement occurred.

4.6.3 Cyclone Activity

The last meteorological parameter that we will investigate is cyclone activity. Although this dataset spans over an equally long-term period as the tropospheric BrO VCD dataset, it lacks spatial resolution. It was too sparse to spatially and temporally interpolate it to the satellite orbits, as we did with all the previous reanalysis datasets. Since it is a vital meteorological parameter for enhanced BrO plumes, some of its aspects will be presented. The dataset was provided by Akperov et al. (2019). More specifically, the number of cyclones that appeared every year and their intensity (the depth or intensity of a cyclone is determined as the difference between the pressure in a cyclone's geometric centre and its outermost closed isobar) (Akperov et al., 2019) will be discussed. Figure 4.38 shows the number of cyclones that occurred every year and the maximum intensity of each cyclone, together with the tropospheric BrO VCDs, averaged for every polar spring:

4. The Relationship between Tropospheric BrO VCD, Sea Ice and Meteorological Conditions

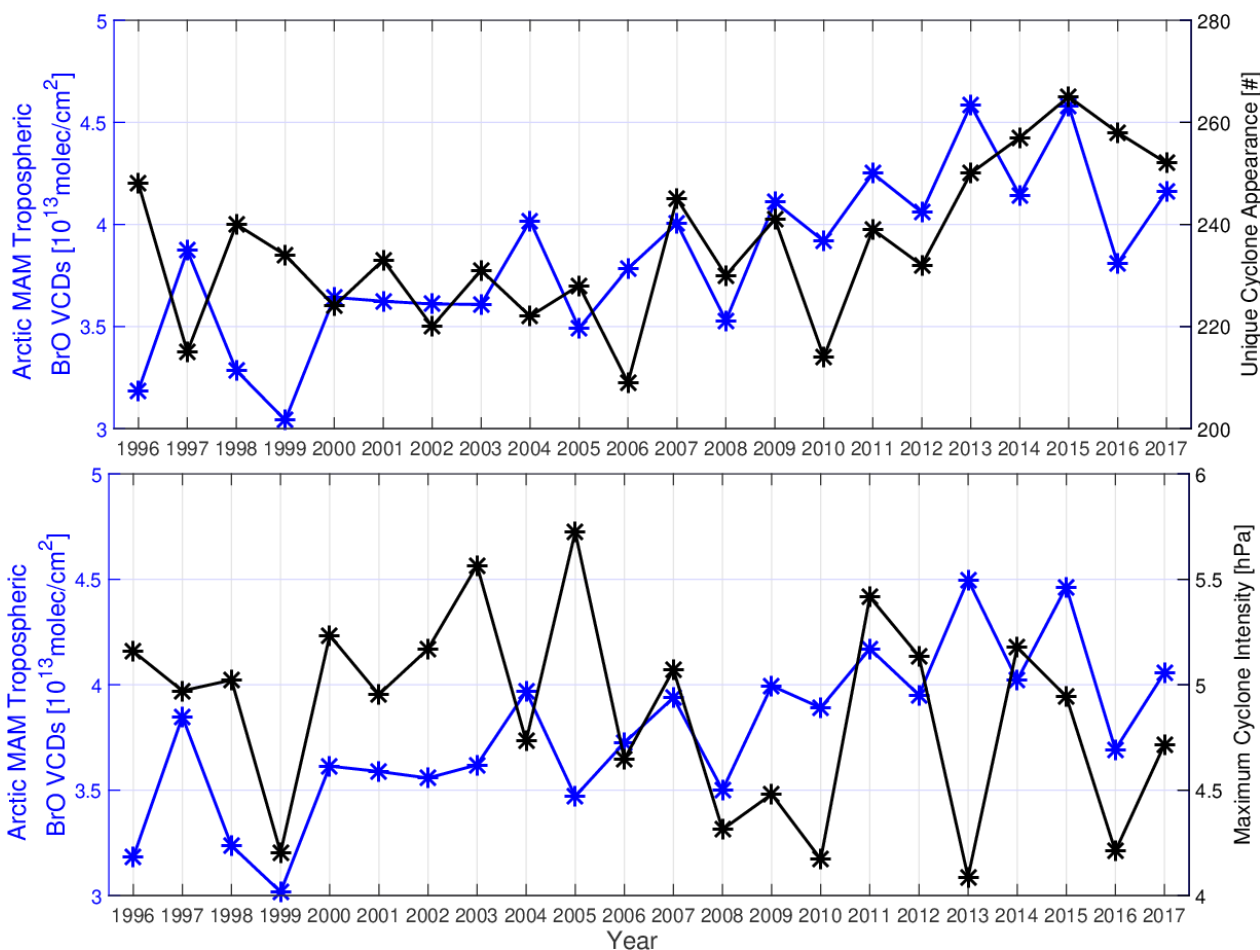
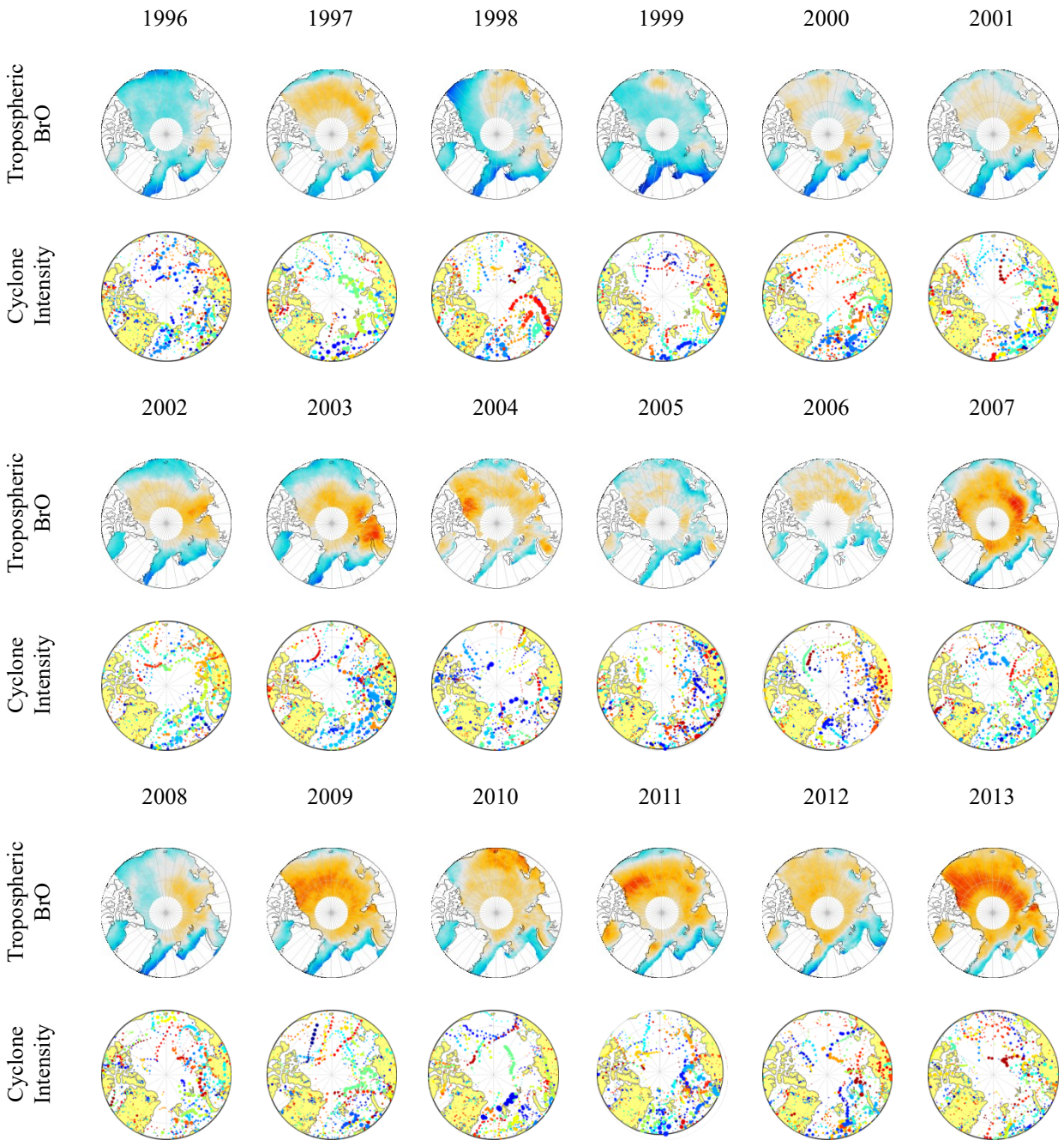


Figure 4.38: Time-series of tropospheric BrO VCDs and cyclone activity. Top: Polar spring averaged time-series of tropospheric BrO VCDs and unique cyclone frequency. Bottom: Polar spring averaged time-series of tropospheric BrO VCDs maximum cyclone intensity.

For the top subplot, where the frequency of cyclone appearance is shown, we considered for every cyclone a unique appearance. In the cyclone dataset, every cyclone is recorded many times, from its genesis to its depletion. Here, for each cyclone instance, we have considered every cyclone only once. There is a general agreement between the two quantities, as both increase over time. In most cases, the correlation is positive (e.g. from 2007 to 2011). The correlation coefficient is moderate, with a value of +0.32. Regarding the bottom plot, between tropospheric BrO VCDs and the maximum cyclone intensity (i.e. we considered the maximum intensity from each cyclone's instance), a strong correlation between the quantities is not seen. Since the maximum intensity seems to decrease over the years, the correlation coefficient has a weak negative value of -0.11. As discussed before, these datasets are not temporally or spatially interpolated to the satellite's orbits due to the resolution of the cyclone dataset.

In Figure 4.39, polar spring averaged maps of tropospheric BrO VCD, together with cyclone intensity maps, are presented. Every cyclone's track and instance is denoted with a specific color, while the magnitude of each circle shows the intensity of each instance:

4. The Relationship between Tropospheric BrO VCD, Sea Ice and Meteorological Conditions



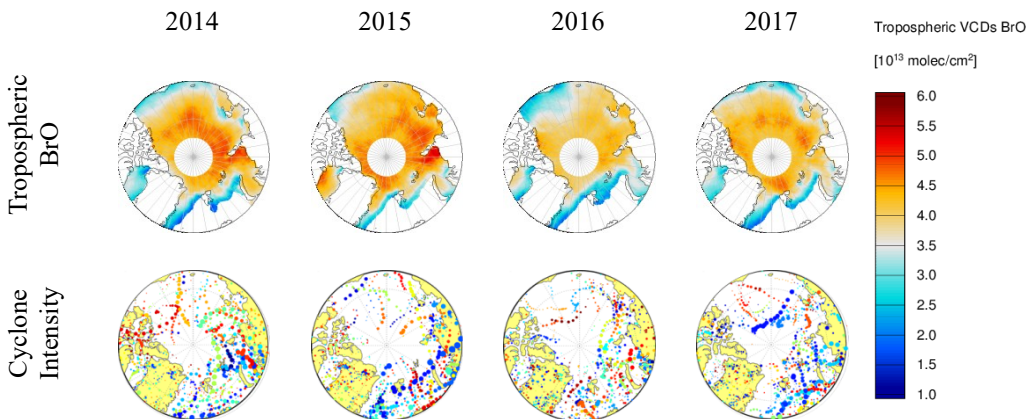


Figure 4.39: Polar spring average maps of tropospheric BrO VCDs [molec/cm^2] and cyclone intensity.

In these maps, every instance of each cyclone is depicted. For example, in 1998, the red circles starting from the Kara Sea and ending in the Arctic Ocean correspond to the same cyclone. For some years, the cyclone activity agrees with the enhanced tropospheric BrO VCD of that year (e.g. 2003, 2007). However, there are also years where the substantial BrO plumes are not in agreement with the intensity and appearance of cyclones (e.g. 2013, 1999). It is interesting but not necessarily related that similar conclusions were drawn from the equivalent wind speed comparisons (i.e. Figure 4.23), although a high wind speed does not imply a cyclone appearance. Still, the two quantities are related. If we focus on the long term spatial increase of tropospheric BrO plumes, we see that increased cyclonic activity cannot explain it (i.e. we do not see increased activity from 2009 onwards inside the Arctic Ocean, compared to previous years, as we do for tropospheric BrO VCDs).

4.7 Summary and Conclusions

In this chapter, the relationship between tropospheric BrO VCDs and some of the most critical driving mechanisms of bromine release and enhanced BrO formation discussed in the literature were thoroughly investigated. Sea ice conditions (i.e. sea ice age, first year ice extent and sea ice thickness) are known to influence the release of bromine molecules into the atmosphere (Blechschmidt et al., 2016; Choi et al., 2018; Jones et al., 2009). For the Arctic, we have seen that the long-term increase of first year ice is in agreement with the increase of tropospheric BrO VCDs, with a correlation coefficient of +0.62 for the time-series of polar spring averages and a correlation coefficient of +0.32 for the daily data scatter plot. A similar correlation can be seen between tropospheric BrO and sea ice age (i.e. -0.72 for the time-series of polar spring averages, -0.32 for the daily data scatter plot). Therefore, we infer that sea ice age is an essential parameter for assessing the changes we see in tropospheric BrO VCDs due to Arctic Amplification. These conclusions can also be validated by polar spring map comparisons between tropospheric BrO VCDs and first year ice extent. These findings come, however, in contrast to the findings of Choi et al. (2018). They used the operational product of the OMI instrument (from 2005 to 2015) and

the same stratospheric separation method as applied here. However, the OMI dataset does not increase as the GOME-2A and GOME-2B data in later years, potentially due to the row anomaly of the OMI instrument. Therefore, they found a negative correlation of -0.35 between tropospheric BrO VCD and first year ice extent.

Regarding the meteorological parameters, which were investigated for both the Arctic and the Hudson Bay, we follow that air temperature seems to be the most significant meteorological parameter for the development of enhanced tropospheric BrO plumes. For both the Arctic and the Hudson Bay, we see strong anti-correlation (i.e. -0.53 for the daily polar spring Arctic scatter plot, -0.46 for the Hudson Bay winter period and -0.77 for the Hudson Bay spring period). Similar conclusions have been drawn by Seo et al. (2020). They performed a ten years analysis for the Arctic and Antarctic, using data from the GOME-2A instrument. Temperature was also the most strongly correlated meteorological parameter in their research for the Arctic region. A very good spatial agreement can also be seen, in all three cases, by comparing trend maps of tropospheric BrO VCD and air temperature. Wind speed magnitude also correlates with the tropospheric BrO VCD dataset, although not in a clear way and not for both the Arctic and the Hudson Bay. Wind speed has a positive correlation coefficient of +0.26 for the polar springs of the Arctic, and spatially from the corresponding trend map, a decrease of wind speed can be seen in the area where the increase of tropospheric BrO VCD is profound. For the Hudson Bay during the winter periods, a spatial anti-correlation can be seen from the trend map comparison, but the equivalent correlation coefficient from the daily scatter plot is very low. Finally, boundary layer height has a moderate daily correlation coefficient of -0.34 for the daily scatter plot of the Arctic polar spring region and a good spatial agreement from the corresponding trend maps too. Similar to wind speed, the correlation of boundary layer height to tropospheric BrO VCD for the Hudson Bay can only be seen from the trend maps, especially during winter.

Table 4.1 summarizes and highlights the essential correlations that were presented in this chapter:

4. The Relationship between Tropospheric BrO VCD, Sea Ice and Meteorological Conditions

Table 4.1: Summary of the most significant correlations between tropospheric BrO and its driving mechanisms.

Driving Parameter	Arctic	Hudson Bay Winter	Hudson Bay Spring
First year ice extent	+0.62 (yearly) +0.32 (daily)	-	-
Sea ice age	-0.72 (yearly) -0.33 (daily)	-	-
Air temperature	-0.53 (daily)	-0.46 (daily)	-0.77 (daily)
Mean sea level pressure	-0.12 (daily)	-2.23 e-02 (daily)	-0.043 (daily)
Wind speed	+0.26 (daily)	+0.011 (daily)	+0.075 (daily)
Boundary layer height	-0.34 (daily)	-0.04 (daily)	+0.3 (daily)

5. ARTIFICIAL INTELLIGENCE FOR TROPOSPHERIC BRO VCD MODELING

In the previous chapter, the link of tropospheric BrO VCD in the Arctic to some major driving parameters of bromine explosion was presented. Although we have found strong correlations to first year ice extent and 2 meter air temperature, it remains unclear to what extent the potential driving parameters affect the release of bromine molecules and the formation of enhanced tropospheric BrO plumes. This is mainly due to the non-linearity that links BrO to its driving mechanisms, the complexity and rapid chemical nature of bromine explosion events and the deep interactions of all the parameters involved. This chapter will extend the comparison of sea ice conditions and meteorological parameters to tropospheric BrO VCD and apply a machine learning approach to model tropospheric BrO VCD from some of the critical parameters that were discussed in the previous chapter. More specifically, we will test if an artificial neural network, which takes as inputs sea ice age, 2 meter air temperature, mean sea level pressure, 10 meter wind speed and direction and boundary layer height, can reproduce the satellite retrieved tropospheric BrO VCD value. All the results discussed are for the Arctic region only and during polar spring periods. The theoretical background of neural networks was presented in chapter 1, while the technical aspects of this machine learning approach were described in chapter 2. Here, sensitivity tests will be presented to identify the influence of each of the input parameters on the modeled tropospheric BrO VCD output. Also, case studies of specific days will be shown, where the artificial neural network performs well, and the output BrO is close to the satellite measurements and days where the output is not in agreement with the measurements. Finally, long-term tropospheric BrO VCD model outputs will be discussed and compared with the satellite measurements, while future and past estimations of polar spring averaged tropospheric BrO maps will also be shown. The chapter will end with a summary and conclusions section.

5.1 Sensitivity Tests

In chapter 2 (i.e. Figure 2.17 top), after performing the neural network training procedure with each year as the training dataset, we concluded that 2007 yields the best performance when we compare the satellite measurements of tropospheric BrO VCD and the output of the neural network. All the results presented in this chapter will be based on the neural network trained with data from 2007. The six input parameters used are namely: sea ice age, 2 meter air temperature, mean sea level pressure, 10 meter wind speed, boundary layer height and 10 meter wind

direction. In this sub-section, the evaluation of the influence of each input parameter on the performance of the network on reproducing satellite retrievals of tropospheric BrO is discussed. In Figure 5.1, seven scatter plots are shown. The first one is with all critical parameters as inputs, while we will be removing one input parameter from each one of the others to see how the performance of the network is affected.

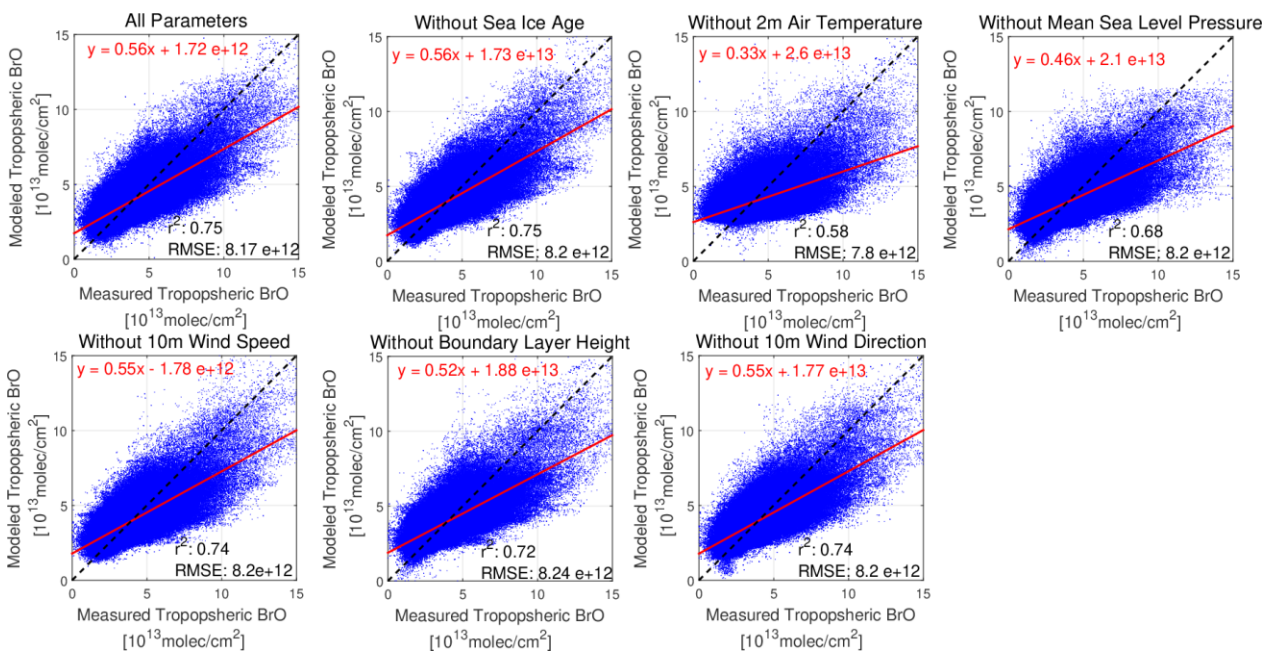


Figure 5.1: Sensitivity tests for the importance of each input parameter, through scatter plots between measured and modeled tropospheric BrO VCD during the training process (2007 polar spring as training dataset).

Sea ice age is the least important parameter regarding the performance of the outputs of the network when compared to the actual measurements. This comes in contradiction to conclusions drawn in chapter 4, where sea ice age (and especially first year ice extent) was identified as a vital parameter to the long-term changes of tropospheric BrO VCDs. This different behaviour can be attributed to the static nature of the sea ice and the fact that the neural network has not seen the long-term evolution of it (as it is trained only with a single year, 2007). Boundary layer height and wind parameters seem to have equal weight on the performance of the neural network, while temperature and mean sea level pressure have a drastic impact on the reproduction of tropospheric BrO VCD. We infer from the scatter plots that temperature is the most critical parameter, as, without it, the correlation coefficient drops to 0.58 (from 0.75 in the case of using all input parameters), while the slope of the best fitting line is 0.33 (from 0.56 respectively). The root mean square error slightly improves (7.8×10^{12} from 8.17×10^{12}). Without mean sea level pressure, the correlation coefficient is 0.68, the slope of the best fitting line 0.46, while the root mean square error 8.2×10^{12} . As stated in chapter 4, temperature is the most crucial meteorological parameter on a daily data basis for the development of enhanced tropospheric BrO plumes, so this result is in accordance with the analysis. Mean sea level pressure was not strongly related to

tropospheric BrO VCD from the statistical analysis performed in chapter 4. We see that it is the second most important parameter for the successful and accurate modeling of tropospheric BrO VCD by the neural network.

Figure 5.2 shows the impact of each input variable, but this time focusing on the projection of other years, rather than the training dataset of 2007. For each year, a polar spring average of the daily spatial root mean square errors and daily spatial correlation coefficients between the measured tropospheric BrO VCDs and the modeled one is shown.

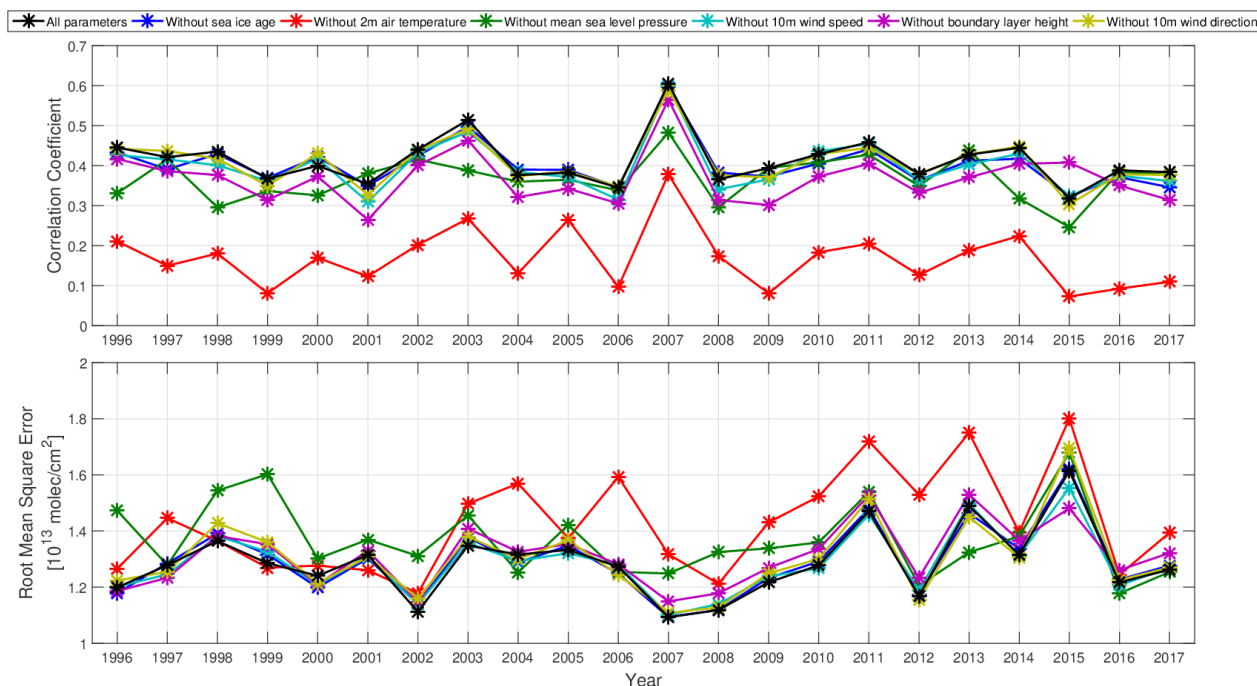


Figure 5.2: Sensitivity tests for the importance of each input parameter for the reproduction of satellite retrieved tropospheric BrO VCDs based on the neural network. Top: the polar spring averaged spatial correlation coefficient of each year between measured and modeled tropospheric BrO VCDs. Bottom: the polar spring averaged spatial root mean square error of each year between measured and modeled tropospheric BrO VCDs.

In the top subplot, if 2m air temperature is excluded from the input parameters, the network's performance drops significantly, as the corresponding red curve is significantly below the others (and for many years, the difference is of a factor of 2). The second most important parameter is the boundary layer height here (and for some years mean sea level pressure), in contrast to the previous scatter plots, where pressure was more important for the network (i.e. lower correlations without it). All the other parameters have a less significant effect on the spatial correlation coefficient and do not significantly alter the network's performance (i.e. when compared with the black curve). It is interesting that for some years, the exclusion of one variable yields better results. Such an example is 2015, where, if boundary layer height is excluded, the spatial correlation coefficient increases. Since the boundary layer height had a very low polar spring average value (i.e. Figure 4.28), the weights the neural network assigned to boundary layer height from the training with 2007 process do not give realistic outcomes for 2015. Regarding the

evaluation of the spatial root mean square errors of the comparison between measured and modeled tropospheric BrO VCDs for each year, a similar change in performance is seen. Air temperature at 2 meters is again the most vital parameter, however, in this case, only starting from 2003 onwards. For the early years, mean sea level pressure is the most significant input parameter, and it stays the second most important for the rest of the years, with some exceptions (i.e. 2013, where, by excluding it, the network yields better results). The general outcome of Figure 5.2 is that 2m air temperature and mean sea level pressure are the two most significant parameters, with boundary layer height following.

It is meaningful to investigate the impact of each input parameter on the magnitude of the modeled tropospheric BrO VCDs. For this purpose, we will range each input variable between the typical minimum and maximum values that appear in the dataset while keeping the other parameters in specific constant values (more specifically, the polar spring average of 2007). Sea ice age was kept at 2.6 years, 2m air temperature at 260 Kelvin, mean sea level pressure at 1015 hPa, 10m wind speed at 6.2 m/s, boundary layer height at 456 m and wind direction at 183 degrees. In this way, we can see the effect of each input (and its changing value) on the magnitude of tropospheric BrO VCD:

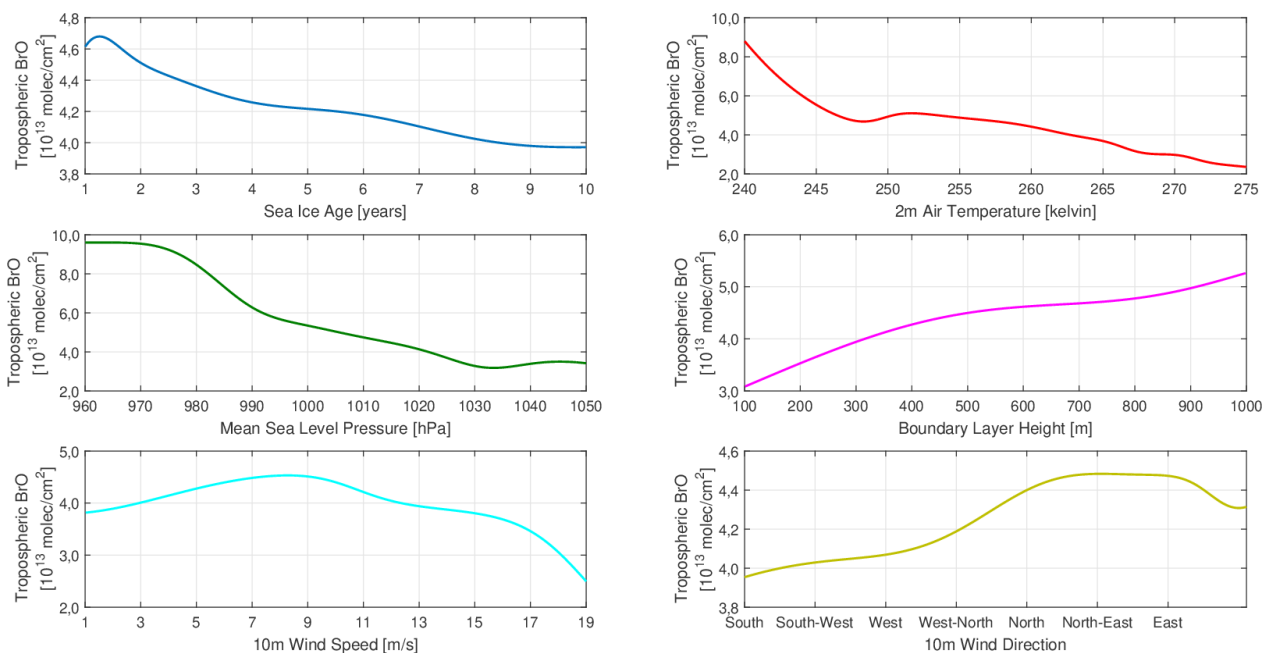


Figure 5.3: Effect of each input parameter on the magnitude of modeled tropospheric BrO VCD. On the x-axis of each subplot, the ranging input parameter is shown, while all the other inputs are assigned the constant value of their polar spring average of 2007.

We infer that 2m air temperature and mean sea level pressure have the most significant impact on the magnitude of tropospheric BrO VCDs. As the air temperature increases, modeled tropospheric BrO VCD decrease, almost at an exponential pace. There is a slight increase in the rate of the decrease at around 245 Kelvin. After 250 Kelvin, the decrease continues at an almost linear pace. The magnitude of tropospheric BrO VCDs ranges from 9.0×10^{13} molecules/cm² to

2.0×10^{13} molecules/cm² by varying 2m air temperature from 240 to 275 Kelvin. Similar conclusions can be drawn from the subplot of mean sea level pressure; modeled tropospheric BrO VCD drop at an exponential rate until approximately 990 hPa, and then follow a linear decrease. The range of modeled tropospheric BrO VCDs is also similar to the ones of the temperature subplot. Regarding sea ice age, the peak of modeled tropospheric BrO VCD occurs on first year ice, and afterwards, a decrease is shown. The range of the magnitude of modeled tropospheric BrO VCDs does not change much by varying sea ice age from 1 to 10 years. Sea ice age does not have a substantial impact on the reproduction of tropospheric BrO VCDs. Boundary layer height seems to increase almost linearly with increasing modeled tropospheric BrO VCDs. This positive relationship contradicts the top right scatter plot of Figure 4.28, where an anti-correlation between boundary layer height and tropospheric BrO VCDs was shown. As the network was trained with 2007 values, it has built the relationships between the input parameters and tropospheric BrO VCD based on the conditions of that year. In Figure 4.29, the maps of tropospheric BrO and boundary layer height for 2007 show that enhanced BrO occurred this year over (compared to other years) higher average values of boundary layer height. This may be the reason the neural network shaped such a strong positive relationship between the two quantities. When we focus on wind speed, tropospheric BrO VCDs reach their peak at around 9 m/s of wind speed and then decrease. By investigating the corresponding polar spring maps (Figure 4.23), we see that in 2007, enhanced tropospheric BrO VCD occurred over (compared to other years) higher average wind speeds of approximately 7.5 m/s. It may be that, during 2007, no higher wind speeds occurred (or when they occurred, low tropospheric BrO VCD were evident), and therefore the neural network estimates a decrease of tropospheric BrO as the wind speed gets higher.

Since in every subplot of Figure 5.3 specific constant values for the other input parameters (i.e. the polar spring averages of 2007) were chosen, it is meaningful to see how the neural network will perform if we choose other constant values every time we span each input parameter projected on the x-axis. In Figure 5.4, 22 curves in each subplot are presented. Each one has the polar spring average values of one year of the dataset (i.e. 1996 to 2017). 2007 will be denoted with a thicker black curve to distinguish it from the rest and see whether it differentiates significantly:

5. Artificial Intelligence for Tropospheric BrO VCD Modeling

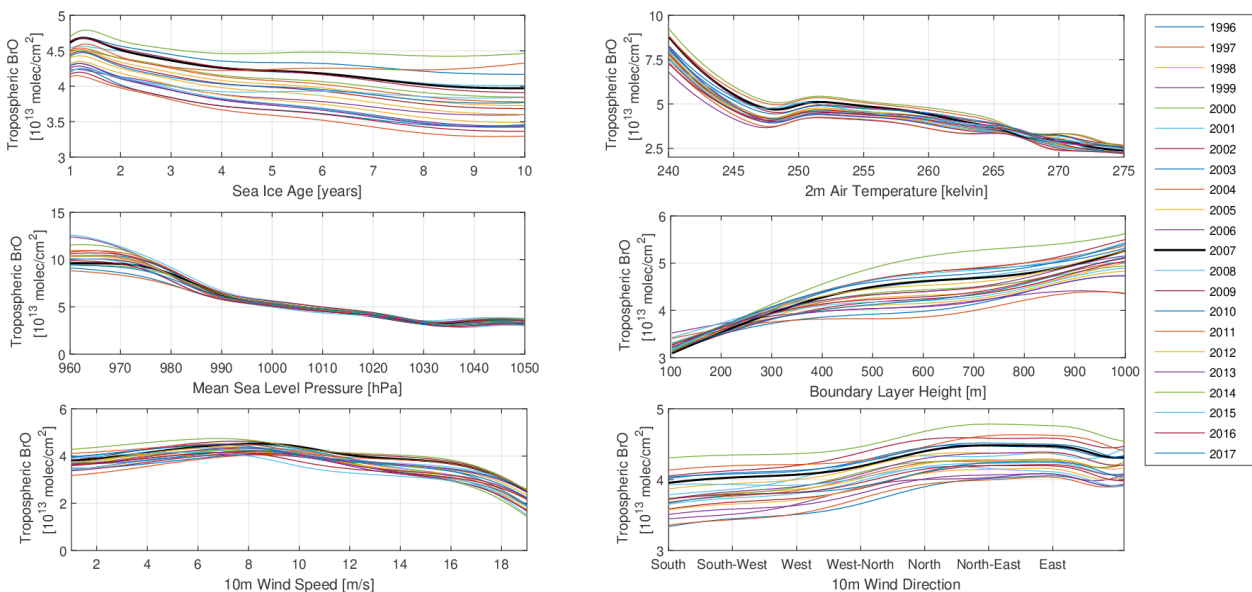


Figure 5.4: Effect of each input parameter on the magnitude of modeled tropospheric BrO VCD. On the x-axis of each subplot, the ranging input parameter is shown, while all the other inputs are assigned the constant value of their polar spring average of each year of the dataset.

In all cases, the 2007 case is similar to the other years, as they follow the same pattern – evolution. There are slight differences for boundary layer height, where for some years (e.g. 2009, the bottom curve of the subplot), modeled tropospheric BrO VCD is not increasing at the same pace as the curve for 2007 (or 2014, which in this case shows the most significant increase). Regarding wind speed, the behaviour of all years is similar, and they all result in decreasing values of modeled tropospheric BrO VCDs for wind speeds more prominent than 8 m/s.

Since all the constant values tried so far were polar spring averages, it is meaningful to try meteorological and sea ice values that favour the formation of enhanced tropospheric BrO VCD from a specific bromine explosion case. The values from the case study of 01.04.2011 will be used. Sea ice age will be set to 1 year, 2m air temperature to 254 Kelvin, mean sea level pressure to 989 hPa, 10m wind speed to 12 m/s, boundary layer height to 820m and 10m wind direction to 130 degrees. These values were chosen as they appear over the regions where enhanced tropospheric BrO plumes also appeared.

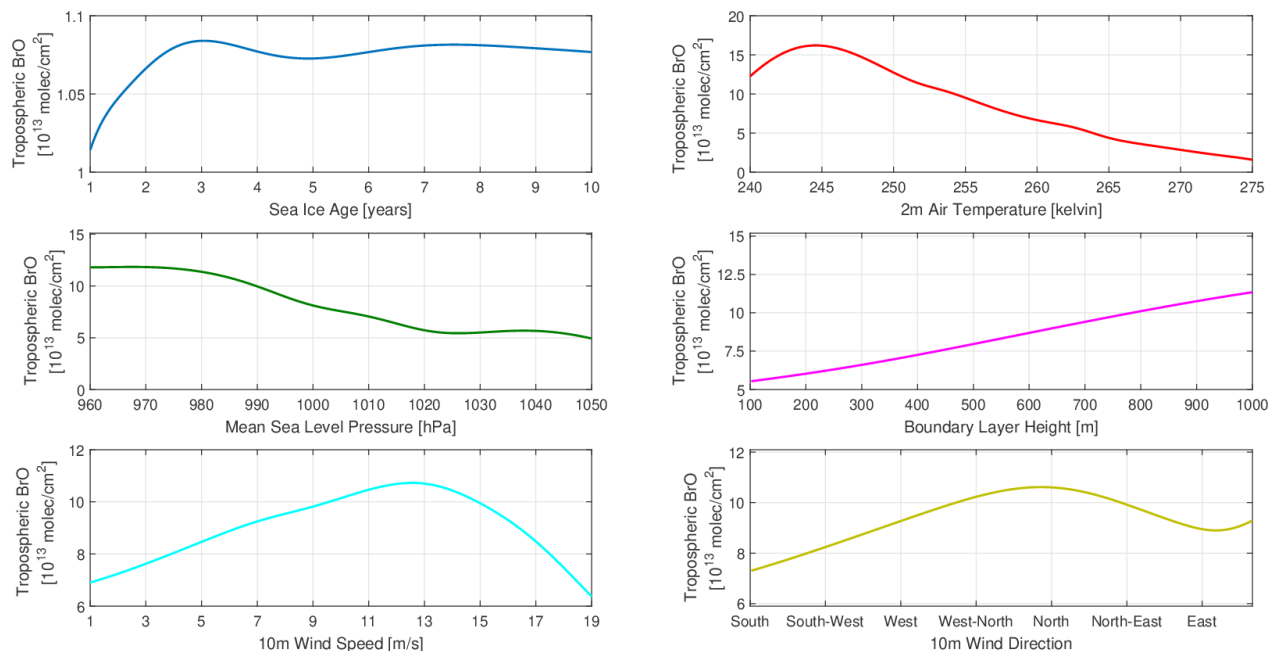


Figure 5.5: Effect of each input parameter on the magnitude of modeled tropospheric BrO VCD. On the x-axis of each subplot, we see the ranging input parameter, while all the other inputs are assigned a typical constant value of conditions that favour enhanced BrO formation.

For sea ice age versus modeled tropospheric BrO VCD, the peak of the magnitude of modeled tropospheric BrO VCD occurs for sea ice of 3 years age. As the sea ice age increases, a decrease of modeled tropospheric BrO VCD is not seen, as for the previous sensitivity tests. The range of modeled tropospheric BrO VCD is small. Sea ice age, in this case, is not affecting the magnitude of modeled tropospheric BrO VCD. Similar responses are seen for all other input parameters, although the range (and therefore the impact of the corresponding input parameter) on modeled tropospheric BrO increased (except mean sea level pressure). This can be attributed to the values we selected for these sensitivity tests, which may be typical for the appearance of enhanced tropospheric BrO, but cannot guarantee that a tropospheric BrO plume will appear. That may be the reason the neural network shows a wide modeled tropospheric BrO VCD range. Regarding 2m air temperature, a slight difference until 245 Kelvin is seen, as modeled tropospheric BrO VCD reaches its peak there (while before, it started decreasing from 240 Kelvin). We can summarize from the sensitivity tests that although we see different responses on the modeled tropospheric BrO VCD, clear patterns exist. The deviations can be attributed to the non-linear nature of the relationships.

5.2 Case Studies

In this section, four daily case studies will be presented, where the measured tropospheric BrO VCDs to the modeled ones will be compared, using the neural network trained with 2007. Also, plots of the sea ice age and meteorological conditions that occurred during these days will be

provided, alongside a comparison of the outputs of neural networks, excluding one input parameter at a time. Figure 5.6 is from 01.04.2011 when we both GOME and SCIAMACHY were providing measurements:

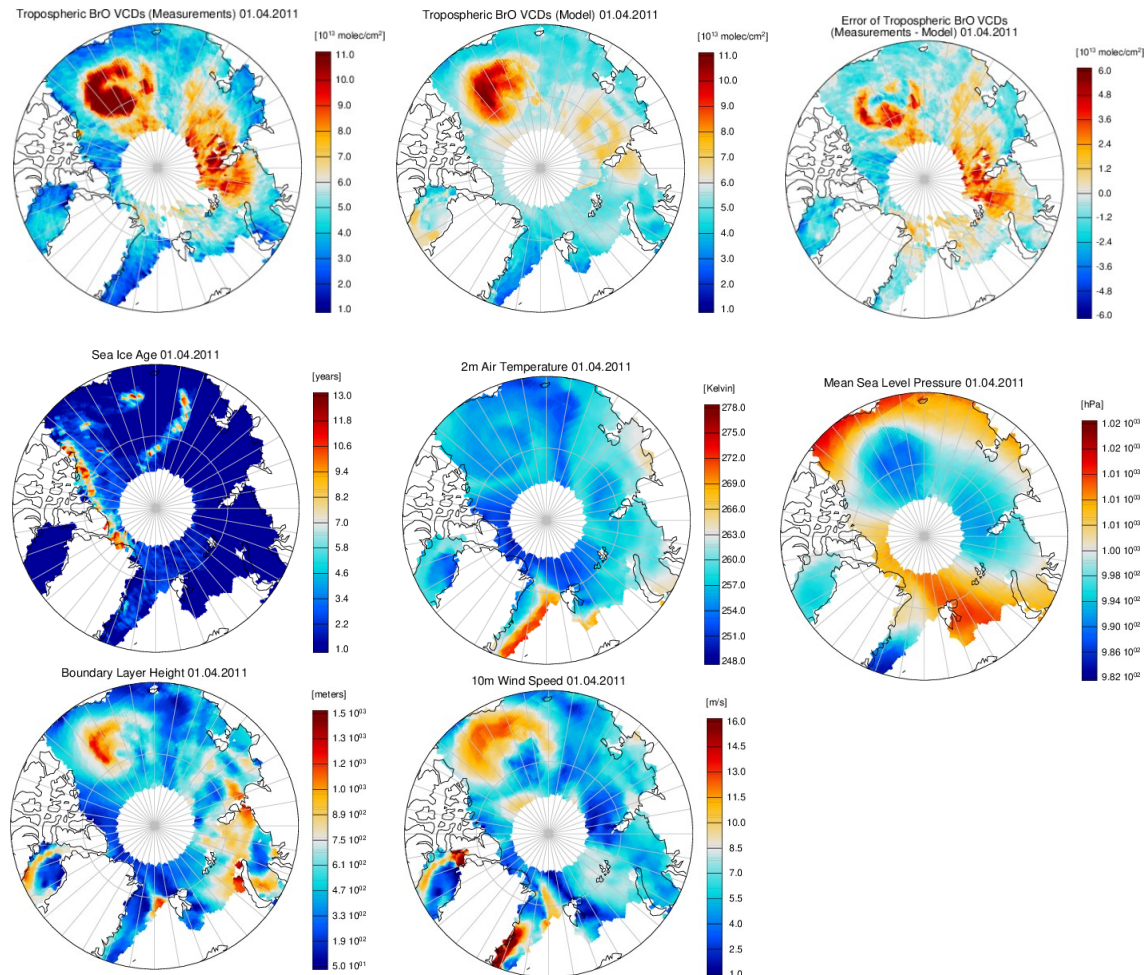


Figure 5.6: Tropospheric BrO VCD measurements, neural network output, the difference between measurements and model, sea ice age and ERA-5 meteorological conditions on the 01.04.2011.

On this day, two enhanced tropospheric BrO plumes occurred in the Arctic, one associated with a cyclone event (over the Beaufort Sea). The neural network can spatially reproduce both plumes, while the magnitude agreement is also acceptable. The modeled tropospheric BrO VCD is slightly higher over the Baffin Bay, but apart from that, there is general agreement over the ambient BrO regions as well. This can be verified by the error map (first row, third column), where the most prominent errors occur over the regions where the enhanced BrO plumes occurred. Regarding the conditions that appeared that day in the Arctic, from the sea ice age map (second row, first column), primarily first year ice was evident over the whole Arctic, especially under the plumes (with a minor exception under the plume over the Beaufort Sea). 2m air temperature (second row, second column) was particularly low in these two regions, while a cyclonic pattern is evident over the Beaufort Sea. However, it should be stated that there were colder regions during that day, where however, no tropospheric BrO plume appeared. We can

infer from the mean sea level pressure (second row, third column) that low pressure systems appeared over both regions of enhanced tropospheric BrO VCD during that day. This is in agreement and verifies the previous results, suggesting that low pressure systems are an indicator for the neural network for enhanced BrO plumes, as they potentially include conditions that favour the formation of enhanced tropospheric BrO VCD. Boundary layer height was high in both regions (but high elsewhere as well, where the neural network did not predict enhanced BrO), while 10m wind speed shows high values for the plume at the Beaufort Sea but low values for the second plume. The neural network spatially identified both regions of high tropospheric BrO VCD, independently of the wind speed velocity.

In Figure 5.7, neural network outputs will be compared, where we exclude one input parameter at a time, in order to investigate the impact of each parameter on the successful spatial prediction of the reconstruction of tropospheric BrO plumes:

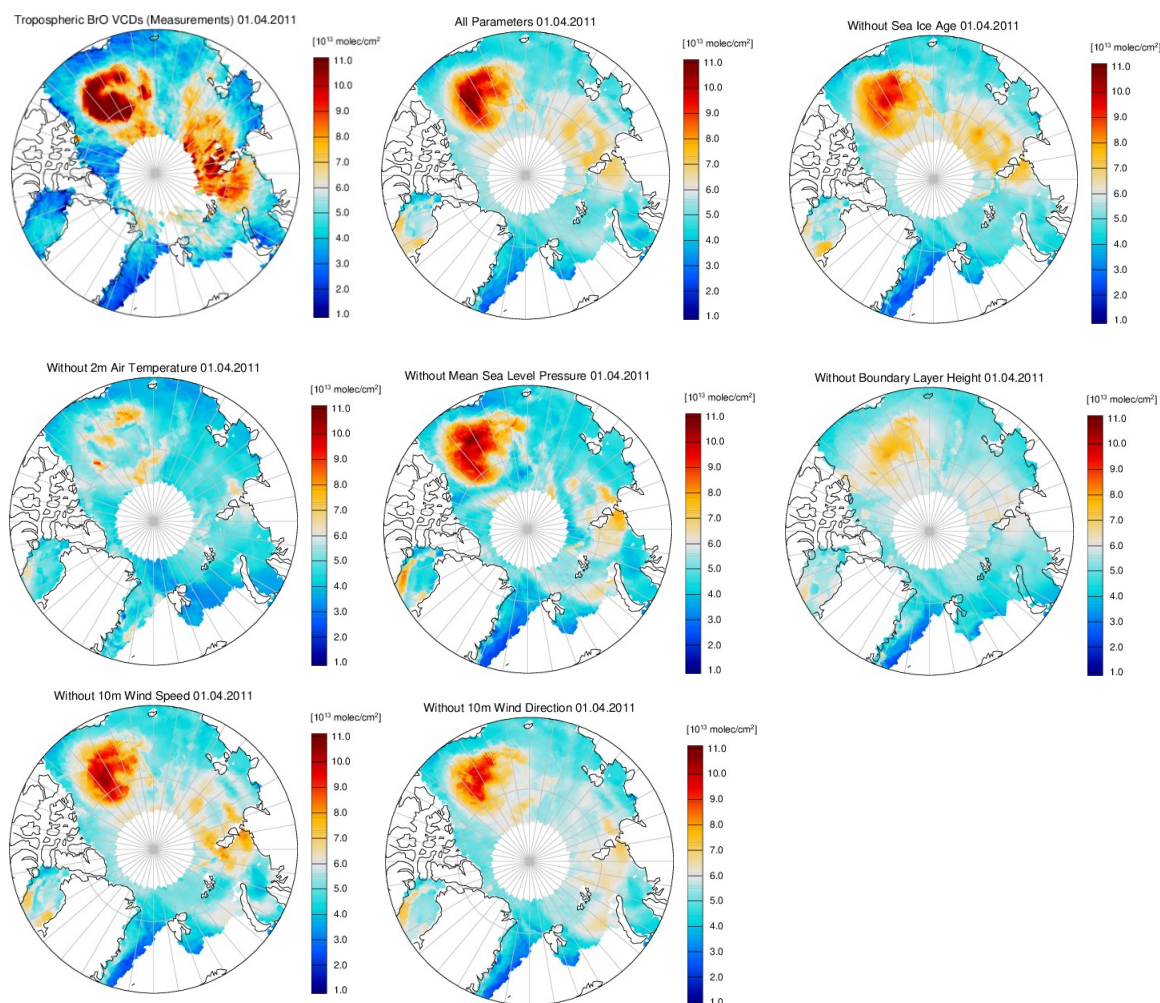


Figure 5.7: Impact of removing each input parameter on the spatial variability and magnitude of tropospheric BrO VCDs modeled by the neural network for the 01.04.2011.

2m air temperature and mean sea level pressure are the most important parameters concerning the neural network's performance. Here, we see clearly that the neural network without 2m air temperature as an input parameter (second row, first column) is the least accurate for the spatial reproduction of the plumes observed during that day. Both plumes are clearly underestimated, with the one over the Arctic Ocean not being identified as enhanced BrO. The exclusion of mean sea level pressure has a minor negative impact on the modeled tropospheric BrO VCD map, and only the plume over the Arctic Ocean is affected. In this case, the second most profound different map compared to the case where we use all input parameters is the one without boundary layer height, where both plumes are underestimated compared to the actual measurements. 10m wind direction also seems to have an impact. For different days and meteorological and sea ice conditions, the impact of each parameter may vary.

In Figure 5.7, a quick comparison for two days will be performed, where the neural network successfully identified enhanced tropospheric BrO plumes. In contrast to the previous example, we will only provide the satellite measurements, the modeled tropospheric BrO VCD by using all the input parameters, and the error map between the measurements and the model (i.e. similar to the first row of Figure 5.6):

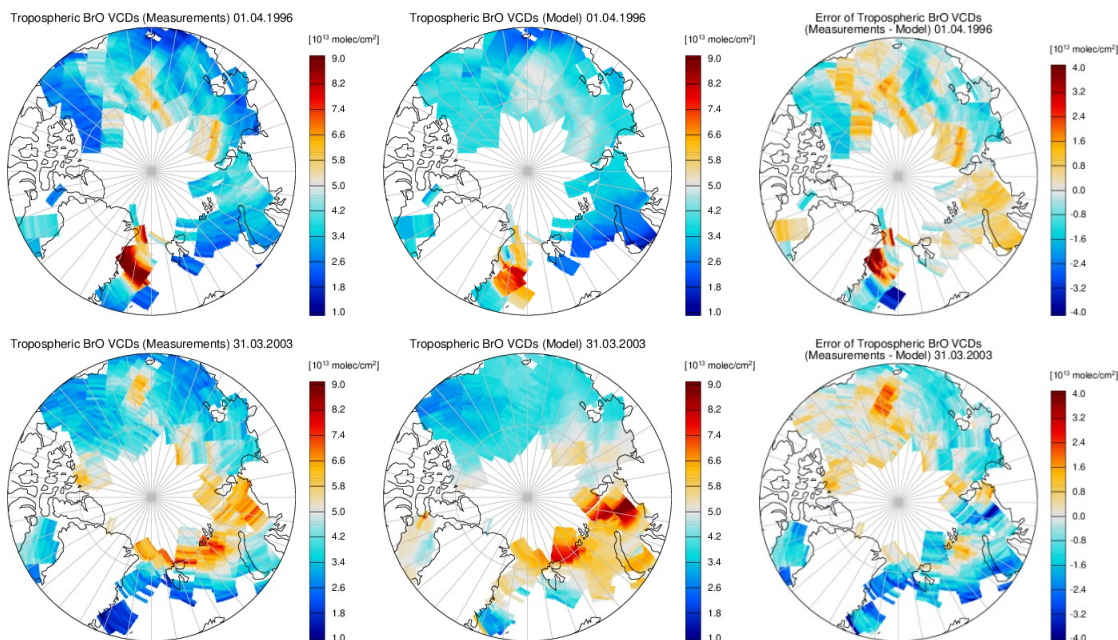


Figure 5.8: Examples of successful spatial reproduction of enhanced tropospheric BrO plumes by the neural network.

The first row of subplots shows results from 01.04.1996 when GOME was the only operating satellite instrument. The neural network can reproduce the spatial variability of tropospheric BrO plumes, independently of the different instrument (i.e. the neural network was trained with data from 2007 only when SCIAMACHY and GOME-2A were operating), and the different location of the plume (i.e. compared to the previous case study of 01.04.2011). Apart from the big plume east of Greenland, the network also reproduced plumes over the Arctic Ocean and the East Siberian Sea, but the magnitude of the values inside the plumes is smaller compared to the

retrieved measurements. Regarding the second row, the selected date is 31.03.2003, when only SCIAMACHY was providing measurements. Here, the most enhanced tropospheric BrO was observed over Barents and Kara Sea. Once again, the neural network has identified the plumes well, but the values inside the plumes are more prominent for the neural network compared to the retrievals. Smaller in magnitude tropospheric BrO VCDs that occurred in the East Siberian Sea were not captured by the neural network and were considered as ambient BrO (i.e. not a distinguishable plume). The neural network successfully reproduces the retrievals for the two days. There are many days in every year where the neural network has similar performance.

In Figure 5.9, a day where the neural network could not identify the measured tropospheric BrO plume (07.04.2017) is investigated. A comparison with the input parameters' maps and the neural networks which do not include one input parameter at a time, similarly to Figures 5.6 and 5.7 for 01.04.2011, is presented:

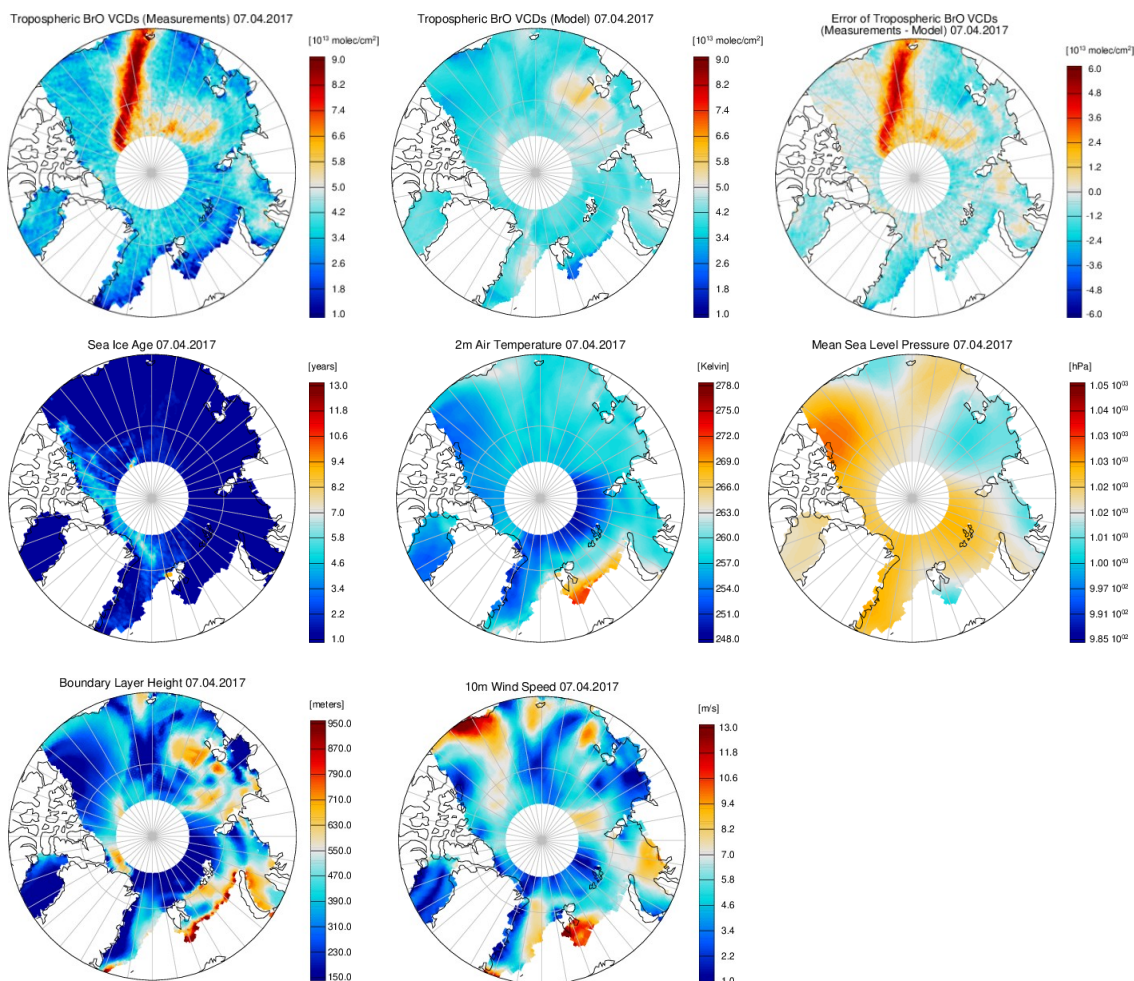
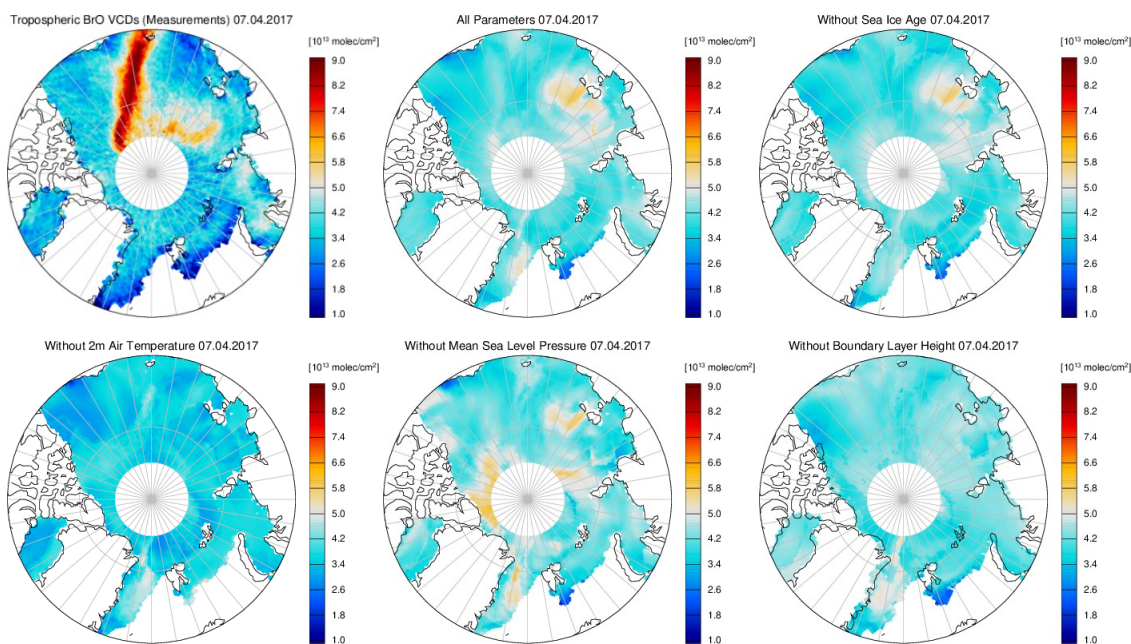


Figure 5.9: Tropospheric BrO VCDs, neural network output, error between measurements and model, sea ice age and meteorological conditions on the 07.04.2017.

An enhanced tropospheric BrO plume in the measurements extends from the East Siberian Sea to the Arctic Ocean. This plume was not identified as enhanced BrO by the neural network

output, as seen in the first row, second column subplot. There is a small enhanced pattern on a similar position (depicted with grey color), but it cannot be considered an accurate representation of the spatial variability of the measurements. This can also be seen from the error between measurements and model for that day (first row, third column), as it is almost identical (except the magnitude) with the spatial pattern of the measurements. By examining sea ice age and meteorological parameters of that day, we infer that mean sea level pressure had high values over the region where the enhanced tropospheric BrO was observed (i.e. around 1001 hPa). This value is much higher than the one observed over the plume on 01.04.2011 (i.e. 982 hPa). 2m air temperature was also higher than on 01.04.2011 (257 Kelvin compared to 248 Kelvin). The values of the two main parameters for the successful prediction of enhanced tropospheric BrO plumes were high in the region where the measured tropospheric BrO plume appeared. It is known in the literature that enhanced BrO can be observed by satellites in higher altitudes (Choi et al., 2012) due to stratospheric intrusion and the exchange of air masses between troposphere and stratosphere. As the measurements do not provide the vertical distribution of BrO (i.e. the satellite provides the vertical column density, but no information on at which altitude the plumes are located), it is possible that during that day, the observed tropospheric BrO plume occurred in higher altitudes, from compression of stratospheric air. It may not originate from sea ice and meteorological parameters. The neural network, which is solely using surface parameters, was not able to identify the region as one having enhanced BrO VCD. Similar results occur even if we use 2017 as the training dataset.

Figure 5.10 examines the performance of neural networks by excluding one input parameter at a time (similar to Figure 5.7) for the 07.04.2017:



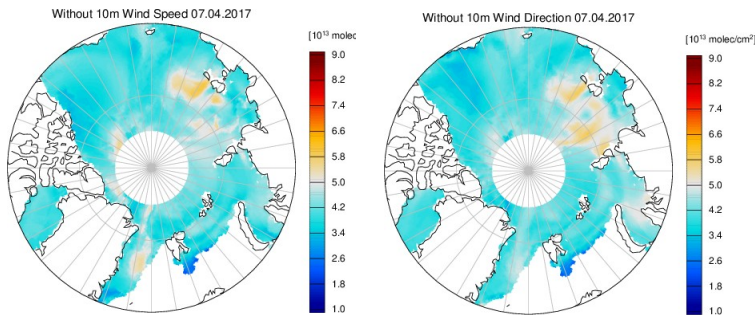
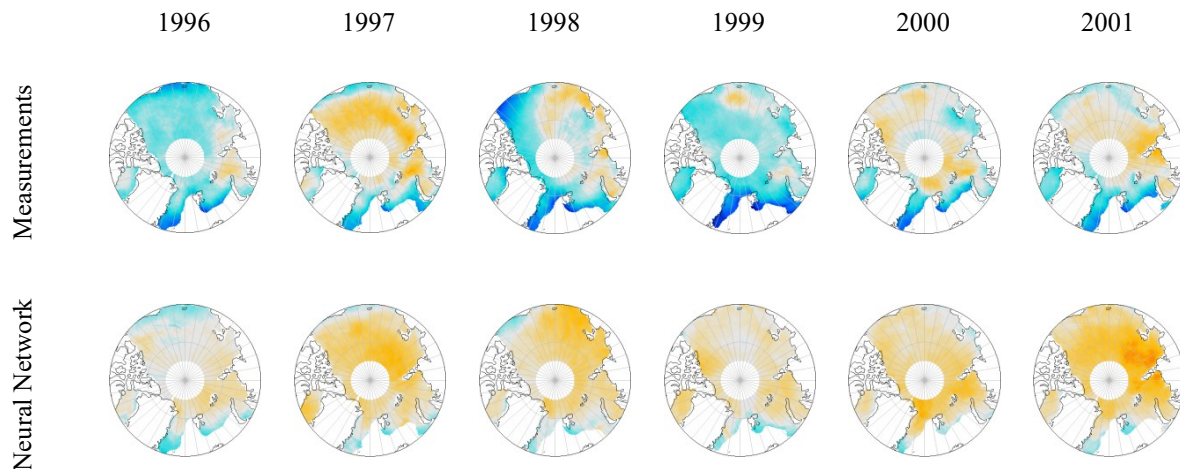


Figure 5.10: Impact of removing individual input parameters on the spatial distribution and magnitude of tropospheric BrO VCDs modeled by the neural network for the 07.04.2017.

In neither case, the corresponding neural network can successfully identify the enhanced measured tropospheric BrO plume. There are minor differences between the outputs of the different neural networks (especially when we exclude 2m air temperature and mean sea level pressure), but they can be considered negligible.

5.3 Long-term Predictions

In this subsection, the reproduction of long-term tropospheric BrO VCDs by the neural network will be discussed. In Figure 5.11, a comparison of polar spring averaged maps of tropospheric BrO measurements, and the neural network outputs is shown:



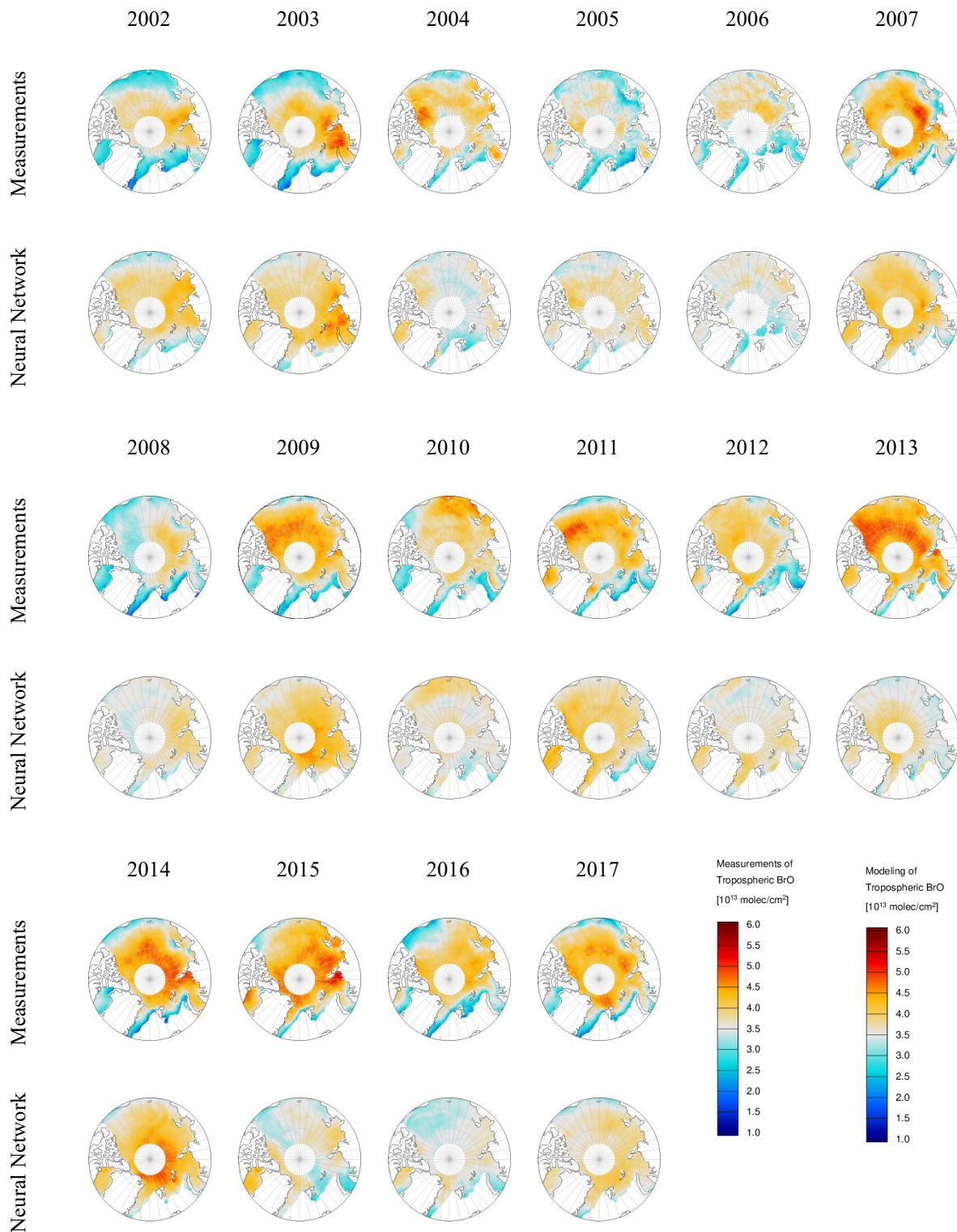


Figure 5.11: Comparison of polar spring average maps of tropospheric BrO VCDs from the measurements and the neural network outputs.

For many years, the spatial variability of enhanced tropospheric BrO plumes, as seen by the satellite measurements, is captured by the neural network. Such successful examples are 1996, 1997, 2002, 2003, 2008. In principle, for all the early years of the dataset (i.e. before 2009), the neural network's performance is considered acceptable, as in most cases, it identifies the regions of enhanced tropospheric BrO VCD. From 2009 onwards, when the satellite retrieved tropospheric BrO VCDs increase, both in magnitude and with respect to the areas where enhanced they appeared, the neural network seems incapable of capturing this increase. Especially for the years 2009, 2011, 2013 and 2015, the spread of tropospheric BrO VCD over the Arctic Ocean is not captured from the neural network. One reason for this disagreement may be the non-evolutionary training dataset (i.e. only one year of data) that was used. As the neural network was trained solely with 2007, it has not seen the increase of first year ice extent (or consequently the decrease of the sea ice age). This increase seems to be connected to the increase of the areas of appearance of enhanced tropospheric BrO VCD. Therefore, it may not be expected from the neural network to follow this increase. Secondly, instrumental degradation (and potentially a decrease of quality of the input parameter datasets), as discussed in chapter 2, can play a role in the neural network's performance. As the training procedure was performed with data from 2007, any degradation that followed may potentially change the relationship between inputs and tropospheric BrO VCD (and consequently the weights the neural network assigns to each input, in order to achieve the maximum possible likeliness to the target, the tropospheric BrO VCD). Thirdly, in chapter 2, we have seen the spatial correlations between tropospheric BrO and input parameters (Figure 2.18). From 2009 onwards, we infer that the correlation between tropospheric BrO VCD measurements and mean sea level pressure came closer to zero (with 2014 being an exception). Since mean sea level pressure is an essential parameter for the neural performance of the neural network, it may be that this decrease in the correlation has a negative impact on the successful tropospheric BrO VCD reproduction by the neural network for the latest years. Also, parameters missing in the input list are preventing a better agreement. The vertical distribution of BrO plumes is such a parameter, as discussed in Figure 5.9. Other such parameters may be aerosol formation, cyclone activity and blowing snow. Considering that there are days in every year of the dataset where the neural network cannot reproduce the measured tropospheric BrO plume, the agreement in the spatial distribution of the polar spring averaged maps is considered satisfactory.

Figure 5.12 shows the long-term time-series of measured tropospheric BrO VCDs and the corresponding time-series of modeled tropospheric BrO VCD.

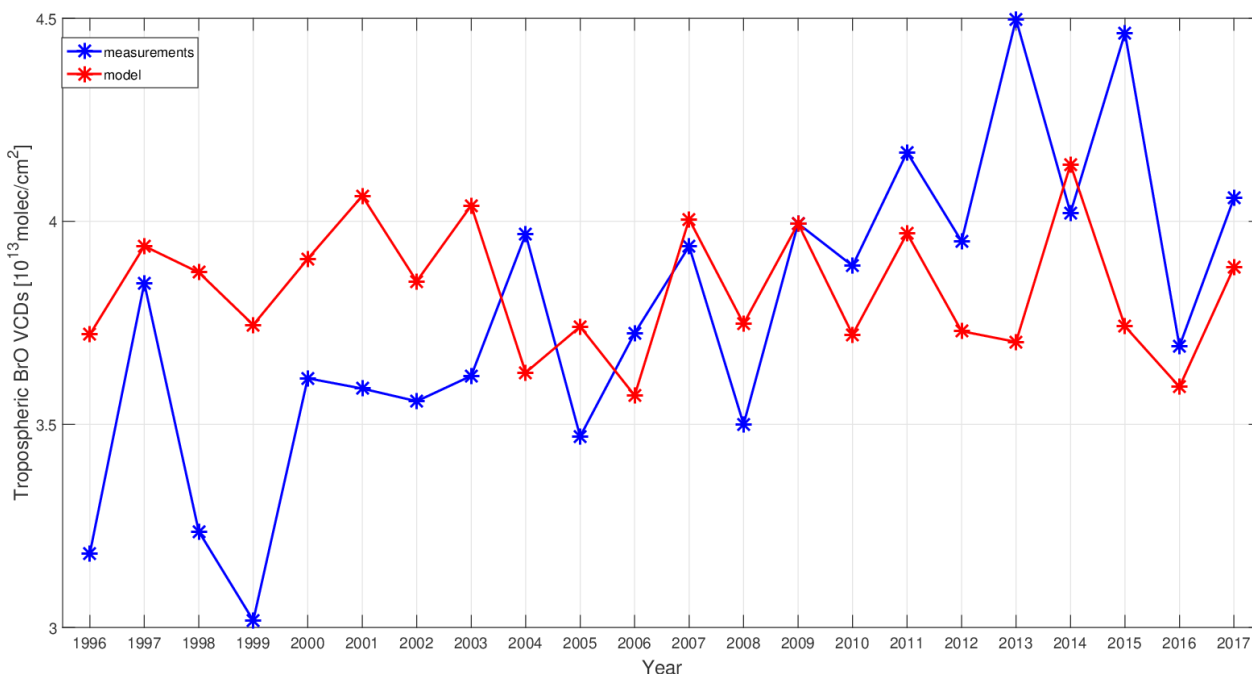


Figure 5.12: Comparison of polar spring averaged time-series between tropospheric BrO VCDs measurements and neural network outputs. 2007 data was used as the training dataset.

The strong trend observed in the measurements from the maps in Figure 5.11 (i.e. 1.5% per year) is not evident in the modeled tropospheric BrO VCD. The absence of the trend from the neural network outputs is a combination of higher values over the early years (i.e. until 2004) and lower values from 2009 onwards. The main strength of the neural network is the spatial reproduction of enhanced measured tropospheric BrO plumes. From the daily case studies we have seen before, the magnitude of the enhanced tropospheric BrO modeled by the neural network is also acceptable. For days like in Figure 5.9 (07.04.2017), where the neural network misses the magnitude of the observed plume by a significant factor, the differences between measurements and model are considerable. Such differences may cause the deviations that we see in the polar spring averaged time-series figure (i.e. Figure 5.12). For many years (e.g. 1997, 2009, 2014), the averaged neural network value is similar to the measured polar spring average. The fact that the neural network shows no trend can also be attributed potentially to the fact that the trend may not result from changes in the input parameters used in the neural network. The trend can be driven by changes in the mechanisms of tropospheric BrO release.

In Figures 5.13 and 5.14, the long-term predictions of the neural network are shown for the future and the past. In Figure 5.13, polar spring averaged maps from 1979 until 1995 are presented. As the sea ice age dataset provided the age of ice data from 1985 onwards, the neural network that was used to produce these maps is trained with data from 2007, but without sea ice age (which, as we saw, has a negligible impact on the performance of the neural network). Sea ice coverage was available from 1979 onwards and was used to flag and only produce data over sea ice:

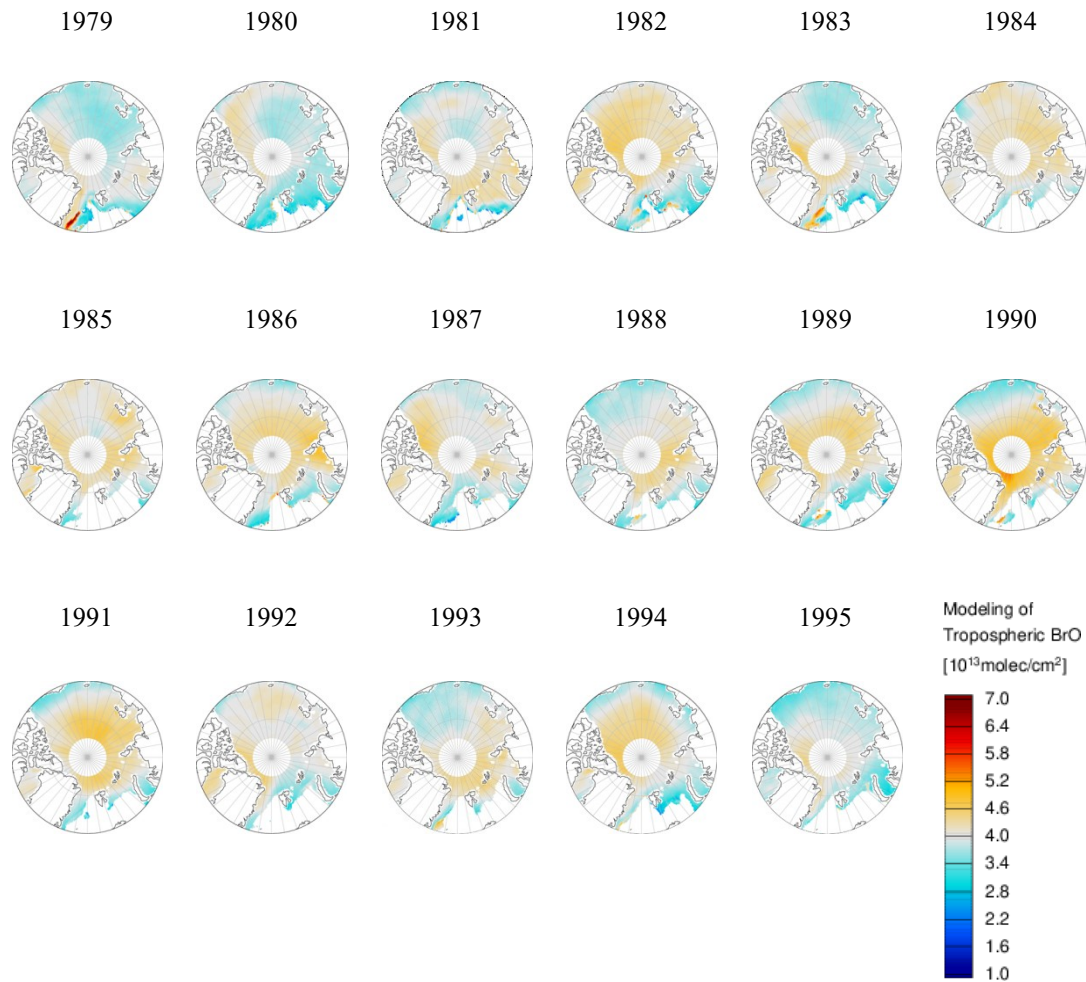


Figure 5.13: Past projections of polar spring averaged maps of tropospheric BrO VCDs.

Some fluctuations can be observed, both on the magnitude and the spatial variability of the modeled tropospheric BrO VCD. Apart from a small artifact appearing in the 1979 map (i.e. east of Greenland), all the other modeled tropospheric BrO VCDs seem reasonable. Higher tropospheric BrO VCDs are seen for 1990 and 1991, while 1995 seems to be the year with the lowest tropospheric BrO VCD. In 1990, the enhanced tropospheric BrO VCDs were spread all over the Arctic Ocean, similarly to some of the years of the dataset that we have measurements (e.g. 2003, 2015).

Figure 5.14 shows some future projections of tropospheric BrO VCD for the Arctic. For this purpose, ERA-5 forecasts (RCP26, RCP45 and RCP85) were used. These scenarios model the projected greenhouse gas future concentrations and affect various meteorological parameters. These projections do not provide information on sea ice age, 10m wind direction and boundary layer height. Therefore, the neural network that was used took as input parameters only 2m air temperature, mean sea level pressure and 10m wind speed:

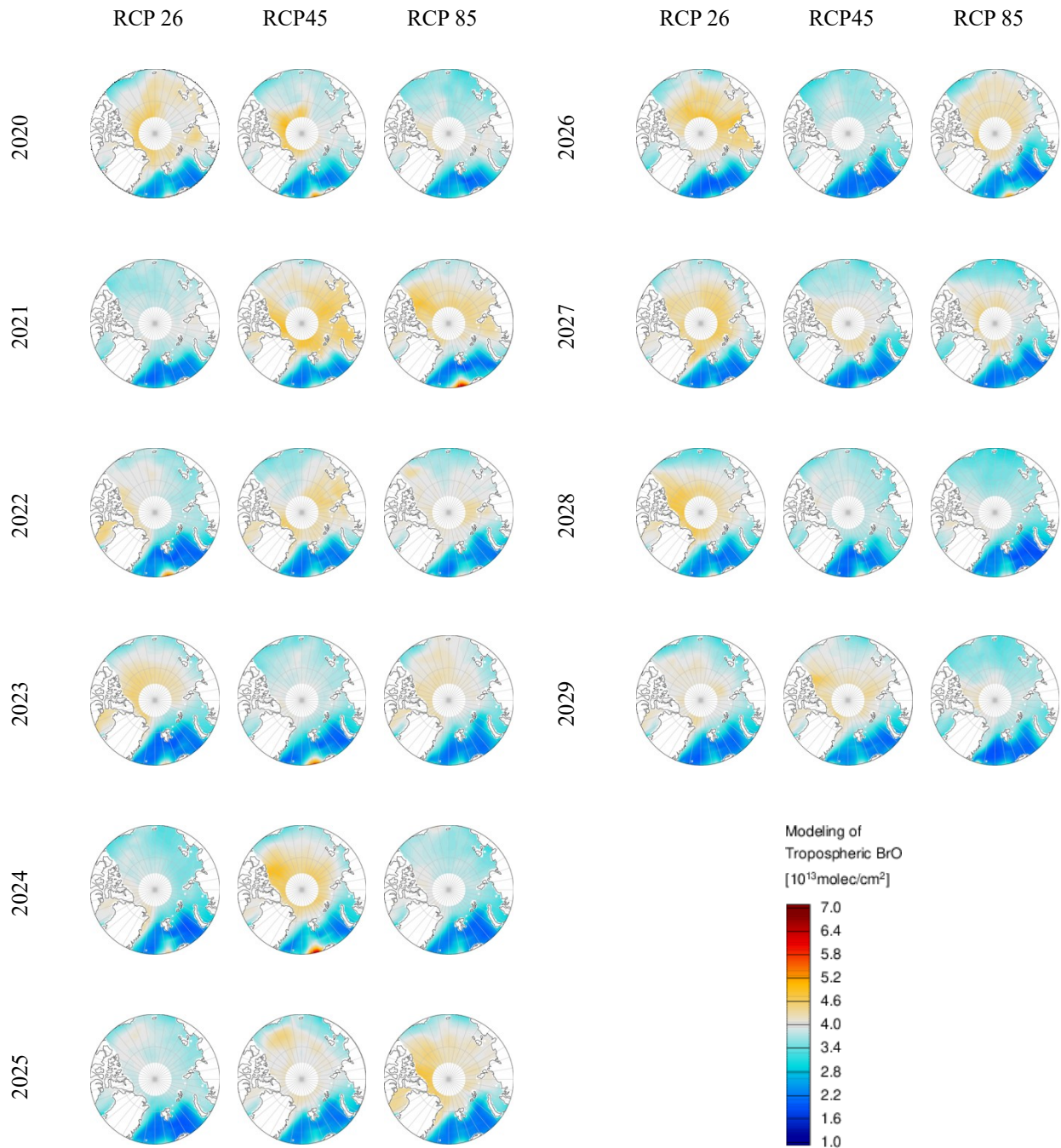


Figure 5.14: Future projections of polar spring averaged maps of tropospheric BrO VCDs based on three different projections of greenhouse gas concentrations.

It is expected that for every year, the RCP26 projections will have the higher tropospheric BrO VCDs (since the temperature increase for them is the smallest) and vice versa for rcp85. There are years (e.g. 2021) where this does not apply. Also, since no future information regarding sea ice age or concentration is available, the maps are only flagged for land. The projected tropospheric BrO VCD is low over the typical regions where open water appears (due to the

higher air temperature). Fluctuations over the years are seen, with 2026 and 2027 (for RCP26 scenario) having the highest polar spring averaged tropospheric BrO VCD. The neural network predicts lower tropospheric BrO VCD for future years than the 1996 – 2017 period. As it does not consider the increase of first year ice extent (which favours bromine release), but only the increase of air temperature (which dampens the magnitude of tropospheric BrO VCD), these projections may not be accurate.

5.4 Summary and Conclusions

A novel approach for tropospheric BrO VCD modeling using an artificial neural network has been presented in this chapter. It is the first such approach for tropospheric BrO VCD modeling to our knowledge. Yang et al. (2020) used a chemistry transport and a chemistry-climate model with a parameterization using blowing snow and compared the resulting BrO fields with GOME-2 columns and ground-based measurements. Fernandez et al. (2019) developed the first implementation of polar halogen chemistry for the CAM-chemistry model, providing four years (2007 – 2011) of polar spring comparisons between GOME-2A and modeling results. Herrmann et al. (2021) implemented 3d time-dependent simulations of BrO in the Weather Research and Forecasting model coupled with chemistry (WRF-Chem) and compared the simulations to GOME-2A satellite observations. A qualitative agreement was found in all studies, but the modeling of bromine explosions is not yet adequate.

The basic principle behind the machine learning approach implemented is that the relationship between the input parameters (sea ice age, 2m air temperature, mean sea level pressure, 10m wind speed and direction and boundary layer height) and the retrieved tropospheric BrO VCDs can be recognized by the neural network, in order to model tropospheric BrO VCDs (and especially the appearance of enhanced tropospheric BrO plumes). The training dataset was selected to be 2007 (i.e. discussed in chapter 2), and sensitivity tests to investigate the impact of each input parameter on the performance of the neural network were performed. Starting with the scatter plots of the training dataset, when all input parameters are used, the correlation coefficient between measurements and model outputs of tropospheric BrO VCD is 0.75, while the slope of the best fitting line is 0.56. 2m air temperature (i.e. without it, the correlation coefficient drops to 0.58, while the slope to 0.33) and mean sea level pressure (i.e. without it, the correlation coefficient is 0.68, while the slope 0.46) are the most critical parameters for the successful prediction of enhanced tropospheric BrO plumes by the neural network. By extrapolating the sensitivity tests to the other years (i.e. 1996 to 2017), these two input parameters remain the most important (by excluding 2m air temperature, the correlation coefficient between measurements and predictions of tropospheric BrO VCD drops by a factor of 2), with boundary layer height following. From sensitivity tests regarding the effect of each input parameter on the magnitude of modeled tropospheric BrO VCD, we infer that projected tropospheric BrO decreases significantly

when 2m air temperature and mean sea level pressure increase, while modeled tropospheric BrO VCDs increase with the increase of boundary layer height.

From case studies performed, it was shown that the neural network can spatially reproduce enhanced tropospheric BrO plumes, which occur under certain meteorological conditions (i.e. low temperatures, low pressure systems, high or low wind speeds and high boundary layer height). Some plumes are captured by the satellite sensors but are not reproduced by the neural network, as they are not linked to the input parameters. Since these plumes do not seem to originate from surface parameters, the integration of other critical parameters in the input set (e.g. vertical distribution of the observed BrO plumes) may improve the neural network's performance.

From polar spring averaged map comparisons between measurements of tropospheric BrO VCD and outputs of the neural network, we infer that the neural network can reproduce the spatial variability of tropospheric BrO VCD for many years. There are years (most of them from 2009 onwards) where the agreement is not that robust. Potential reasons for this degradation in the agreement could be the lack of knowledge of the neural network regarding the increase of first year ice extent (as it was trained only with measurements from 2007), instrumental degradation and missing key input parameters for tropospheric BrO VCD formation (e.g. blowing snow, vertical distribution of the BrO VCD, temperature and wind information at higher altitudes). The overall comparison is considered satisfactory. From the comparison of the polar spring average time-series between tropospheric BrO VCD measurements and neural network's output, the trend observed in the measurements cannot be seen in the modeled tropospheric BrO VCD. Potential reasons for this may be that the trend does not originate from changing surface parameters, the fact that the neural network is instantaneous and transported events cannot be well represented, and that additional input parameters which may drive the trend are missing. Since the neural network is a robust and fast approach and only requires some fundamental input data, it can be used for future short and medium scale projections of the spatial distribution of tropospheric BrO plumes. Also, it can be integrated into numerical chemical transport models and be used as a fast and straightforward parameterization sub-tool to predict tropospheric BrO for planning purposes of future measurement campaigns.

6. CONCLUSIONS AND OUTLOOK

In this chapter, the overall findings of the thesis and its contributions to the relevant literature are concluded. Also, additional prospects for future research that were identified will be discussed. The chapter will be divided based on the three main chapters of the thesis.

6.1 BrO Retrieval and Tropospheric BrO Trends

The main topic of this thesis is the study of the impact of Arctic Amplification on tropospheric BrO abundances and the link of their changes to the main driving mechanisms of bromine release. Since the Arctic is one of the most remote places on Earth, satellite remote sensing is the only source for continuous long-term measurements of BrO in the region. Therefore, a satellite based long-term BrO dataset was derived from measurements of four UV-VIS instruments. The dataset covers a 22 year time span, the longest reported in literature.

Many sensitivity tests were performed for all four satellite instruments to assess the optimal wavelength range for satellite BrO retrievals for the Arctic region. For the final settings, the root mean square error of the fit is for all the days of the dataset below 2.5×10^{-03} for the Arctic region, the Hudson Bay and the pacific reference area. Alongside the qualitative assessment of the retrieved BrO, the agreement for the overlapping periods of the sensors was evaluated. The final set of settings for each sensor resulted in datasets having satisfactory quality and a good agreement between them (correlation coefficients between 0.9 and 0.97 in the Arctic and 0.9 to 0.93 in the Hudson Bay). A stratospheric separation method was used to derive the tropospheric BrO constituent from the total (geometric) satellite vertical column density.

The tropospheric BrO dataset shows a similar agreement for the overlapping periods of the sensors as the geometric columns (correlation coefficients between 0.79 to 0.94 in the Arctic and 0.88 to 0.89 in the Hudson Bay). Thorough comparisons were performed for these periods to verify the agreement between the different satellite instruments. Since the deviations were minimal, a merged tropospheric BrO dataset was created, which was the basis for the trend analysis. In addition, a merged tropospheric BrO dataset was derived for the Hudson Bay region since it is a well known bromine explosion hotspot. By studying the trends appearing in the merged tropospheric BrO datasets, we infer a general increase over time in both regions. The increase is pronounced during the seasons when bromine explosions are more frequent (i.e. polar spring for the Arctic, with an increase of 1.5% per year, winter for the Hudson Bay, with an increase of 2.3% per year and spring for the Hudson Bay with an increase of 0.9% per year). Although the trends are not monotonically increasing in any region or period (i.e. there is

interannual variability and in recent years lower values were observed), it seems that during the years of Arctic Amplification, an upward trend in tropospheric BrO VCDs is also evident. A spatial trend investigation was also performed, which showed that tropospheric BrO VCD increased all over the Hudson Bay for both winter and spring seasons, while for the Arctic, there are regions of profound increase and decrease.

Although the BrO dataset is the longest to our knowledge, further temporal expansion of it (i.e. including measurements from recently launched and future sensors) will shape a better image regarding the impact of Arctic Amplification on bromine release and BrO formation. In addition, the spatial resolution of the new sensors is higher, enabling the identification of smaller in extent BrO plumes and their link to their sources and driving mechanisms.

6.2 Relationship between Tropospheric BrO VCD and Driving Mechanisms

In order to link the changes of tropospheric BrO for the Arctic and the Hudson Bay to its driving mechanisms, external datasets of related quantities were acquired. A sea ice age dataset was initially used to flag and only use satellite scenes where sea ice was present. Only these scenes were used in the analysis performed (trend analysis and the connection to external datasets). A long-term general agreement is inferred from comparisons of tropospheric BrO VCD and sea ice age (correlation coefficient of +0.62), which is evident in both time-series and maps for the Arctic region. The increase of tropospheric BrO VCD correlates with the increase of first year ice in the Arctic.

Meteorological parameters from 2 different reanalysis datasets were evaluated, and similar comparisons as with sea ice age were performed. From the meteorological parameters, 2m air temperature seems to be the most important for the formation of enhanced tropospheric BrO plumes on a daily basis, as it is strongly anti-correlated with tropospheric BrO VCD, for both the Arctic and the Hudson Bay (-0.53 for the Arctic, -0.46 for winter in the Hudson Bay and -0.77 for spring in the Hudson Bay). This anti-correlation was also seen in trend maps between tropospheric BrO VCD and 2m air temperature. While air temperature has a substantial impact on the appearance of enhanced tropospheric BrO plumes on a daily and short-term basis, it does not have a strong influence on an annual basis, as the sea ice age.

10m wind speed and boundary layer height also showed significant correlations to tropospheric BrO VCD without giving a clear picture of their actual relationship (i.e. both positive and negative correlations appeared in our analysis). Mean sea level pressure, although affecting tropospheric BrO VCD formation, did not show any strong correlation. Other parameters that were evaluated (e.g. cyclonic activity, sea ice thickness) did not have the appropriate spatial or temporal resolution to extract concrete conclusions.

An analysis of a longer (and higher resolution) tropospheric BrO VCD dataset may yield more precise conclusions on the relationship of tropospheric BrO VCD to its sources and driving mechanisms. Additional external datasets (i.e. blowing snow) known to affect the appearance of enhanced tropospheric BrO VCD should be evaluated.

6.3 Tropospheric BrO VCD Modeling

A modeling approach for Arctic tropospheric BrO VCD modeling was implemented using an artificial neural network. Such an effort is the first to our knowledge. The neural network uses as critical input parameters sea ice age, 2m air temperature, mean sea level pressure, 10m wind speed and direction and boundary layer height, and models tropospheric BrO VCD. 2m air temperature and mean sea level pressure are identified as the most important input parameters for the neural network's successful tropospheric BrO VCD reproduction.

By training the neural network with only one year of data, it can accurately reproduce spatial patterns of enhanced tropospheric BrO VCD occurring in different years. The correlation coefficient between satellite measurements and neural network outputs is approximately 0.4 for the modeled years, while the root mean square error is 35%. According to the neural network, the combination of low temperature and low mean sea level pressure is the one under which enhanced tropospheric BrO VCD can be identified. The magnitude of the plumes is also satisfactory in many cases. Since the procedure is speedy and not computationally demanding, the neural network can be implemented as a parameterization sub-tool to predict future appearances of tropospheric BrO plumes.

The neural network cannot reproduce and identify all the tropospheric BrO plumes in the measurements dataset. This can be attributed to the lack of additional information regarding both the tropospheric BrO VCD and the input parameters. The absence of the vertical distribution of tropospheric BrO VCD is crucial. Since all the input parameters we used are occurring at the surface level, plumes potentially occurring at higher altitudes and being transported away from the initial source region cannot be modeled accurately. The addition of long-term information of other key parameters, such as aerosol vertical distribution and snowpacks, which can transfer and recycle tropospheric BrO VCD far away from the source region, would improve the neural network's accuracy. Also, spatial and temporal information would allow the neural network to understand the potential transport of tropospheric BrO plumes and improve its performance.

BIBLIOGRAPHY

Afe, O. T., Richter, A., Sierk, B., Wittrock, F., and Burrows, J. P.: BrO emission from volcanoes: A survey using GOME and SCIAMACHY measurements, 31, <https://doi.org/10.1029/2004GL020994>, 2004.

Akperov, M., Rinke, A., Mokhov, I. I., Matthes, H., Semenov, V. A., Adakudlu, M., Cassano, J., Christensen, J. H., Dembitskaya, M. A., Dethloff, K., Fettweis, X., Glisan, J., Gutjahr, O., Heinemann, G., Koenig, T., Koldunov, N. V., Laprise, R., Mottram, R., Nikiéma, O., Parfenova, M., Scinocca, J. F., Sein, D., Sobolowski, S., Winger, K., and Zhang, W.: Trends of intense cyclone activity in the Arctic from reanalyses data and regional climate models (Arctic-CORDEX), IOP Conf. Ser.: Earth Environ. Sci., 231, 012003, <https://doi.org/10.1088/1755-1315/231/1/012003>, 2019.

Alexeev, V. A., Langen, P. L., and Bates, J. R.: Polar Amplification of surface warming on an aquaplanet in “ghost forcing” experiments without sea ice feedbacks, *Climate Dynamics*, 24, 655–666, <https://doi.org/10.1007/s00382-005-0018-3>, 2005.

Alvarado, L. M. A., Richter, A., Vrekoussis, M., Wittrock, F., Hilboll, A., Schreier, S. F., and Burrows, J. P.: An improved glyoxal retrieval from OMI measurements, 7, 4133–4150, <https://doi.org/10.5194/amt-7-4133-2014>, 2014.

Ariya, P. A., Dastoor, A. P., Amyot, M., Schroeder, W. H., Barrie, L., Anlauf, K., Raofie, F., Ryzhkov, A., Davignon, D., Lalonde, J., and Steffen, A.: The Arctic: a sink for mercury, 56, 397–403, <https://doi.org/10.3402/tellusb.v56i5.16458>, 2004.

Arrhenius, S.: On the Influence of Carbonic Acid in the Air upon the Temperature of the Ground, 22, n.d.

Barrie, L. and Platt, U.: Arctic tropospheric chemistry: an overview, 49, 450–454, <https://doi.org/10.1034/j.1600-0889.49.issue5.2.x>, 1997.

Barrie, L. A., Bottenheim, J. W., Schnell, R. C., Crutzen, P. J., and Rasmussen, R. A.: Ozone destruction and photochemical reactions at polar sunrise in the lower Arctic atmosphere, 334, 138–141, <https://doi.org/10.1038/334138a0>, 1988.

Begoin, M., Richter, A., Weber, M., Kaleschke, L., Tian-Kunze, X., Stohl, A., Theys, N., and Burrows, J. P.: Satellite observations of long range transport of a large BrO plume in the Arctic, 10, 6515–6526, <https://doi.org/10.5194/acp-10-6515-2010>, 2010.

Blackwell, W. J. and Chen, F. W.-M.: *Neural Network Applications in High-Resolution Atmospheric Remote Sensing*, 2005.

Blechschmidt, A.-M., Richter, A., Burrows, J. P., Kaleschke, L., Strong, K., Theys, N., Weber, M., Zhao, X., and Zien, A.: An exemplary case of a bromine explosion event linked to cyclone development in the Arctic, 16, 1773–1788, <https://doi.org/10.5194/acp-16-1773-2016>, 2016.

Boersma, K. F., Eskes, H. J., and Brinksma, E. J.: Error analysis for tropospheric NO₂ retrieval from space, 109, <https://doi.org/10.1029/2003JD003962>, 2004.

Boersma, K. F., Eskes, H. J., Richter, A., De Smedt, I., Lorente, A., Beirle, S., van Geffen, J. H. G. M., Zara, M., Peters, E., Van Roozendaal, M., Wagner, T., Maasakkers, J. D., van der A, R. J., Nightingale, J., De Rudder, A., Irie, H., Pinardi, G., Lambert, J.-C., and Compernelle, S. C.: Improving algorithms and uncertainty estimates for satellite NO₂ retrievals: results from the quality assurance for the essential climate variables (QA4ECV) project, 11, 6651–6678, <https://doi.org/10.5194/amt-11-6651-2018>, 2018.

Bovensmann, H., Burrows, J. P., Buchwitz, M., Frerick, J., Noël, S., Rozanov, V. V., Chance, K. V., and Goede, A. P. H.: SCIAMACHY: Mission Objectives and Measurement Modes, 56, 127–150, [https://doi.org/10.1175/1520-0469\(1999\)056<0127:SMOAMM>2.0.CO;2](https://doi.org/10.1175/1520-0469(1999)056<0127:SMOAMM>2.0.CO;2), 1999.

Bracher, A., Lamsal, L. N., Weber, M., Bramstedt, K., Coldewey-Egbers, M., and Burrows, J. P.: Global satellite validation of SCIAMACHY O₃ columns with GOME WFDOAS, 5, 2357–2368, <https://doi.org/10.5194/acp-5-2357-2005>, 2005.

Budyko, M. I.: The effect of solar radiation variations on the climate of the Earth, 21, 611–619, <https://doi.org/10.3402/tellusa.v21i5.10109>, 1969.

Burrows, J. P., Hölzle, E., Goede, A. P. H., Visser, H., and Fricke, W.: SCIAMACHY—scanning imaging absorption spectrometer for atmospheric chartography, *Acta Astronautica*, 35, 445–451, [https://doi.org/10.1016/0094-5765\(94\)00278-T](https://doi.org/10.1016/0094-5765(94)00278-T), 1995.

Burrows, J. P., Weber, M., Buchwitz, M., Rozanov, V., Ladstätter-Weißmayer, A., Richter, A., DeBeek, R., Hoogen, R., Bramstedt, K., Eichmann, K.-U., Eisinger, M., and Perner, D.: The Global Ozone Monitoring Experiment (GOME): Mission Concept and First Scientific Results, 56, 151–175, [https://doi.org/10.1175/1520-0469\(1999\)056<0151:TGOMEG>2.0.CO;2](https://doi.org/10.1175/1520-0469(1999)056<0151:TGOMEG>2.0.CO;2), 1999.

Burrows, J. P., Platt, U., and Borrell, P. (Eds.): *The Remote Sensing of Tropospheric Composition from Space*, Springer-Verlag, Berlin Heidelberg, <https://doi.org/10.1007/978-3-642-14791-3>, 2011.

Callies, J., Corpaccioli, E., Eisinger, M., Hahne, A., and Lefebvre, A.: GOME-2 – Metop’s Second-Generation Sensor for Operational Ozone Monitoring, 9, 2000.

Chance, K.: Analysis of BrO measurements from the Global Ozone Monitoring Experiment, 25, 3335–3338, <https://doi.org/10.1029/98GL52359>, 1998.

Chance, K., Kurosu, T. P., and Sioris, C. E.: Undersampling correction for array detector-based satellite spectrometers, *Appl. Opt.*, 44, 1296, <https://doi.org/10.1364/AO.44.001296>, 2005.

Chapman, S.: XXXV. On ozone and atomic oxygen in the upper atmosphere, 10, 369–383, <https://doi.org/10.1080/14786443009461588>, 1930.

Choi, S., Theys, N., Salawitch, R. J., Wales, P. A., Joiner, J., Canty, T. P., Chance, K., Suleiman, R. M., Palm, S. P., Cullather, R. I., Darmenov, A. S., Silva, A. da, Kurosu, T. P., Hendrick, F., and Roozendaal, M. V.: Link Between Arctic Tropospheric BrO Explosion Observed From Space and Sea-Salt Aerosols From Blowing Snow Investigated Using Ozone Monitoring Instrument BrO Data and GEOS-5 Data Assimilation System, 123, 6954–6983, <https://doi.org/10.1029/2017JD026889>, 2018.

Choi, S., Wang, Y., Salawitch, R. J., Canty, T., Joiner, J., Zeng, T., Kurosu, T. P., Chance, K., Richter, A., Huey, L. G., Liao, J., Neuman, J. A., Nowak, J. B., Dibb, J. E., Weinheimer, A. J., Diskin, G., Ryerson, T. B., Silva, A. da, Curry, J., Kinnison, D., Tilmes, S., and Levelt, P. F.: Analysis of satellite-derived Arctic tropospheric BrO columns in conjunction with aircraft measurements during ARCTAS and ARCPAC, 12, 1255–1285, <https://doi.org/10.5194/acp-12-1255-2012>, 2012.

Cicerone, R. J.: Halogens in the atmosphere, *Rev. Geophys.*, 19, 123, <https://doi.org/10.1029/RG019i001p00123>, 1981.

Comrie, A. C.: Comparing Neural Networks and Regression Models for Ozone Forecasting, 47, 653–663, <https://doi.org/10.1080/10473289.1997.10463925>, 1997.

Coumou, D., Di Capua, G., Vavrus, S., Wang, L., and Wang, S.: The influence of Arctic Amplification on mid-latitude summer circulation, 9, 2959, <https://doi.org/10.1038/s41467-018-05256-8>, 2018.

Crutzen, P. J.: Geology of mankind, 415, 23–23, <https://doi.org/10.1038/415023a>, 2002.

Cvijanovic, I., Santer, B. D., Bonfils, C., Lucas, D. D., Chiang, J. C. H., and Zimmerman, S.: Future loss of Arctic sea-ice cover could drive a substantial decrease in California's rainfall, 8, 1947, <https://doi.org/10.1038/s41467-017-01907-4>, 2017.

Errera, Q. and Fonteyn, D.: Four-dimensional variational chemical assimilation of CRISTA stratospheric measurements, 106, 12253–12265, <https://doi.org/10.1029/2001JD900010>, 2001.

Falk, S. and Sinnhuber, B.-M.: Polar boundary layer bromine explosion and ozone depletion events in the chemistry–climate model EMAC v2.52: implementation and evaluation of AirSnow algorithm, 11, 1115–1131, <https://doi.org/10.5194/gmd-11-1115-2018>, 2018.

Fan, S.-M. and Jacob, D. J.: Surface ozone depletion in Arctic spring sustained by bromine reactions on aerosols, 359, 522–524, <https://doi.org/10.1038/359522a0>, 1992.

Farman, J. C., Gardiner, B. G., and Shanklin, J. D.: Large losses of total ozone in Antarctica reveal seasonal ClO_x/NO_x interaction, 315, 207–210, <https://doi.org/10.1038/315207a0>, 1985.

Fernandez, R. P., Carmona-Balea, A., Cuevas, C. A., Barrera, J. A., Kinnison, D. E., Lamarque, J.-F., Blaszcak-Boxe, C., Kim, K., Choi, W., Hay, T., Blechschmidt, A.-M., Schönhardt, A., Burrows, J. P., and Saiz-Lopez, A.: Modeling the Sources and Chemistry of Polar Tropospheric Halogens (Cl, Br, and I) Using the CAM-Chem Global Chemistry-Climate Model, 11, 2259–2289, <https://doi.org/10.1029/2019MS001655>, 2019.

Fickert, S., Adams, J. W., and Crowley, J. N.: Activation of Br₂ and BrCl via uptake of HOBr onto aqueous salt solutions, 104, 23719–23727, <https://doi.org/10.1029/1999JD900359>, 1999.

Fleischmann, O. C., Hartmann, M., Burrows, J. P., and Orphal, J.: New ultraviolet absorption cross-sections of BrO at atmospheric temperatures measured by time-windowing Fourier transform spectroscopy, *Journal of Photochemistry and Photobiology A: Chemistry*, 168, 117–132, <https://doi.org/10.1016/j.jphotochem.2004.03.026>, 2004.

Francis, J. A. and Vavrus, S. J.: Evidence linking Arctic Amplification to extreme weather in mid-latitudes, 39, <https://doi.org/10.1029/2012GL051000>, 2012.

Fyfe, J. C.: Midlatitudes unaffected by sea ice loss, 9, 649–650, <https://doi.org/10.1038/s41558-019-0560-3>, 2019.

Galley, R. J., Babb, D., Ogi, M., Else, B. G. T., Geilfus, N.-X., Crabeck, O., Barber, D. G., and Rysgaard, S.: Replacement of multiyear sea ice and changes in the open water season duration in the Beaufort Sea since 2004, 121, 1806–1823, <https://doi.org/10.1002/2015JC011583>, 2016.

Georgoulias, A. K., van der A, R. J., Stammes, P., Boersma, K. F., and Eskes, H. J.: Trends and trend reversal detection in 2 decades of tropospheric NO₂ satellite observations, 19, 6269–6294, <https://doi.org/10.5194/acp-19-6269-2019>, 2019.

Grainger, J. F. and Ring, J.: Anomalous Fraunhofer Line Profiles, 193, 762–762, <https://doi.org/10.1038/193762a0>, 1962.

Halfacre, J. W., Shepson, P. B., and Pratt, K. A.: pH-dependent production of molecular chlorine, bromine, and iodine from frozen saline surfaces, 19, 4917–4931, <https://doi.org/10.5194/acp-19-4917-2019>, 2019.

Hansen, J., Sato, M., and Ruedy, R.: Radiative forcing and climate response, 102, 6831–6864, <https://doi.org/10.1029/96JD03436>, 1997.

Haykin, S. S. and Haykin, S. S.: Neural networks and learning machines, 3rd ed., Prentice Hall, New York, 906 pp., 2009.

Hendrick, F., Johnston, P. V., Mazière, M. D., Fayt, C., Hermans, C., Kreher, K., Theys, N., Thomas, A., and Roozendaal, M. V.: One-decade trend analysis of stratospheric BrO over Harestua (60°N) and Lauder (45°S) reveals a decline, 35, <https://doi.org/10.1029/2008GL034154>, 2008.

Herrmann, M., Sihler, H., Frieß, U., Wagner, T., Platt, U., and Gutheil, E.: Time-dependent 3D simulations of tropospheric ozone depletion events in the Arctic spring using the Weather Research and Forecasting model coupled with Chemistry (WRF-Chem), 21, 7611–7638, <https://doi.org/10.5194/acp-21-7611-2021>, 2021.

Hersbach, H., Bell, B., Berrisford, P., Hirahara, S., Horányi, A., Muñoz-Sabater, J., Nicolas, J., Peubey, C., Radu, R., Schepers, D., Simmons, A., Soci, C., Abdalla, S., Abellan, X., Balsamo, G., Bechtold, P., Biavati, G., Bidlot, J., Bonavita, M., Chiara, G. D., Dahlgren, P., Dee, D., Diamantakis, M., Dragani, R., Flemming, J., Forbes, R., Fuentes, M., Geer, A., Haimberger, L., Healy, S., Hogan, R. J., Hólm, E., Janisková, M., Keeley, S., Laloyaux, P., Lopez, P., Lupu, C., Radnoti, G., Rosnay, P. de, Rozum, I., Vamborg, F., Villaume, S., and Thépaut, J.-N.: The ERA5 global reanalysis, 146, 1999–2049, <https://doi.org/10.1002/qj.3803>, 2020.

Hollwedel, J., Wenig, M., Beirle, S., Kraus, S., Kühl, S., Wilms-Grabe, W., Platt, U., and Wagner, T.: Year-to-year variations of spring time polar tropospheric BrO as seen by GOME, *Advances in Space Research*, 34, 804–808, <https://doi.org/10.1016/j.asr.2003.08.060>, 2004.

Hooyberghs, J., Mensink, C., Dumont, G., Fierens, F., and Brasseur, O.: A neural network forecast for daily average PM₁₀ concentrations in Belgium, *Atmospheric Environment*, 39, 3279–3289, <https://doi.org/10.1016/j.atmosenv.2005.01.050>, 2005.

Hörmann, C., Sihler, H., Beirle, S., Penning de Vries, M., Platt, U., and Wagner, T.: Seasonal variation of tropospheric bromine monoxide over the Rann of Kutch salt marsh seen from space, *Atmos. Chem. Phys.*, 16, 13015–13034, <https://doi.org/10.5194/acp-16-13015-2016>, 2016.

Hornik, K.: Approximation capabilities of multilayer feedforward networks, *Neural Networks*, 4, 251–257, [https://doi.org/10.1016/0893-6080\(91\)90009-T](https://doi.org/10.1016/0893-6080(91)90009-T), 1991.

Huang, J., Jaeglé, L., Chen, Q., Alexander, B., Sherwen, T., Evans, M. J., Theys, N., and Choi, S.: Evaluating the impact of blowing-snow sea salt aerosol on springtime BrO and O₃ in the Arctic, 20, 7335–7358, <https://doi.org/10.5194/acp-20-7335-2020>, 2020.

Jacob, D. J.: *Introduction to Atmospheric Chemistry*, Princeton University Press, 266 pp., 1999.

Jones, A. E., Anderson, P. S., Begoin, M., Brough, N., Hutterli, M. A., Marshall, G. J., Richter, A., Roscoe, H. K., and Wolff, E. W.: BrO, blizzards, and drivers of polar tropospheric ozone depletion events, 9, 4639–4652, <https://doi.org/10.5194/acp-9-4639-2009>, 2009.

Kaleschke, L., Richter, A., Burrows, J., Afe, O., Heygster, G., Notholt, J., Rankin, A. M., Roscoe, H. K., Hollwedel, J., Wagner, T., and Jacobi, H.-W.: Frost flowers on sea ice as a source of sea salt and their influence on tropospheric halogen chemistry, 31, <https://doi.org/10.1029/2004GL020655>, 2004.

Kalnay, E., Kanamitsu, M., Kistler, R., Collins, W., Deaven, D., Gandin, L., Iredell, M., Saha, S., White, G., Woollen, J., Zhu, Y., Chelliah, M., Ebisuzaki, W., Higgins, W., Janowiak, J., Mo, K. C., Ropelewski, C., Wang, J., Leetmaa, A., Reynolds, R., Jenne, R., and Joseph, D.: The NCEP/NCAR 40-Year Reanalysis Project, 77, 437–472, [https://doi.org/10.1175/1520-0477\(1996\)077<0437:TNYRP>2.0.CO;2](https://doi.org/10.1175/1520-0477(1996)077<0437:TNYRP>2.0.CO;2), 1996.

Kashiwase, H., Ohshima, K. I., Nihashi, S., and Eicken, H.: Evidence for ice-ocean albedo feedback in the Arctic Ocean shifting to a seasonal ice zone, 7, 8170, <https://doi.org/10.1038/s41598-017-08467-z>, 2017.

Kirtman, B., Power, S. B., Adedoyin, A. J., Boer, G. J., Bojariu, R., Camilloni, I., Doblus-Reyes, F., Fiore, A. M., Kimoto, M., Meehl, G., Prather, M., Sarr, A., Schar, C., Sutton, R., van Oldenborgh, G. J., Vecchi, G., and Wang, H.-J.: Chapter 11 - Near-term climate change: Projections and predictability, in: *Climate Change 2013: The Physical Science Basis*. IPCC Working Group I Contribution to AR5, edited by: IPCC, Cambridge University Press, Cambridge, 2013.

Knutson, T., Kossin, J. P., Mears, C., Perlwitz, J., Wehner, M. F., Wuebbles, D. J., Fahey, D. W., Hibbard, K. A., Dokken, D. J., Stewart, B. C., and Maycock, T. K.: Ch. 3: Detection and Attribution of Climate Change. *Climate Science Special Report: Fourth National Climate*

Assessment, Volume I, U.S. Global Change Research Program, <https://doi.org/10.7930/J01834ND>, 2017.

Krijger, J. M., Snel, R., Aben, I., and Landgraf, J.: Absolute calibration and degradation of SCIAMACHY/GOME reflectances, 2007.

Krishnan, S., Ekman, A. M. L., Hansson, H.-C., Riipinen, I., Lewinschal, A., Wilcox, L. J., and Dallafior, T.: The Roles of the Atmosphere and Ocean in Driving Arctic Warming Due to European Aerosol Reductions, 47, e2019GL086681, <https://doi.org/10.1029/2019GL086681>, 2020.

Kroon, M., Haan, J. F. de, Veeffkind, J. P., Froidevaux, L., Wang, R., Kivi, R., and Hakkarainen, J. J.: Validation of operational ozone profiles from the Ozone Monitoring Instrument, 116, <https://doi.org/10.1029/2010JD015100>, 2011.

Lelieveld, J., Gromov, S., Pozzer, A., and Taraborrelli, D.: Global tropospheric hydroxyl distribution, budget and reactivity, 16, 12477–12493, <https://doi.org/10.5194/acp-16-12477-2016>, 2016.

Levelt, P. F., Joiner, J., Tamminen, J., Veeffkind, J. P., Bhartia, P. K., Stein Zweers, D. C., Duncan, B. N., Streets, D. G., Eskes, H., van der A, R., McLinden, C., Fioletov, V., Carn, S., de Laat, J., DeLand, M., Marchenko, S., McPeters, R., Ziemke, J., Fu, D., Liu, X., Pickering, K., Apituley, A., González Abad, G., Arola, A., Boersma, F., Chan Miller, C., Chance, K., de Graaf, M., Hakkarainen, J., Hassinen, S., Ialongo, I., Kleipool, Q., Krotkov, N., Li, C., Lamsal, L., Newman, P., Nowlan, C., Suleiman, R., Tilstra, L. G., Torres, O., Wang, H., and Wargan, K.: The Ozone Monitoring Instrument: overview of 14 years in space, 18, 5699–5745, <https://doi.org/10.5194/acp-18-5699-2018>, 2018.

Lu, J. Y., Schroeder, W. H., Barrie, L. A., Steffen, A., Welch, H. E., Martin, K., Lockhart, L., Hunt, R. V., Boila, G., and Richter, A.: Magnification of atmospheric mercury deposition to polar regions in springtime: The link to tropospheric ozone depletion chemistry, *Geophysical Research Letters*, 28, 3219–3222, <https://doi.org/10.1029/2000GL012603>, 2001.

Manabe, S. and Wetherald, R. T.: The Effects of Doubling the CO₂ Concentration on the climate of a General Circulation Model, *J. Atmos. Sci.*, 32, 3–15, [https://doi.org/10.1175/1520-0469\(1975\)032<0003:TEODTC>2.0.CO;2](https://doi.org/10.1175/1520-0469(1975)032<0003:TEODTC>2.0.CO;2), 1975.

McElroy, M. B., Salawitch, R. J., and Wofsy, S. C.: Antarctic O₃: Chemical mechanisms for the spring decrease, 13, 1296–1299, <https://doi.org/10.1029/GL013i012p01296>, 1986.

Molina, M. J., Tso, T.-L., Molina, L. T., and Wang, F. C.-Y.: Antarctic Stratospheric Chemistry of Chlorine Nitrate, Hydrogen Chloride, and Ice: Release of Active Chlorine, 238, 1253–1257, <https://doi.org/10.1126/science.238.4831.1253>, 1987.

Mouginot, J., Rignot, E., Bjørk, A. A., van den Broeke, M., Millan, R., Morlighem, M., Noël, B., Scheuchl, B., and Wood, M.: Forty-six years of Greenland Ice Sheet mass balance from 1972 to 2018, *Proc Natl Acad Sci USA*, 116, 9239, <https://doi.org/10.1073/pnas.1904242116>, 2019.

Müller, M. D., Kaifel, A., Weber, M., and Burrows, J. P.: Neural network scheme for the retrieval of total ozone from Global Ozone Monitoring Experiment data, *Appl. Opt.*, AO, 41, 5051–5058, <https://doi.org/10.1364/AO.41.005051>, 2002.

Munro, R., Lang, R., Klaes, D., Poli, G., Retscher, C., Lindstrot, R., Huckle, R., Lacan, A., Grzegorski, M., Holdak, A., Kokhanovsky, A., Livschitz, J., and Eisinger, M.: The GOME-2 instrument on the Metop series of satellites: instrument design, calibration, and level 1 data processing – an overview, 9, 1279–1301, <https://doi.org/10.5194/amt-9-1279-2016>, 2016.

Nicely, J. M., Duncan, B. N., Hanisco, T. F., Wolfe, G. M., Salawitch, R. J., Deushi, M., Haslerud, A. S., Jöckel, P., Josse, B., Kinnison, D. E., Klekociuk, A., Manyin, M. E., Marécal, V., Morgenstern, O., Murray, L. T., Myhre, G., Oman, L. D., Pitari, G., Pozzer, A., Quaglia, I., Revell, L. E., Rozanov, E., Stenke, A., Stone, K., Strahan, S., Tilmes, S., Tost, H., Westervelt, D. M., and Zeng, G.: A Machine Learning Examination of Hydroxyl Radical Differences Among Model Simulations for CCMI-1, *Gases/Atmospheric Modelling/Troposphere/Chemistry* (chemical composition and reactions), <https://doi.org/10.5194/acp-2019-772>, 2019.

Nicolet, M.: On the molecular scattering in the terrestrial atmosphere : An empirical formula for its calculation in the homosphere, *Planetary and Space Science*, 32, 1467–1468, [https://doi.org/10.1016/0032-0633\(84\)90089-8](https://doi.org/10.1016/0032-0633(84)90089-8), 1984.

Perovich, D. K. and Richter-Menge, J. A.: Loss of Sea Ice in the Arctic, *Annu. Rev. Mar. Sci.*, 1, 417–441, <https://doi.org/10.1146/annurev.marine.010908.163805>, 2009.

Peterson, P. K., Pöhler, D., Zielcke, J., General, S., Frieß, U., Platt, U., Simpson, W. R., Nghiem, S. V., Shepson, P. B., Stirm, B. H., and Pratt, K. A.: Springtime Bromine Activation over Coastal and Inland Arctic Snowpacks, *ACS Earth Space Chem.*, 2, 1075–1086, <https://doi.org/10.1021/acsearthspacechem.8b00083>, 2018.

Pithan, F. and Mauritsen, T.: Arctic Amplification dominated by temperature feedbacks in contemporary climate models, 7, 181–184, <https://doi.org/10.1038/ngeo2071>, 2014.

Platt, U. and Perner, D.: Measurements of Atmospheric Trace Gases by Long Path Differential UV/Visible Absorption Spectroscopy, in: *Optical and Laser Remote Sensing*, edited by:

Killinger, D. K. and Mooradian, A., Springer, Berlin, Heidelberg, 97–105, https://doi.org/10.1007/978-3-540-39552-2_13, 1983.

Platt, U. and Stutz, J.: Differential Optical Absorption Spectroscopy: Principles and Applications, Springer-Verlag, Berlin Heidelberg, 2008.

Platt, U. and Wagner, T.: Satellite mapping of enhanced BrO concentrations in the troposphere, 395, 486–490, <https://doi.org/10.1038/26723>, 1998.

Rasp, S. and Lerch, S.: Neural Networks for Postprocessing Ensemble Weather Forecasts, *Mon. Wea. Rev.*, 146, 3885–3900, <https://doi.org/10.1175/MWR-D-18-0187.1>, 2018.

Research, N. C. for A. R. C. for A. and University, P. M. G. P. and C. R. C. O. S.: Arctic System Reanalysis version 2, <https://doi.org/10.5065/D6X9291B>, 2017.

Richter, A., Wittrock, F., Eisinger, M., and Burrows, J. P.: GOME observations of tropospheric BrO in northern hemispheric spring and summer 1997, *Geophys. Res. Lett.*, 25, 2683–2686, <https://doi.org/10.1029/98GL52016>, 1998.

Richter, A., Wittrock, F., Ladstätter-Weissenmayer, A., and Burrows, J. P.: Gome measurements of stratospheric and tropospheric BrO, *Advances in Space Research*, 29, 1667–1672, [https://doi.org/10.1016/S0273-1177\(02\)00123-0](https://doi.org/10.1016/S0273-1177(02)00123-0), 2002.

Ridley, B. A., Zeng, T., Wang, Y., Atlas, E. L., Browell, E. V., Hess, P. G., Orlando, J. J., Chance, K., and Richter, A.: An ozone depletion event in the sub-arctic surface layer over Hudson Bay, Canada, *J Atmos Chem*, 57, 255–280, <https://doi.org/10.1007/s10874-007-9072-z>, 2007.

Rinke, A., Maturilli, M., Graham, R. M., Matthes, H., Handorf, D., Cohen, L., Hudson, S. R., and Moore, J. C.: Extreme cyclone events in the Arctic: Wintertime variability and trends, *Environ. Res. Lett.*, 12, 094006, <https://doi.org/10.1088/1748-9326/aa7def>, 2017.

Roedel, W. and Wagner, T.: Physik unserer Umwelt: Die Atmosphäre, 5th ed., Springer Spektrum, <https://doi.org/10.1007/978-3-662-54258-3>, 2017.

Saiz-Lopez, A. and Glasow, R. von: Reactive halogen chemistry in the troposphere, 41, 6448–6472, <https://doi.org/10.1039/C2CS35208G>, 2012.

Salawitch, R. J.: Biogenic bromine, 439, 275–277, <https://doi.org/10.1038/439275a>, 2006.

Salawitch, R. J., Weisenstein, D. K., Kovalenko, L. J., Sioris, C. E., Wennberg, P. O., Chance, K., Ko, M. K. W., and McLinden, C. A.: Sensitivity of ozone to bromine in the lower stratosphere, 32, <https://doi.org/10.1029/2004GL021504>, 2005.

Sander, R. and Crutzen, P. J.: Model study indicating halogen activation and ozone destruction in polluted air masses transported to the sea, 101, 9121–9138, <https://doi.org/10.1029/95JD03793>, 1996.

Sander, R., Burrows, J., and Kaleschke, L.: Carbonate precipitation in brine ? a potential trigger for tropospheric ozone depletion events, 6, 4653–4658, 2006.

Screen, J. A.: Far-flung effects of Arctic warming, 10, 253–254, <https://doi.org/10.1038/ngeo2924>, 2017.

Seigneur, C. and Lohman, K.: Effect of bromine chemistry on the atmospheric mercury cycle, 113, <https://doi.org/10.1029/2008JD010262>, 2008.

Seinfeld, J. H., Pandis, S. N., and Noone, K.: Atmospheric Chemistry and Physics: From Air Pollution to Climate Change, *Physics Today*, 51, 88–90, <https://doi.org/10.1063/1.882420>, 1998.

Sellers, W. D.: A Global Climatic Model Based on the Energy Balance of the Earth-Atmosphere System, *J. Appl. Meteor.*, 8, 392–400, [https://doi.org/10.1175/1520-0450\(1969\)008<0392:AGCMBO>2.0.CO;2](https://doi.org/10.1175/1520-0450(1969)008<0392:AGCMBO>2.0.CO;2), 1969.

Seo, S., Richter, A., Blechschmidt, A.-M., Bougoudis, I., and Burrows, J. P.: First high-resolution BrO column retrievals from TROPOMI, 12, 2913–2932, <https://doi.org/10.5194/amt-12-2913-2019>, 2019.

Seo, S., Richter, A., Blechschmidt, A.-M., Bougoudis, I., and Burrows, J. P.: Spatial distribution of enhanced BrO and its relationship to meteorological parameters in Arctic and Antarctic sea ice regions, 20, 12285–12312, <https://doi.org/10.5194/acp-20-12285-2020>, 2020.

Serdyuchenko, A., Gorshelev, V., Weber, M., Chehade, W., and Burrows, J. P.: High spectral resolution ozone absorption cross-sections – Part 2: Temperature dependence, 7, 625–636, <https://doi.org/10.5194/amt-7-625-2014>, 2014.

Serreze, M. C. and Barrett, A. P.: Characteristics of the Beaufort Sea High, *J. Climate*, 24, 159–182, <https://doi.org/10.1175/2010JCLI3636.1>, 2010.

Serreze, M. C. and Barry, R. G.: Processes and impacts of Arctic Amplification: A research synthesis, *Global and Planetary Change*, 77, 85–96, <https://doi.org/10.1016/j.gloplacha.2011.03.004>, 2011.

Serreze, M. C. and Francis, J. A.: The Arctic Amplification Debate, *Climatic Change*, 76, 241–264, <https://doi.org/10.1007/s10584-005-9017-y>, 2006.

Serreze, M. C. and Meier, W. N.: The Arctic's sea ice cover: trends, variability, predictability, and comparisons to the Antarctic, 1436, 36–53, <https://doi.org/10.1111/nyas.13856>, 2019.

Sihler, H., Platt, U., Beirle, S., Marbach, T., Kühl, S., Dörner, S., Verschaeve, J., Frieß, U., Pöhler, D., Vogel, L., Sander, R., and Wagner, T.: Tropospheric BrO column densities in the Arctic derived from satellite: retrieval and comparison to ground-based measurements, 5, 2779–2807, <https://doi.org/10.5194/amt-5-2779-2012>, 2012.

Simpson, W. R., Carlson, D., Hönninger, G., Douglas, T. A., Sturm, M., Perovich, D., and Platt, U.: First-year sea-ice contact predicts bromine monoxide (BrO) levels at Barrow, Alaska better than potential frost flower contact, 7, 621–627, 2007.

Simpson, W. R., Peterson, P. K., Frieß, U., Sihler, H., Lampel, J., Platt, U., Moore, C., Pratt, K., Shepson, P., Halfacre, J., and Nghiem, S. V.: Horizontal and vertical structure of reactive bromine events probed by bromine monoxide MAX-DOAS, *Atmos. Chem. Phys.*, 17, 9291–9309, <https://doi.org/10.5194/acp-17-9291-2017>, 2017.

Sinnhuber, B.-M., Rozanov, A., Sheode, N., Afe, O. T., Richter, A., Sinnhuber, M., Wittrock, F., Burrows, J. P., Stiller, G. P., Clarmann, T. von, and Linden, A.: Global observations of stratospheric bromine monoxide from SCIAMACHY, 32, <https://doi.org/10.1029/2005GL023839>, 2005.

Steffen, W., Crutzen, P. J., and McNeill, J. R.: The Anthropocene: Are Humans Now Overwhelming the Great Forces of Nature, *ambi*, 36, 614–621, [https://doi.org/10.1579/0044-7447\(2007\)36\[614:TAAHNO\]2.0.CO;2](https://doi.org/10.1579/0044-7447(2007)36[614:TAAHNO]2.0.CO;2), 2007.

Stjern, C. W., Lund, M. T., Samset, B. H., Myhre, G., Forster, P. M., Andrews, T., Boucher, O., Faluvegi, G., Fläschner, D., Iversen, T., Kasoar, M., Kharin, V., Kirkevåg, A., Lamarque, J.-F., Olivié, D., Richardson, T., Sand, M., Shawki, D., Shindell, D., Smith, C. J., Takemura, T., and Voulgarakis, A.: Arctic Amplification Response to Individual Climate Drivers, 124, 6698–6717, <https://doi.org/10.1029/2018JD029726>, 2019.

Stone, D., Sherwen, T., Evans, M. J., Vaughan, S., Ingham, T., Whalley, L. K., Edwards, P. M., Read, K. A., Lee, J. D., Moller, S. J., Carpenter, L. J., Lewis, A. C., and Heard, D. E.: Impacts of bromine and iodine chemistry on tropospheric OH and HO₂: comparing observations with box and global model perspectives, 18, 3541–3561, <https://doi.org/10.5194/acp-18-3541-2018>, 2018.

Stroeve, J. C., Kattsov, V., Barrett, A., Serreze, M., Pavlova, T., Holland, M., and Meier, W. N.: Trends in Arctic sea ice extent from CMIP5, CMIP3 and observations, 39, <https://doi.org/10.1029/2012GL052676>, 2012.

Tanzi, C., Snel, R., Hasekamand, O., and Aben, I.: Degradation of UV earth albedo observations by GOME, 2000.

Theys, N., Van Roozendael, M., Errera, Q., Hendrick, F., Daerden, F., Chabrillat, S., Dorf, M., Pfeilsticker, K., Rozanov, A., Lotz, W., Burrows, J. P., Lambert, J.-C., Goutail, F., Roscoe, H. K., and De Mazière, M.: A global stratospheric bromine monoxide climatology based on the BASCOE chemical transport model, 9, 831–848, <https://doi.org/10.5194/acp-9-831-2009>, 2009.

Theys, N., Van Roozendael, M., Hendrick, F., Yang, X., De Smedt, I., Richter, A., Begoin, M., Errera, Q., Johnston, P. V., Kreher, K., and De Mazière, M.: Global observations of tropospheric BrO columns using GOME-2 satellite data, 11, 1791–1811, <https://doi.org/10.5194/acp-11-1791-2011>, 2011.

Toohey, D. W., Anderson, J. G., Brune, W. H., and Chan, K. R.: In situ measurements of BrO in the Arctic stratosphere, 17, 513–516, <https://doi.org/10.1029/GL017i004p00513>, 1990.

Toyota, K., McConnell, J. C., Lupu, A., Neary, L., McLinden, C. A., Richter, A., Kwok, R., Semeniuk, K., Kaminski, J. W., Gong, S.-L., Jarosz, J., Chipperfield, M. P., and Sioris, C. E.: Analysis of reactive bromine production and ozone depletion in the Arctic boundary layer using 3-D simulations with GEM-AQ: inference from synoptic-scale patterns, 11, 3949–3979, <https://doi.org/10.5194/acp-11-3949-2011>, 2011.

Tschudi, M. and Univ Of CO: EASE-Grid Sea Ice Age, <https://doi.org/10.5067/UTAV7490FEPB>, 2019.

Tuckermann, M., Ackermann, R., Golz, C., Lorenzen-Schmidt, H., Senne, T., Stutz, J., Trost, B., Unold, W., and Platt, U.: DOAS-observation of halogen radical-catalysed arctic boundary layer ozone destruction during the ARCTOC-campaigns 1995 and 1996 in Ny-Alesund, Spitsbergen, *Tellus B*, 49, 533–555, <https://doi.org/10.1034/j.1600-0889.49.issue5.9.x>, 1997.

Van Roozendael, M., De Smedt, I., Fayt, C., Wittrock, F., Richter, A., and Afe, O.: First Validation of SCIAMACHY BrO Columns, 2004.

Vlahavas, P. K., Bassiliades, N., Kokkoras, F., and Sakellariou, I.: Artificial Intelligence-3rd Edition, 2011.

Vogt, R., Crutzen, P. J., and Sander, R.: A mechanism for halogen release from sea-salt aerosol in the remote marine boundary layer, 383, 327–330, <https://doi.org/10.1038/383327a0>, 1996.

Vountas, M., Rozanov, V. V., and Burrows, J. P.: RING EFFECT: IMPACT OF ROTATIONAL RAMAN SCATTERING ON RADIATIVE TRANSFER IN EARTH'S ATMOSPHERE, *Journal*

of Quantitative Spectroscopy and Radiative Transfer, 60, 943–961, [https://doi.org/10.1016/S0022-4073\(97\)00186-6](https://doi.org/10.1016/S0022-4073(97)00186-6), 1998.

Wagner, T., Leue, C., Wenig, M., Pfeilsticker, K., and Platt, U.: Spatial and temporal distribution of enhanced boundary layer BrO concentrations measured by the GOME instrument aboard ERS-2, 106, 24225–24235, <https://doi.org/10.1029/2000JD000201>, 2001.

Wahner, A., Ravishankara, A. R., Sander, S. P., and Friedl, R. R.: Absorption cross section of BrO between 312 and 385 nm AT 298 and 223 K, Chemical Physics Letters, 152, 507–512, [https://doi.org/10.1016/0009-2614\(88\)80450-0](https://doi.org/10.1016/0009-2614(88)80450-0), 1988.

Wallace, J. M. and Hobbs, P. V.: Atmospheric Science: An Introductory Survey: Second Edition, 1 pp., 2006.

Wang, S.-C.: Artificial Neural Network, in: Interdisciplinary Computing in Java Programming, edited by: Wang, S.-C., Springer US, Boston, MA, 81–100, https://doi.org/10.1007/978-1-4615-0377-4_5, 2003.

Wang, Z., Li, Z., Zeng, J., Liang, S., Zhang, P., Tang, F., Chen, S., and Ma, X.: Spatial and Temporal Variations of Arctic Sea Ice From 2002 to 2017, 7, e2020EA001278, <https://doi.org/10.1029/2020EA001278>, 2020.

Warsito, B., Santoso, R., Suparti, and Yasin, H.: Cascade Forward Neural Network for Time Series Prediction, J. Phys.: Conf. Ser., 1025, 012097, <https://doi.org/10.1088/1742-6596/1025/1/012097>, 2018.

Weatherhead, E. C., Reinsel, G. C., Tiao, G. C., Meng, X.-L., Choi, D., Cheang, W.-K., Keller, T., DeLuisi, J., Wuebbles, D. J., Kerr, J. B., Miller, A. J., Oltmans, S. J., and Frederick, J. E.: Factors affecting the detection of trends: Statistical considerations and applications to environmental data, 103, 17149–17161, <https://doi.org/10.1029/98JD00995>, 1998.

Weber, M., Coldewey-Egbers, M., Fioletov, V. E., Frith, S. M., Wild, J. D., Burrows, J. P., Long, C. S., and Loyola, D.: Total ozone trends from 1979 to 2016 derived from five merged observational datasets – the emergence into ozone recovery, 18, 2097–2117, <https://doi.org/10.5194/acp-18-2097-2018>, 2018.

Yang, W. and Magnusdottir, G.: Year-to-year Variability in Arctic Minimum Sea Ice Extent and its Preconditions in Observations and the CESM Large Ensemble Simulations, 8, 9070, <https://doi.org/10.1038/s41598-018-27149-y>, 2018.

Yang, X., Blechschmidt, A.-M., Bognar, K., McClure–Begley, A., Morris, S., Petropavlovskikh, I., Richter, A., Skov, H., Strong, K., Tarasick, D., Uttal, T., Vestenius, M., and Zhao, X.: Pan-

Arctic surface ozone: modelling vs measurements, 1–33, <https://doi.org/10.5194/acp-2019-984>, 2020.

Zhao, X., Strong, K., Adams, C., Schofield, R., Yang, X., Richter, A., Friess, U., Blechschmidt, A.-M., and Koo, J.-H.: A case study of a transported bromine explosion event in the Canadian high arctic, 121, 457–477, <https://doi.org/10.1002/2015JD023711>, 2016.

Zurada, J. M.: Introduction To Artificial Neural Systems, 1992.
